



ISSN 1811-1165 (Print)  
ISSN 2413-2179 (Online)

# EURASIAN PHYSICAL TECHNICAL JOURNAL

VOLUME 20, NO. 4(46), 2023

[phtj.buketov.edu.kz](http://phtj.buketov.edu.kz)

# EURASIAN PHYSICAL TECHNICAL JOURNAL

p - ISSN 1811-1165  
e - ISSN 2413-2179

Volume 20, No. 4(46), 2023

1<sup>st</sup> issue – March, 2004

## Journal Founder:

**NLC “KARAGANDY UNIVERSITY  
OF THE NAME OF ACADEMICIAN  
E.A. BUKETOV”**

<https://phtj.buketov.edu.kz>

Registration Certificate No. 4382-Zh,  
November 7, 2003.

Re-registration Certificate No. KZ50VPY00027647,  
October 6, 2020 issued by Information Committee  
of the Ministry of Information and Public  
Development of the Republic of Kazakhstan

## Contact information:

Editorial board of EAPhTJ (Build. 2, room 216)  
Karaganda Buketov University  
Universitetskaya Str., 28, Karaganda,  
Kazakhstan, 100024  
Subscription index: 75240

Tel: +7(7212) 77-04-03  
Fax: +7(7212) 35-63-98  
E-mail: [ephtj@mail.ru](mailto:ephtj@mail.ru), [ephtj2021@gmail.com](mailto:ephtj2021@gmail.com)

Signed to print on 19.12.2023.  
Format 60x84 1/8. Offset paper.  
Volume 18.5 p.sh. Circulation 300 copies.  
Order No. 119.

Printed in the Publishing House of  
Karagandy University of the name  
of academician E.A. Buketov

Tel. (7212) 35-63-16.  
E-mail: [izd\\_kargu@mail.ru](mailto:izd_kargu@mail.ru)

## Chief EDITOR

**Sakipova S.E.**, Karaganda Buketov University, Karaganda,  
Kazakhstan

## EDITORIAL BOARD

**Aringazin A.K.**, L.N. Gumilyov Eurasian National University,  
Astana, Kazakhstan

**Dzhumanov S.**, Institute of Nuclear Physics, Uzbekistan Academy  
of Sciences, Tashkent, Uzbekistan

**Ibrayev N.Kh.**, Institute of Molecular Nanophotonics, Karaganda  
Buketov University, Karaganda, Kazakhstan

**Jakovics A.**, Institute of Numerical Modelling, University of Latvia,  
Riga, Latvia

**Kadyrzhanov K.K.**, L.N. Gumilyov Eurasian National University,  
Astana, Kazakhstan

**Kucherenko M.G.**, Director of the Laser and Information  
Biophysics Centre, Orenburg State University, Orenburg, Russia

**Kuritnyk I.P.**, Department of Electronics and Automation, High  
school in Oswiecim, Poland

**Kushpil S.**, Heavy Ion Group, Nuclear Physics Institute of the  
Czech Academy of Science, Řež near Prague, Czech Republic

**Miau J.J.**, Department of Aeronautics and Astronautics, National  
Cheng Kung University, Tainan, Taiwan

**Miroshnichenko A.S.**, Department of Physics and Astronomy,  
University of North Carolina at Greensboro, North Carolina, USA

**Narimanova G.N.**, Tomsk State University of Control Systems and  
Radioelectronics, Tomsk, Russia

**Potapov A.A.**, V.A. Kotelnikov Institute of Radio Engineering and  
Electronics of RAS, Moscow, Russia

**Pribaturin N.A.**, Institute of Thermal Physics, SB RAS,  
Novosibirsk, Russia

**Saulebekov A.O.**, Kazakhstan Branch of Lomonosov Moscow  
State University, Astana, Kazakhstan

**Senyut V.T.**, Joint Institute of Mechanical Engineering of National  
Academy of Sciences of Belarus, Minsk, Belarus

**Shrager E.R.**, National Research Tomsk State University, Tomsk,  
Russia

**Stoev M.**, South-West University «Neofit Rilski», Blagoevgrad,  
Bulgaria

**Suprun T.**, Institute of Engineering Thermophysics of NASU, Kyiv,  
Ukraine

**Trubitsyn A.A.**, Ryazan State Radio Engineering University,  
Ryazan, Russia

**Zeinidenov A.K.**, Karaganda Buketov University, Karaganda,  
Kazakhstan

**Zhanabaev Z.Zh.**, Al-Farabi Kazakh National State University,  
Almaty, Kazakhstan

## TECHNICAL EDITOR

**Kambarova Zh.T.**, Karaganda Buketov University, Karaganda,  
Kazakhstan

## Eurasian Physical Technical Journal, 2023, Vol. 20, No. 4(46)

## CONTENTS

<b>PREFACE</b> .....		4
<b>MATERIALS SCIENCE</b>		
1	<b>Tareq M.H., Lafta Sadeq H., Hussain Wafaa A.</b> INVESTIGATION THE MAGNETIC PROPERTIES OF $Cs_yCo_{1-0.5y}Fe_2O_4$ NANOPARTICLES AT LOW MOLAR RATIO VARIATION. ....	6
2	<b>Soldatkhan D., Amangeldi N., Makhanov K.M., Smagulov Zh.K., Anuar A., Mauzey B.</b> APPLICATION OF THE NEW B3Y-FETAL POTENTIAL IN THE SEMI-MICROSCOPIC ANALYSIS OF THE SCATTERING OF ACCELERATED ${}^6Li$ - LITHIUM AND ${}^{16}O$ - OXYGEN NUCLEI FROM THE ${}^{12}C$ - CARBON NUCLEUS. ....	17
3	<b>Nuritdinov I., Tashmetov M.Yu., Khodzhaev U.O., Umarov S.Kh., Khallokov F.K.</b> INFLUENCE OF ELECTRON IRRADIATION ON THE CRYSTAL STRUCTURE, SURFACE MICRORELIEF AND BANDGANP WIDTH OF THE TRIPLE CRYSTALS OF IRON DOPED MONOSELINIDE OF THALLIUM AND INDIUM. ....	23
4	<b>Kopbalina K.B., Makhmutova A.S., Turdybekov D.M., Turdybekov K.M., Tolenova G.K.</b> QUANTUM-CHEMICAL STUDY OF THE STRUCTURE AND PROPERTIES OF MOLECULE OF THE LUPININE ALKALOID DERIVATIVE.....	33
5	<b>Kayumova A.S., Serikov T.M., Omarova G.S., Dzhakupova M.S.</b> EFFECT OF THE CONCENTRATION OF SILVER NANOPARTICLES ON THE PHOTOCATALYTIC ACTIVITY OF TITANIUM DIOXIDE NANORODS.....	39
<b>ENERGY</b>		
6	<b>Bezrodny M.K., Maistrenko O.O.</b> THERMODYNAMIC ANALYSIS OF THE HEAT PUMP - ADSORPTION AIR DRYING SYSTEM USING A RECOVERY. ....	46
7	<b>Medetbekov B.S., Vurim A.D., Prozorova I.V., Popov Yu.A.</b> FISSION PRODUCT RELEASE FROM HIGH AND LOW-ENRICHED URANIUM FUELS OF THE IVG.1M RESEARCH REACTOR. ....	54
<b>ENGINEERING</b>		
8	<b>Tsyganov V.V., Sheyko S.P., Shalomeev V.A., Vodennikova O.S., Kulabnieva O.A.</b> ACCELERATED TESTING OF MECHANICAL AND CHEMICAL EFFECT OF THE ENVIRONMENT ON WEAR RESISTANCE OF PARTS OF TRIBOCOUPLES UNDER COMPLEX DYNAMIC LOADING. ....	61
9	<b>Shynarbek A.B., Rakhadilov B.K., Stepanova O.A., Kusainov R.K., Zhassulan A.Zh., Daumova G.K.</b> INVESTIGATION OF THE PROCESS OF ELECTRIC ARC METALIZATION OF COATINGS FROM STEEL 30KhGSA. ....	67
10	<b>Ibraimov M.K., Kozhagulov Y.T., Zhexebay D.M., Sarmanbetov S.A.</b> IMPLEMENTATION OF FUNCTIONAL BLOCK RADIO UNIT BASED ON SYSTEM-ON-CHIP .....	74

11	<b>Loboda Yu., Galtseva O., Biryukova N.</b> STUDYING THE PHYSICAL CHARACTERISTICS OF THE SNAKE ROBOT MOTION BASED ON THE “BIOLOID PREMIUM KIT” CONSTRUCTION .....	81
12	<b>Turlykozhaeva D., Ussipov N.M., Baigalieva A., Temesheva S., Bolysbay A., Abdrakhmatova G., Akhtanov S.</b> ROUTING METRIC AND PROTOCOL FOR WIRELESS MESH NETWORK BASED ON INFORMATION ENTROPY THEORY.....	90
13	<b>Plotnikov I.B., Korotkiy I.A., Neverov E.N., Korotkaya E.V., Plotnikova L.V.</b> MODERNIZATION OF THE MECHATRONIC WATER TREATMENT MODULE FOR PROCESSING PLANTS OF THE AGRO-INDUSTRIAL COMPLEX.....	99
14	<b>Zhanabaev Z.Zh., Akhtanov S.N., Tileu A.O., Almen D.B.</b> COHERENT AMPLITUDE MODULATION IN A LASER GAS SENSOR.....	111
15	<b>Malikov V.N., Katasonov A.O., Ishkov A.V., Fadeev D.A., Voinash S.A., Vornacheva I.V., Zagidullin R.R., Shmykova P.A.</b> EDDY CURRENT METHOD FOR STUDYING INHOMOGENEITIES AND DEFECTS IN THIN METAL FILMS.....	116
<b>PHYSICS AND ASTRONOMY</b>		
16	<b>Shishulin A.V., Potapov A.A., Shishulina A.V.</b> FRACTAL NANOPARTICLES OF PHASE-SEPARATING SOLID SOLUTIONS: MORPHOLOGY - DEPENDENT PHASE EQUILIBRIA IN TUNGSTEN HEAVY PSEUDO- ALLOYS.....	125
	<b>SUMMARIES</b> .....	133
	<b>INFORMATION ABOUT AUTHORS</b> .....	143
	<b>GUIDELINES FOR AUTHOR</b> .....	147

**Dear authors and readers!**

**Dear colleagues!**

In the Preface, we traditionally write to authors and readers about the most important achievements of the Eurasian Physical Technical Journal as a peer-reviewed scientific journal. In 2023, our journal is included in the Q3 quarter by all 4 scientific areas: Energy; Engineering; Materials Science; Physics and Astronomy. Indexing of the journal in the Scopus database has been continue. As of December 5, 2023, the CiteScoreTracker rating is 1.1 with max percentile 25% on Engineering area. In 2023, a large amount of information was processed, website materials were edited in accordance with international criteria, information blocks are regularly updated, <https://phtj.buketov.edu.kz/index.php/EPTJ/index>.

During 2023, according to statistical data, the journal's website received 130 materials, of which the proportion of rejected materials was 51%. In four 2023 issues of Eurasian phys. tech.j." 51 articles were published. The geography of authors who presented new research results aimed at solving current problems of technical physics has expanded.

In this issue, the "Materials Science" section presents new original results on the study of the properties of various materials. Readers will be interested in the results of a "study on the effect of replacing ferrite with previously unused elements to control magnetic properties" by researchers of Baghdad University of Technology, Iraq. In the article, scientists from Astana analyzed experimentally obtained elastic scattering data within the framework of the optical model and the binary fold model." In the work of scientists from Uzbekistan, "the influence of electron irradiation on the structure, surface morphology and band gap of mono- and polycrystals of iron-doped ternary crystals of thallium and indium monoselenides was studied. It has been established that "synthesized polycrystalline samples, as well as grown single crystals of thallium and indium monoselenides are single-phase."

In the domestic authors paper, a "quantum chemical study of the structure and properties of the lupinine alkaloid derivative molecule was carried out," the geometric characteristics of which confirmed that this molecule is a rigid reagent." In an article by our university staff, the "influence of the silver nanoparticles concentration in films made from titanium dioxide nanorods on their photocatalytic activity was studied."

In an article in the "Energy" section, Kyiv authors, based on thermodynamic analysis, showed that the use of "an integrated air-drying system significantly reduces specific energy costs," and its efficiency, regardless of the parameters of the outside air, is superior to similar systems without a recuperator.

In an article on nuclear energy by authors from Kurchatov, based on the results of "testing water-cooled technological channels with low-enriched fuel in the IVG.1M reactor, were done comparative measurements of the content of fission products and activation products in the coolant of technological channels" with low-enriched and highly enriched fuel".

The "Engineering" section offers ways to solve pressing problems of modern communication systems, various automation and control technologies. Authors from Zaporozhie, Ukraine studied "the wear of parts of tribo-couplings under conditions of complex dynamic loading. The possibility of assessing the effectiveness of the influence of destruction products of high-molecular compounds in the composition of the cutting fluid on the wear resistance of metals in the contact zone of tribological interfaces" has been shown. The article by East Kazakhstani authors examines "technological modes of electric arc metallization of 30KhGSA steel wires, affecting the structure formation and properties of coatings." Almaty scientists presented the results of "the implementation of a functional block of a radio device based on a system-on-chip, where the main attention is paid to the integration of blocks of a radio device, such as modulation and fast Fourier transform, on programmable gate arrays." The authors from Tomsk examined "the physical characteristics of the

---

---

movement of a snake robot, which will allow both an industrial robotic arm and a mobile robot to move in various environmental conditions.”

Domestic researchers presented “a routing algorithm based on the theory of information entropy to calculate an indicator that takes into account the probability of packet loss.” The developed “algorithm is shown to outperform traditional routing methods in optimizing data transmission quality and overall network efficiency.” Authors from Kemerovo “upgraded the mechatronic water treatment module for processing industries of the agro-industrial complex, which uses “cryoconcentration, which consists in the crystallization of moisture with subsequent displacement of the solid phase.”

The article by Almaty authors examines an urgent problem of modern science and technology - non-contact “determination of the type and concentration of gas using a laser.” Based on spectral analysis, it is shown that “the corresponding power spectra are sensitive to low-frequency fluctuations of molecules and their clumps.” The article by Altai scientists presents an original “design of a subminiature eddy current transducer designed to study the electrical conductivity, thickness and degree of damage of thin metal films,” for which “a hardware and software complex was designed” to control it.

The article in the “Physics and Astronomy” section is devoted to the study of the physicochemical properties of nanostructured heavy tungsten pseudoalloys, which are used in modern powder metallurgy. In the work of Russian authors, “the dependence of phase equilibria on morphology for nanoparticles with a core-shell structure of an exfoliating solid solution was thermodynamically modeled using the example of a heavy W-Cr alloy. The morphology of nanoparticles was specified using fractal geometry methods.”

The article in the “Physics and Astronomy” section is devoted to the study of the physicochemical properties of nanostructured heavy tungsten pseudo-alloys, which are used in modern powder metallurgy. Russian authors, “using the example of a heavy W-Cr alloy, the dependence of phase equilibria on morphology for nanoparticles with a core-shell structure of an exfoliating solid solution was thermodynamically modeled. The morphology of the nanoparticles was refined using fractal geometry methods.”

We hope that the information presented in this issue will be interesting and useful to scientists, teachers, researchers, doctoral students and undergraduates. I would like the presented research and development results to be used in practice and in production in the future.

I would especially like to express our deep gratitude to our reviewers for their objective and qualified examination of materials, which helps ensure the quality of articles. The valuable and helpful recommendations of reviewers contributed to the production of this issue. We look forward to fruitful cooperation in the future.

We are really appreciated our authors, editors and reviewers for choosing our journal and contributing to the creation of present and future issues.

We hope to see you among our readers and authors of the next issues, where the publish review articles by leading scientists on current and priority areas of modern physics and technology will be planned.

Happy New 2024 Year!

With wishes of health and prosperity to all our authors, editors and readers,  
Editor-in-chief,  
Professor Sakipova Saule  
December, 2023

## INVESTIGATION THE MAGNETIC PROPERTIES OF $Cs_yCo_{1-0.5y}Fe_2O_4$ NANOPARTICLES AT LOW MOLAR RATIO VARIATION

Tareq M.H., Lafta Sadeq H., Hussain Wafaa A.

Applied Science Department, University of Technology, Iraq, Baghdad

*The effect of substitution ferrite by previously not used elements to control magnetic properties is of great interest to researchers. This study illustrates the effect of low substitution of Cs, with molar ratios of  $y$  of 0.0, 0.05, 0.15, and 0.25 on the structural and magnetic properties of  $Cs_yCo_{1-0.5y}Fe_2O_4$  nanoparticles. The synthesizing method was the co-precipitation method. The metal chlorides were used to perform the reaction in the distilled water using NaOH to reach a pH of 10. The X-ray diffraction, Field Emission Scanning Electron Microscopy, Electron Dispersive X-ray and Vibrating Sample Magnetometry analyses were conducted for all samples. All samples had the patterns of the spinel structure coincide to a high degree with the Co ferrite pattern. There was a general increase in the lattice constant with the increase in the Cs content, while the crystallite size decreased from about 18 to 12.2 nm as the molar ratio increased from 0 to 0.25. The Electron Microscopy investigation showed that all samples owing spherical nanoparticles with no other shapes. The average particle sizes were between 40 to 60 nm, which increased  $Cs^{1+}$  content. The magnetic parameters mainly showed a relatively high coercivity (wide loops) and a decrease in magnetization saturation (down to 50.43 emu/g), crystalline anisotropic constant, and the squareness ratio.*

**Keywords:** Cesium Cobalt Ferrite, Structural properties, Hysteresis loop, Nanoparticles, Magnetization.

### 1. Introduction

Spinel ferrite nanoparticles of the composition ( $MFe_2O_4$ ) have attracted considerable interest due to their unique chemical and physical properties. Cesium Cobalt ferrites are hard ferrite materials because of their excellent chemical stability and mechanical hardness. Cobalt ferrite is an important material because of its excellent properties, such as moderate saturation magnetization, large coercivity, large magneto-crystalline anisotropy, high Curie temperature, high electrical resistivity, and high stability [1].

Ferrites are prepared by various methods including such as sol-gel, hydrothermal, microemulsion, thermal decomposition, co-precipitation methods, hydrothermal and solvothermal [2], etc. The main difficulty during synthesis by these methods is to control the particle size and shape in addition to the purity of the product phase. Among these methods, is the co-precipitation method, which has different advantages like its production of inexpensive nanomaterials, less energy requirement, uniformity in particle size, easy experimental conditions adjusting, and easy removal of soluble impurities [3]. Changing the experimental conditions in the co-precipitation synthesis may lead to tailoring the morphological, magnetic, electric, and optical behavior of the produced particles [4]. In the co-precipitation method, nanoparticles are synthesized by adjusting the concentration of precipitating agents to produce stable nanoparticles. On the other hand, the precipitating agents play an important role in determining the various properties of materials. The strength of bases strongly influences the rate of reaction. NaOH has ionic bonding whereas  $NH_4OH$  has covalent bonding due to which the reaction rate with other ions could be different [5]. It may lead to different growth and crystallization rates, which could affect the various properties of the synthesized material.

The physical properties of ferrite may be controlled by alteration of the particle size, shape, cation distribution in their lattices, and/or composition [6]. The wide range of each property determines the application of ferrite. These applications extend to various fields including the automobile industry, ultrasonic generation and detection, magneto-restrictive filters, sensors, transformers, and high-density recording industries as well as in the medical industry [7].

Various literature deals with synthesizing Co ferrite by the co-precipitation method, but nearly no study deals with Co ferrite properties due to substitution by Cs. Houshiar et al. [7], prepared Co ferrite nanoparticles by co-precipitation method where metal chlorides as starting materials and sodium hydroxide are used as a precipitating agent. The obtained sample was heated at 600°C for 10h. X-ray analysis reported

that the crystallite size of the prepared sample was 49.5nm. Vibrating Sample Magnetometry (VSM) study showed that the saturation magnetization ( $M_s$ ) of the synthesized sample was 55.8 emu/g and coercivity ( $H_c$ ) was 850 Oe. Surface morphology was studied by SEM and by Transmission Electron Microscopy (TEM) images. Devi Gole et al. [8], synthesized Co ferrite with different pH via the co-precipitation method. The X-ray diffraction (XRD) pattern of this study investigated the lattice parameter varied from 8.4057 to 8.3754Å for different pH and crystallite size varied in the range of 328 to 351Å. The in-vitro antibacterial activity reported that cobalt ferrite at pH of 7 showed the highest antibacterial effects and cobalt ferrite at pH of 8 showed antifungal effects. Kim et al., [9] fabricated cobalt ferrite by co-precipitation technique using chlorides are precursors and sodium hydroxide as a precipitating agent. The authors reported the structural, magnetic, and Mossbauer studies of obtained samples. X-ray patterns of prepared samples have been taken at various temperatures. XRD analysis revealed that the average particle size increased with increasing temperature. The morphology of samples was carried out by TEM images.

Ferrites, especially Cs ferrite and Co ferrite, have promising applications in various fields of magnetics, electronics, and biomedical sciences [5]. Alteration and controlling magnetic properties is regarded as a great challenge aim for most researchers in the field of magnetic materials. The object of this work is to study the effect of variation Cs content, at a low ratio, on the  $Cs_yCo_{1-0.5y}Fe_2O_4$  ferrite structural and magnetic properties, prepared by the Co-precipitation route. To the best of the authors' knowledge, it is the first time to synthesize such nanoparticles of ferrite and investigate their properties.

## 2. Experimental part

The starting materials for synthesizing the  $Cs_yCo_{1-0.5y}Fe_2O_4$  nanoparticles were cobalt di-chloride  $CoCl_2$ , cesium di-chloride ( $CsCl_2$ ), iron tri-chloride ( $FeCl_3$ ), sodium hydroxide (NaOH) and distilled water. Preparation of the  $Cs_yCo_{1-0.5y}Fe_2O_4$  by co-precipitation wet method involved weighting of the mentioned salts to verify the molar ratios ( $y$ ) of 0.0, 0.05, 0.15, and 0.25. The weights of the salts, for each sample (molar-ratio) are shown in Table 1.

**Table 1.** The weights of the precursors (metal salts) at each molar ratio ( $y$ ).

Sample	$y$	Weight of $CsCl$ (g) ( $M=168.36$ g/mol)	Weight of $CoCl_2 \cdot 6H_2O$ (g) ( $M=237.9309$ g/mol)	Weight of $FeCl_3$ (g) ( $M=162.2$ g/mol)
S1	0	0	2.3793	3.2440
S2	0.05	0.16835	4.6396	6.488
S3	0.15	0.5051	4.4017	6.488
S4	0.25	0.8418	4.1638	6.488

The next step is mixing the salts together with 150ml of distilled water under strong stirring to prepare a clear precursor solution. Then, adding NaOH dropwise to the solution up to make pH of 10, associated continuing with magnetic stirring to ensure the solution homogeneity. After that, the suspension was heated at 80 for 1h. This is followed by washing the suspension with distilled water several times to remove soluble impurities of salts. The next step is drying the suspension with centrifugal tubes and heating it in an oven at 80°C. Finally, a heat treatment for 4h at 250°C was conducted to accomplish the calcination. The synthesizing steps are shown in the block diagram in Fig.1.

The resulting nanoparticles for the four samples were subjected to different structural and magnetic analyses, which were XRD Shimadzu 6000 as the x-ray diffractometer, Scanning Electron Microscope (SEM) MIRA3 TESCAN as the scanning electron microscope, ALPHA II Compact FTIR Spectrometer as the Fourier Transform Infrared Spectroscopy (FTIR) device, and MDK as the VSM device at 300K temperature with an applied magnetic field 30.000 Oe.

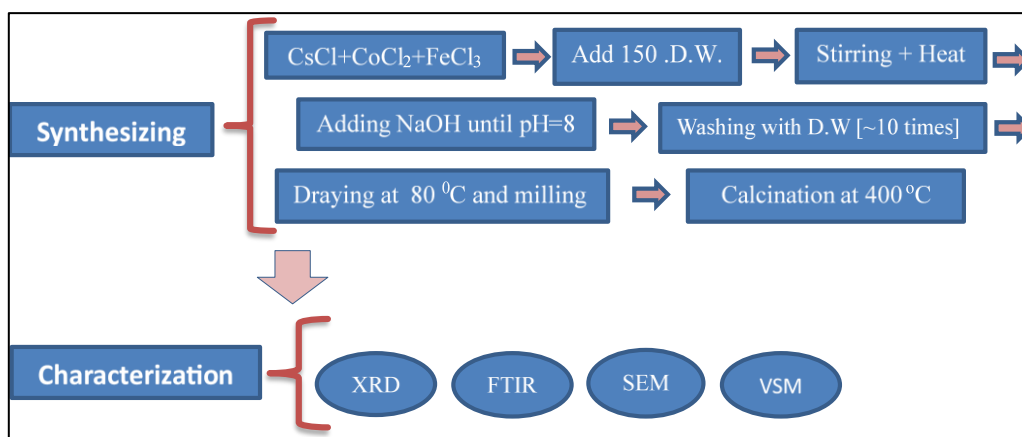


**Fig.1.** The steps for synthesizing the Cesium Cobalt Ferrite  $Cs_yCo_{1-0.5y}Fe_2O_4$  nanoparticles by co-precipitation method and their characterization.

### 3. Results and discussion

#### 3.1. Structure Properties

Studying the XRD of the prepared nanoparticles reveals the phase and crystallinity of the nanoparticles. The XRD patterns of  $Cs_yCo_{1-0.5y}Fe_2O_4$  ferrite for  $y=0, 0.05, 0.15,$  and  $0.25$  are shown in Fig. (2). The resulting patterns reveal that the synthesized nanoparticles have a face-centered cubic spinel structure with good crystallinity. The common Bragg diffraction peaks for all samples were at  $2\theta$  of  $30.15^\circ, 35.52^\circ, 43.15^\circ, 53.63^\circ, 57.04^\circ,$  and  $62.61^\circ$ , which correspond to the reflection planes (220), (311), (222), (400), (422), (511), and (440), respectively. These peaks are in agreement with the XRD pattern of cobalt ferrite (JCPDS card No. 221086). One can note a small shift in the peak of the (311) planes to the lower  $2\theta$  values due to the substitution of  $Co^{2+}$  by  $Cs^{1+}$  where the latter has a larger ionic radius (170pm) than the former (79pm) [10]. The calculated data are shown in Table 2. Finally, the peaks around  $25^\circ$  and  $33^\circ$  mainly related to the formation of a small quantity of  $\alpha-Fe_2O_3$ , where these peaks coincide with its (012) and (104) plane [11]. Hematite,  $\alpha-Fe_2O_3$  phase, is usually formed during synthesizing ferrite under un-optimized conditions [12].

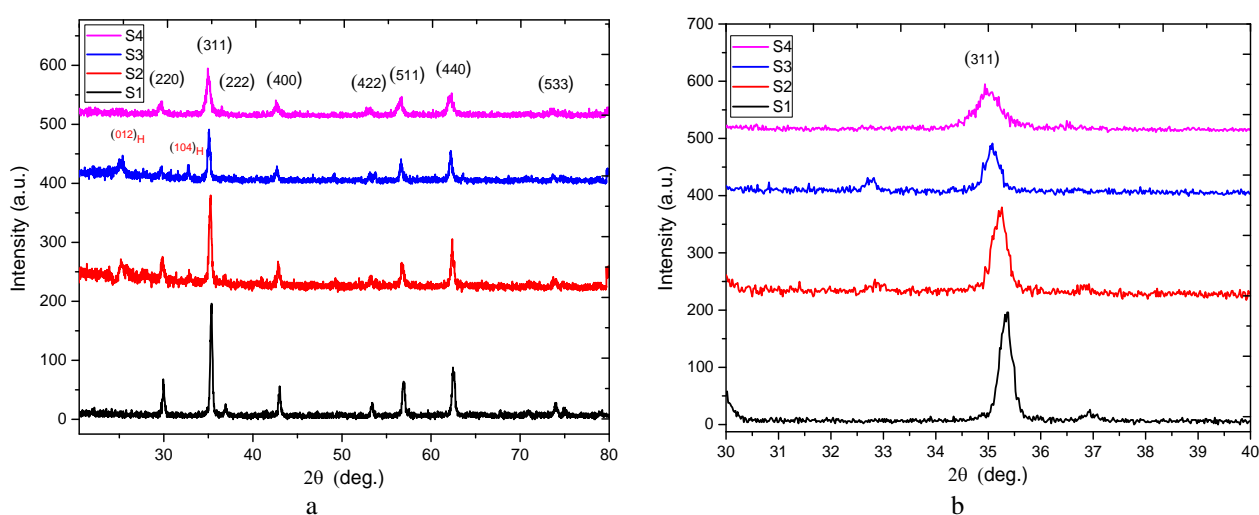
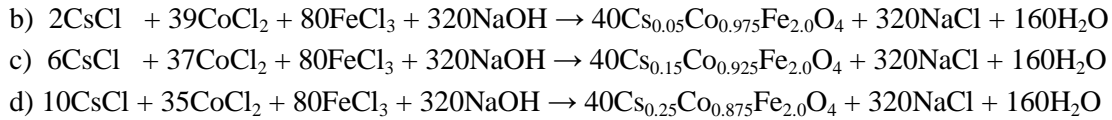


**Fig.2.** (a) The XRD patterns of the synthesized  $Cs_yCo_{1-0.5y}Fe_2O_4$  ferrite nanoparticles by co-precipitation method, (b) The peak shifts of the planes (311) for the four samples.

The following reactions are suggested to synthesize the  $Cs_yCo_{1-0.5y}Fe_2O_4$  ferrite at the molar ratios  $y$  of 0, 0.05, 0.15, and 0.25 respectively:





The average crystallite size  $D$  was calculated by the Scherrer formula as in eq. (1) [11]:

$$D = 0.9 \lambda / \beta \cos \theta \quad (1)$$

where  $\beta$  is the full width at half maximum of the for the planes (311),  $\lambda$  is the wavelength of x-rays (1.5406Å), and  $\theta$  is the diffraction angle. All the calculated average crystallite sizes were in the nanometer range.

The crystallite size shows a clear reduction in its value as the molar ratio increases as shown in Table 2, where it dropped from about 18.1nm to about 12.2nm as the molar ratio increases from 0.05 to 0.25. This reduction may be related to the increase of nucleation rate compared to growth rate, i.e., increasing Cs content will improve the nucleation rate and subsequently reduce the crystallite size.

The dislocation density ( $d_D$ ) is proportion inversely to the crystallite size, as given in eq. (2) [12].

$$d_D = 1/D^2 \quad (2)$$

This equation explains the reason behind the increasing dislocation density as in Table 2. The lattice constant ( $a$ ) for the spinel structure was calculated by the following formula [13]:

$$a = d (h^2 + k^2 + l^2)^{1/2} \quad (3)$$

$$d = n \lambda / \sin \theta \quad (4)$$

where  $h$ ,  $k$ , and  $l$ , are the Miller indices of crystal planes. The calculated lattice constants ( $a$ ) values were generally increased as the molar ratio increased.

**Table 2.** The effect of Cs content on some structural parameters for S1, S2, S3, and S3. crystallite size  $D$ , dislocation density ( $d_D$ ), lattice constants ( $a$ ), X-ray density ( $\rho_{XRD}$ ), The hopping lengths for A-site ( $L_A$ ) and B-site ( $L_B$ ), and The tetrahedral ( $r_A$ ) ionic radii and octahedral ionic radii ( $r_B$ )

Sample	D (nm)	$d_D \times 10^{-3}$ (nm <sup>-2</sup> )	a (nm)	$\rho_{XRD}$ (g/cm <sup>3</sup> )	$L_A$ (nm)	$L_B$ (nm)	$r_A$ (nm)	$r_B$ nm
S1	18.12	3.044	0.840	5.24	0.3641	0.2973	0.047	0.0752
S2	14.98	4.45	0.838	5.42	0.3629	0.2962	0.046	0.0745
S3	12.62	6.27	0.848	5.45	0.3671	0.2998	0.048	0.0770
S4	12.27	6.64	0.841	5.83	0.3637	0.2969	0.049	0.0750

The calculated data are shown in Table 2. As  $\text{Cs}^{1+}$  content increases and as  $\text{Cs}^{1+}$  has a larger ionic radius than  $\text{Co}^{2+}$  this will produce an increase in the calculated lattice constants ( $a$ ). The measured lattice parameter of sample S1 is comparable to the bulk one of Co ferrite (0.838) [14] where the difference may be related to the low temperature of the preparation. The nanoparticle XRD density ( $\rho$ ) was calculated by eq. (5) depending on the lattice constant and molecular mass ( $M$ ). The x-ray density can be calculated using the relation [15]:

$$\rho_{XRD} = 8M/N_A a^3 \quad (5)$$

where  $N_A$  is the Avogadro number and  $M$  is the molecular weight of each structure. The  $\rho_{XRD}$  values for the 4 composition nanoparticles are given in Table 2.

The  $\rho_{XRD}$  increases as the molar ratio (Cs content) increases despite the expansion in the lattice constant because of the molecular weight increase is more effective than the lattice constant expansion.

The structural parameters such as the hopping lengths for A-site ( $L_A$ ) and B-site ( $L_B$ ) were calculated using standard equations (6) and (7), and the ionic radii ( $r_A$  and  $r_B$ ) were determined considering the oxygen positional parameter ' $\mu$ ' with the standard value of 0.0375 nm and using the radius of oxygen anions  $r_o$  of 0.135nm [16]. The tetrahedral ionic radii (A-site) and octahedral ionic radii (B-site) were determined by equations (8) and (9), respectively [17].

$$L_A = a \sqrt{3}/4 \quad (6)$$

$$L_B = a \sqrt{2}/4 \quad (7)$$

$$r_A = \left(\mu - \frac{1}{4}\right)\sqrt{3} - r_o \quad (8)$$

$$r_B = \left(\frac{5}{8} - \mu\right)a - r_o \quad (9)$$

The calculated values of the previous parameters,  $L_A$ ,  $L_B$ ,  $r_A$ , and  $r_B$  are given in Table 3. These parameters are raised as the Cs content is increased. In other words, they follow the lattice constant and so their behaviors follow the lattice constant behavior [18]. One may deduce that the tetrahedral substitution has a main effect on the lattice constant value.

### 3.2 The FTIR analysis

Fig.3 illustrates the FTIR spectra of the prepared samples. All samples showed obvious bands below  $700\text{cm}^{-1}$ , as magnified in the inset Figure, while they showed a low absorption from  $700\text{cm}^{-1}$  to  $3900\text{cm}^{-1}$  at room temperature. This may be related to the high strength of the ferrite bond due to the ionic nature of the metal-oxygen bond and the nature of the stretching vibration mode. The presence of such ferrite characteristic bands refers to the cubic spinel structure and completion of the chemical reaction [19].

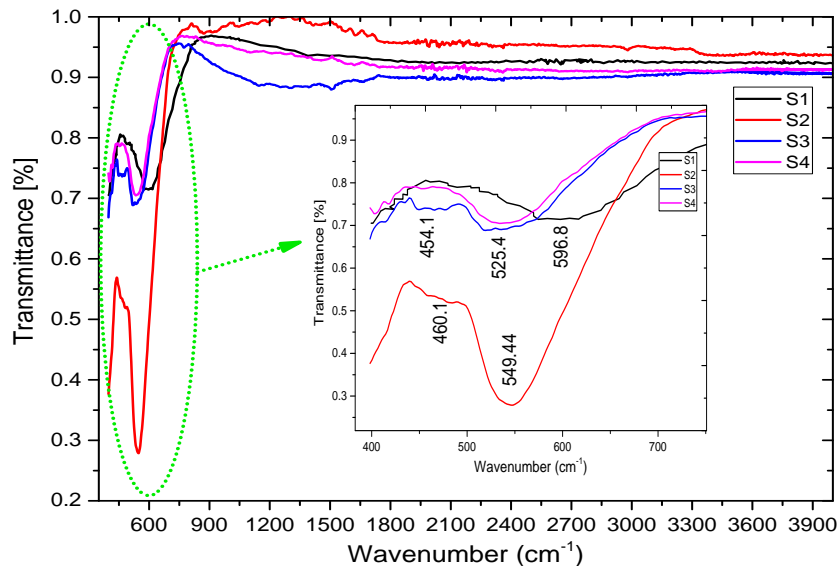


**Fig.3.** FTIR spectra of the synthesized  $\text{Cs}_x\text{Co}_{1-0.5x}\text{Fe}_2\text{O}_4$  nanoparticles at 0.0, 0.05, 0.15, and 0.25 for S1, S2, S3, and S4 respectively.

The band around  $596\text{cm}^{-1}$ , the higher wavenumber, is associated with the stretching mode of the bond of metal at tetrahedral sites and oxygen anion ( $\text{Fe}^{3+}-\text{O}^{2-}$  bond), and it is commonly denoted by  $\nu_1$  [20]. On the other hand, the  $\nu_2$ -lowest band is observed lower than  $500\text{cm}^{-1}$ , which results from the octahedral-metal stretching ( $\text{M}^{2+}-\text{O}^{2-}$  bond M is Co or Cs). The  $\nu_2$  band in this study, lower wavenumber, is observed as a strong absorption band between  $400\text{cm}^{-1}$  and  $500\text{cm}^{-1}$  and may extend to values lower than  $400\text{cm}^{-1}$  [21].

The  $\text{Co}^{2+}$  cations generally occupy octahedral sites, whereas  $\text{Fe}^{3+}$  cations occupy mostly both octahedral and tetrahedral sites. The reason behind the difference in the tetrahedral and octahedral sites is basically associated with the lengths of these two site bond lengths. The precise observation in the inset Figure indicates that there is a general shift in the  $\nu_1$  band to the lower wavenumber as the Cs content increases, while the  $\nu_2$  band exhibits no clear shift. This, in turn, indicates that Cs may mainly occupy the tetrahedral sites rather than octahedral sites. One can observe there is no organic, commonly higher than  $2300\text{cm}^{-1}$  [22], or inorganic band or peak that can be related to any impurity or undesirable phase. This perhaps supports the precise synthesizing procedure that was followed. No band around  $3410\text{cm}^{-1}$ , which is related to the metal-hydroxide bond [21], is not observed. A weak peak around  $1500\text{cm}^{-1}$  may be related to the symmetric and asymmetric stretching vibration of  $\text{CO}_2$  molecules in the environment of the test or adsorbed on the particle surfaces [21].

### 3.3. The SEM analysis

The SEM images of the nanoparticles for all samples are given in Fig.4. All samples of  $Cs_yCo_{1-0.5y}Fe_2O_4$  ( $y=0, 0.05, 0.15, 0.25$ ) showed homogeneous spherical nanoparticles without any other observed shape or exotic morphologies. All particle sizes are lower than 100nm as measured by the scale bar. The SEM images substantiate a clear agglomeration. The agglomeration occurred due to surface interaction due to nanosize and magnetic interaction between magnetic nanoparticles [23]. This interaction decreases with increasing cesium concentration in the cobalt ferrite nanoparticles as for other cations.

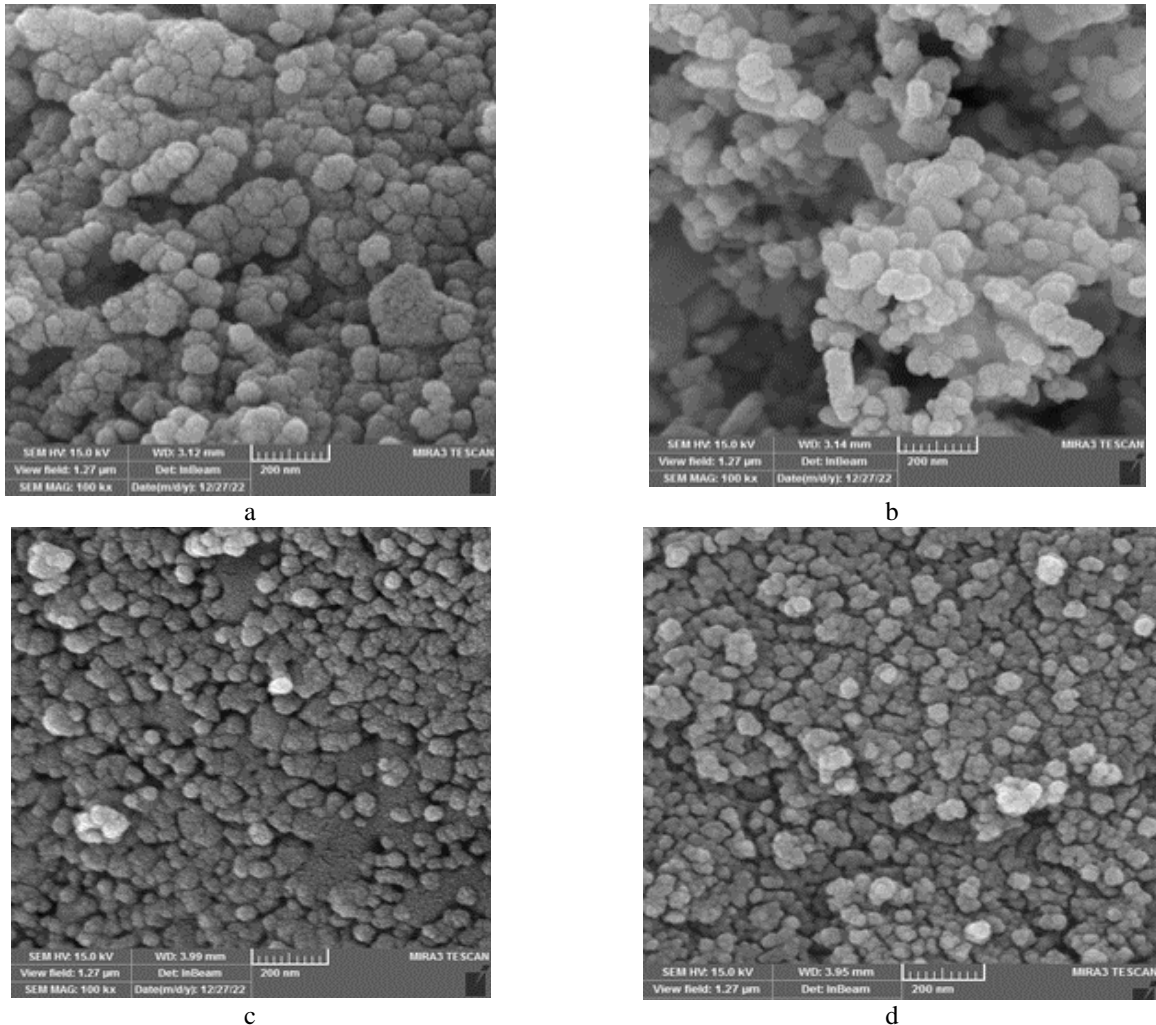


**Fig.4.** SEM images of  $Cs_yCo_{1-0.5y}Fe_2O_4$  samples. (a) sample S1, (b) sample S2, (c) sample S3 and (d) sample S4.

In Fig.5, the particle distributions for the 4 samples are given. The minimum particle size is about 15nm, while it extends to more than 100nm. Most particle sizes are found in the range (40-60) nm. As the molar ratio ( $y$ ) increases, there is a decrease in the average particle size. This decrease can be attributed to that the presence of  $Cs^{1+}$  improves the nucleation rate and, in turn, increases the nucleation centers (seeds) at the expense of single-particle growth [24]. This result is in agreement with the results of crystallite size mentioned previously. In the same context, one can conclude that each particle has more than one crystal.

The elemental composition of samples was carried out by Energy-dispersive X-ray spectroscopy (EDX). Fig.6 shows EDX spectra for all synthesized cesium-substituted cobalt ferrite nanoparticles, which clearly indicates the presence of Co, Cs, O, and Fe elemental corresponding peaks. No presence of any other elemental impurity peak was observed in the EDX spectrum which refers to good choosing synthesizing and measuring conditions. The elemental compositions of all elements for the prepared samples are shown in the inset Tables in the spectra. This result points to obtaining a well-matched atomic ratio of all elements (Co, Cs, O, and Fe) with the expected stoichiometric proportion of elements in the synthesized nanoparticle. The appearance of carbon in the spectra is related to the use of carbon tape for conducting the test.

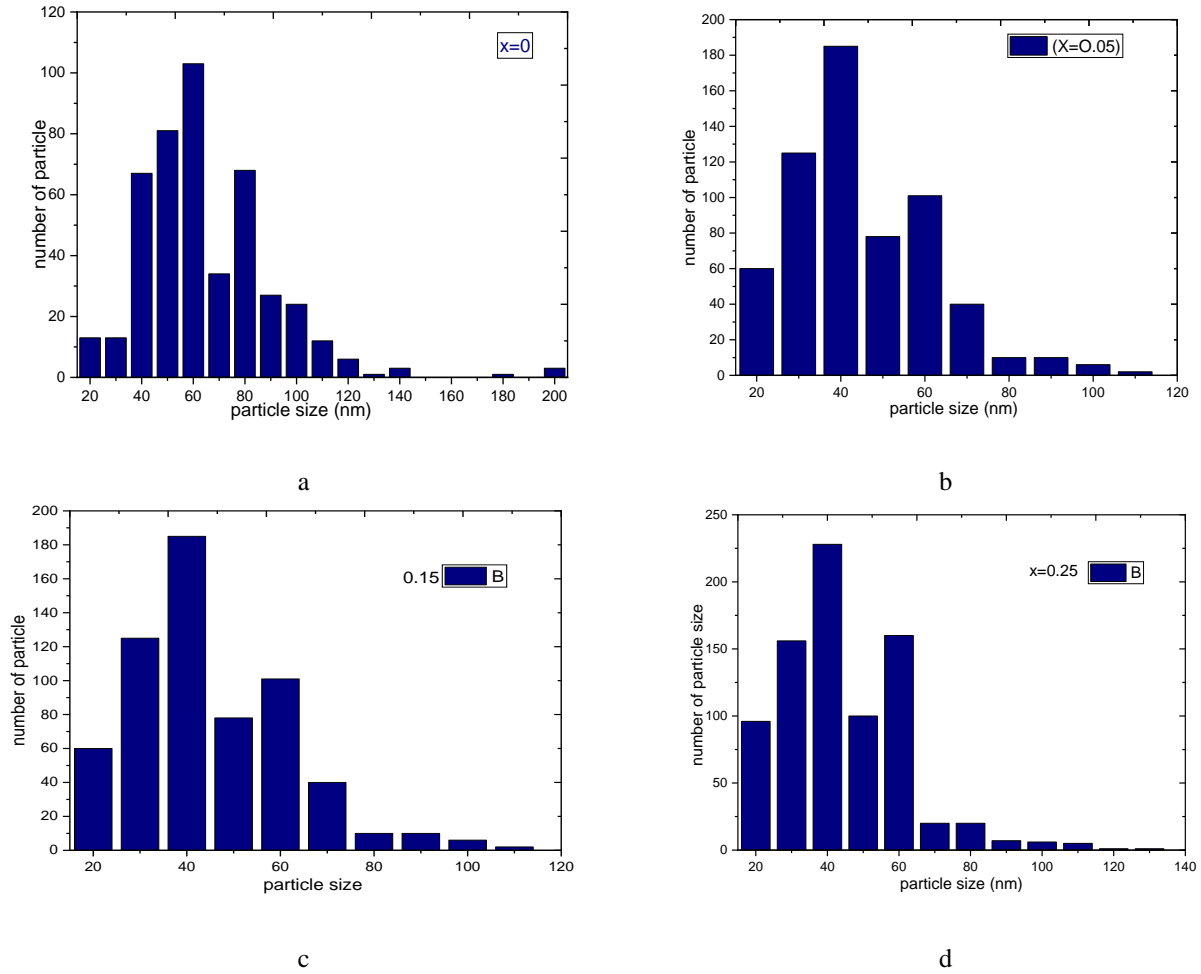


**Fig.5.** The particle size distributions, as measured from the SEM images, for the samples: (a) - sample S1, (b) - sample S2, (c) - sample S3 and (d) - sample S4.

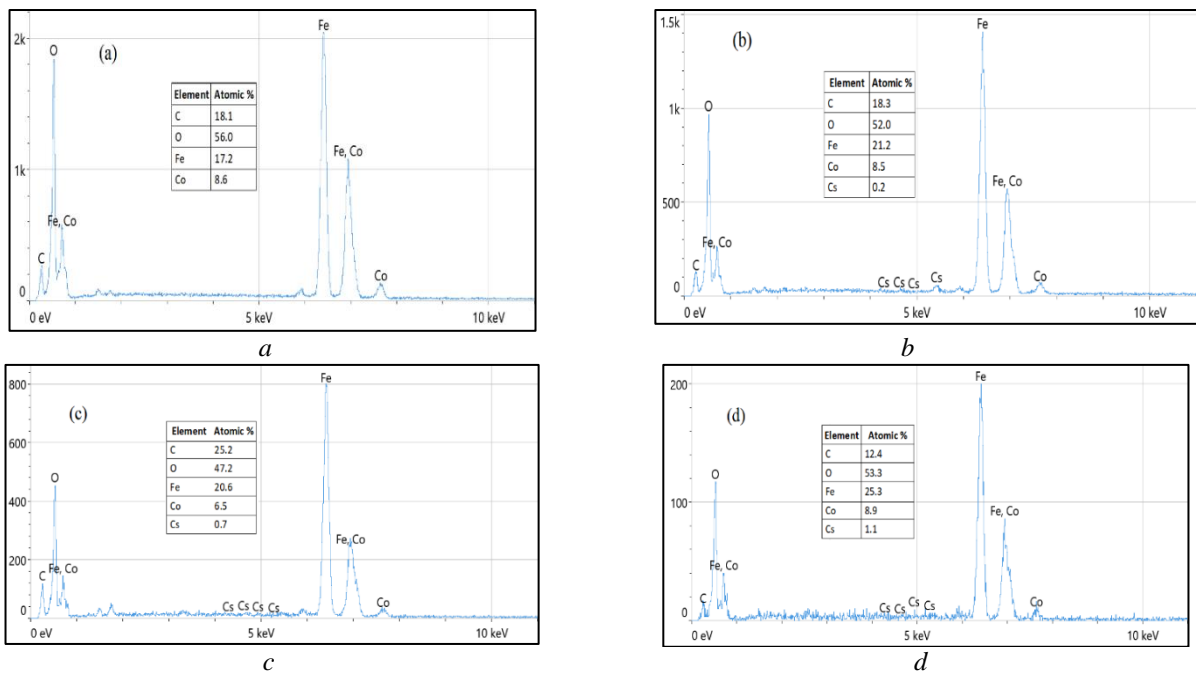


**Fig.6.** The SEM-EDX spectra for the prepared  $Cs_yCo_{1-0.5y}Fe_2O_4$  samples, (a) for  $y=0$ , (b) for  $y=0.05$ , (c) for  $y=0.15$  and (d) for  $y=0.25$ .

### 3.4. Magnetic hysteresis loops analysis

Fig.7 shows the Magnetic hysteresis loops of the synthesized nanoparticles as measured by the VSM magnetometer, these loops correspond to the sample s1, s2, s3, and s4. All samples show nearly hard magnetic behavior compared to cesium ferrite [25].

The saturation magnetization ( $M_s$ ) of the samples showed a generally small reduction as the molar ratio ( $y$ ) raised from 0 to 0.25, although the presence of some tolerance of about 5emu/g, as given in Table 3. Despite of that  $Cs^{+1}$  has no magnetic moment but substitution by Cs in tetrahedral or octahedral sites.  $Co^{2+}$  ions have a strong preference to take the octahedral site [26]. On the other hand, Cs ferrite is an inverse spinel where all the  $Cs^{+1}$  ions occupy octahedral sites while  $Fe^{3+}$  ions occupy both octahedral sites and tetrahedral sites [27]. So, according to ratios that were mixed, it is believed that Cs ions usually substitute Co ions. Under this context, the degradation of the  $M_s$  is believed due to that  $Cs^{+1}$  is owing zero magnetic moment and as it substitutes the  $Co^{2+}$ , which has a magnetic moment, the magnetization was reduced.

The effect of  $Fe^{3+}$  cations is eliminated because an equal number of them occupy A-site and B-sites. Some researchers found that the substitution of  $Cs^{+1}$  ions at the tetrahedral (A) site replaces magnetic  $Fe^{3+}$  ions which causes a decreased magnetic moment at the A-site [27]. Some other researchers explained the degradation of  $M_s$  of Co ferrite when substituted by non-magnetic ions in B-site on the basis of the magnetization of Co ferrite is higher than that non-magnetic ions ferrite hence, doping by Cs in cobalt ferrite causes a decrease in magnetization [28].

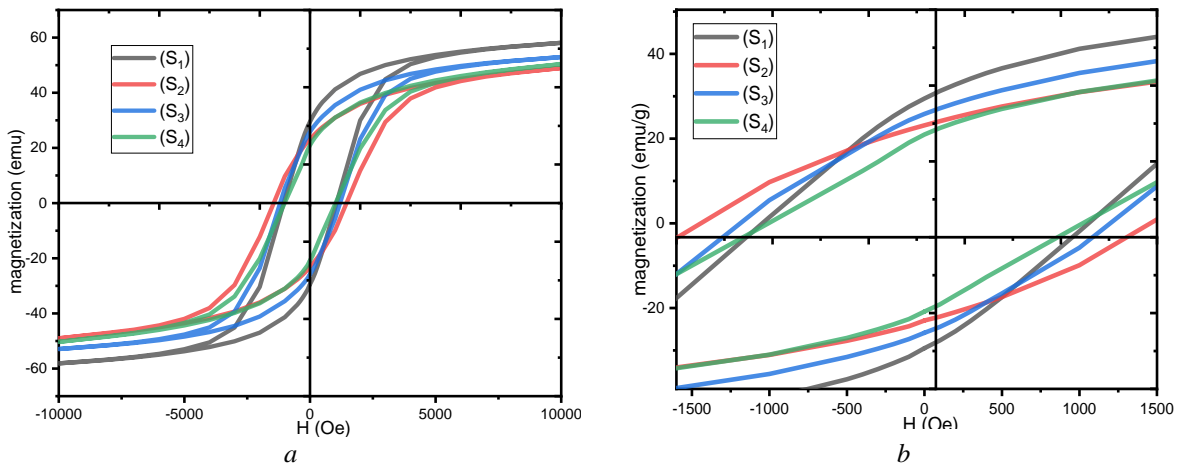


**Fig.7.** The magnetic hysteresis loops of the synthesized  $Cs_yCo_{1-0.5y}Fe_2O_4$  ( $y= 0, 0.05, 0.15,$  and  $0.25$ ) ferrite: a) full hysteresis loops of the prepared samples; b) a magnification of the origin around to show the details.

**Table 3.** Some magnetic parameters as measured from the magnetic hysteresis loops.

Sample	$M_s$ (emu/g)	$M_r$ (emu/g)	$H_c$ (Oe)	$M_r/M_s$	$m_f$ (emu/mol)	$K_{an} \times 10^3$ (emu.Oe/g)	$m_p$ ( $\mu_B$ )
S1	58.075	28.87	1078.36	0.497	3.037	63.88	0.5290
S2	48.53	19.03	1495.32	0.454	3.986	74.06	0.3388
S3	52.91	23.97	1196.98	0.453	4.430	57.06	0.4396
S4	50.43	22.04	1056.79	0.377	4.302	53.95	0.4224

In addition to cation distribution and substitution ion type, the  $M_s$  of ferrite also depends on the particle size [29]. The  $M_s$  dependence on particle size is given in eq. (10) [30, 31]:

$$M_{s/nano} = M_{s/bulk} [1 - (B/p_s)] \quad (10)$$

where  $M_{s/nano}$  and  $M_{s/bulk}$  are the saturation magnetization of nano and bulk materials, respectively,  $B$  is a constant, and  $p_s$  is the particle size. The remanence magnetization  $M_r$  also decreased in general from about 30 emu/g to 20 emu/g). The remanence magnetization usually follows  $M_s$  and for the same reasons.

The coercivity ( $H_c$ ) showed a tolerant behavior, where it was increased and then decreased as the molar ratio increased. It is believed the two parameters of composition and the particle size contributed to this behavior. The variation was explained graphically in Fig. (6) in the inset Figure. The mentioned  $M_s$  and  $H_c$  parameters reveal the ferromagnetic nature of all compositions but not the superparamagnetic one where the main effecting factor here is the particle size.

Some other magnetic parameters are also given in Table 3. The loop squareness ratio ( $M_r/M_s$ ) decreased as the Cs content increased. This behavior depends on the intense surface spin disordering of these nanoparticles and proves the nanoparticles are multidomain ones [32]. For all samples, the  $M_r/M_s$  ratio is lower than 0.5, which agrees with the previous result [33]. The crystalline anisotropic constant ( $K_{an}$ ) values are calculated by eq. (11). The  $K_{an}$  value is generally minimized as  $Cs^{1+}$  content grows. Also, Co ferrite substitution by  $Al^{3+}$  showed the same result because of the crystallite size reduction [34].

$$K_{an} = H_c \cdot M_s / 0.98 \quad (11)$$

The magnetic moment per unit formula is calculated by eq. (12). The values decreased as the  $Cs^{1+}$  concentration increased. The reduction in  $\mu_m$  follows the reduction in  $M_s$ .

$$m_f = \frac{M \cdot M_s}{5585} \quad (12)$$

The magnetic moment per particle ( $m_p$ ) was calculated for each sample by the Langevin fitting equation using the Origin Lab program and the values are given in Table 3. This parameter depends on A-B interaction and sharply decreases from (0.5290 to 0.3388 (emu/g) when the value of x is varied from 0 to 0.25. It is also decreased as the  $Cs^{1+}$  content increases. The magnetic moment per formula and the magnetic moment per particle are both magnetization saturation dependent, so they follow its behavior.

#### 4. Conclusion

Substitutions cations by ions with the oxidation state of +1 like Cs in ferrite is one of the most challenging topics in magnetic material studies. Here, a Co ferrite was chosen to conduct the substitution on its cations satisfying the compositions  $Cs_yCo_{1-0.5y}Fe_2O_4$  with  $y= 0, 0.05, 0.15,$  and  $0.25$ . The substitution by  $Cs^{1+}$  increases the lattice constant and reduces the crystallite size. A clear shift in the tetrahedral band of the FTIR spectrum supports the substitution occurrence. The magnetization saturation decreased when Co ferrite is substituted by  $Cs^{1+}$  cations from about 58 emu/gm down to 50.43 emu/g with low molar ratio variation.

The magnetic moment also decreased as the molar ratio increased. Substitution Co by Cs worked on lowering the average particle sizes as found by the SEM images, but not the particle shape where all samples showed spherical particle shapes. The low Cs substitution did not mainly affect the coercivity where the loops were still wide. There was also a decrease in the crystalline anisotropic constant and the squareness ratio due to such variation in the composition.

#### REFERENCES

- 1 Gore S.K., Jadhav S.S., Jadhav V V. The structural and magnetic properties of dual phase cobalt ferrite. *Scientific Reports*, 2017, Vol.7(1). doi:10.1038/s41598-017-02784-z.
- 2 Abdel Maksoud M.I., El-Sayyad G.S., Fayad E., et al. Gamma irradiation assisted the sol-gel method for silver modified-nickel molybdate nanoparticles synthesis: Unveiling the antimicrobial, and antibiofilm activities against some pathogenic microbes. *Journal of Inorganic and Organometallic Polymers and Materials*, 2021, Vol. 32(2), pp. 728–740. doi:10.1007/s10904-021-02132-9.
- 3 Tijerina-Rosa A., Greneche J.M., Fuentes A.F., et al. Partial substitution of cobalt by rare-earths (gd or SM) in cobalt ferrite: Effect on its microstructure and magnetic properties. *Ceramics International*, 2019, 45(17), pp. 22920–22929. doi:10.1016/j.ceramint.2019.07.335.
- 4 Slimani Y., Almessiere M.A., Hannachi E., Baykal A., Manikandan A., Mumtaz M., Ben Azzouz F. Influence of WO3 nanowires on structural, morphological and flux pinning ability of YBa2Cu3Oy superconductor. *Ceramics International*, 2019, Vol.45, Issue 2, Part A, pp. 2621 – 2628. doi:10.1016/j.ceramint.2018.10.201.
- 5 Almessiere M.A., Slimani Y., Hannachi E., et al. Impact of DY2O3 nanoparticles additions on the properties of porous YBCO Ceramics. *Journal of Materials Science: Materials in Electronics*, 2019, Vol. 30(19), pp. 17572–17582. doi:10.1007/s10854-019-02106-1.
- 6 Irfan M., Khan U., Li W., et al. Structural and magnetic properties of fe3ga alloy nanowires: Effect of post annealing treatment. *Journal of Alloys and Compounds*, 2017, Vol. 691, pp. 1–7. doi:10.1016/j.jallcom.2016.08.241.

- 7 Kounsalye J.S., Kharat P.B., Shisode M.V., et al. Influence of  $\text{Ti}^{4+}$  ion substitution on structural, electrical and dielectric properties of  $\text{Li}_0.5\text{Fe}_2.5\text{O}_4$  nanoparticles. *Journal of Materials Science: Materials in Electronics*, 2017, Vol. 28(22), pp. 17254–17261. doi:10.1007/s10854-017-7656-1.
- 8 Vinayak, V., Khirade P.P., Birajdar S.D., et al. Structural, microstructural, and magnetic studies on magnesium ( $\text{Mg}^{2+}$ )-substituted  $\text{CoFe}_2\text{O}_4$  nanoparticles. *Journal of Superconductivity and Novel Magnetism*, 2016. Vol. 29(4), pp.1025–1032. doi:10.1007/s10948-015-3348-3.
- 9 Joshi S., Kamble V.B., Kumar M., et al. Nickel substitution induced effects on gas sensing properties of cobalt ferrite nanoparticles. *Journal of Alloys and Compounds*, 2016, Vol.654, pp. 460–466. doi:10.1016/j.jallcom.2015.09.119.
- 10 Lafta S.H. Evaluation of hematite nanoparticles weak ferromagnetism. *Journal of Superconductivity and Novel Magnetism*, 2020, Vol.33(12), pp. 3765–3772. doi:10.1007/s10948-020-05626-8.
- 11 Lafta S.H. Hydrothermal temperature influence on magnetic and fmr properties of hematite nanoparticles. *SSRN Electronic Journal*, 2021 [Preprint]. doi:10.2139/ssrn.3989692.
- 12 Anu K., Hemalatha J. Magnetic and electrical conductivity studies of zinc doped cobalt ferrite nanofluids. *Journal of Molecular Liquids*, 2019, Vol. 284, pp. 445–453. doi:10.1016/j.molliq.2019.04.018.
- 13 Kurian M., Thankachan S., Nair D.S., et al. Structural, magnetic, and acidic properties of cobalt ferrite nanoparticles synthesised by wet chemical methods. *Journal of Advanced Ceramics*, 2015, Vol.4(3), pp. 199–205. doi:10.1007/s40145-015-0149-x.
- 14 Patterson A.L. The Scherrer formula for X-ray particle size determination. *Physical Review*, 1939, Vol.56(10), pp. 978–982. doi:10.1103/physrev.56.978.
- 15 Topkaya R., Baykal A., Demir A. Yafet–Kittel-type magnetic order in Zn-substituted cobalt ferrite nanoparticles with uniaxial anisotropy. *Journal of nanoparticle research*, 2013, Vol.15, pp.1-18. doi:10.1007/s11051-012-1359-6.
- 16 Demortière A., Panissod P., Pichon B.P., Pourroy G., Guillon D., Donnio B., Bégin-Colin S. Size-dependent properties of magnetic iron oxidenanocrystals. *Nanoscale*, 2011, Vol. 3(1), pp. 225 – 232.
- 17 Abdel-Mohsen L.H., Lafta S.H., Hashim M.S. Comparing the role of NaOH and  $\text{NH}_4\text{OH}$  on structural and magnetic properties of spinel Ba ferrite synthesized by autocombustion method. *Journal of Physics: IOP Conference Series*, 2022, 2322(1), 012081. doi:10.1088/1742-6596/2322/1/012081.
- 18 Penchal Reddy M., Zhou X., Yann A., Du S., Huang Q., Mohamed A.M.A. Low temperature hydrothermal synthesis, structural investigation and functional properties of  $\text{Co Mn}_1\text{-Fe}_2\text{O}_4$  ( $0 \leq x \leq 1.0$ ) nanoferrites. *Superlattices and Microstructures*, 2015, Vol.81, pp. 233 – 242.
- 19 Sagar S., Iqbal N., Maqsood A., Shahid M., Shah N.A., Jamil T., Bassyouni M.I. Fabrication and thermal characteristics of functionalized carbon nanotubes impregnated polydimethylsiloxane nanocomposites. *Journal of Composite Materials*, 2014, Vol. 49(8), pp. 995 – 1006.
- 20 Kumar H., Singh J.P., Srivastava R.C., Negi P., Agrawal H.M., Asokan K. FTIR and Electrical Study of Dysprosium Doped Cobalt Ferrite Nanoparticles. *Journal of Nanoscience*, 2014, pp.1-10.
- 21 Ibrahim I., Ali I.O., Salama T.M., Bahgat A., Mohamed M.M. Synthesis of magnetically recyclable spinel ferrite ( $\text{MFe}_2\text{O}_4$ ,  $\text{M} = \text{Zn, Co, Mn}$ ) nanocrystals engineered by sol gel-hydrothermal technology: High catalytic performances for nitroarenes reduction. *Applied Catalysis B: Environmental*, 2016, Vol.181, pp. 389 – 402.
- 22 Gutiérrez L., De la Cueva L., Moros M., Mazarío E., De Bernardo S., De la Fuente J.M., Morales M.P., Salas G. Aggregation effects on the magnetic properties of iron oxide colloids. *Nanotechnology*, 2019, Vol. 30(11), pp.112001.
- 23 Gbashi K.R., Bahari A., Lafta, S.H. Thin films for nano-electronics applications based on  $\text{BaCaTiO}_3\text{-SrZnTiO}_3$  perovskite with Au electrodes. *Applied Physics A*, 2023, 129(5), 350. doi:10.1007/s00339-023-06621-1.
- 24 Sathya A., Guardia P., Brescia R., Silvestri N., Pugliese G., Nitti S., Manna L., Pellegrino T.  $\text{CoFe}_{3-x}\text{O}_4$  Nanocubes for Theranostic Applications: Effect of Cobalt Content and Particle Size. *Chemistry of Materials*, 2016, Vol.28(6), pp.1769-1780. doi:10.1021/acs.chemmater.5b04780.
- 25 Andersen H.L., Saura-Múzquiz M., Granados-Miralles C., Canévet E., Lock N., Christensen M. Crystalline and magnetic structure–property relationship in spinel ferrite nanoparticles. *Nanoscale*, 2018, Vol. 10(31), pp.14902-14914.
- 26 Gupta M., Randhawa B. Microstructural, magnetic and electric properties of mixed Cs–Zn ferrites prepared by solution combustion method. *Solid State Sciences*, 2012, Vol.14(7), pp.849-856.
- 27 Rotjanasuworapong K, Lerdwijitjarud W, Sirivat A. Synthesis and Characterization of  $\text{Fe}_{0.8}\text{Mn}_{0.2}\text{Fe}_2\text{O}_4$  Ferrite Nanoparticle with High Saturation Magnetization via the Surfactant Assisted Co-Precipitation. *Nanomaterials*, 2021, Vol.11(4), pp.876. doi:10.3390/nano11040876.
- 28 Biswal D, Peebles BN, Peebles C, Pradhan AK. Tuning of magnetic properties in cobalt ferrite by varying Fe +2 and Co+2 molar ratios. *Journal of Magnetism and Magnetic Materials*, 2013; 345:1-6. doi:10.1016/j.jmmm.2013.05.052.
- 29 Lafta SH. Broadband ferromagnetic resonance of non-stoichiometric nano Nickel ferrite with different  $\text{Ni}^{2+}$  content. *Materials Research Express*, 2019, Vol. 6(4), pp. 046103. doi:10.1088/2053-1591/aafb80

30 Lafta SH. The Relation of Crystallite Size and Ni<sup>2+</sup> Content to Ferromagnetic Resonance Properties of Nano Nickel Ferrites. *Journal of Magnetism*, 2017, Vol. 22(2), pp.188-195. doi:10.4283/jmag.2017.22.2.188.

31 Jahan N, Uddin MM, Khan MNI, Chowdhury F-U-Z, Hasan MR, Das HN, Hossain M.M. Impact of particle size on the magnetic properties of highly crystalline Yb<sup>3+</sup> substituted Ni–Zn nanoferrites. *Journal of Materials Science: Materials in Electronics*, 2021, Vol. 32(12), pp. 6528-16543. doi:10.1007/s10854-021-06209-6.

32 Kumar Y., Shirage P.M. Highest coercivity and considerable saturation magnetization of CoFe<sub>2</sub>O<sub>4</sub> nanoparticles with tunable band gap prepared by thermal decomposition approach. *Journal of Materials Science*, 2017 Vol. 52(9), pp.4840-4851. doi:10.1007/s10853-016-0719-5.

33 Sarmah S., Borah R., Maji P., Ravi S., Bora T. Effect of Al<sup>3+</sup> substitution on structural, magnetic and dielectric properties of cobalt ferrite synthesized by sol-gel method and its correlation with cationic distribution. *Physica B: Condensed Matter*, 2022, Vol.639, pp. 414017. doi:10.1016/j.physb.2022.414017.

34 Zhang L., Huang Z, Shao H, Li Y., Zheng H. Effects of  $\gamma$ -Fe<sub>2</sub>O<sub>3</sub> on  $\gamma$ -Fe<sub>2</sub>O<sub>3</sub>/Fe<sub>3</sub>O<sub>4</sub> composite magnetic fluid by low-temperature low-vacuum oxidation method. *Materials & Design*, 2016, Vol. 105, pp. 234 – 239. doi:10.1016/j.matdes.2016.05.077.

Article received 28.10.2023

Article accepted 02.11.2023

DOI 10.31489/2023No4/17-22

UDC 539.171

## APPLICATION OF THE NEW B3Y-FETAL POTENTIAL IN THE SEMI-MICROSCOPIC ANALYSIS OF THE SCATTERING OF ACCELERATED ${}^6\text{Li}$ - LITHIUM AND ${}^{16}\text{O}$ - OXYGEN NUCLEI FROM THE ${}^{12}\text{C}$ - CARBON NUCLEUS

Soldatkhan D.<sup>1</sup>, Amangeldi N.<sup>1,2\*</sup>, Makhanov K.M.<sup>1</sup>, Smagulov Zh.K.<sup>3</sup> Anuar A.<sup>1</sup>, Mauyey B.<sup>1,4</sup>

<sup>1</sup>L.N. Gumilyov Eurasian National University, Astana, Kazakhstan; soldathan.dauren@mail.ru

<sup>2</sup>Institute of nuclear physics, Almaty, Kazakhstan

<sup>3</sup>Karaganda Buketov University, Karaganda, Kazakhstan

<sup>4</sup>Joint Institute for Nuclear Research, Dubna, Russia

*The phenomenological and semi-microscopic values of the potentials found in the angular distribution of scattering of ions  ${}^6\text{Li}$  - lithium,  ${}^{16}\text{O}$  - oxygen from the target nucleus  ${}^{12}\text{C}$  - carbon accelerated at low energies are determined. The experimental data of elastic scattering were analyzed based on the optical model and the double folding model. Based on the folding model, the density-dependent new Fetal potential of Yukawa 3 terms of effective nucleon-nucleon interactions was first used. The density-dependent Fetal, Paris, Reid microfolding potentials were constructed in the double folding model as a real part of the optical potential. The efficacy of the new Fetal micropotential at laboratory energies of 28 MeV and 30 MeV for the  ${}^{16}\text{O}+{}^{12}\text{C}$  nuclear system was studied in comparison with the Reid, Paris variants. The efficacy of the new Fetal potential at laboratory energies of 12.3 MeV and 20 MeV for the  ${}^6\text{Li}+{}^{12}\text{C}$  system has been studied in comparison with Reid and Paris potentials. The relative errors of phenomenological theoretical analysis and experimental cross-sections were determined in the range of 1.1 -3.0. As a result of semimicroscopic analysis, the coefficients of renormalization of folding potentials in the range  $Nr=0.8-1.0$  were determined. The data obtained will be used in various fundamental research, in particular in future thermonuclear installations and nuclear astrophysics.*

**Keywords:** nuclear matter, elastic scattering, semi-microscopic analysis, Botswana three Yukawa-Fetal potential

### 1. Introduction

The study of the interaction of accelerated ions with heavy nuclei will become an urgent topic as fundamental research in nuclear astrophysics and thermonuclear energy. Analysis of experimental data based on various models, the construction of the equation of state of nuclei is a theoretically important issue. The article presents a phenomenological and semi-microscopic analysis of the angular distribution of elastic scattering of low-energy weakly coupled  ${}^6\text{Li}+{}^{12}\text{C}$ ,  ${}^{16}\text{O}+{}^{12}\text{C}$  nuclear systems. The significance of the phenomenological and microfolding potentials was determined within the framework of the Optical Model (OM) and double folding model (DFM) core. For the microscopic study of nuclear interactions, the equation of state can be constructed depending on the saturation property of the nucleus.  $K$  - nuclear incompressibility is the only value characterizing the saturation of nuclear matter [1, 2].

The Yukawa's Michigan three Yukawa (M3Y)-Reid, M3Y-Paris potentials were calculated based on effective nucleon-nucleon (NN) interactions as a real part of the optical potential. Effective NN interactions are generated in the  $G$  - matrix and consist of central, spin-orbital, and tensor members. In the calculation of their matrix interaction, all spin, isospin interaction components are formed. When calculating the folding potential, it is important to be an isospin independent center. Taking into account the spin-orbital interaction of two nuclei with NN interactions at low energy gives a successful characteristic for asymmetric systems. To understand the reaction, direct and exchange potentials are created based on the transformation of the isovector from a microscopic point of view. D.T. Khoa, G.R. Satchler scientists introduced density-dependent parameters into the NN interaction [3-5].

The purpose of introducing density-dependent parameters was to clarify the saturation property of nuclear matter. The new potential of B3Y-Fetal was obtained by applying a lowest-order constrained variational (LOCV) to the elements of the nuclear matrix of two bodies [6]. Based on these studies, Ochala

[7, 8] first used the B3Y-Fetal potential obtained in the LOCV approach. The novelty of this article is that we introduce density-dependent parameters for B3Y-Fetal potency.

The DFM can study the real potential depending on the mass and energy of the nucleus. The Woods-Saxon potential form correctly describes the diffuse surface of the nucleus from the point of view of the nucleon density distribution. Accounting for effective NN forces and correlations is a way of constructing potentials in a microscopic approach. The article uses for the first time the potential of B3Y-Fetal for the  ${}^6\text{Li}+{}^{12}\text{C}$  nuclear system. And for the  ${}^{16}\text{O}+{}^{12}\text{C}$  system, the analysis is carried out for the first time at energies  $E_{\text{lab}}=28$  MeV and 30 MeV. Based on the B3Y-Fetal interaction, the analysis of symmetric systems  ${}^{12}\text{C}+{}^{12}\text{C}$ ,  ${}^{16}\text{O}+{}^{16}\text{O}$  at energies  $E_{\text{lab}}=145 - 450$  MeV was carried out [8, 9]. For an asymmetric  ${}^{16}\text{O}+{}^{12}\text{C}$  system in the low-energy range  $E_{\text{lab}}=20 - 140$  MeV, the analysis was carried out on the basis of a folding model [10, 11].

## 2. NN - interaction potentials

Effective NN interaction takes into account even and odd components of the central forces. The real potential is the sum of direct and exchange potentials [12].

$$\vec{V} = V^D + V^{EX} \quad (1)$$

The direct potential is completely elastic and is written as follows [13, 14]:

$$V^D(\vec{R}) = \int \int \rho^{(1)}(r_1)V_D(s)\rho^{(2)}(r_2)dr_1dr_2 \quad (2)$$

where,  $V_D(s)$  - is the direct component of the effective NN interaction,  $\rho^{(1)}, \rho^{(2)}$  - densities of colliding nuclei,  $s = r_2 - r_1 + R$ .

When calculating the exchange potential, absorption processes are taken into account [15, 16]:

$$V^{EX}(\vec{R}) = \int \int \rho^{(1)}(r_1, r_1' + s)v_{EX}(s)\rho^{(2)}(r_2, r_2' - s)\exp[i\vec{k}(R)s/\eta]dr_1dr_2 \quad (3)$$

where  $v_{EX}(s)$  - is the exchange component of the effective NN - interaction,  $\rho^{(i)}(r, r')$  - is the density matrix of colliding nuclei.

Direct and exchange components of the M3Y-Reid potential based on the elements of the G-matrix [17]:

$$v_D(s) = 7999,0 \cdot \frac{e^{-4s}}{4s} - 2134,25 \cdot \frac{e^{-2,5s}}{2,5s} \quad (4)$$

$$v_{EX}(s) = 4631,4 \cdot \frac{e^{-4s}}{4s} - 1787,1 \cdot \frac{e^{-2,5s}}{2,5s} - 7,8474 \cdot \frac{e^{-0,7072s}}{0,7072s} \quad (5)$$

Components of the direct and exchange potential of M3Y-Paris, [3, 4]:

$$v_D(s) = 11061,6 \cdot \frac{e^{-4s}}{4s} - 2537,5 \cdot \frac{e^{-2,5s}}{2,5s} \quad (6)$$

$$v_{EX}(s) = -1524,0 \cdot \frac{e^{-4s}}{4s} - 518,8 \cdot \frac{e^{-2,5s}}{2,5s} - 7,8474 \cdot \frac{e^{-0,7072s}}{0,7072s} \quad (7)$$

Components of the direct and exchange potential of B3Y-Fetal [6, 8]:

$$v_D(s) = 10472,13 \cdot \frac{e^{-4s}}{4s} - 2203,11 \cdot \frac{e^{-2,5s}}{2,5s} \quad (8)$$

$$v_{EX}(s) = 499,63 \cdot \frac{e^{-4s}}{4s} - 1347,77 \cdot \frac{e^{-2,5s}}{2,5s} - 7,8474 \cdot \frac{e^{-0,7072s}}{0,7072s} \quad (9)$$

## 3. Introduction of density-dependent parameters

The equation of state of the optical potential is constructed depending on the density and energy [18].

$$v_{D(EX)}(E, \rho, s) = g(E)f(\rho)v'_{D(EX)}(s) \quad (10)$$

where,  $g(E)$  - energy-dependent type of potential,  $f(\rho)$  - two forms of density-dependent factor [2]:

- 1)  $f(\rho) = C(1 + \alpha e^{-\beta\rho})$ , the density-dependent M3Y (DDM3Y) – type
  - 2)  $f(\rho) = C(1 - \alpha\rho^\beta)$ , the  $\beta$ -parameter dependent M3Y (BDM3Y) - type
- (11)

Energy dependence [18, 2]:

$$g(E) = (1 - 0.003 \cdot E/A) \quad (12)$$

Density dependence function when introducing the  $\gamma$  – parameter [2]:

$$f(\rho) = C(1 + \alpha \exp(-\beta\rho) - \gamma\rho) \quad (13)$$

The harmonic oscillator (HO) model [19] was used to distribute the matter density of nuclei  ${}^6\text{Li}$ ,  ${}^{16}\text{O}$  and  ${}^{12}\text{C}$ :

$$\rho(r) = \rho_0(1 + \alpha(r/a)^2) \exp(-(r/a)^2) \quad (14)$$

#### 4. Analysis of the ${}^6\text{Li}+{}^{12}\text{C}$ nuclear system

Experimental data for the  ${}^6\text{Li}+{}^{12}\text{C}$  system were analyzed in the framework of OM, DFM at energies  $E_{\text{lab}}=12.3$  MeV [20] and,  $E_{\text{lab}}=20$  MeV [21]. Microfolding potentials were created in the  $C^{++}$  program. The density-dependent parameters included in the folding potentials are shown in the following table 1.

**Table 1.** Density-dependent parameters included in the  $\gamma$ -parameter dependent M3Y (CDM3Y2) and CDB3Y2 potential types created in the Yukawa 3 term (M3Y).  $K$  - incompressibility value [4, 9]

Density-dependent types	$C$	$a$	$\beta$ (fm <sup>3</sup> )	$\gamma$ (fm <sup>3</sup> )	$K$ (MeV)
CDM3Y2, CDB3Y2	0.3346	3.0357	3.0685	1.0	204

As a real part of the optical potential, CDM3Y2, CDM3Y2, CDB3Y2 - folding potentials are used. The optical potential of the nuclear-nuclear interaction is written as follows:

$$U(r) = N_r V_F(r) - iW_0 f(r, r_w, a_w) + V_C(r) \quad (15)$$

where,  $N_r$  - renormalized factor,  $V_F$  - folding potential,  $W_0$  - imaginary potential,  $a_w$  - diffusion,  $r_w$  - radius, and  $V_C(r)$  - Coulomb potential.

The values of the  $\sigma_R$  - section of each analysis are presented in the table 2.

The phenomenological and semi-microscopic cross sections constructed on the basis of the parameters found in the energies  $E_{\text{lab}}=12.3$  and  $E_{\text{lab}}=20$  MeV are shown in the following figures 1-2.

**Table 2.**  ${}^6\text{Li}+{}^{12}\text{C}$  - nuclear system, parameters detected as a result of the analysis of OM and DFM at energies of  $E_{\text{lab}}=12.3$  MeV and  $E_{\text{lab}}=20$  MeV. Coulomb radius fixed:  $R_C=1.3$ fm.

$E_{\text{Lab}}$ , MeV	Potential	$V_0$ , MeV	$r_r$ , fm	$a_r$ , fm	$W_0$ , MeV	$r_w$ , fm	$a_w$ , fm	$\sigma_R$ , mb	$\chi^2/N$	$N_r$
12.3	OM	140.7	1.0	0.58	14.4	1.15	0.12	1005	1.1	-
	CDM3Y2-Reid				12.0	1.12	0.2	-	0.84	
	CDM3Y2-Paris				12.0	1.12	0.2	-	0.84	
	CDB3Y2- Fetal				12.0	1.12	0.2	-	0.84	
20	OM	160.8	0.92	0.59	5.9	1.24	0.85	1261	1.8	-
	CDM3Y2-Reid				5.4	1.24	0.85	1357	-	0.85
	CDM3Y2-Paris				5.9	1.24	0.8	1369	-	0.80
	CDB3Y2- Fetal				5.4	1.24	0.8	-	0.82	

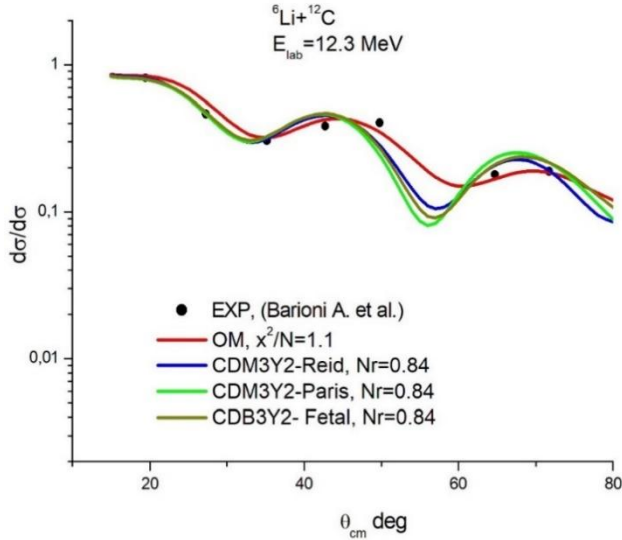


**Fig. 1.**  ${}^6\text{Li}+{}^{12}\text{C}$  - nuclear system, cross sections in energies  $E_{\text{lab}}=12.3$  MeV

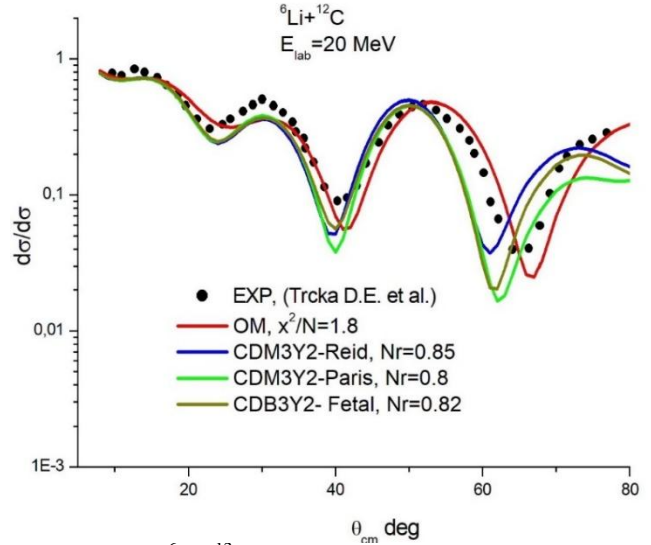


**Fig. 2.**  ${}^6\text{Li}+{}^{12}\text{C}$  - nuclear system, cross sections in energies  $E_{\text{lab}}=20$  MeV

### 5. Analysis of the ${}^{16}\text{O}+{}^{12}\text{C}$ nuclear system

Experimental data for the  ${}^{16}\text{O}+{}^{12}\text{C}$  system were analyzed in the framework of OM, DFM at energies  $E_{\text{lab}}=28$  MeV [22] and,  $E_{\text{lab}}=30$  MeV [23]. The density-dependent parameters included in the folding potentials are shown in the following table 3-4.

**Table 3.** Density-dependent parameters included in the CDM3Y1, BDM3Y1 and DDB3Y1 potential types created in the Yukawa 3 term (M3Y). K - incompressibility value [4, 9]

Density dependent version	$C$	$\alpha$	$\beta$	$\gamma$	K (MeV)
CDM3Y1-Paris	0.3429	3.0232	3.5512	0.5	188
BDM3Y1-Reid	1.2521	0.0 3.1757	1.7452	0.0	270
DDB3Y1-Fetal	0.2986		2.9605	0.0	176

**Table 4.**  ${}^{16}\text{O}+{}^{12}\text{C}$  - nuclear system, Parameters detected as a result of the analysis of OM and DFM at energies of  $E_{\text{lab}}=28$  MeV and  $E_{\text{lab}}=30$  MeV. Coulomb radius fixed:  $R_C=1.3\text{fm}$ .

$E_{\text{Lab}}$ MeV	Potential	$V_0$ MeV	$r_v$ (fm)	$a_v$ fm	$W_0$ MeV	$r_w$ (fm)	$a_w$ fm	$\chi^2/N$	$N_r$
28	OM	96.0	1.18	0.507	6.05	1.15	0.854	3.0	-
	BDM3Y1-Reid				6.05	1.15	0.854	-	1.0
	CDM3Y1-Paris				6.05	1.15	0.854	-	0.8
	DDB3Y1-Fetal				6.05	1.15	0.854	-	0.9
30	OM	95	0.948	0.640	6.8	0.951	0.2	2.39	-
	BDM3Y1-Reid				6.8	0.951	0.2	-	1.0
	CDM3Y1-Paris				6.8	0.951	0.2	-	0.8
	DDB3Y1-Fetal				6.8	0.951	0.2	-	0.9

The phenomenological and semi-microscopic cross sections constructed on the basis of the parameters found in the energies  $E_{\text{lab}}=28$  and  $E_{\text{lab}}=30$  MeV are shown in the following figures 3-4.

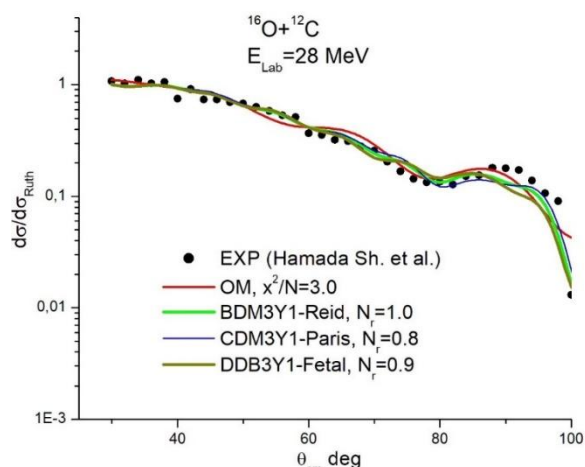


**Fig. 3.**  $^{16}\text{O}+^{12}\text{C}$  - nuclear system, cross sections in energies  $E_{\text{lab}}=28$  MeV

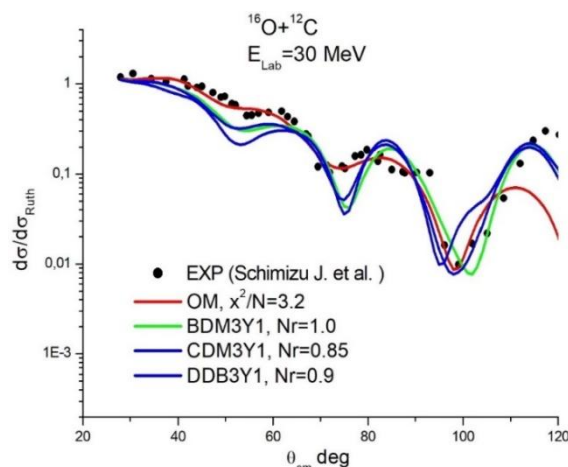


**Fig. 4.**  $^{16}\text{O}+^{12}\text{C}$  - nuclear system, cross sections in energies  $E_{\text{lab}}=30$  MeV

## 6. Conclusion

A phenomenological and semi-microscopic analysis of weakly coupled nuclear systems  $^6\text{Li}+^{12}\text{C}$ ,  $^{16}\text{O}+^{12}\text{C}$  was carried out. Microfolding potentials - BDM3Y1-Reid, CDM3Y1-Paris, DDB3Y1-Fetal, CDM3Y2-Reid, CDM3Y2-Paris, CDB3Y2-Fetal have been created in the DFM.

As a result of the phenomenological analysis, the relative errors of experimental and theoretical cross sections in the range  $\chi^2/N=1.1 - 3.0$  were revealed. As a result of semimicroscopic analysis, the coefficients of  $Nr$  - renormalization of microfolding potentials in the range  $Nr=0.8 - 1.0$  were determined.

The efficacy of B3Y-Fetal potentials has been studied in comparison with M3Y - Reid, M3Y - Paris potentials. The values of the  $\sigma_R$  - cross-section of each analysis were determined.

The introduction of the density dependence in NN interactions in the study of collisions of heavy ions with light nuclei makes it possible to clarify the saturation property of nuclear matter, that is, to fully take into account nuclear nuclei.

## Acknowledgments

This research is funded by the Science Committee of the Ministry of Education and Science of the Republic of Kazakhstan (Grant No. AP19680284)

## REFERENCES

- 1 Khoa D.T., Von Oertzen W. A nuclear matter study using the density dependent M3Y interaction. *Physics Letters B*, 1993, 304(1-2), pp. 8 – 16. doi:10.1016/0370-2693(93)91391-Y.
- 2 Khoa D.T., Von Oertzen W., Bohlen H.G. Double-folding model for heavy-ion optical potential: Revised and applied to study  $\text{C}^{12}$  and  $\text{O}^{16}$  elastic scattering. *Physical Review C*, 1994, 49(3), pp. 1652. doi:10.1103/PhysRevC.49.1652.
- 3 Khoa D.T., Von Oertzen, W., Bohlen H.G., Bartnitzky G., et al. Equation of State for Cold Nuclear Matter from Refractive  $\text{O}^{16}+\text{O}^{16}$  Elastic Scattering. *Physical review letters*, 1995, 74(1), 34. doi:10.1103/PhysRevLett.74.34.
- 4 Khoa D.T., Satchler, G. R., Von Oertzen, W. Nuclear incompressibility and density dependent NN interactions in the folding model for nucleus-nucleus potentials. *Physical Review C*, 1997, 56(2), 954. doi:10.1103/PhysRevC.56.954.
- 5 Khoa D.T., Von Oertzen W. Refractive alpha-nucleus scattering: a probe for the incompressibility of cold nuclear matter. *Physics Letters B*, 1995, 342(1-4), 6-12. doi:10.1016/0370-2693(94)01393-Q.
- 6 Fiase J.O., Devan K.R.S., Hosaka A. Mass dependence of M3Y-type interactions and the effects of tensor correlations. *Physical Review C*, 2002, 66(1), pp. 014004. doi:10.1103/PhysRevC.66.014004.
- 7 Ochala I. *Application of the New M3Y-Type Effective Interaction to Nuclear Matter and Optical Model Analyses*. Unpublished PhD Thesis. Benue State University. Makurdi, 2016, 186 p.

- 8 Ochala I., Fiase J.O. Symmetric nuclear matter calculations: A variational approach. *Physical Review C*, 2018, 98(6), 064001. doi:10.1103/PhysRevC.98.064001.
- 9 Ochala I., Fiase J.O. B3Y-FETAL effective interaction in the folding analysis of elastic scattering of  $^{16}\text{O}+^{16}\text{O}$ . *Nuclear Science and Techniques*, 2021, 32(8), pp. 81. doi:10.1007/s41365-021-00920-z.
- 10 Soldatkhan D., Yergaliuly G., Amangeldi N., Mauvey B., Odsuren M., Ibraheem A.A., Hamada S.. New Measurements and Theoretical Analysis for the  $^{16}\text{O}+^{12}\text{C}$  Nuclear System. *Brazilian Journal of Physics*, 2022, 52(5), pp.152. doi:10.1007/s13538-022-01153-0.
- 11 Soldatkhan, D., Amangeldi, N., Baltabekov, A., Yergaliuly. Investigation of the energy dependence of the interaction potentials of the  $^{16}\text{O}+^{12}\text{C}$  nuclear system with a semi-microscopic method. *Eurasian Physical Technical Journal*, 2022, Vol. 19(3(41)), pp. 39–44. doi: 10.31489/2022No3/39-44.
- 12 Khoa D.T., Knjazkov O.M. Obmennye efekty v yadro-yadernyh potencialah i yadernoe raduzhnoe rassejanie. *Fizika jelementarnyh chastic i atomnogo yadra*, 1990, 21(6), 1456-1498. [in Russian].
- 13 Bertsch G., Borysowicz J., McManus H., Love W.G. Interactions for inelastic scattering derived from realistic potentials. *Nuclear Physics A*, 1977, 284(3), 399-419. doi:10.1016/0375-9474(77)90392-X.
- 14 Sinha B. The optical potential and nuclear structure. *Physics Reports*, 1975, 20(1), 1-57. doi:10.1016/0370-1573(75)90011-3.
- 15 Gupta S.K., Sinha B. Intrinsic density and energy dependence: Exchange effects in alpha-nucleus scattering. *Physical Review C*, 1984, 30(3), 1093. doi:10.1103/PhysRevC.30.1093.
- 16 Chaudhuri A.K., Sinha B. A microscopic optical model analysis of heavy ion elastic scattering data using the realistic NN interaction. *Nuclear Physics A*, 1986, 455(1), 169-178. doi:10.1016/0375-9474(86)90350-7.
- 17 Satchler G.R. *Direct Nuclear Reactions*. Oxford Univ. Press, New York. 1983, 396 p.
- 18 Kobos A.M., Brown B.A., Lindsay R., Satchler G.R. Folding-model analysis of elastic and inelastic  $\alpha$ -particle scattering using a density-dependent force. *Nuclear Physics A*, 1984, 425(2), pp. 205 – 232. doi:10.1016/0375-9474(84)90073-3.
- 19 De Vries H., De Jager C.W., De Vries C. Nuclear charge-density-distribution parameters from elastic electron scattering. *Atomic data and nuclear data tables*, 1987, 36(3), pp. 495-536. doi: 10.1016/0092-640X(87)90013-1.
- 20 Barioni A., Zamora J.C., Guimaraes V., Paes B., et al. Elastic scattering and total reaction cross sections for the  $\text{B}^8$ ,  $\text{Be}^7$ , and  $^6\text{Li}+^{12}\text{C}$  systems. *Physical Review C*, 2011, 84(1), 014603. doi:10.1103/PhysRevC.84.014603.
- 21 Trcka D.E., Frawley A.D., Kemper K.W., Robson D., Fox J.D., Myers E.G. Angular momentum dependent absorption in  $\text{Li}^6$  scattering. *Physical Review C*, 1990, 41(5), 2134. doi:10.1103/PhysRevC.41.2134.
- 22 Hamada S., Burtebayev N., Gridnev K.A., Amangeldi N. Analysis of alpha-cluster transfer in  $^{16}\text{O}+^{12}\text{C}$  and  $^{12}\text{C}+^{16}\text{O}$  at energies near Coulomb barrier. *Nuclear Physics A*, 2011, 859(1), 29-38. doi:10.1016/j.nuclphysa.2011.04.006.
- 23 Schimizu J., Wada R., Fujii K., Takimoto K., Muto J.A. Study of the Anomaly at Ec. m=13.7 MeV in the  $^{12}\text{C}+^{16}\text{O}$  System. *Journal of the Physical Society of Japan*, 1978, 44(1), 7-15. doi:10.1143/JPSJ.44.7.

Article received: 27.07.2023  
Article accepted 07.10.2023

DOI 10.31489/2023No4/23-32

UDC 538.911, 538.951

## INFLUENCE OF ELECTRON IRRADIATION ON THE CRYSTAL STRUCTURE, SURFACE MICRORELIEF AND BANDGAP WIDTH OF THE TRIPLE CRYSTALS OF IRON DOPED MONOSELENIDE OF THALLIUM AND INDIUM

Nuritdinov I.<sup>1</sup>, Tashmetov M.Yu.<sup>1</sup>, Khodzhaev U.O.<sup>1\*</sup>, Umarov S.Kh.<sup>2</sup>, Khallokov F.K.<sup>2</sup>

<sup>1</sup> Institute of Nuclear Physics, Academy of Sciences of Uzbekistan, Ulugbek, Tashkent, Uzbekistan, utkirjon1974@gmail.com

<sup>2</sup> Bukhara State Medical Institute, Uzbekistan, Bukhara, Uzbekistan

*In this work, the effect of electron irradiation on the structure, surface morphology and band gap of single- and polycrystals of iron-doped ternary crystals of thallium and indium monoselenides was investigated. It has been established that the synthesized polycrystalline samples, as well as the grown single crystals of thallium and indium monoselenides, are single-phase. The crystals have a tetragonal unit cell (space group  $I4/mcm$ ) with the following lattice parameters:  $a \sim b = 8.12 \text{ \AA}$ ,  $c = 6.88 \text{ \AA}$ ,  $\alpha = \beta = \gamma = 90^\circ$ . Irradiation with electrons with an energy of 2 MeV and a beam current density of  $0.085 \mu\text{A}/\text{cm}^2$  leads to changes in the structure and properties of crystals in a complex manner depending on the electron fluence. Leads to a change in the parameters of the crystal lattice, an increase in the maximum value of the arithmetic mean deviation of the profile, as well as a decrease in the height of the average surface roughness of the irradiated crystals. Irradiation of a powder sample with electrons with a fluence of  $5 \times 10^{16} \text{ electron}/\text{cm}^2$  helps to increase the size of nanocrystallites from 32.50 nm to 43.33 nm.*

**Keywords:** single crystal, crystal structure, unit cell, space group, electron irradiation, fluence, crystallite size, roughness.

### 1. Introduction

Ternary crystals of thallium and indium monoselenides  $\text{TlInSe}_2$  belong to the group of ternary chalcogenide compounds of type  $A^{\text{III}}B^{\text{III}}C_2^{\text{VI}}$  with a pronounced layered structure. A characteristic feature of crystals of this family is their manifestation of both semiconductor [1-3] and tensor-resistive [4,5] properties. Since the crystal structure of compounds of this type is layered, this, as a rule, leads to the formation of polytypic modifications, which significantly affects their physical properties. Crystals of these compounds are attractive from the point of view of their practical application - they are promising materials for the manufacture of photoelectric converters, spectrum analyzers and detectors of X-ray, gamma and neutron radiation on their basis [6,7] and it is important to develop methods for targeted control of the properties of these materials.

It is known that one of the powerful methods for controlling the properties of solids is the introduction of impurities into their structure [8], as well as irradiation of them with various types of nuclear and ionizing radiation [9], which requires a targeted study of physical processes in doped and irradiated materials. However, radiation effects in chalcogenide compounds of the  $A^{\text{III}}B^{\text{III}}C_2^{\text{V}}$  type, especially in doped samples, have been studied very poorly and unsystematically. Available data are sometimes contradictory. For example, in [7] a study was carried out of the effect of electron irradiation on the dielectric constant  $\epsilon$  and electrical conductivity  $\sigma$  of  $\text{TlInS}_2$  and  $\text{TlGaS}_2$  crystals in the low temperature region and it was shown that under the influence of electron beam irradiation, the dielectric constant  $\epsilon$  of  $\text{TlInS}_2$  and  $\text{TlGaS}_2$  crystals decreases, and the conductivity  $\sigma$  significantly growing. In contrast, in [10] it was established that in  $\text{TlInS}_2$  crystals of the hexagonal modification (HM), starting from a certain dose, radiation defects accumulate and electrical conductivity decreases. As the radiation dose increases, due to the interaction of radiation defects with the original inhomogeneities, complex defects are formed, as a result of which the electrical conductivity value increases exponentially. The authors of [10] suggested that the decrease in electrical conductivity at low doses is associated with partial compensation of the initial level of the donor type. Irradiation with large doses of n- $\text{TlInS}_2$  (above 200 krad) leads to the formation of accumulations of radiation defects and strong compensation of the material. According to the authors, the indicated nature of the change

in the electrical conductivity of n-TlInS<sub>2</sub> HM crystals indicates the formation of a continuous series of deep acceptor levels during irradiation in the band gap of TlInS<sub>2</sub> [11], which accept part of the electrons. With further irradiation, the nature of the dependence  $\sigma \sim f(T)$  changes.

An analysis of the results of experiments carried out in [10] showed that non-equilibrium point radiation defects formed in the layers, migrating, accumulate in the interlayer space and thereby reduce the anisotropy of the crystal at high irradiation doses. There is very little information about radiation effects in doped TlInSe<sub>2</sub> crystals. We are aware of the works [12-14] where the influence of  $\gamma$ -radiation on the thermal conductivity, electrical conductivity and dielectric properties of TlInSe<sub>2</sub> single crystals in the temperature range of 80-600 K was studied. It was found that in irradiated crystals above 400 K the thermal conductivity increases, which is associated with a decrease in concentration defects during  $\gamma$ -irradiation of the crystal.

Taking into account the above, the purpose of this work is to study the effect of electron irradiation on the crystal structure, surface morphology and band gap of crystals p-TlIn<sub>0,98</sub>Fe<sub>0,02</sub>Se<sub>2</sub> doped with an iron impurity, since experimental data on the effect of irradiation on the physicochemical characteristics of these crystals are not available in the literature.

## 2. Material and Methods

To achieve this goal, crystals were used that were synthesized by fusing the components in a stoichiometric ratio in evacuated ( $\sim 10^{-3}$  Pa) and sealed quartz ampoules. Highly pure elements of thallium, indium, iron and selenium were used as starting components for the synthesis. Single crystals of the synthesized compounds were grown using the improved Bridgman method [15].

The possibility of replacing indium atoms in the TlInSe<sub>2</sub> crystal lattice with iron atoms is indicated by the fact that the ionic radius of the dopant Fe<sup>3+</sup> (0.62 Å) is closer to the ionic radius of In<sup>3+</sup> (0.81 Å) than to the ionic radius of Tl<sup>1+</sup> (1.38 Å) [16], i.e., partial replacement of indium with iron in a layered TlInSe<sub>2</sub> crystal corresponds to the condition for the formation of a substitutional solid solution.

Irradiation of samples of the crystals under study with electrons with an energy of 2 MeV and a beam current density of 0.085  $\mu\text{A}/\text{cm}^2$  was carried out at the “Electronics U-003” accelerator of the Institute of Nuclear Physics of the Academy of Sciences of the Republic of Uzbekistan [17]. The electron energy was selected based on the density and thickness of the sample, and was determined using a standard measuring wedge (P4701) Riso 2 Piece Aluminum (Belgium) made of aluminum. The sample was installed perpendicular to the direction of the electron beam at a distance of 0.4 m from the accelerator sweep and irradiation was carried out to an electron fluence of  $1.5 \times 10^{17}$  electron/cm<sup>2</sup>.

A three-dimensional image of the surface relief of the samples was obtained using an SPM 9700HT scanning probe microscope (Shimadzu). The study was carried out in the contact mode of operation of a scanning probe microscope. To do this, a section of the sample measuring 30x30  $\mu\text{m}$  was selected and the number of “peaks-protrusions”, their half-width and height, was determined before and after irradiation. In what follows in the text we will use the following notation:  $R_a$  is the arithmetic mean deviation of the profile from the center line drawn using the least squares method within the base length,  $R_z$  is the height of profile irregularities at 10 points, i.e. the average value of the absolute heights of the five largest protrusions of the profile and the depths of the five largest depressions of the profile within the base length. The base length is the length of the line used to highlight irregularities that characterize surface roughness and quantify its parameters.

X-ray diffraction studies of the structure of TlIn<sub>0,98</sub>Fe<sub>0,02</sub>Se<sub>2</sub> were carried out on a Malvern Panalytical Empyrean diffractometer. XRD data were recorded using a Malvern Panalytical Empyrean analytical diffractometer with CuK $\alpha$  radiation ( $\lambda=1.54$  Å). In this experiment, the accelerating voltage of the radiation generator was set to 45 kV and the emission current was set to 40 mA. X-ray diffraction patterns were recorded in the Bragg–Brentano beam geometry at  $2\theta_{\text{B}} = 20^\circ - 120^\circ$  continuously with a scanning speed of 0.33 deg/min.

The X-ray diffraction data were processed by the Rietveld method using the FullProf program [18]. Based on the obtained powder X-ray diffraction data, the crystallite size was determined using the Debye-Scherrer formula [19]:

$$D = K\lambda / (\beta \cos \theta) \quad (1)$$

where  $D$  is the average crystallite size,  $K$  is the geometric coefficient (0.9),  $\lambda$  is the X-ray wavelength (1.5406 Å),  $\beta$  is the diffraction reflection width at half maximum (FWHM),  $\theta$  is the diffraction angle. The dislocation density was determined from the equation [20]:

$$\delta = 1/D^2 \quad (2)$$

The microstress value in the  $\text{TlIn}_{0.98}\text{Fe}_{0.02}\text{Se}_2$  crystal was calculated using the Stokes-Wilson equation:

$$\varepsilon = \beta / (4 \tan \theta) \quad (3)$$

The optical absorption of the  $\text{TlIn}_{1-x}\text{Fe}_x\text{Se}_2$  ( $x=0.02$ ) single crystal was studied using a Lambda-35 UF-V spectrophotometer (Perkin Elmer) in the wavelength range 190–1100 nm. To determine the band gap of  $\text{TlIn}_{0.98}\text{Fe}_{0.02}\text{Se}_2$  from absorption spectra in the UF-visible region, we used the Tauc relation[22]:

$$(\alpha h\nu)^2 = A(h\nu - E_g) \quad (4)$$

where  $E_g = hc/\lambda$  – optical band gap energy,  $h$  – Planck's constant ( $6.626 \times 10^{-34}$  J•s),  $c$  – speed of light ( $3 \times 10^8$  m/s),  $\lambda$  – absorbed wavelength,  $\alpha$  – absorption coefficient,  $h\nu$  is the energy of the incident photon in eV,  $A$  is the band edge steepness constant.

### 3. Experimental results and discussion

The results of measuring and processing X-ray diffraction data of  $\text{TlIn}_{0.98}\text{Fe}_{0.02}\text{Se}_2$  single crystals, measured under the same conditions, are shown in Fig. 1 and Table 1. It was revealed that the synthesized samples were single-phase. Interplanar distances calculated from X-ray patterns can be unambiguously identified on the basis of the tetragonal system, that the lattice parameters have the following values:  $a \sim b = 8.067746$  Å,  $c = 6.815503$  Å, (space group  $I4/mcm$ )  $\alpha = \beta = \gamma = 90^\circ$ .

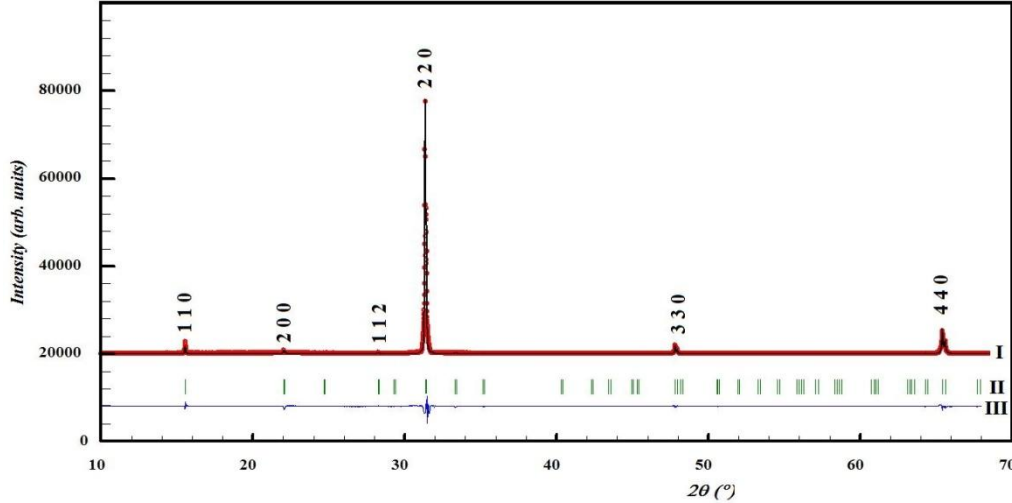


**Fig.1.** X-ray diffraction pattern of the initial  $\text{TlIn}_{0.98}\text{Fe}_{0.02}\text{Se}_2$  single crystal: I – experimental and calculated data; II – Bragg reflections; III – difference curve between experimental and calculated data

To obtain relatively complete information about the structure and compare the structural data of a single crystal and a powdered sample of  $\text{TlIn}_{0.98}\text{Fe}_{0.02}\text{Se}_2$ , an X-ray diffraction study of a powdered sample of  $\text{TlIn}_{0.98}\text{Fe}_{0.02}\text{Se}_2$  was carried out, the results were compared with the X-ray diffraction characteristics of the single crystal (Fig. 2, Table 2). It can be seen that in the range of Bragg scattering angles  $2\theta_B = 10^\circ - 60^\circ$  (Fig. 2) there is a sufficient number of reflections that make it possible to obtain complete information about the structural characteristics of the sample. Processing by the full-profile method of X-ray diffraction data from a sample of  $\text{TlIn}_{0.98}\text{Fe}_{0.02}\text{Se}_2$  powder showed that the sample, like the  $\text{TlIn}_{0.98}\text{Fe}_{0.02}\text{Se}_2$  single crystal, has a tetragonal unit cell (space group  $I4/mcm$ ) with the following lattice parameters:  $a \sim b = 8.12$  Å,  $c = 6.88$  Å,  $\alpha = \beta = \gamma = 90^\circ$ .

**Table 1.** Structural characteristics of a  $\text{TlIn}_{0.98}\text{Fe}_{0.02}\text{Se}_2$  single crystal irradiated with accelerated electrons.

Electron radiation dose, $\text{e}/\text{cm}^2$	$2\theta(^{\circ})$	$\beta$ - (FWHM) ( $^{\circ}$ )	$D$ - Crystallite size (nm)	$\delta$ - Dislocation density ( $\times 10^{15}$ lines/ $\text{m}^2$ )	$\varepsilon$ - Lattice strain (%)
0	31.34	0.099	76.56	0.17	0.15
$5.10^{14}$	31.28	0.0956	80.03	0.156	0.149
$1.10^{15}$	31.26	0.095	80.53	0.154	0.148
$5.10^{15}$	31.27	0.094	81.39	0.15	0.146
$5.10^{16}$	31.32	0.104	73.41	0.18	0.16

Based on calculations of X-ray diffraction data, the crystal structure was constructed (Fig. 3), the sizes of  $\text{TlIn}_{0.98}\text{Fe}_{0.02}\text{Se}_2$  crystallites and some other characteristics were determined (Table 2), from which it can be seen that the crystallite size increases with increasing fluence of electron irradiation.

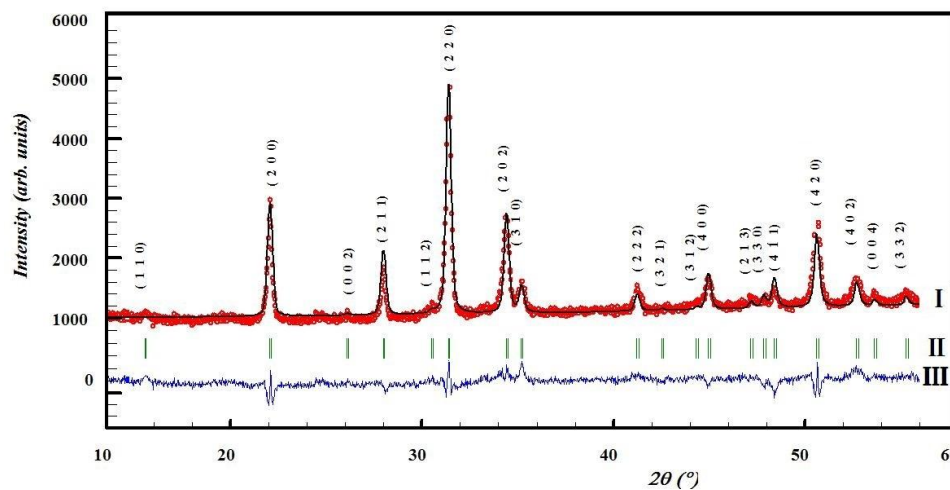


**Fig.2.** X-ray diffraction pattern of powdered  $\text{TlIn}_{0.98}\text{Fe}_{0.02}\text{Se}_2$  irradiated with electrons with a fluence of  $5 \times 10^{16}$   $\text{el}/\text{cm}^2$ : I – experimental and calculated data; II – Bragg reflections; III – difference curve between experimental and calculated data

**Table 2.** Structural characteristics of a  $\text{TlIn}_{0.98}\text{Fe}_{0.02}\text{Se}_2$  powder sample irradiated with accelerated electrons

Electron radiation dose, $\text{e}/\text{cm}^2$	$2\theta(^{\circ})$	$\beta$ - (FWHM) ( $^{\circ}$ )	$D$ - Crystallite size, (nm)	$\delta$ - Dislocation density ( $\times 10^{15}$ lines/ $\text{m}^2$ )	$\varepsilon$ -Lattice strain, (%)
0	31.2472	0.2387	32.05	0.97	0.37
$5.10^{15}$	31.2492	0.2241	34.14	0.86	0.35
$5.10^{16}$	31.2498	0.2156	35.49	0.79	0.34

A comparison of the results obtained in  $\text{TlIn}_{0.98}\text{Fe}_{0.02}\text{Se}_2$  crystals irradiated with different doses of accelerated electrons reveals an interesting picture. With an increase in the electron fluence to  $5 \times 10^{15}$ , it leads to a decrease in the parameters of the unit cell of the crystal, and above this fluence value the parameters begin to increase (Table 3). In this case, the band gap of the crystal, determined using the Tauc[22] relation, changes in the opposite direction, i.e., it increases with an increase in electron fluence up to  $5 \times 10^{15}$   $\text{el}/\text{cm}^2$ , and above this fluence it begins to decrease (Fig. 4 and Table 3). Previously, similar phenomena were discovered during the irradiation of  $\text{TlInSe}_2$  crystals and other varieties of thallium chalcogenides [10] and [23,24].

For example, in [23,24] it was established that the photosensitivity of  $\text{TlInSe}_2$  crystals depends in a complex way on the fluence of electrons and neutrons. With an increase in electron fluence to  $1 \times 10^{13}$   $\text{el}/\text{cm}^2$ ,

photosensitivity increases by 30-80%, and with a further increase in electron fluence it decreases and at a fluence of  $10^{15}$  el/cm<sup>2</sup> it is 30-40% of the sensitivity of the original non-irradiated samples. The authors admitted the possibility of a relationship between this phenomenon and the effect of small doses, the essence of which is as follows.

It is known [25] that during irradiation in solids, unstable Frenkel pairs are created with a frequency 1-2 orders of magnitude higher than stable defects, which manage to have a significant impact on the processes of radiation-stimulated migration of point defects. During the irradiation of solids (metals, alloys, semiconductor and dielectric materials), metastable Frenkel pairs are created, which lead to changes in various physicochemical properties of the irradiated material [26.27]. One of the characteristic phenomena associated with unstable radiation defects is the so-called “radiation shaking” of crystals [26-29].

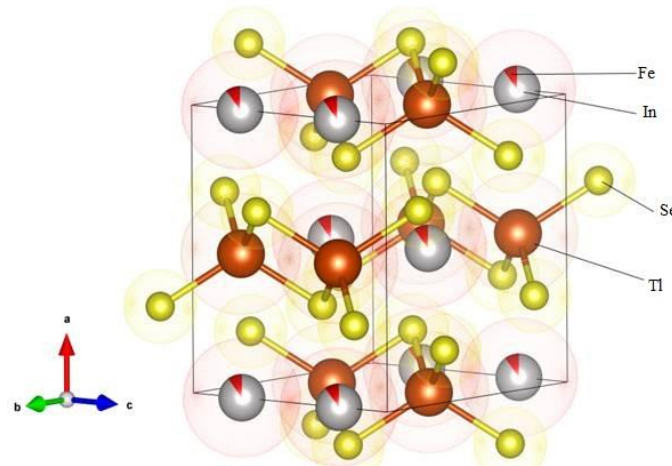


**Fig.3.** Crystal structure of  $\text{TlIn}_{0.98}\text{Fe}_{0.02}\text{Se}_2$ .

**Table 3.** Change in lattice parameters and band gap of  $\text{TlIn}_{0.98}\text{Fe}_{0.02}\text{Se}_2$  crystals under the influence of accelerated electrons

No.	Radiation dose, el/cm <sup>2</sup>	Singonia	Lattice parameters	E <sub>g</sub> , eV
1	unirradiated	I4/mcm tetragonal	$a = 8.067746$ ; $b = 8.067746$ ; $c = 6.815503$ ; $\alpha = \beta = \gamma = 90^\circ$	1.652
2	$5 \times 10^{14}$	I4/mcm tetragonal	$a = 8.061345$ ; $b = 8.061345$ ; $c = 6.795211$ ; $\alpha = \beta = \gamma = 90^\circ$	1.657
3	$5 \times 10^{15}$	I4/mcm tetragonal	$a = 8.056042$ ; $b = 8.056042$ ; $c = 6.771103$ ; $\alpha = \beta = \gamma = 90^\circ$	1.666
4	$5 \times 10^{16}$	I4/mcm tetragonal	$a = 8.062459$ ; $b = 8.062459$ ; $c = 7.135920$ ; $\alpha = \beta = \gamma = 90^\circ$	1.663

The authors [25] of theoretically showed that during the irradiation of solids, unstable Frenkel pairs are created in them with a frequency 1-2 orders of magnitude higher than stable defects, therefore they manage to have a significant impact on the processes of radiation-stimulated migration of point defects. It has been

established [30-35] that during irradiation, metastable Frenkel pairs are created in various solid materials: metals, alloys, materials of a semiconductor and dielectric nature and leads to a change in various physicochemical properties of the irradiated material. One of the characteristic phenomena associated with unstable radiation defects is the so-called “radiation shaking” of the crystal [26,28,29].

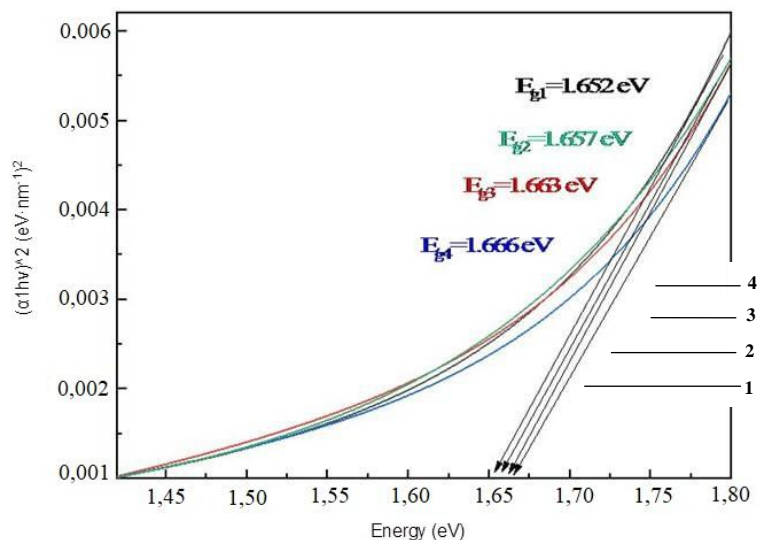


**Fig.4.** Absorption spectra of TlIn<sub>0.98</sub>Fe<sub>0.02</sub>Se<sub>2</sub> single crystals irradiated at different electron fluences: 1-initial; 2-  $5 \cdot 10^{14}$  el/cm<sup>2</sup>; 3-  $5 \cdot 10^{15}$  el/cm<sup>2</sup>; 4-  $5 \cdot 10^{16}$  el/cm<sup>2</sup>

Indenbom [26] proposed a mechanism for the phenomenon of “radiation shaking”, which leads to radiation-accelerated diffusion, caused by the birth and death of unstable Frenkel pairs (NFPs). The essence of this phenomenon is that during the creation and annihilation of Frenkel pairs of radiation defects, elastic stress waves arise as a result of the resulting local volume change in the crystal.

The interaction of these waves with existing point defects can lead to the non-activation migration of interstitial atoms and their annihilation with the corresponding vacancies, which does not lead to the accumulation of structural defects, but, on the contrary, to their elimination and transfer of the material to a more equilibrium state compared to the initial one [26,28].

The proposed mechanism was confirmed by the results of numerous computer and real physical [28-35] experiments. It has been established that there is a so-called low-dose effect ( $D = 10^3 - 10^7$  R), in which, in contrast to large doses, the crystal structure is rearranged and ordered due to the release of energy stored in the crystal as a result of chain reactions of defect annihilation initiated by ionization. The transition of a material to an equilibrium state is accompanied by an improvement in a number of its physical properties: a change in the concentration of traps, an increase in conductivity, an increase in the lifetime of minority charge carriers, etc.

In our opinion, the observed decrease in the lattice parameter of the TlIn<sub>0.98</sub>Fe<sub>0.02</sub>Se<sub>2</sub> crystal and the increase in the band gap is associated precisely with the ordering of growth defects - the effect of low doses. When the number of radiation-induced defects begins to exceed the number of biographical growth defects, an accumulation of radiation defects is observed in the crystal, which begins to deteriorate the characteristics of the crystals. The results of studying the ACM surface microrelief of undoped TlInSe<sub>2</sub> and iron-doped TlIn<sub>0.98</sub>Fe<sub>0.02</sub>Se<sub>2</sub> single crystals before and after irradiation with accelerated electrons are shown in Fig. 5 and 6, as well as in Table 4. The study was carried out without preliminary treatments. According to the data obtained, the introduction of iron impurities into TlInSe<sub>2</sub> crystals significantly changes the surface morphology: it leads to a decrease in the maximum value of the arithmetic mean deviation of the profile from  $R_a = 40.869$  to  $R_a = 17.7$  nm, and also leads to a decrease in the height of the average roughness from  $R_z = 398.036$  nm to  $R_z = 189.915$  nm. (Fig. 5 and 6; Table 4). Thus, doping TlInSe<sub>2</sub> crystals with iron will significantly improve the condition of the crystal surface; it will become smoother during doping.

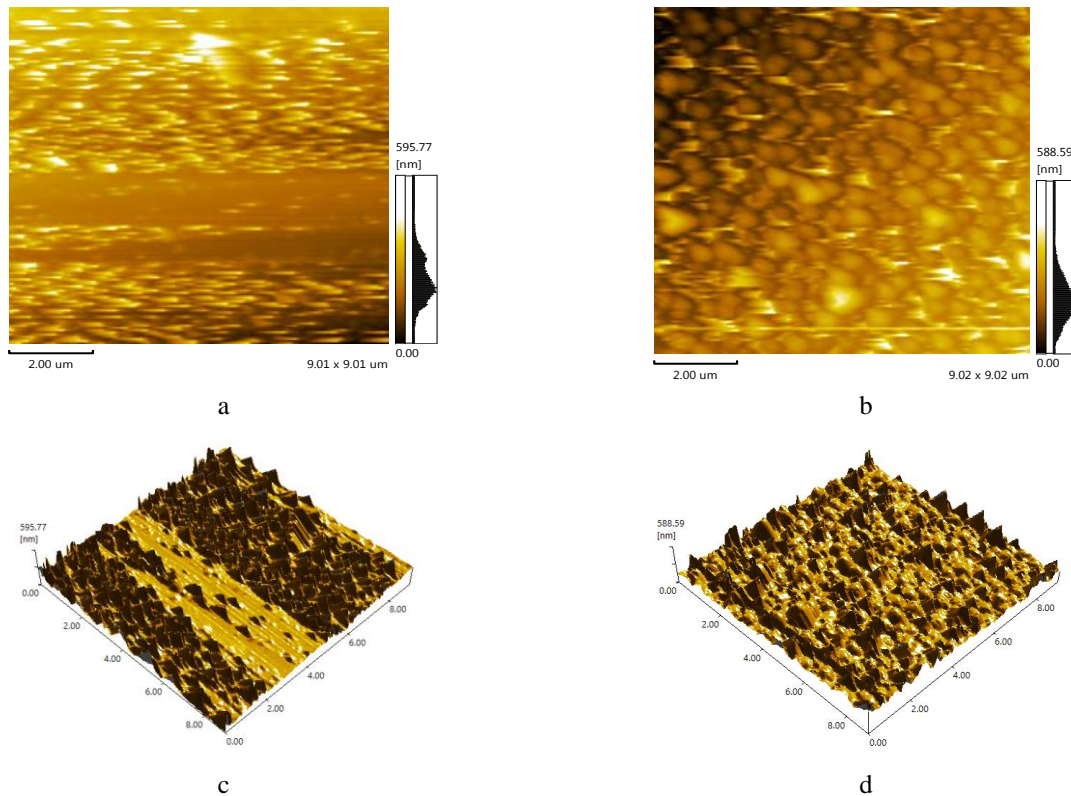


**Fig.5.** Two-dimensional (a and b) and volumetric (c and d) AFM images of the surface of a TIInSe<sub>2</sub> single crystal before (a and c) and after (b and d) irradiation with electrons with a fluence of  $5 \times 10^{16}$  electron/cm<sup>2</sup>.

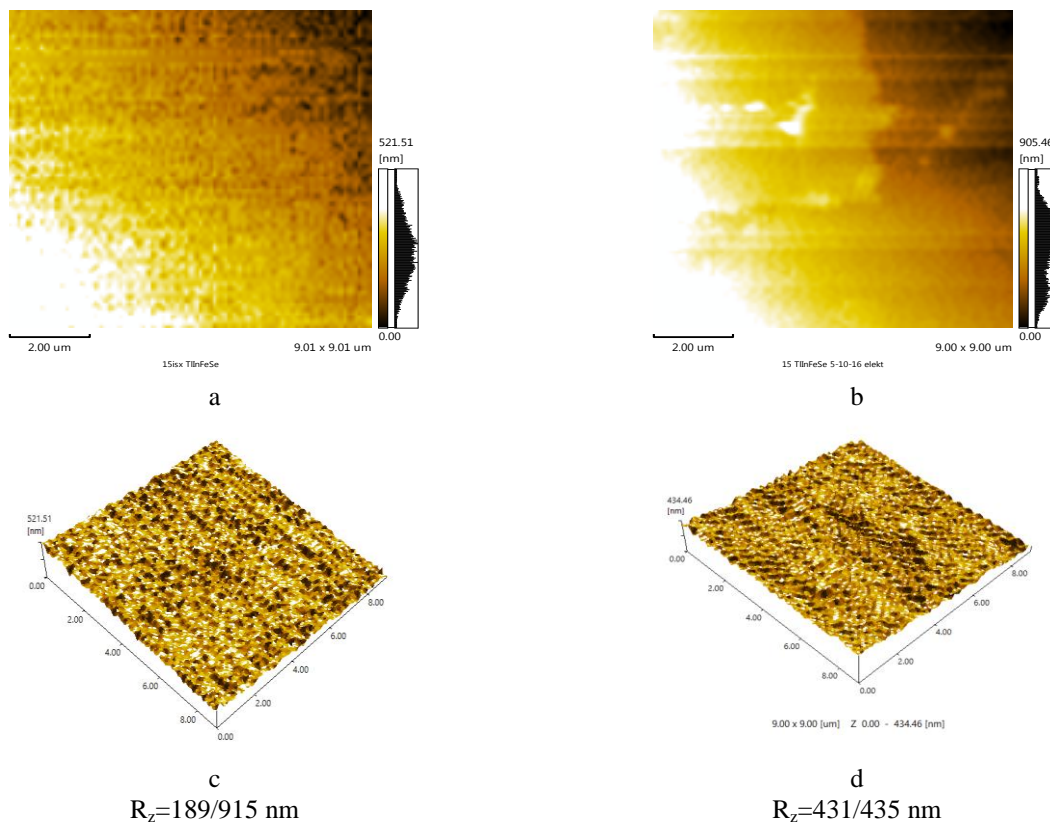


**Fig.6.** Two-dimensional (a and b) and volumetric (c and d) AFM images of the surface of a doped TIIn<sub>0.98</sub>Fe<sub>0.02</sub>Se<sub>2</sub> single crystal before (a and c) and after (b and d) irradiation with electrons with a fluence of  $5 \times 10^{16}$  electron/cm<sup>2</sup>.

**Table 4.** Changes in the surface microrelief of TlInSe<sub>2</sub> single crystals upon doping with iron and irradiation with electrons with a fluence of  $5 \times 10^{16}$  electron/cm<sup>2</sup>

Sample	Original		Electronirradiated, $5 \times 10^{16}$ electron/cm <sup>2</sup>	
	R <sub>a</sub> , nm	R <sub>z</sub> , nm	R <sub>a</sub> , nm	R <sub>z</sub> , nm
TlInSe <sub>2</sub>	40.869	398.036	40.998	444.579
TlIn <sub>0,98</sub> Fe <sub>0,02</sub> Se <sub>2</sub>	17.693	189.915	33.716	431.435

In contrast to doping, irradiation with electrons with a fluence of  $5 \times 10^{16}$  el/cm<sup>2</sup> significantly worsens the surface condition of both undoped and, especially, doped crystals. If the morphological characteristics of an undoped sample change insignificantly, then in doped samples these changes are significant (see Fig. 5 and 6; Table 3): in iron-containing crystals, when irradiated with electrons with a fluence of  $5 \times 10^{16}$  electron/cm<sup>2</sup>, the maximum value of the arithmetic mean deviation of the profile increases from R<sub>a</sub> = 17.693 nm to R<sub>a</sub> = 33.716 nm, and average roughness heights from R<sub>z</sub> = 189.915 nm to R<sub>z</sub> = 398.036 nm. (Table 4).

Thus, electron irradiation significantly worsens the surface condition of TlIn<sub>0,98</sub>Fe<sub>0,02</sub>Se<sub>2</sub> crystals.

#### 4. Conclusion

In this work, using X-ray diffraction research, it was established that when doping TlInSe<sub>2</sub> crystals with 2 mol. % TlFeSe<sub>2</sub>, as well as their irradiation with accelerated electrons with an energy of 2 MeV and a beam current density of 0.085 μA/cm<sup>2</sup> to a fluence of  $10^{17}$  electron/cm<sup>2</sup>, the samples remain single-phase and tetragonal, with space group *I4/mcm*. With increasing exposure to electrons to a fluence of  $5 \times 10^{15}$  electron/cm<sup>2</sup>, the unit cell parameter of the TlIn<sub>0,98</sub>Fe<sub>0,02</sub>Se<sub>2</sub> crystal decreases, and the band gap E<sub>g</sub> increases. With a further increase in the electron fluence, the value of the crystal lattice parameter increases, and E<sub>g</sub> decreases. The observed phenomenon is explained from the point of view of the effect of low doses: during irradiation of solids with ionizing radiation, unstable Frenkel pairs are created in them with a frequency 1-2 orders of magnitude higher than stable structural defects. During the birth and annihilation of unstable Frenkel pairs of defects, short-term local volume changes in the crystal and its rapid recovery occur, resulting in elastic stress waves. The interaction of these waves with existing point defects can lead to the non-activation migration of interstitial atoms existing in the crystal volume and their annihilation with the corresponding vacancies, which leads to their healing and transfer of the material to a more equilibrium state compared to the initial defective one. Therefore, at low doses of irradiation, in our case up to an electron fluence of  $5 \times 10^{15}$  electron/cm<sup>2</sup>, as a result of the recombination of biographical complementary pairs of defects, the irradiated crystal becomes more defect-free. At those irradiation doses when the number of radiation-induced defects becomes greater than the number of initial biographical defects (in our case, the fluence of electron irradiation is  $F > 5 \times 10^{15}$  electron/cm<sup>2</sup>), structural defects begin to accumulate in the crystal, the parameters of the crystal lattice begin to increase, and accordingly the band gap of the crystal decreases.

Along with the above, doping, as well as electron irradiation of TlInSe<sub>2</sub> crystals, greatly changes the surface morphology of TlFeSe<sub>2</sub> and TlIn<sub>0,98</sub>Fe<sub>0,02</sub>Se<sub>2</sub> crystals. The introduction of iron impurities into TlFeSe<sub>2</sub> crystals leads to an improvement in the surface condition, a decrease in the maximum value of the arithmetic mean deviation of the profile (from R<sub>a</sub> = 40.869 to R<sub>a</sub> = 17.7 nm), as well as a decrease in the height of the average roughness (from R<sub>z</sub> = 398.036 nm to R<sub>z</sub> = 189.915 nm). In contrast, irradiation with electrons with a fluence of  $5 \times 10^{16}$  el/cm<sup>2</sup> significantly worsens the surface condition in both undoped and, especially, doped crystals. If the morphological characteristics of an undoped sample after irradiation change insignificantly, then in doped samples these changes are significant: in iron-containing crystals, when irradiated with electrons with a fluence of  $5 \times 10^{16}$  electron/cm<sup>2</sup>, the maximum value of the arithmetic mean deviation of the profile increases (from R<sub>a</sub> = 17.693 nm to R<sub>a</sub> = 33.716 nm), and the height of the average roughness increases (from R<sub>z</sub> = 189.915 nm to R<sub>z</sub> = 398.036 nm).

#### Acknowledgments

The work was carried out on fundamental research topic No. PP-4526 of the Institute of Nuclear Physics of the Academy of Sciences of the Republic of Uzbekistan.

## REFERENCES

- 1 Umarov S.Kh., Nuritdinov I. Study of photoelectric properties of  $\text{TlInS}_{2x}\text{Se}_{2(1-x)}$  solid solutions. *Perspective materials*, 2002, No. 3, pp. 25 – 27. [in Russian]
- 2 Nuritdinov I., Umarov S.Kh., Rustamov V.D. The influence of group I and IV impurities on the photoelectric properties of  $\text{TlInSe}_2$  single crystals. *Perspective materials*, 2003, No.1, pp. 46 – 48. [in Russian]
- 3 Umarov S.Kh., Nuritdinov I., Dluraev Sh.N. Study of structural phase transitions of  $\text{TlInSe}_2$  crystals using electrical and photoelectric methods. *Perspective materials*, 2003, No. 5, pp. 34 – 36. [in Russian]
- 4 Guseinov G.D., Mateev A.K., Malsagov M.A., Umarov S.Kh., Abdullaev E.G., Yuraev N.D. Effect of Pressure in Electrical Conductivity of  $\text{TlInSe}_2$  Single Crystals. *Phys. Stat. Sol.*, 1985, Vol. 90, pp.703 – 708. doi:10.1515/9783112494806-035
- 5 Umarov S.Kh., Rustamov V.D., Nuritdinov I.  $\text{TlInS}_{2x}\text{Se}_{2(1-x)}$  ( $0 \leq x \leq 0.3$ ) single crystals are an effective material for semiconductor strain gauging. *Advanced materials*, 2002, No. 6, pp.41 – 42. [in Russian]
- 6 Alekseev I.V. A Neutron Semiconductor Detector Based on  $\text{TlInSe}_2$ . *Instruments and Experimental Techniques*, 2008, Vol. 51, No. 3, pp. 331–335. doi:10.1134/S0020441208030020
- 7 Sheleg A.U., Gurtova V.G., Shevtsova V.V., Mustafaeva S.N., Kerimova E.M. The influence of ionizing radiation on the dielectric characteristics of  $\text{TlInS}_2$  and  $\text{TlGaS}_2$  single crystals. *Solid State Physics*, 2012, Vol.54, Is.9, pp. 1754 – 1757. doi:10.1134/S1063783412090284
- 8 Shalimova K.V. *Physics of semiconductors*. Moscow, Energy. 1976, pp.24 – 26. [in Russian]
- 9 Chernyaev A.P. *Radiation technologies. The science. National economy. Medicine*. Moscow, Moscow Univ. Publ. House. 2019, 231 p. [in Russian]. doi:10.3103/S0027134915060090
- 10 Madatov R.S., Najafov A.I., Mamedov V.S., Mamedov M.A. Anisotropy of electrical conductivity in irradiated  $\text{TlInS}_2$  crystals. *Electronic processing of materials*, 2010, No. 2, pp. 77 – 79. doi:10.3103/S1068375510020122
- 11 Smirnova L.S. *Physical processes in irradiated semiconductors*. Novosibirsk, Nauka. 1977, 256 p. [in Russian]
- 12 Sardarova N.S., Barkhalov B.Sh., Nurullaev Yu.G., Verdieva N.A., Jafarov M.B. Electrical properties of crystals of  $\text{TlInS}_2\text{-TlEuS}_2$  solid solutions of various compositions. *Science, technology and education*, 2016. No.11(29), pp. 6 – 9.
- 13 Gahramanov N.F., Barkhalov B.Sh., Nurullaev Yu.G., Sardarova N.S., Verdieva N.A. Effect of irradiation on the thermal conductivity of single crystals of the  $\text{TlIn}_{0.97}\text{Dy}_{0.03}\text{Se}_2$  solid solution. *Science, technology and education*, 2020, No. 9(73), pp. 6 – 11. [in Russian]
- 14 Samedov O.A., Dadashov I.Sh., Samedov S.F., Bayramov A.A., Nurullayev Y.Q., Salmanov F.T. Influence of gamma irradiation on dielectric properties of  $\text{TlInS}_2$  doped by ytterbium. *Proceeding of the International Conference “Nuclear Science and its Applications”*, Samarkand, Uzbekistan, 2012, pp. 180 – 190. <https://www.researchgate.net/publication/373076563>
- 15 Umarov S.Kh., Gasanov N.Z., Ashurov Zh.J., Khodzhaev U.O., Narzullaeva Z.M. Technology for producing doped layered single crystals  $\text{TIMC}_2^{\text{VI}}$  (M- In, Ga; C- S, Se). Way Science. *Proceedings of the 2<sup>nd</sup> Intern. Scientific and Practical Conference “Integration of education, science and business in the current environment: summer debates”*. Dnipro, Ukraine, 2020, pp.495. [in Russian]
- 16 Tashmetov M.Yu., Khallokov F.K., Ismatov N.B., Yuldashova I.I., Nuritdinov I., Umarov S.Kh.. Study of the influence of electronic radiation on the surface, structure and Raman spectrum of a  $\text{TlInS}_2$  single crystal // *Physica B: Condensed Matter*, 2021, Vol.613, 412879. doi: 10.1016/j.physb.2021.412879
- 17 Tashmetov M. Yu., Ismatov N.B., Saidov R.P., Maxkamov Sh.M. Radiation treatment complex on the base of the “electronics U-003” electron accelerator. *Problems of Atomic Science and Technology*, 111(5):91-97. [in Russian] <https://www.researchgate.net/publication/321154001>
- 18 Rodriguez-Carvajal J. Structural analysis from powder diffraction data : the Rietveld method *Ecolethématique « Cristallographie et neutrons »*, JournéesRossatMignod, 1997, Cours - Tome I , 32 p.
- 19 Langford J.I., Wilson A.J.C., Scherrer P. After Sixty Years: A survey and some new results in the determination of crystallite size. *Journal of Applied Crystallography*, 1978, Vol.11, pp. 102 – 113.
- 20 Hassan M., Younas S., Sher F., Husain S.S., Riaz S., Naseem S. Room temperature ferromagnetism in single-phase  $\text{Zn}_{1-x}\text{Mn}_x\text{S}$  diluted magnetic semiconductors fabricated by co-precipitation technique. *Applied Physics A.*, 2017, Vol. 123(1), pp. 352. doi:10.1007/s00339-017-0975-5
- 21 Bhargava R.N., Gallagher D., Hong X., Nurmikko A. Optical Properties of Manganese-Doped Nanocrystals of  $\text{ZnS}$ . *Physical Review Letter*, 1994, Vol.72, pp. 416- 419. doi:10.1103/PhysRevLett.72.416
- 22 Ukhanov Yu.I. *Optical properties of semiconductors*. Moscow, Science, 1977, 368 p.
- 23 Nuritdinov I., Umarov S.K. Effect of ionizing radiation and heat treatment on the photosensitivity of  $\text{TlInSe}_2$  crystals. *At Energy*, 2000, Vol. 88, Is. 4, 322–324. doi:10.1007/BF02673619.
- 24 Nuritdinov I., Umarov S.Kh. The influence of ionizing radiation on the photoelectric and electrophysical characteristics of  $\text{TlInSe}_2$  crystals. In the book: *Nuclear and radiation physics*, Almaty, 2001, pp.111 – 118. [in Russian]

25 Koshkin V.I., Mankov B.I., Galchinetsky L.P., Kulik V.V. Thermodynamics of unstable vacancy-atom pairs at an interstitial site. *FTT*, 1973, Vol.15, pp. 128-132.[in Russian]

26 Indenbom V.L. A new hypothesis about the mechanism of radiation-stimulated processes. *Letters to ZhTF*, 1979, Vol.5, pp. 489 – 492. [in Russian]:[https://inis.iaea.org/search/search.aspx?orig\\_q=RN:11496581](https://inis.iaea.org/search/search.aspx?orig_q=RN:11496581)

27 Annenkov Yu.M. *Defect formation and mass transfer in ionic structures under intense irradiation with ionizing radiation*. Diss. for the scientific degree of doctor... Tomsk, 2002, 471 p.

28 Chernov I.P. Ordering the structure of crystals by ionizing radiation (the effect of small doses of ionizing radiation). *News of Tomsk Polytechnic Univ.*, 2000, Vol.303, Is.1. pp.74-80.<http://earchive.tpu.ru/handle/11683/2671>

29 Zhetbaeva M.P., Indenbom V.L., Kirsanov V.V., Chernov V.M. Migration of defects stimulated by the formation and collapse of an unstable Frenkel pair. *Letters to ZhTP*, 1979, Vol. 5, pp.1157 – 1161.[in Russian]

30 Zolnikov K.P., Korchuganov A.V., Kryzhevich D.S., Chernov V.M., Psakhye S.G. Shock waves in metal crystallites under radiation exposure. *VANT. Ser. Thermonuclear synthesis*, 2015, Vol.38, No. 2, pp. 68-74. doi:10.21517/0202-3822-2015-38-2-68-74

31 Mamontov A.P., Chernov I.P. *Small dose ionizing radiation effect. [Effekt malykh doz ioniziruiushchego izlucheniia]*. Tomsk, 2009. 286 p. [in Russian]

32 Rakhmatov A.Z., Tashmetov M.Yu., Sandler L.S. The influence of penetrating radiation on the parameters of high-voltage planar rectifier diodes. *Issues of atomic science and technology, series Physics of radiation damage and radiation materials science*, 2011, Vol. 98, No. 4, pp. 26 – 33.

33 Bilenko D.I., Galushka V.V., Zharkova E.A., *et al.* The effect of low doses of gamma radiation on the electrophysical properties of mesoporous silicon. *Tech. Phys. Lett.*, 2017, 43, pp.166–168. doi:10.1134/S1063785017020031.

34 Chernov I. P., Mamontov A.P., Botaki A.A., Cherdantsev P.A., Chakhlov B.V., Sharov S.R., Timoshnikov Yu.A., Filipenko L.A. Anomalous effect of small doses of ionizing radiation on metals and alloys. *Radiation Effects*, 1986, Vol. 97, No.1-2, pp. 155 – 160. doi:10.1080/00337578608208729

35 Annenkov Yu.M. The nature of high-temperature radiation-accelerated diffusion in alkali halide crystals. *News of Tomsk Polytechnic University*, 2006, Vol.309, No.3, pp. 46 – 50.

Article received 10.10.2023

Article accepted 31.10.2023

DOI 10.31489/2023No4/33-38

UDC 539.261, 539.193, 539.194

## QUANTUM-CHEMICAL STUDY OF THE STRUCTURE AND PROPERTIES OF MOLECULE OF THE LUPININE ALKALOID DERIVATIVE

Kopbalina K.B.<sup>1,2</sup>, Makhmutova A.S.<sup>3\*</sup>, Turdybekov D.M.<sup>2</sup>, Turdybekov K.M.<sup>1</sup>, Tolenova G.K.<sup>4</sup><sup>1</sup>Karaganda Buketov University, Karaganda, Kazakhstan<sup>2</sup>A. Saginov Karaganda Technical University, Karaganda, Kazakhstan<sup>3</sup>Karaganda Medical University, Karaganda, Kazakhstan, almagul\_312@mail.ru<sup>4</sup>Altynsarin Arkalyk Pedagogical Institute, Arkalyk, Kazakhstan

*The paper presents the results of a quantum-chemical study of the molecule 1-((4-(3-methoxyphenyl)-1H-1,2,3-triazol-1-yl) methyl) octahydro-1H-quinolizine. The geometrical characteristics of this molecule obtained from quantum-chemical calculations have been analysed and compared with experimental data of X-ray diffraction analysis. According to the results of the conformational analysis carried out by rotation along the labile bonds C11-N12 and C7-C11, the most favourable conformational states of the molecule have been established. It is shown that the localisation of the boundary molecular orbitals falls on the 1-ethyl-4-(4-methoxyphenyl)-1H-1,2,3-triazole substituent at the C11 atom, which suggests its participation in the subsequent modification reactions carried out to find new biologically active substances.*

**Keywords:** quantum-chemical calculations, quinolizine derivatives, conformational analysis, lupinin derivatives, X-ray diffraction analysis.

### 1. Introduction

It is well known that alkaloids are among the most promising compounds in terms of possible modification and creation of new biologically active substances based on them. Quinolizidine derivatives are the most interesting among them in terms of their structure. For example, the authors of work [1] obtained compounds with octahydroquinolizine nucleus and found that they are ligands of serotonin receptors 5-HT<sub>3</sub> and 5-HT<sub>4</sub>. Analysis of literature data showed that similar compounds also exhibit antimalarial [2,3], antitubercular [4] and anticholinesterase activities [5-8].

A wide range of biological properties of quinolizidine derivatives allows to accumulate specific material for the bank of data on their structural derivatives and use them in the search for new drugs. Therefore, the problem of a comprehensive study of the spatial structure of quinolizidine derivative molecules, their conformational states, pathways and barriers of conformational transitions, as well as their reactivity data remains relevant.

### 2. Research Methods

Quantum chemical calculations, which are now an integral part of modern chemistry, have been widely used not only as a tool for explaining chemical laws, but also for solving complex, in some cases impossible, problems, one of which is the determination of energy characteristics.

Currently, there are many methods and basis set available to obtain results close to the experiment, but the success of the calculation depends on the proper choice of method and basis set for each specific case. The object of this work is the molecule of the lupinine alkaloid derivative 1-((4-(3-methoxyphenyl)-1H-1,2,3-triazol-1-yl) methyl) octahydro-1H-quinolizine (Molecule 1) (Fig.1), previously synthesized by the authors of work [9]. Selection of the optimal method and basis for further study of this molecule was made by us on the basis of comparison of experimental (data of X-ray structure analysis) and calculated data of geometrical characteristics.

The X-ray diffraction study of compound (1) was performed on an Xcalibur, Ruby diffractometer with CCD detector (CuK $\alpha$ -radiation, graphite monochromator,  $\lambda=1.54184$  Å,  $\omega$ -scanning). Processing of the initial array of measured intensities and absorption accounting was performed using the CrysAlisPro (multi-scan) program [10]. The structure was deciphered by the direct method. The positions of non-hydrogen atoms were refined in the anisotropic approximation by full-matrix least squares. Hydrogen atoms were

placed in geometrically calculated positions and their positions were refined in the isotropic approximation with fixed positional and thermal parameters (“rider” model). The structures were decoded by the direct method and refined using the SHELXS-2014 and SHELXL-2014 software packages [11].

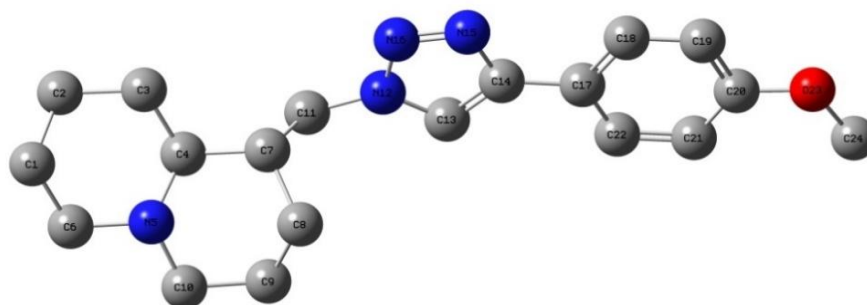


**Fig.1.** 1-1 - ((4 - (4 - (3 -methoxyphenyl) - 1H - 1, 2, 3 - triazol - 1 - il) methyl) octahydro - 1H- quinolizine

The semi-empirical PM6 method and non-empirical quantum chemical methods with basis sets 3-21, 6-31, 6-311\*\*, B3LYP/3-21, B3LYP6-311\*\* were used for the quantum chemical study of molecule 1. The calculations were performed using the MOPAC 9.0 [12] and GAUSSIAN 16 [13] programs.

### 3. Results and discussions

To study the spatial structure of Molecule 1, the geometrical characteristics obtained from quantum-chemical calculations and data of X-ray structure analysis were compared. The values of bond lengths, valence angles, and torsion angles are given in Tables 1-3.

**Table 1.** Values of interatomic distances in Molecule 1.

Bond	X-ray structure analysis	PM6	3-21	6-31	6-311**	B3LYP/3-21	B3LYP6-311**
C2-C1	1.526(2)	1.532	1.535	1.528	1.527	1.543	1.538
C3-C2	1.519(2)	1.531	1.533	1.527	1.526	1.541	1.537
C4-C3	1.516(1)	1.546	1.540	1.537	1.535	1.543	1.539
N5-C4	1.471(1)	1.505	1.473	1.467	1.469	1.491	1.484
C6-N5	1.479(1)	1.504	1.474	1.464	1.465	1.484	1.475
C7-C4	1.549(1)	1.560	1.560	1.558	1.556	1.566	1.565
C8-C7	1.539(1)	1.538	1.537	1.536	1.535	1.543	1.539
C9-C8	1.506(1)	1.529	1.531	1.525	1.525	1.547	1.543
C10-N5	1.472(1)	1.504	1.478	1.468	1.468	1.482	1.472
C11-C7	1.526(1)	1.549	1.539	1.537	1.536	1.542	1.545
N12-C11	1.461(1)	1.476	1.464	1.456	1.455	1.478	1.464
C13-N12	1.320(1)	1.400	1.351	1.353	1.352	1.362	1.365
C14-C13	1.373(1)	1.407	1.366	1.370	1.367	1.388	1.389
N15-C14	1.354(1)	1.414	1.370	1.369	1.370	1.385	1.387
N16-N15	1.355(1)	1.299	1.300	1.286	1.289	1.344	1.331
C17-C14	1.485(1)	1.454	1.463	1.464	1.465	1.461	1.464
C18-C17	1.379(1)	1.415	1.395	1.399	1.399	1.409	1.410
C19-C18	1.408(2)	1.386	1.373	1.378	1.377	1.384	1.388
C20-C19	1.353(1)	1.412	1.389	1.391	1.390	1.404	1.401
C21-C20	1.360(1)	1.399	1.381	1.385	1.383	1.398	1.398
C22-C17	1.373(1)	1.398	1.383	1.388	1.387	1.395	1.398
O23-C20	1.376(1)	1.376	1.371	1.373	1.374	1.385	1.394
C24-O23	1.388(2)	1.448	1.435	1.427	1.425	1.459	1.452

**Table 2.** Valence angles in Molecule 1.

Valence angles	X-ray structure analysis	PM6	3-21	6-31	6-311**	B3LYP/3-21	B3LYP6-311**
C3-C2-C1	109.6(1)	109.4	108.1	108.8	109.0	109.6	110.6
C4-C3-C2	110.3(9)	111.7	112.5	113.1	113.2	111.4	111.9
N5-C4-C3	111.7(7)	109.2	110.5	110.6	110.7	109.7	109.8
C6-N5-C4	107.2(7)	111.5	114.9	115.9	115.3	111.5	112.6
C7-C4-C3	112.2(7)	108.9	108.6	109.1	109.3	110.5	111.6
C8-C7-C4	110.3(8)	112.1	111.8	112.2	112.2	110.4	111.1
C9-C8-C7	109.7(9)	111.1	109.8	110.4	110.6	111.6	112.4
C10-N5-C4	112.0(7)	112.5	113.8	115.8	115.1	110.6	112.2
C11-C7-C4	113.4(7)	111.2	108.8	108.9	108.9	111.8	110.2
N12-C11-C7	111.4(7)	112.1	111.8	113.0	113.2	111.0	113.0
C13-N12-C11	130.2(8)	127.6	130.6	129.7	129.6	129.8	129.8
C14-C13-N12	105.0(8)	104.9	105.9	105.3	105.3	106.2	105.7
N15-C14-C13	111.1(8)	106.7	107.3	106.9	106.9	108.3	107.6
N16-N15-C14	106.9(7)	109.6	110.0	109.8	109.7	109.7	109.6
C17-C14-C13	130.7(8)	130.2	130.7	131.3	131.4	130.1	130.8
C18-C17-C14	121.3(8)	120.0	119.5	120.1	120.1	119.2	120.1
C19-C18-C17	122.0(9)	120.6	120.8	120.9	120.9	120.9	121.0
C20-C19-C18	119.2(1)	118.8	120.5	120.2	120.2	120.5	120.1
C21-C20-C19	121.4(1)	121.7	119.3	119.9	119.8	119.1	120.0
C22-C17-C14	120.6(8)	118.5	122.3	121.8	121.8	120.1	119.4
O23-C20-C19	114.5(9)	112.6	116.2	116.0	116.0	115.9	115.7
C24-O23-C20	117.1(1)	117.9	120.8	121.6	121.3	118.0	119.2

**Table 3.** Values of torsion angles in Molecule 1.

Torsionangle	X-ray structure analysis	PM6	3-21	6-31	6-311**	B3LYP/3-21	B3LYP6-311**
C4-C3-C2-C1	-56.6(1)	56.8	58.0	56.5	55.8	55.0	53.0
N5-C4-C3-C2	58.9(1)	-57.2	-53.2	-51.5	-51.7	-56.3	-55.0
C6-N5-C4-C3	-58.0(9)	57.5	50.4	48.7	49.5	59.2	58.2
C7-C4-C3-C2	-175.0(9)	-178.0	-173.9	-173.9	-174.3	-178.0	-178.7
C8-C7-C4-C3	179.3(8)	134.4	138.4	139.5	139.0	112.0	110.5
C9-C8-C7-C4	54.1(1)	43.9	42.8	40.4	40.9	58.4	56.4
C10-N5-C4-C3	-58.0(9)	179.4	177.4	-180.0	179.2	-175.4	-172.4
C11-C7-C4-C3	-54.3(1)	-102.9	-97.1	-95.0	-95.3	-124.1	-123.3
N12-C11-C7-C4	179.2(7)	69.0	169.1	167.2	167.5	61.1	171.7
C13-N12-C11-C7	123.9(1)	-94.3	111.5	109.0	110.6	-138.5	105.8
C14-C13-N12-C11	-176.2(8)	178.1	-179.6	179.9	179.7	-178.1	-179.3
N15-C14-C13-N12	-0.53(1)	-0.2	-0.1	-0.1	-0.1	0.0	0.0
N16-N15-C14-C13	0.72(1)	-0.1	0.0	0.0	0.0	0.2	-0.1
C17-C-14-C13-N12	179.9(9)	179.6	-180.0	-180.0	-179.9	-179.7	-179.8
C18-C17-C14-C13	-155.6(1)	-177.9	179.9	179.6	179.3	179.7	-179.7
C19-C18-C17-C14	176.6(9)	180.0	-180.0	-180.0	-180.0	180.0	179.8
C20-C19-C18-C17	-178.8(9)	0.0	0.0	0.0	0.0	0.0	0.0
C21-C20-C19-C18	-1.2(2)	0.0	0.0	0.0	0.0	0.0	0.0
C22-C17-C14-C13	21.6(1)	0.0	-0.1	-0.4	-0.7	0.0	0.0
O23-C20-C19-C18	-178.7(9)	-180.0	180.0	180.0	180.0	180.0	180.0
C24-O23-C20-C19	175.0(2)	56.8	58.0	56.5	55.8	55.0	53.0

The configurations of the chiral centers C4 and C7 are correlated with the absolute in the crystal structure of lupinin chloride [14]. From the obtained data it follows that the bond lengths and valence angles in compound (1) are close to the usual ones [15].

The conformations of the six-membered cycles N5, C1 ... C6 (A) and N5, C4 ... C10 (B) in the quinolizidine framework in molecule (1) are close to the corresponding ones in the crystal structure of lupinin [16,17] and are in a conformation close to a slightly distorted armchair. In molecule (1), the orientation of the 1,2,3-triazole cycle is equatorial: torsion angle C7-C11-N12-N16 = 123.9°. The 1,2,3-triazole and phenyl cycles are planar to within  $\pm 0.013\text{\AA}$ . The angles between the planes of the triazole and aryl substituents in crystal (1) are 23 and 21°, respectively. The geometrical characteristics of molecule 1 obtained from quantum-chemical calculations are close to the corresponding data of X-ray structural analysis, which indicates the correctness of the calculated data.

To determine the most favorable conformational states of Molecule 1, a conformational analysis was performed by rotation along the C11-N12 and C7-C11 labile bonds. The conformational states along these bonds are shown in Figures 2 and 3, respectively.

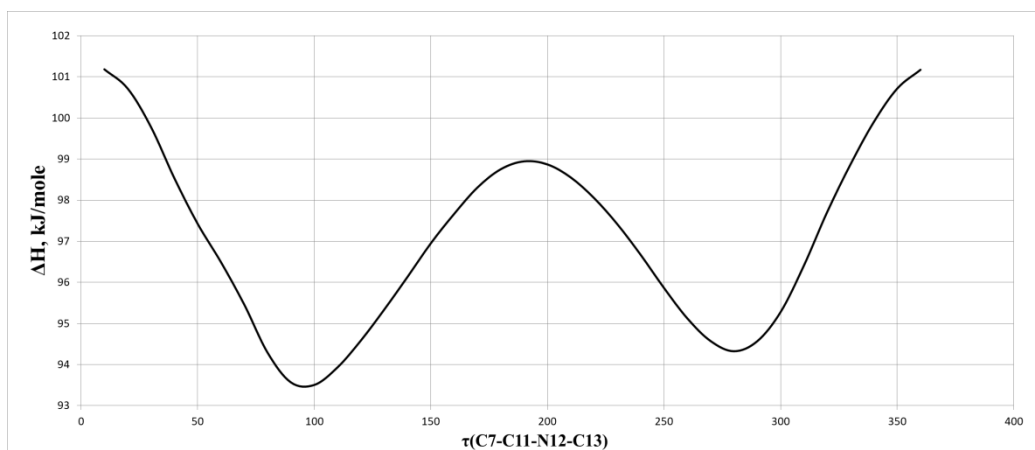


**Fig.2.** Dependence of the heat of formation on the conformation along the C11-N12 bond.

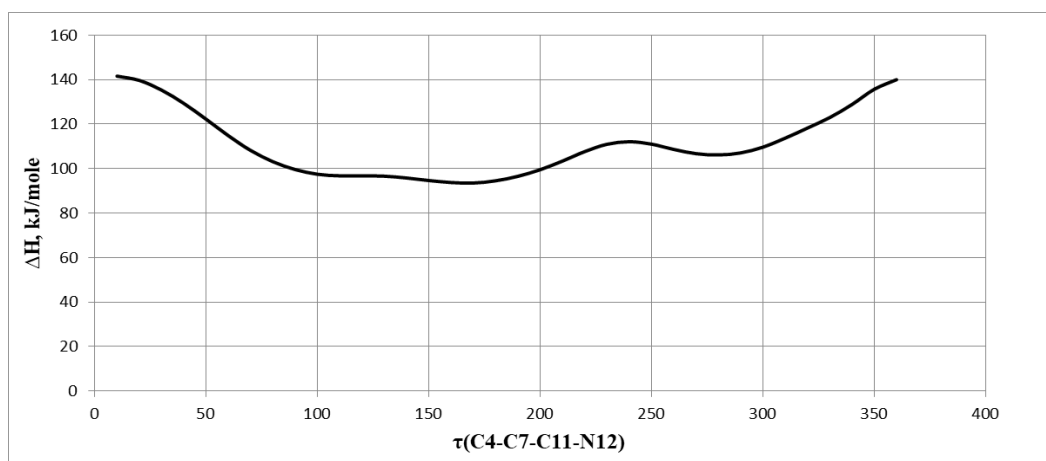


**Fig.3.** Dependence of the heat of formation on the conformation along the C7-C11 bond.

From the analysis of the obtained data we can conclude that the free molecule 1 adopts the most thermodynamically favourable conformational states (with the minimum electron energy of the molecule) at values of the torsion angle C7-C11-N12-C13 equal to 100° and 280° with a barrier of 5 kJ/mol between them. The conformation along the C7-C11 bond does not have a pronounced energy minimum in the 50-330° range. The conformational mismatch along the N12-C13 bond in quantum chemical calculations and data of X-ray structure analysis is probably due to the influence of intermolecular interactions of Molecule 1 in the crystal. To determine the thermodynamic stability of Molecule 1, the heats of formation were calculated and the results are presented in Table 4. The obtained negative values of the heats of formation indicate that molecule 1 is thermodynamically stable.

The reactivity of a molecule is characterized by the values and localization of the HOMO (highest occupied molecular orbital) and LUMO (the lowest unoccupied molecular orbital) [18-20]. Reactivity analysis based on boundary molecular orbitals showed that the localization of the HOMO and LUMO falls on the 1-ethyl-4-(4-methoxyphenyl)-1H-1,2,3-triazole substituent at the C11 atom (Figure 4), thus subsequent reactions of modification are expected to occur with the participation of the substituent. The reactivity is also affected by the hardness/softness of the molecules [21].

**Table 4.** Energy characteristics of Molecule 1.

Basis	3-21	6-31	6-311**	B3LYP/3-21	B3LYP6-311**
$\Delta H$ , Hartrey	-1021.018	-1026.292	-1026.499	-1027.739	-1033.358
HOMO, eV	-7.713	-7.740	-7.832	-5.409	-5.841
LUMO, eV	3.563	3.411	3.169	-0.326	-0.919
$\eta$ , eV	5.638	5.575	5.501	2.541	2.461

Knowing of the values of the HOMO and LUMO energies makes it possible to determine the "hardness" or "softness" of the studied molecules. The Pearson indices of "hardness  $\eta$  /softness  $S$ " of the molecules can be calculated on the basis of the following calculation formulae:

$$\eta = (E_{\text{LUMO}} - E_{\text{HOMO}})/2,$$

$$S = 1/(2\eta) = 1/(E_{\text{LUMO}} - E_{\text{HOMO}}).$$

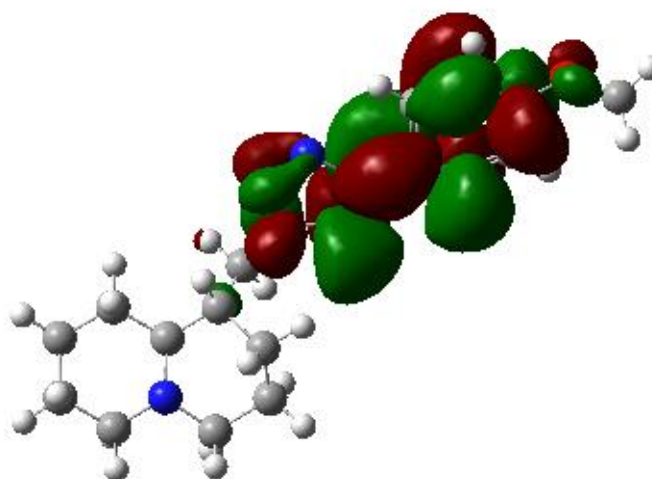


**Fig.4.** Localization of HOMO and LUMO in Molecule 1.

The application of the above formulae allowed us to show that all the studied molecular systems are "hard" reagents, since they have an energy gap between HOMO and LUMO greater than 1 eV. The calculated stiffness ( $\eta$ ) shows that this molecule is quite rigid, indicating its low reactivity and high electronic stability

#### 4. Conclusion

The results of the conducted studies showed that the geometrical parameters are close to the standard parameters. For the free molecule 1, two conformers with torsion angle values C7-C11-N12-C13 equal to 100° and 280° can be realized. The energy barrier between them is negligible and is equal to 5 kJ/mole. The conformation along the C7-C11 bond does not have a pronounced energy minimum in the 50-330° range.

The orbital control data show that both HOMO and LUMO are almost completely centered on the 1-ethyl-4-(4-methoxyphenyl)-1H-1,2,3-triazole substituent at the C11 atom, indicating that this substituent can act as both an electron donor and acceptor in the following reactions. Thus, the established quantum-

chemical properties can be the basis for further synthesis and the search for new drugs based on quinolizidine derivatives.

## REFERENCES

- 1 Sparatore A., Cagnotto A., Sparatore F. Quinolizidinyl derivatives of 2,3-dihydro-2-oxo-1H-benzimidazole-1-carboxylic acid and 1-homolupinanoyl benzimidazolones as ligands for 5-HT<sub>3</sub> and 5-HT<sub>4</sub> receptors. *Farmaco*, 1999, Vol. 54, pp. 248–254. doi: 10.1016/s0014-827x (99)00025-7
- 2 Basilico N., Parapini S., Sparatore A., Romeo S., et al. In vivo and in vitro activities and ADME-tox profile of a quinolizidine-modified 4-aminoquinoline: A potent anti-*P. falciparum* and anti-*P. vivax* blood-stage antimalarial. *Molecules*, 2017, Vol. 22, pp. 2102. doi: 10.3390/molecules22122102
- 3 Rusconi C., Vaiana N., Casagrande M., Basilico N., Parapini S., Taramelli D., Romeo S., Sparatore A. Synthesis and comparison of antiplasmodial activity of (+), (-) and racemic 7-chloro-4-(N-lupinyl) aminoquinoline. *Bioorg. Med. Chem.*, 2012, Vol. 20, pp. 5980–5985. doi:10.1016/j.bmc.2012.07.041
- 4 Vazzana I., Novelli F., Sparatore F., Sparatore A., Fadda G., Manca C. Quinolizidine derivatives with antitubercular activity. *Farmaco*, 1994, Vol. 49, pp. 105-110.
- 5 Basova N.E., Kormilitsyn B.N., Perchenok A., Rozengart E.V., Saakov V.S., Suvorov A.A. Reversible lupinin inhibitors of cholinesterases of mammalian blood and of optical ganglia of individuals of the commander squid *Beryteuthis magister* from different zones of species areal. *Zh. Evol. Biokhim.Fiziol.*, 2012, Vol. 48, pp. 213–218.
- 6 Rozengart E.V. Bisalkaloid derivatives of dicarboxylic acids on the basis of lupinine, anabasine, and cytisine as reversible cholinesterase inhibitors. *Dokl. Biochem-Biophys.*, 2003, Vol. 388, pp. 39–42. doi: 10.1023/a:1022560630021.
- 7 Tasso B., Catto M., Nicolotti O., Novelli F., Tonelli M., Giangreco I., Pisani L., Sparatore A., Boido V., Carotti A., Sparatore F. Quinolizidinyl derivatives of bi- and tricyclic systems as potent inhibitors of acetyl- and butyrylcholinesterase with potential in Alzheimer's disease. *Eur. J. Med. Chem.*, 2011, Vol. 46, pp. 2170–2184. doi: 10.1016/j.ejmech.2011.02.071
- 8 Tonelli M., Catto M., Tasso B., Novelli F., Canu C., Iusco G., Pisani L., De Stradis A., Denora N., Sparatore A., Boido V., Carotti A., Sparatore F. Multitarget Therapeutic Leads for Alzheimer's Disease: Quinolizidinyl Derivatives of Bi- and Tricyclic Systems as Dual Inhibitors of Cholinesterases and  $\beta$ -Amyloid ( $A\beta$ ) Aggregation. *ChemMedChem.*, 2015, Vol. 10, pp. 1040–1053. doi: 10.1002/cmdc.201500104
- 9 Nurmaganbetov Zh.S., Fazylov S.D., Turdybekov K.M., Nurkenov, et al. Synthesis and structure of 4-substituted (1S,9aR)-1-[(1,2,3-triazol-1-yl) methyl] octahydro1H-quinolysines of lupinine. *Bulletin of the University of Karaganda – Chemistry*, 2022, Vol.106(2), pp. 12–22. doi:10.31489/2022Ch2/2-22-5
- 10 *CrysAlisPro*. Yarnton, Oxford shire, England: Agilent Technologies Ltd., 2014, 60 p.
- 11 Sheldrick G.M. A short history of SHELX. *Acta Crystallogr A*. 2008, Vol. 64(Pt 1), pp.112-122. doi:10.1107/S0108767307043930.
- 12 Stewart J.J.P. Optimization of parameters for semiempirical methods V: Modification of NDDO approximations and application to 70 elements. *J. Mol. Modeling*, 2007, Vol. 13, pp. 1173–1213. doi: 10.1007/s00894-007-0233-4
- 13 Frisch M.J., et. al. Gaussian 09, Revision D.01, Gaussian, Inc., Wallingford CT, 2009. <https://gaussian.com/g09citation/>
- 14 Koziol A.E., Gdaniec M., Kosturkiewicz Z. Structure of (-) – lupinine. *Acta Crystallogr*, 1980, Vol. 36, pp. 980-981. doi: 10.1107/S0567740880005080
- 15 Allen F.H., Kennard O., Watson D.G., Brammer L., Guy Orpen A., Taylor R. Tables of bond lengths determined by X-ray and neutron diffraction. *J. Chem. Soc. Perkin Trans.*, 1987, Vol. 2, Issue 12, pp. 1–19.
- 16 Koziol A.E., Kosturkiewicz Z., Podkowinska H. Structure of the alkaloid lupinine. *Acta Crystallogr*, 1978, Vol.34, pp. 3491-3494.
- 17 Duax W.L., Norton D.A. *Atlas of Steroid Structure*, New-York, 1975, 18 p.
- 18 Shirayayev A.K. *Kvantovaya khimiya*. Samara: Samara State Technical University, 2020, 134 p. [in Russian]
- 19 Kovalskiy Y., Kostiv I., Marshalok O., Vytrykush N. Quantum-chemical research of mechanism of the reaction dehydration of 2,3-dimethylbutan-2,3-diol and it's hexahydrate. *Eastern-European Journal of Enterprise Technologies*, 2013, Vol. 6/6, (66), pp.11-15. doi:10.15587/1729-4061.2013.18864
- 20 Kopbalina K.B., Mazhenov N.A., Bimbetova G.M. Quantum-chemical calculations of the structure and electron transitions of multimolecular films. *Eurasian Physical Technical Journal*, 2019, Vol.16, No.1(31), pp.62-68. doi:10.31489/2019No1/62-68
- 21 Tsyshevskiy R.V. *Kvantovo-khimicheskiye raschety mekhanizmov khimicheskikh reaktsiy*: teaching manual. Kazan, Kazan National Research Technological University, 2012, 88 p. [in Russian]

Article received 08.11.2023

Article accepted 29.11.2023

DOI 10.31489/2023No4/39-45

UDC 539.1.044

## EFFECT OF THE CONCENTRATION OF SILVER NANOPARTICLES ON THE PHOTOCATALYTIC ACTIVITY OF TITANIUM DIOXIDE NANORODS

Kayumova A.S., Serikov T.M. \*, Omarova G.S., Dzhakupova M.S.

Karaganda Buketov University, Karaganda, Kazakhstan, serikov-timur@mail.ru

*In this paper the results of a study of the effect of the concentration of silver nanoparticles in films of titanium dioxide nanorods on their photocatalytic activity are presented. Titanium dioxide nanorods with a rutile structure was obtained using the method of hydrothermal synthesis. Due to changing with the amount of substance of the transition metal silver salt ( $\text{AgNO}_3$ ) and chemical reduction on the surface of the titanium dioxide nanorods, Ag nanoparticles of different concentrations were obtained. The photocatalytic activity of the samples was assessed by the amount of photocurrent obtained from a unit of film surface and photodegradation of methylene blue dye when illuminating the surface with a light source of a Xenon lamp. Surface morphologies and energy dispersive X-ray studies showed that Ag nanoparticles were uniformly distributed and anchored on the titanium dioxide nanorods surface.*

**Keywords:** nanorods, titanium dioxide, silver nanoparticles, Ag, photocatalysis.

### 1. Introduction

Titanium dioxide  $\text{TiO}_2$  is one of the most researched and widely used materials for water purification, air purification, hydrogen production and solar cells due to its many advantages and unique physical and chemical properties [1-4]:

1. Low cost:  $\text{TiO}_2$  is cheap and readily available, making it attractive for mass production.
2. Chemical stability:  $\text{TiO}_2$  is chemically stable and does not degrade in aggressive environments, which allows it to be used in various conditions.
3. Suitable zone position:  $\text{TiO}_2$  zones are suitable for inducing oxidation and reduction reactions, making it effective for a variety of catalyst processes.
4. Non-toxic and biocompatible:  $\text{TiO}_2$  is a non-toxic and biocompatible material, which is important for medical and biological applications.
5. Possibility of controlling the geometric structure, depending on the synthesis method, for example nanorods, nanotubes, nanofilaments and  $\text{TiO}_2$  nanoparticles [5-9].

However, despite the many structures,  $\text{TiO}_2$  has two main disadvantages: firstly, it can only absorb ultraviolet radiation due to its wide band gap ( $\sim 3.2$  eV), secondly, its high photogenerated carrier recombination rate leads to low quantum efficiency [10, 11].

Among the variety of nanostructures, titanium dioxide nanorods (TNR) are the most promising because they have one-dimensional electron transport, high specific surface area and high crystallinity [12-14]. At the same time, the possibility of using one-dimensional electron transport will make it possible to somehow reduce the recombination rate of photogenerated TNR charge carriers, but the problem of the absorption capacity of only the ultraviolet region has not yet been resolved.

The spectral sensitivity of TNR in the visible range can be expanded by adding noble metal nanoparticles [15, 16], sensitization with dye molecules [17], and adding nanomaterials with lower band gap energy [18-20]. The introduction of Ag nanoparticles into the  $\text{TiO}_2$  structure is an effective method for improving its photocatalytic properties. The introduction of Ag nanoparticles into  $\text{TiO}_2$  is an effective method for improving its photocatalytic properties. On the one hand, a Schottky barrier can form between  $\text{TiO}_2$  and Ag nanoparticles [21, 22], restraining the reverse current of injected electrons from  $\text{TiO}_2$  to Ag and thereby suppressing the recombination of electron-hole pairs. On the other hand, Ag nanoparticles generate localized surface plasmon resonance (LSPR) effect under visible light, and excited hot electrons can be

injected onto the TiO<sub>2</sub> surface [23, 24]. Thus, the performance of TiO<sub>2</sub>/Ag composite is superior to that of TiO<sub>2</sub> [25]. Despite the huge number of published works on the photocatalytic activity of TNR and the use of LSPR in these processes, there is no information on the optimal concentration of Ag nanoparticles on the surface of TiO<sub>2</sub> nanorods obtained by chemical method.

The purpose of this work is to determine the optimal concentration of Ag nanoparticles on the surface of TNR films at which the best photocatalytic activity will be observed.

## 2. Experimental part

TNRs are synthesized by hydrothermal synthesis. Cleaned fluorine-doped tin oxide (FTO) substrates were prepared from a solution containing 7.5 ml - of deionized water, 7.5 ml of hydrochloric acid, and 0.25 ml of titanium butoxide C<sub>16</sub>H<sub>36</sub>O<sub>4</sub>Ti - in a 25 ml fluoroplastic embedded stainless steel tube was placed in an autoclave. The solution was kept in a furnace for 6 hours at a temperature of 180°C. The samples were then removed and washed with deionized water. To improve crystallization and remove synthesis byproducts, the nanorods films were heated in a high temperature oven at 500°C for 2 hours.

Ag nanoparticles were prepared by chemical deposition method. 0.2 g of polyvinylpyrrolidone was added to 40 ml of H<sub>2</sub>O and C<sub>2</sub>H<sub>6</sub>O<sub>2</sub> (1:1% by volume), then 2 mmol of NaBH<sub>4</sub> was added to the solution mixture with vigorous stirring. The resulting mixture was stirred for about 5 minutes. Then 0.5, 0.75, 1 and 2 mmol AgNO<sub>3</sub> were added at different concentrations. Substrates containing TNR were dipped upwards into the bottom of the dish and kept in an oven at 70°C for 2 minutes. The sample was then washed with deionized water and dried at room temperature.

Using a scanning electron microscope Mira 3MLU from Tescan at a voltage of 20 kV, a study of surface morphology, energy dispersive X-ray analysis (EDX) analysis and distribution of elements on the surface was carried out. Spectrophotometric measurements were carried out on a Solar CM 2203 scanning spectrophotometer (Solar) in the wavelength range 190-750 nm.

The resistance of the films was determined using impedance spectroscopy. For this purpose, the working electrode (test samples) and the counter electrode made of Pt (Platisol T/SP, Solaronix) deposited on FTO were glued together with a polymer film 25 μm thick (Melotonix, Solaronix). Iodide/triiodide electrolyte (Iodolyte Z-150, Solaronix) was used as the electrolyte.

The photocatalytic activity of the samples was assessed by measuring the photoinduced current with an illuminated area of 1 cm<sup>2</sup> in a standard three-electrode cell using a CS350 potentiostat/galvanostat with a built-in EIS analyzer (Corrtest Instruments, China). Platinum foil served as the counter electrode, and an AgCl electrode was used as the reference electrode. The measurements were carried out in a 0.1 mmol NaOH electrolyte in a specially manufactured photoelectrochemical cell with a quartz window. In addition, the photoactivity of the films was assessed by the photodegradation of the dye methylene blue (MB), which is used as a model pollutant. The radiation source used in the experiments was a xenon lamp with a power of 300 W/cm<sup>2</sup> (Newport, USA).

## 3. Results and discussion

Figure 1 shows micrographs of the surface morphology of the TNR film before and after deposition of Ag nanoparticles. From Figure 1a, it can be seen that hydrothermal synthesis produces titanium dioxide nanorods on the surface of the FTO substrate, predominantly perpendicular to the substrate surface. The length of the nanorods is about 1.48 μm, the average diameter of the nanorods is 50-60 nm. Chemical reduction of silver nitrate resulted in the formation of Ag nanoparticles on the surface of TNR (see Figure 1 b, c, d and f). The deposited Ag nanoparticles are uniformly distributed over the entire surface of the samples and envelop the walls of the TNR films, thereby creating roughness. It can be seen from the figures that with an increase in the concentration of AgNO<sub>3</sub> from 0.5 to 2 mmol used in reduction, the number of Ag nanoparticles increases.

This is especially noticeable from Figure 1d and 1f, where the concentration is 1 and 2 mmol. At the same time, the number of Ag nanoparticles is so large that the presence of TNR underneath is practically invisible. The sizes of silver nanoparticles were measured using the dynamic light scattering method on a Zetasizer Nano ZS. For this purpose, solutions were used from which Ag nanoparticles were deposited. It was found that the average diameter of nanoparticles is 25-30 nm, which is also confirmed by SEM image processing.

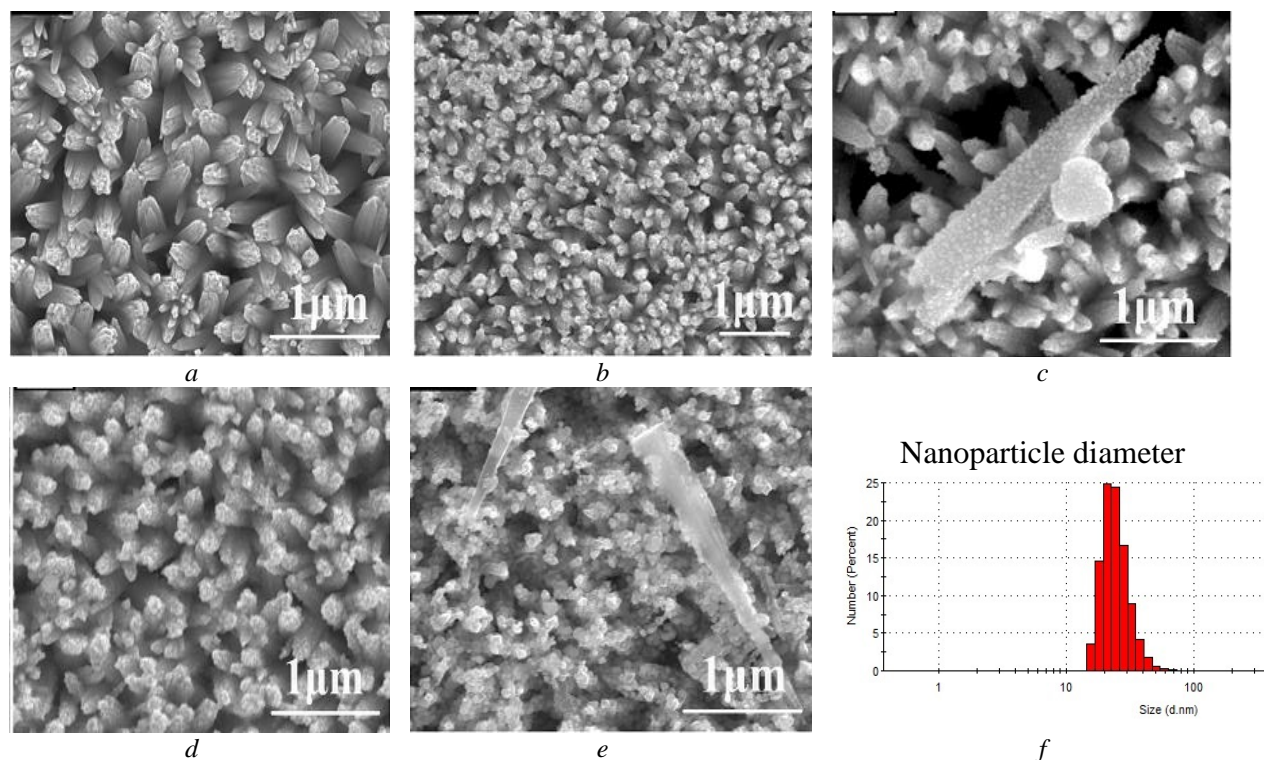


**Fig.1.** SEM images of the TNR surface before and after Ag deposition:

a) TNR; b) TNR/Ag\_0.5 mmol; c) TNR/Ag\_0.75 mmol; d) TNR/Ag\_1 mmol; e) TNR/Ag\_2 mmol; f) Diameter of nanoparticles measured on Zetasizer Nano

Surface mapping and EDX spectrum of TNR doped with Ag nanoparticles of different concentrations are presented in Figure 2. In all samples, 5 elements were identified, such as Ti, O, Ag, Na and Si. The elements Ti and O belong to the titanium dioxide nanorods that form the basis of the film, so its percentage is much higher than the others. The presence of peaks in the energy ranges from 3.4 to 4 keV and 1.8 keV, 1 keV correspond to the peaks of Sn, Si and Na, respectively, which belong to the FTO substrates. Peaks in the 3 keV region correspond to Ag nanoparticles.

Five spectra were taken from the surface of each sample: at the center and at the corners. The inset in Figure 2 shows the content of elements (in percentage) relative to the entire total spectrum of the map. From the data obtained, it is clear that with an increase in the amount of silver transition metal salt ( $\text{AgNO}_3$ ) used in chemical reduction, the concentration of reduced Ag nanoparticles on the TNR surface increases. Thus, with an amount of substance of 0.5 mmol  $\text{AgNO}_3$ , the proportion of Ag nanoparticles relative to the entire total spectrum was 2.3%, for 0.75, 1 and 2 mmol it was 2.8, 6.5 and 6.8%, respectively.

The normalized absorption spectra of the samples are presented in Figure 3. From the absorption spectra presented in Figure 3 it is clear that doping Ag NPs significantly expands the absorption spectrum of the photocatalyst relative to undoped  $\text{TiO}_2$ . The absorption peak of silver nanoparticles in the spectrum is located in the range of 410-420 nm. The introduction of Ag nanoparticles into TNR structures leads to an expansion of spectral sensitivity in the visible range.

This is confirmed by the pronounced small peaks of Ag nanoparticles in TNR/Ag nanocomposite materials in the region of 420–480 nm. In addition, TNR/Ag nanocomposites effectively absorb light in the ultraviolet region of the spectrum.

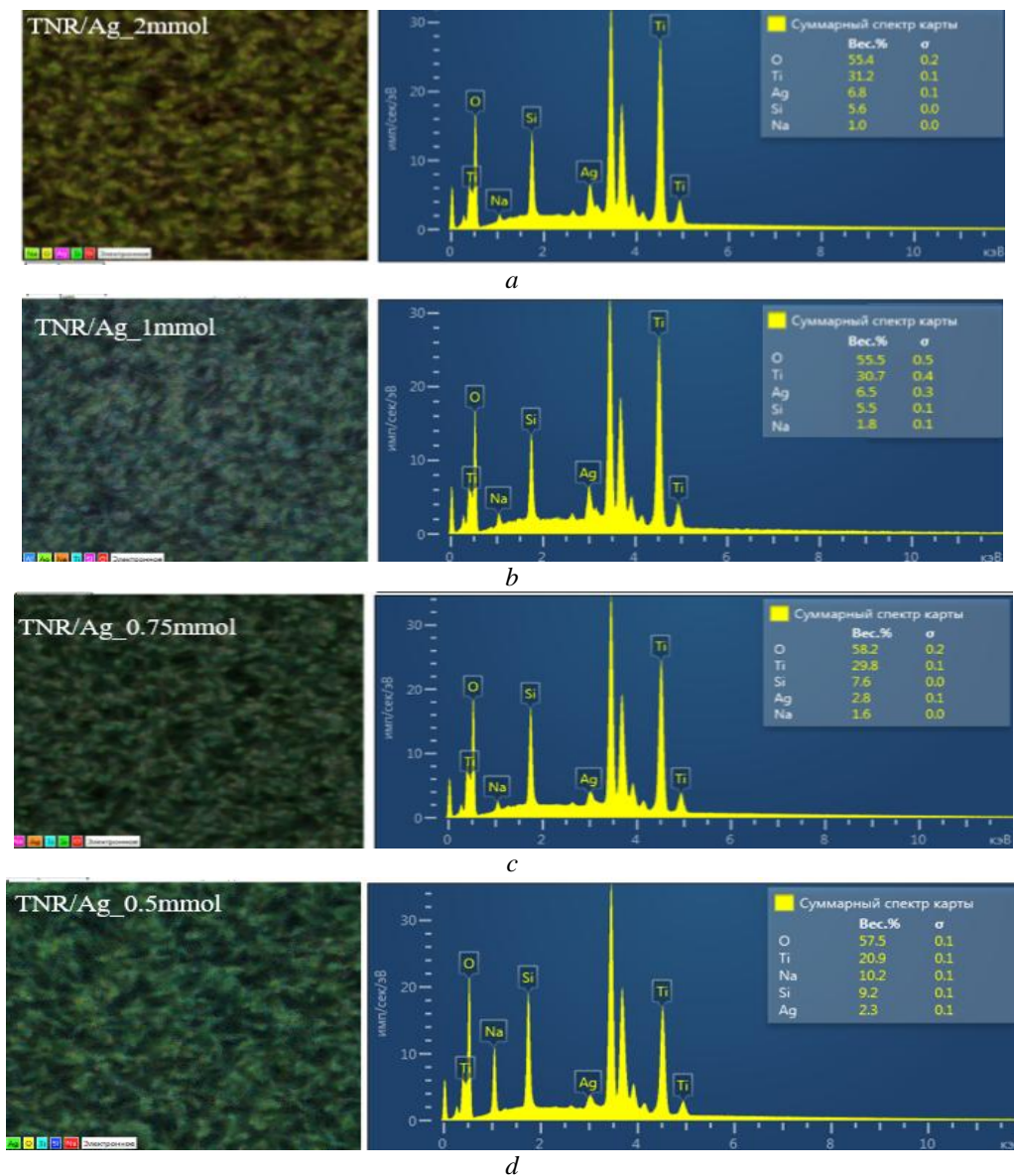


**Fig. 2.** Surface mapping and EDX spectrum of TNR doped with Ag nanoparticles of different concentrations: a) TNR/Ag\_2 mmol; b) TNR/Ag\_1 mmol; c) TNR/Ag\_0.75 mmol; d) TNR/Ag\_0.5 mmol.

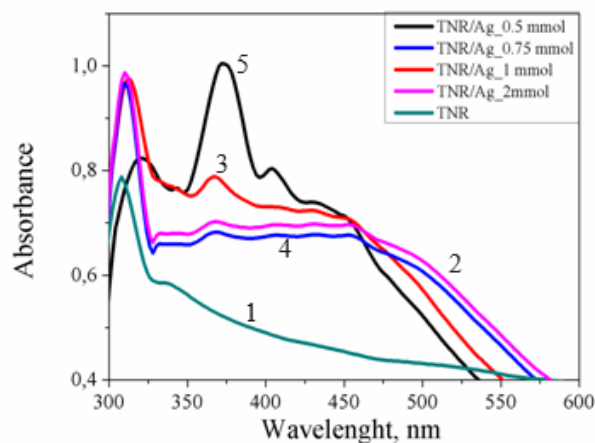
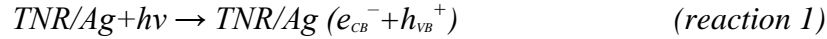


**Fig. 3.** Absorption spectrum of TNR/Ag at different concentrations: 1-TNR, 2- TNR/Ag\_2 mmol, 3-TNR/Ag\_1 mmol, 4-TNR/Ag\_0,75 mmol, 5-TNR/Ag\_0,5 mmol

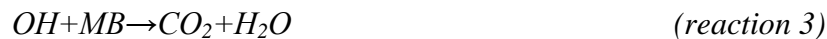
The photocatalytic activity of the samples was assessed by the decomposition reaction of the dye methylene blue (MB) and it is a model pollutant. The process of photocatalytic oxidation is as follows: after irradiation and excitation of electrons from the valence band of the photocatalyst, photogenerated holes can directly oxidize the dye to a reactive intermediate (reaction 1) or lead to the formation of highly reactive oxidative hydroxyl radicals (OH•), leading to degradation and discoloration dye (reactions 2 and 3).



or



or



The initial concentration of the MB dye was  $10^{-6}$  mol/L. Before the experiment, the samples were kept in a different solution of the MB dye for 8 hours to eliminate errors associated with the adsorption of the dye on its surface. The original optical density of the MB dye was 0.55 at the wavelength of its 662 nm absorption maximum and was obtained per unit.

An example of the degradation process of the MV dye and its assessment by optical density are presented in Figure 4a. From this figure it can be seen that with an increase in the duration of radiation, the optical density of the dye decreases, which leads to its discoloration and degradation of molecules. Further, at the absorption peak of 662 nm, a change in the absorbance of the MB dye was observed in the presence of TNR and TNR/Ag films with different silver concentrations. The curves for changes in optical density or dye concentration in the absence and presence of nanocomposite films are presented in Figure 4b. From the presented data it is clear that during long-term irradiation of the dye without immersed films, its degradation is insignificant and amounts to only 7%. In the presence of the film formed by TNR, the degradation rate increased significantly and reached 40% in 180 minutes of radiation. In the presence of TNR films with condemned Ag nanoparticles, the rate of dye degradation increased. Thus, when using a TNR/Ag film with an amount of reduced silver nitrate of 0.5 mmol, the degradation was 48%, and for 0.75, 1 and 2 mmol it was 60, 81 and 70%, respectively (see Fig. 4b) for a similar irradiation time.

Also, the photocatalytic activity of the samples was assessed by the photocurrent response when irradiated with artificial sunlight with periodic switching on and off of the light. In the absence of illumination, the photocurrent of the samples is zero; when the light was turned on, the photocurrent density instantly increased for all samples. It can be seen from Figure 4c that the maximum photocurrent value under light illumination for the TNR/Ag\_1mmol sample is  $890 \mu\text{A}/\text{cm}^2$  and is the highest among all samples. It is clear from the data that with an increase in the amount of reduced  $\text{AgNO}_3$  and, accordingly, reduced Ag nanoparticles on the surface, TNR first increases the photocurrent density and then decreases, indicating the presence of an optimal concentration.

Figure 4d shows the impedance hodographs in the Nyquist coordinates for all the samples under study. According to the godograph M. Adachi, M. Sakamoto, J. Jiu, et al. according to the methodology proposed in his works, the main electrical transfer properties of films were calculated [26]. The electron transport resistance in the  $R_w$  nanocomposite and the  $R_k$  charge transport resistance will directly depend on the number of electrons coming from the number of free electrons. The charge transfer resistance  $R_k$  of TNR/Ag films at a concentration of 1 mmol is 2.5 times less than in a film with a concentration of 0.5 mmol and is 1748 Ohm and 685 Ohm. Effective electron lifetime  $\tau_{eff}$  in films and nanocomposite materials. According to the results obtained, the duration of the effective lifetime of an electron in a sample with a concentration of 1 mmol is also 2 times less than the other samples. As the silver concentration increases, the effective lifetime of an electron in the sample increases. Long electron lifetimes increase the probability of electron recombination. Ag on the surface of TNR can resist oxidizing agents from solution or, conversely, are oxidized, since silver is a strong oxidizing agent. Unlike other noble metals such as Pt or Au, when Ag nanoparticles are combined with TNR, the Fermi level of the metal is located near the conduction band of  $\text{TiO}_2$ , and a Schottky barrier cannot be formed.

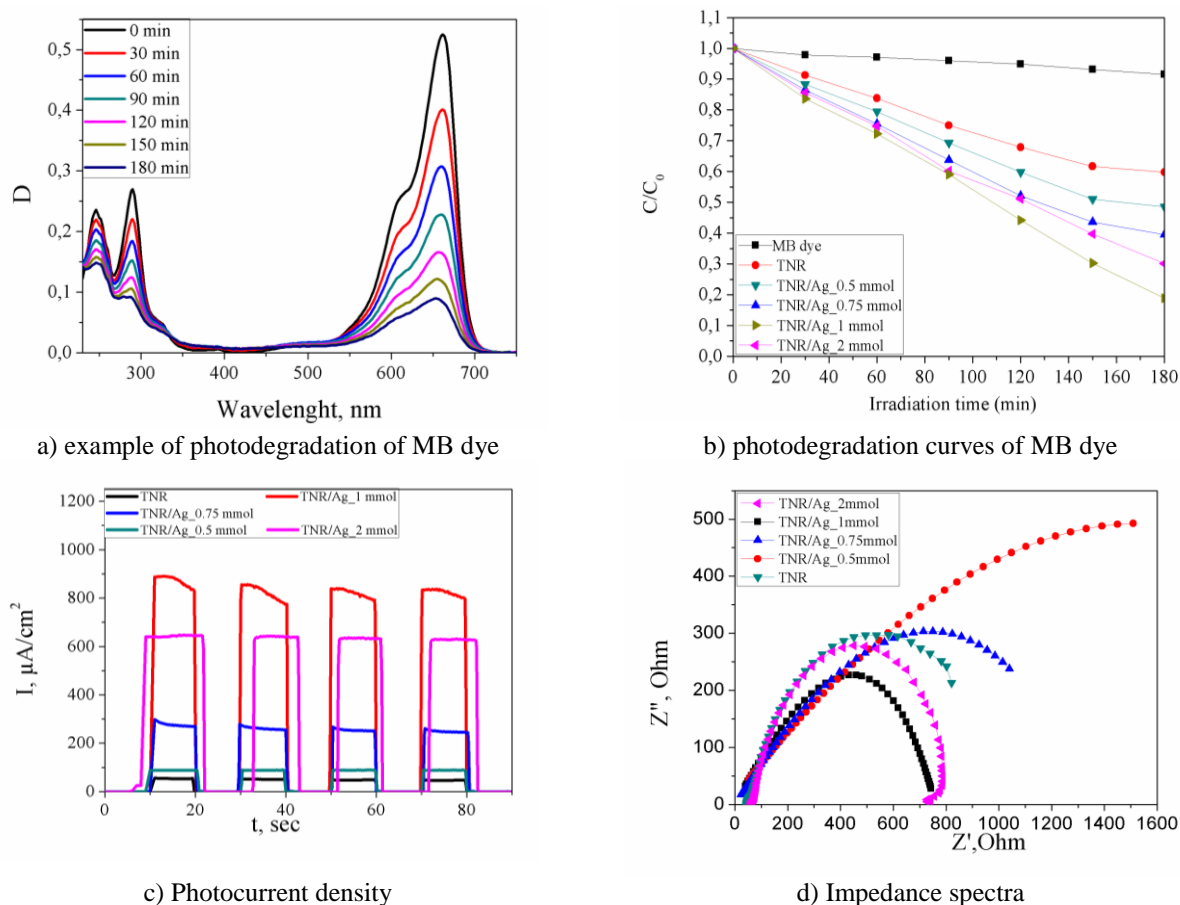


**Fig. 4.** Photocatalytic properties of TNR/Ag films at different concentrations.

Therefore, electrons can flow in both directions, allowing holes to be effectively captured by the silver particle. Researchers presented possible mechanisms of decomposition of various substances on the surface of  $\text{TiO}_2$  at different concentrations of silver nanoparticles [27]. However, they used  $\text{TiO}_2$  in nanoparticle form. The increase in photocatalytic activity of TNR in the presence of Ag may be due to the unusual electronic properties of silver and hot electrons, which are efficiently transferred to the conduction band of  $\text{TiO}_2$  and participate in photochemical reactions. The results obtained can be useful in creating effective photocatalysts for wastewater treatment and water splitting to produce hydrogen gas.

#### 4. Conclusions

Thus, the work compares  $\text{TiO}_2$  nanorods with a rutile structure, which were used to create composite materials with different concentrations of  $\text{AgNO}_3$ . From the results of the study, we can see that as the concentration of  $\text{AgNO}_3$  increases, its photocatalytic activity also increases. As the concentration of Ag nanoparticles on the TNR surface increases to 1 mmol, the photocatalytic activity increases and then decreases at 2 mmol, indicating the presence of an optimal concentration. The photocurrent density generated by a TNR film with a concentration of Ag nanoparticles of 1 mmol is 10 and 1.4 times higher than 0.5 mmol and 2 mmol, respectively. In the presence of a TNR film with a concentration of Ag nanoparticles of 1 mmol, the degradation of the dye reached 71%, which is 1.7 times higher than without Ag nanoparticles. The resistance of TNR/Ag films at a concentration of 1 mmol is 2.5 times less than that of a film with a concentration of 0.5 mmol.

#### REFERENCES

- 1 Ge M., Cao C., Huang J., et al. A review of one-dimensional  $\text{TiO}_2$  nanostructured materials for environmental and energy applications. *J. Mater. Chem. A*, 2016, Vol. 4., pp. 6772-6801. doi: 10.1039/C5TA09323F
- 2 Haider A.J., Jameel Z.N., Al-Hussaini I.M. Review on: titanium dioxide applications, *Energy Procedia*, 2019, Vol. 157, pp. 17-29. doi: 10.1016/j.egypro.2018.11.159
- 3 Allahverdiyev A.M., Abamor E.S., Bagirova M., et al. Antimicrobial effects of  $\text{TiO}_2$  and  $\text{Ag}_2\text{O}$  nanoparticles against drug-resistant bacteria and leishmania parasites. *Future Microbiology*, 2011, Vol.6, pp. 933-940. doi:10.2217/fmb.11.78

- 4 Huang Z., Maness P.-C., Blake D. M. et al. Bactericidal mode of titanium dioxide photocatalysis. *Journal of Photochemistry and Photobiology A: Chemistry*, 2000, Vol.130, pp. 163–170. doi: [10.1016/s1010-6030\(99\)00205-1](https://doi.org/10.1016/s1010-6030(99)00205-1)
- 5 Serikov T.M., Ibrayev N. Kh., Savilov S.V., et al. T. M. Influence of the hydrothermal synthesis conditions on the photocatalytic activity of titanium dioxide nanorods. *Russian journal of applied chemistry*, 2021, Vol. 94, pp. 438–445. doi: [10.1134/S1070427221040030](https://doi.org/10.1134/S1070427221040030)
- 6 Serikov T.M., Ibrayev N. Kh., Isaykina O.Ya., et al. Nanocrystalline TiO<sub>2</sub> films: synthesis, low-temperature luminescent and photovoltaic properties. *Journal of Inorganic Chemistry*, 2021, Vol. 66, pp. 107–114. doi: [10.1134/S0036023621010071](https://doi.org/10.1134/S0036023621010071)
- 7 Fei Y.C., Ye X.F., Kang J.Y. Enhanced photocatalytic performance of TiO<sub>2</sub> nanowires by substituting noble metal particles with reduced graphene oxide. *Current applied physics*, 2022, Vol.44, pp.33–39. doi: [10.1016/j.cap.2022.09.008](https://doi.org/10.1016/j.cap.2022.09.008)
- 8 Mukametkalia T.M., Ilyassov B.R., Aimukhanov A.K., et al. Effect of the TiO<sub>2</sub> electron transport layer thickness on charge transfer processes in perovskite solar cells. *Physica B: Condensed Matter*, 2023, Vol. 659, pp. 414784. doi: [10.1016/j.physb.2023.414784](https://doi.org/10.1016/j.physb.2023.414784)
- 9 Serikov T.M., Baltabekov A.S., Aidarova D.D., et al. Effect of anodizing voltage on the photocatalytic activity of films formed by titanium dioxide nanotubes. *Eurasian Physical Technical Journal*, 2022, Vol.19, pp.28 – 33. doi: [10.31489/2022No4/28-33](https://doi.org/10.31489/2022No4/28-33)
- 10 Liu Y., Zhou Y., Yang L., et al. Hydrothermal synthesis of 3Durchin-like Ag/TiO<sub>2</sub>/reduced graphene oxide composites and its enhanced photocatalytic performance. *J Nanopart Res*, 2016, Vol.18, pp.283–295. doi: [10.1007/s11051-016-3596-6](https://doi.org/10.1007/s11051-016-3596-6)
- 11 Liang Y.T., Vijayan B.K., Gray K.A. et al. Minimizing graphene defects enhances titania nanocomposite-based photocatalytic reduction of CO<sub>2</sub> for improved solar fuel production. *Nano Lett*, 2011, Vol.11, pp.2865–2870. doi: [10.1021/nl2012906](https://doi.org/10.1021/nl2012906)
- 12 Cozzoli P.D., Kornowski A., Weller H. Low-temperature synthesis of soluble and processable organic-capped anatase TiO<sub>2</sub> nanorods, *Journal of the american chemical society*, 2003, Vol.47, pp.14539–14548. doi: [10.1021/ja036505h](https://doi.org/10.1021/ja036505h)
- 13 Xu J.M., Chen D.F., Wu J.F., et al. Nanowires-assembled TiO<sub>2</sub> nanorods anchored on multilayer graphene for high-performance anodes of lithium-ion batteries. *Nanomaterials*, 2022, Vol.12, pp.3697. doi: [10.3390/nano12203697](https://doi.org/10.3390/nano12203697)
- 14 Nada F. M., Saleem A.H., Shawki K.M. Hydrothermally growth of TiO<sub>2</sub> nanorods, characterization and annealing temperature effect. *Kuwait journal of science*, 2021, Vol.48, pp.3–6. doi: [10.48129/kjs.v48i3.10417](https://doi.org/10.48129/kjs.v48i3.10417)
- 15 Chakhtouna H., Benzeid H., Zari N. et al. Recent progress on Ag/TiO<sub>2</sub> photocatalysts: photocatalytic and bactericidal behaviors. *Environmental science and pollution research*, 2021, Vol.33, pp. 44638–44666. doi: [10.1007/s11356-021-14996-y](https://doi.org/10.1007/s11356-021-14996-y)
- 16 Gupta B., Melvin A.A., Matthews T., et al. TiO<sub>2</sub> modification by gold (Au) for photocatalytic hydrogen (H<sub>2</sub>) production. *Renewable & sustainable energy reviews*, 2016, Vol.58, pp. 1366–1375. doi: [10.1016/j.rser.2015.12.236](https://doi.org/10.1016/j.rser.2015.12.236)
- 17 Molinari R., Lavorato C., Argurio P. The Evolution of Photocatalytic Membrane Reactors over the Last 20 Years: A State of the rt Perspective. *Catalyst*, 2021, Vol.11, pp. 775. doi: [10.3390/catal11070775](https://doi.org/10.3390/catal11070775)
- 18 Stroyuk A.L., Kryukov A.I., Kuchmii S.Y. Semiconductor photocatalytic systems for the production of hydrogen by the action of visible light. *Theoretical and experimental chemistry*, 2009, Vol.45, No.4, pp.209–233. doi: [10.1007/s11356-009-9095-4](https://doi.org/10.1007/s11356-009-9095-4)
- 19 Karthikeyan C., Arunachalam P., Ramachandran K. Recent advances in semiconductor metal oxides with enhanced methods for solar photocatalytic applications. *Journal of alloys and compounds*, 2020, Vol.828, pp.154281. doi: [10.1016/j.jallcom.2020.154281](https://doi.org/10.1016/j.jallcom.2020.154281)
- 20 Dhinesh K.R., Thangappan R. R. Synthesis and characterization of LaFeO<sub>3</sub>/TiO<sub>2</sub> nanocomposites for visible light photocatalytic activity. *Journal of Physical and Chemistry of Solids*, 2016, Vol. 23, pp. PCS7876. doi: [10.1016/j.jpcc.2016.10.005](https://doi.org/10.1016/j.jpcc.2016.10.005)
- 21 Fu L., Zheng Y., Fu Z., et al. Synthesis of Ag decorated gra-phene-hierarchical TiO<sub>2</sub> nanocomposite with enhanced photocatalytic activity. *Funct Mater Lett*, 2015, Vol.8, pp. 1550036–1550039. doi: [10.1142/S1793604715500368](https://doi.org/10.1142/S1793604715500368)
- 22 Samir M., Geioushy R.A., El-Sherbiny S., et al. Enhancing the anti-ageing, antimicrobial activity and mechanical properties of surface-coated paper by Ag@TiO<sub>2</sub>-modified nanopigments, *Environmental science and pollution research*, 2022, Vol.29, pp. 72515–72527. doi: [10.1007/s11356-022-20935-2](https://doi.org/10.1007/s11356-022-20935-2)
- 23 Ke C.R., Guo J.S., Su Y.H., et al. The effect of silver nanopar-ticles/graphene-coupled TiO<sub>2</sub> beads photocatalyst on the photoconversion efficiency of photoelectrochemical hydrogen production. *Nanotechnology*, 2016, Vol.27, pp. 435405–435412. doi: [10.1088/0957-4484/27/43/435405](https://doi.org/10.1088/0957-4484/27/43/435405)
- 24 Paul K.K., Giri P.K. Role of Surface plasmons and hot electrons on the multi-step photocatalytic decay by defect enriched Ag@TiO<sub>2</sub> nanorods under visible light. *Journal of physical chemistry C*, 2017, Vol.36, pp.20016–20030. doi: [10.1021/acs.jpcc.7b05328](https://doi.org/10.1021/acs.jpcc.7b05328)
- 25 Serikov T.M., Kayumova A.S., Baltabekov A.S. et al. Photocatalytic activity of nanocomposites based on titania nanorods and nanotubes doped with Ag and reduced graphene oxide nanoparticles. *Nanobiotechnology Reports*, 2023, Vol. 18, pp. 207–215. doi: [10.1134/S2635167623700040](https://doi.org/10.1134/S2635167623700040)
- 26 Adachi M., Sakamoto M., Jiu J., et al. Determination of parameters of electron transport in dye-sensitized solar cells using electrochemical impedance spectroscopy. *J. Phys. Chem.B*, 2006, Vol. 110, pp. 13872. doi: [10.1021/jp061693u](https://doi.org/10.1021/jp061693u)
- 27 Wodka D., Bielańska E., Socha R.P., et al. Photocatalytic activity of titanium dioxide modified by silver nanoparticles. *ACS Applied Materials & Interfaces*, 2010, Vol. 2, pp.1945–1953. doi: [10.1021/am1002684](https://doi.org/10.1021/am1002684)

DOI 10.31489/2023No4/46-53

UDC 536.24.02+62.768+62.747

## THERMODYNAMIC ANALYSIS OF THE HEAT PUMP-ADSORPTION AIR DRYING SYSTEM USING A RECOVERY

Bezrodny M.K., Maistrenko O.O.\*

National Technical University of Ukraine "Igor Sikorsky Kyiv Polytechnic Institute", Kyiv, Ukraine,  
maistrenko1010@gmail.com

*This paper describes the development of a heat pump and adsorption system that incorporates a recuperator. A theoretical model is developed to analyze the system's operation numerically. The study includes a numerical analysis of the thermodynamic efficiency, an examination of the changes in air parameters at different points in the system, an investigation of the impact of variations in temperature and relative humidity of the surrounding air, and also an analysis of the effect of the regeneration air temperature on the system's performance. Graphical representations of the system's efficiency are generated by modifying the parameters of the outside air and the re-generation air temperature following the heat pump condenser. The study also explores the influence of the recuperator's efficiency on the overall energy efficiency of the system. The results demonstrate that this advanced system significantly reduces the specific electrical energy consumption for air drying compared to systems lacking a recuperator or a recuperator and a heat pump, regardless of the outdoor air parameters.*

**Keywords:** protection of metal equipment from corrosion, conservation of energy equipment, air drying, adsorption dryer, heat pump, heat recovery.

### 1. Introduction

The prevention of corrosion in metal structures is a pressing concern within the contemporary energy industry. The detrimental effects of corrosion contribute significantly to emergency incidents and financial expenses using energy equipment which is exploited at the high temperatures and pressures. It is crucial to address corrosion in order to mitigate the risk of equipment failure, as any component affected by corrosion has the potential to jeopardize the entire system's integrity.

In today's operating conditions, power equipment operates intermittently, experiencing extended periods of inactivity. During these downtime periods, it is crucial to protect the equipment from the adverse effects of corrosion, which poses the greatest risk. Without proper preservation measures, the equipment's lifespan is shortened, resulting in increased financial expenses for repairs and depreciation charges [1].

The presence of moisture in the air acts as the primary catalyst for the corrosion process, with higher relative humidity accelerating the deterioration of metal components in equipment [2]. However, when the relative air humidity is low (below 40 %), corrosion processes nearly come to a halt, preserving the integrity of the metal. Therefore, to effectively preserve power equipment, it is essential to maintain the relative humidity of the air in contact with the metal below 40 %. [3].

There are many ways of dehumidifying the air, which have different physics of the process. The main methods of air drying include: condensation, adsorption, absorption and membrane methods [4].

In work [5] the development and analysis of the operation of adsorption air drying systems with an electric regeneration air heater and an already improved system of heat pump adsorption air drying, where the heat pump unit uses the heat of the exhaust regeneration air in the evaporator of the heat pump to heat fresh regeneration air in the condenser.

The purpose of the work is to increase the energy efficiency of the air-drying scheme by combining a heat pump-adsorption air drying unit with a recuperator for the preliminary utilization of the heat of the exhaust regeneration air after the adsorption rotor. These actions are caused by high costs of electricity for heating the regeneration air in ordinary adsorption dryers, which increases the financial costs of withdrawing energy equipment into reserve.

## 2. Description of the operation of the scheme

The adsorption dehumidifier operates based on the characteristic of silica gel to absorb moisture from the air within a moderate temperature range ( $-40^{\circ}\text{C}$  to  $+40^{\circ}\text{C}$ ) and release the adsorbed moisture when exposed to hot regeneration air ( $+60^{\circ}\text{C}$  to  $+150^{\circ}\text{C}$ ). To ensure a continuous process of drying the working air and regenerating the adsorbent, a specially designed rotor is employed (see Figure 1). This rotor features a honeycomb structure, which maximizes the contact surface area and facilitates the airflow through the silica gel volume. The rotor is divided into two zones, with a ratio of 1 to 3. The larger zone is dedicated to the passage of the working air, where drying and heating take place, while the preheated regeneration air flows through the smaller zone [6]. In this smaller zone, moisture is evaporated from the rotor, resulting in humidification and cooling of the regeneration air. Fig. 2 depicts a heat pump-adsorption system with a recuperator for energy conservation in equipment.

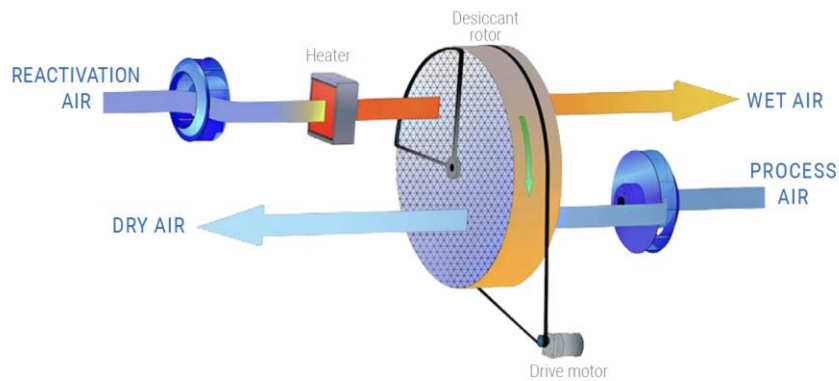


**Fig.1.** The principle of operation of the adsorption dehumidifier.

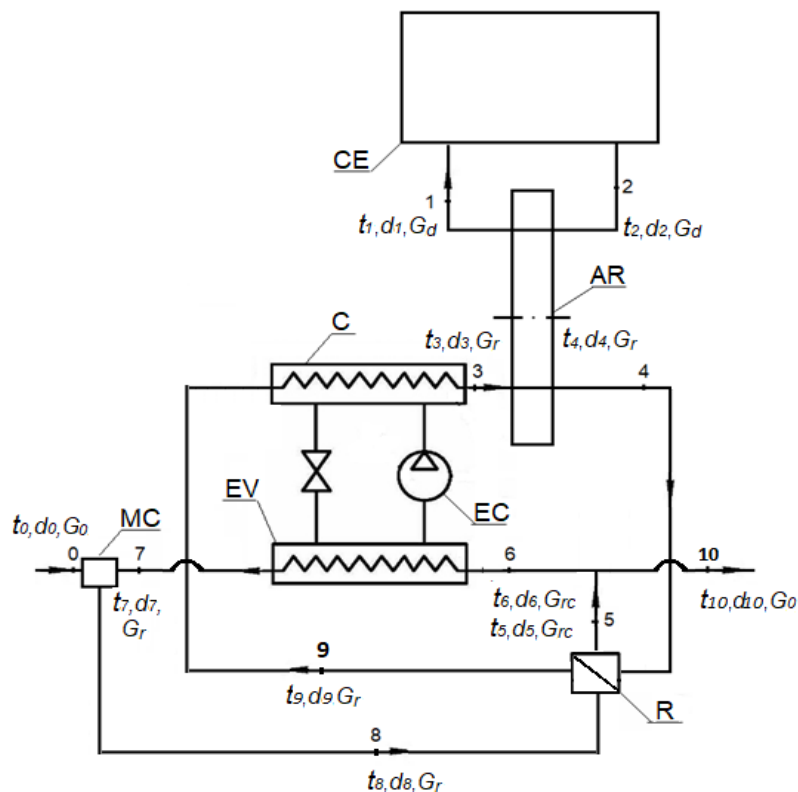


**Fig.2.** Schematic diagram of a heat pump-adsorption air drying scheme using a recuperator: C – HP condenser; EV – HP evaporator; EC – compressor; AR – adsorption rotor; MC - mixing chamber; R – recuperator; CE is a canning facility.

This system incorporates a silica gel adsorption rotor to achieve thorough air drying for preservation purposes. The system also utilizes a heat pump and recuperator to efficiently heat and regenerate the air, with a portion of the regeneration air being recirculated. This recirculation process results in substantial energy savings compared to electric heating methods. The operational principle of the system can be described as follows: The upper section of the diagram illustrates the canning object (CE), from which moist air (working air) is directed into the adsorption rotor. Inside the rotor, the air is heated, dried, and then returns to the canning object with a temperature of  $t_1$  and moisture content of  $d_1$ .

In the lower part of the diagram, the scheme illustrates the preparation, supply, and removal of regeneration air from the rotor. Simultaneously, external air (0) with a temperature of  $t_0$ , moisture content of  $d_0$ , and mass flow rate of  $G_0$  is drawn from the surrounding environment and directed into the mixing chamber. In the mixing chamber, it combines with recirculated regeneration air (7), which emerges from the heat pump evaporator with a temperature of  $t_7$ , moisture content of  $d_7$ , and a mass flow rate of  $G_r$ .

Once mixed, the air mixture (8) passes through the recuperator, where it is heated to a temperature of  $t_9$  (9), before entering the heat pump condenser. Inside the condenser, the air mixture is further heated to a temperature of  $t_3$  (3) and then directed into the rotor for regeneration, allowing the removal of adsorbed moisture. While passing through the rotor, the regeneration air undergoes cooling and humidification.

After leaving the rotor, the regenerated air (4) with a temperature of  $t_4$  and moisture content of  $d_4$  goes through the recuperator, where it cools down to a temperature of  $t_5$  and moisture content of  $d_5$ . Subsequently, it splits into two streams: one is discharged into the environment (10), while the other is routed through the heat pump evaporator (6), where it undergoes cooling and partial drying. Finally, it returns to the mixing chamber, where it mixes with fresh air.

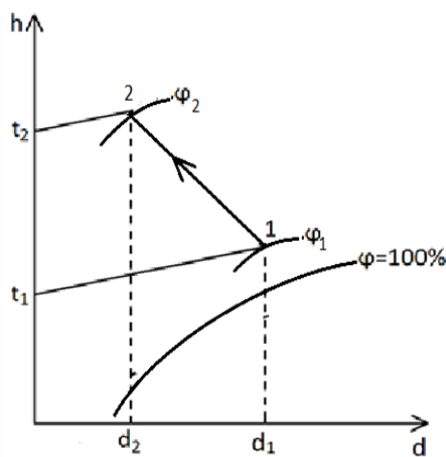


**Fig. 3.** The process of drying the working air when passing through the adsorption rotor.

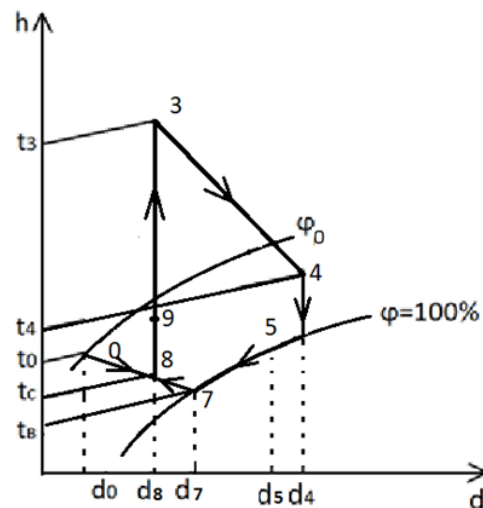


**Fig. 4.** The process of preparing and changing of regeneration air when passing through the adsorption rotor, HP and recuperator.

Figures 3 and 4 present the working processes of drying the working air and changing the state of the regeneration air in the elements of the heat pump-adsorption installation using a recuperator in the  $hd$  diagram of moist air.

### 3. Thermodynamic analysis of scheme efficiency

The efficiency analysis of the system can be conducted by examining the thermodynamic state of the adsorption rotor's regeneration scheme. This analysis relies on determining the parameters at key points within the scheme. These parameters include the temperature and humidity of the regeneration air after the evaporator, both at the entrance and exit of the mixing chamber, as well as at the exit of the adsorption rotor or the entrance of the heat pump evaporator. Additionally, the airflow of ambient air and the recirculation air entering the evaporator are also essential unknowns. The relationships governing these parameters can be derived from heat and material balance equations for individual elements and the entire system.

Considering the moisture evaporation process in the rotor as isoenthalpic, where the enthalpies  $h_3$  and  $h_4$  are equal, the overall heat balance equation for the heat pump-adsorption air drying system (with the enthalpy of the condensate after the heat pump evaporator neglected) can be written as

$$Q_0 + L_{ec} = Q_{ex}, \quad (1)$$

where  $Q_0$  is the heat flow supplied to the system with fresh air, kW;

$L_{ec}$ - heat pump compressor drive power, kW;

$Q_{ex}$  - heat flow discharged into the environment with exhaust air, kW,

or in more detail in the form

$$G_0 h_0 + \frac{Q_{ev}}{\varphi - 1} = G_0 h_4, \quad (2)$$

where  $Q_{ev}$  is the heat flow removed from the recirculation air in the evaporator, kW;

$G_0$  – consumption of fresh air, kg d.a./h;

$h_4$ - enthalpy of regeneration air after the adsorption rotor, kJ/kg d.a.;

$h_0$ - enthalpy of fresh air, kJ/kg d.a.;

$\varphi$  is the HP transformation coefficient.

The effective coefficient of heat transformation of the heat pump is defined as:

$$\varphi = \varphi_T \eta_{HP}, \quad (3)$$

where  $\eta_{HP}$  is the loss coefficient, which takes into account the real processes carried out by the working body in HP, which, according to a number of sources, can vary in the range of 0.6...0.8 (we assume  $\eta_{HP} = 0.6$ );

$\varphi_T$  is the theoretical coefficient of transformation of HP.

The coefficient of heat transformation of the ideal Carnot cycle  $\varphi_T$  taking into account thermal irreversibility in the evaporator and condenser HP is determined by the ratio

$$\varphi_T = \frac{1}{1 - \frac{T_{EV}^{HP}}{T_C^{HP}}} = \frac{1}{1 - \frac{273 + t_{EV} - \Delta t_{EV}}{273 + t_C + \Delta t_C}}, \quad (4)$$

where  $T_{EV}^{HP}$  – the absolute temperature of evaporation of the refrigerant in the HP evaporator, K;

$T_C^{HP}$  – the absolute temperature of condensation of the refrigerant in the condenser HP, K;

$t_7$ – the temperature of the exhaust air at the outlet of the HP evaporator, °C;

$t_3$ – air temperature at the outlet of the condenser HP, °C;

$\Delta t_{ev}$  – temperature difference between the flows of exhaust air and refrigerant at the outlet of the HP evaporator, °C;

$\Delta t_c$  is the temperature difference between the refrigerant and regenerative air flows at the outlet of the HP condenser, °C.

Numerical values of temperature differences in the condenser and evaporator of HP are given in the literature. According to [7],  $\Delta t_{ev} = \Delta t_c = 10^\circ\text{C}$  can be taken for the "air-air" HP type for the evaporator and condenser.

Taking into account the expression for the heat flow of the HP evaporator

$$Q_{EV} = G_{rc} (h_4 - h_7) \quad (5)$$

and material balance equations for the dry air of the mixing chamber

$$G_0 + G_{rc} = G_r, \quad (6)$$

where  $h_7$  is the enthalpy of recirculation air after the evaporator, kJ/kg d.a.,

$G_{rc}$ – consumption of air recirculation flow, kg d.a./h,

$G_r$ – consumption of regenerative air flow, kg d.a./h,

equation (2) after transformations can be written in the form

$$K \frac{h_5 - h_7}{\varphi - 1} = (1 - K)(h_5 - h_0) \quad (7)$$

where  $K$  is the coefficient of recirculation of regenerative air  $K = G_{rc} / G_r$ .

Then, from equation (7) we get the expression for the regeneration air recirculation coefficient

$$K = \frac{1}{\frac{(h_5 - h_7)}{(\varphi - 1)(h_5 - h_0)} + 1} \quad (8)$$

Other parameters of the system will be determined from the material and heat balances of individual elements of the scheme. At the same time, from the equation of the thermal balance of HP

$$Q_{ev} + L_{ec} = Q_c, \quad (9)$$

which can be represented as

$$\frac{G_{rc}(h_6 - h_7)}{\varphi - 1} = \frac{G_r(h_3 - h_9)}{\varphi}, \quad (10)$$

we get the formula for the air enthalpy at the outlet of the HP evaporator

$$h_7 = h_5 - \frac{h_3 - h_9}{K} \cdot \frac{\varphi - 1}{\varphi}. \quad (11)$$

The enthalpy of the air mixture after mixing recirculation and fresh air in the mixing chamber is determined from the equation of the heat balance of the mixing chamber

$$G_o h_0 + G_{rc} h_7 = G_r h_8, \quad (12)$$

where

$$h_8 = (1 - K)h_0 + Kh_7. \quad (13)$$

From the material balance of the adsorption rotor

$$G_d(d_2 - d_1) = G_r(d_4 - d_3), \quad (14)$$

where  $G_d$  is the flow of air that is dried and is a preservative agent, kg d.a./h, and  $d_1, d_2, d_3, d_4$  are the moisture content of the air at the corresponding points of the diagram, we will get the expression for the moisture content of the discharge air

$$d_4 = d_3 + \frac{G_d}{G_r}(d_2 - d_1). \quad (15)$$

From the equation of the material moisture balance for the mixing chamber

$$G_o d_0 + G_{rc} d_7 = G_r d_3 \quad (16)$$

we get an expression for the moisture content of the air at the outlet of the HP evaporator

$$d_7 = \frac{d_3 - (1 - K)d_0}{K}. \quad (17)$$

Knowing  $d_7$ , we can obtain the air temperature at the outlet of the HP evaporator from the interpolation equation on the saturation line ( $\varphi=100\%$ ) on the  $h$ - $d$  diagram of moist air [8]

$$t_7 = 14,752 \ln(d_7) - 18,929 \quad (18)$$

Since  $d_3 = d_8$ , we can determine

$$d_8 = Kd_7 + (1 - K)d_0. \quad (19)$$

According to (18), we determine  $t_8$ , and accordingly based on the efficiency of the recuperator  $\eta_{rec}$ , which lies within 0...1, we can determine the regeneration air temperature  $t_9$

$$t_9 = t_7 + \eta_{rec}(t_4 - t_8). \quad (20)$$

Having determined  $t_9$  and calculated the enthalpy  $h_9$ , we can determine the enthalpy of regeneration air after cooling in the recuperator  $h_5$

$$h_5 = h_4 - (h_9 - h_8). \quad (21)$$

The numerical implementation of the above system of equations for air parameters at the nodal points of the system allows to determine the energy efficiency of the use of the heat pump in the rotor regeneration system by the usual ratio of the useful effect of the circuit to the energy spent on the HP compressor drive

$$\eta = \frac{Q_c}{L_{ec}}, \quad (22)$$

where  $\eta$  - coefficient of energy efficiency of the scheme.

Defining the useful effect as the heat flux used to evaporate moisture from the adsorption rotor, according to Eq.

$$Q_{us} = G_r(d_4 - d_3)r(t), \quad (23)$$

where  $r(t)$  - the latent heat of water vaporization, and the power of the HP compressor drive according to the equation

$$L_{ec} = \frac{G_r(h_4 - h_8)}{(\varphi - 1)}, \quad (24)$$

we will get the final expression for the coefficient of energy efficiency of the scheme in the form

$$\eta = \frac{(d_4 - d_3)r(t)(\varphi_T - 1)}{K(h_5 - h_7)}. \quad (25)$$

#### 4. Computational analysis of the system

By employing the method of successive approximations and utilizing equations (3), (4), (8), (11), (13), (15), (17), (18), (20), (21), and (25), a numerical analysis of the system can be conducted. This analysis allows for the assessment of how specified variables (such as the temperature and relative humidity of the outside air, temperature, and moisture content of the regeneration air before the adsorption rotor, and the efficiency of the recuperator) impact the performance characteristics of individual elements (such as the exhaust air recirculation coefficient and the heat pump transformation coefficient), as well as the overall energy efficiency of the heat pump-adsorption air drying system with a recuperator.

The parameters and operating ranges were chosen with the same constraints as in previous publication [5]. Figure 5 illustrates the graphical relationship between the recirculation coefficient and the outside air temperature, considering the efficiency of the recuperator.

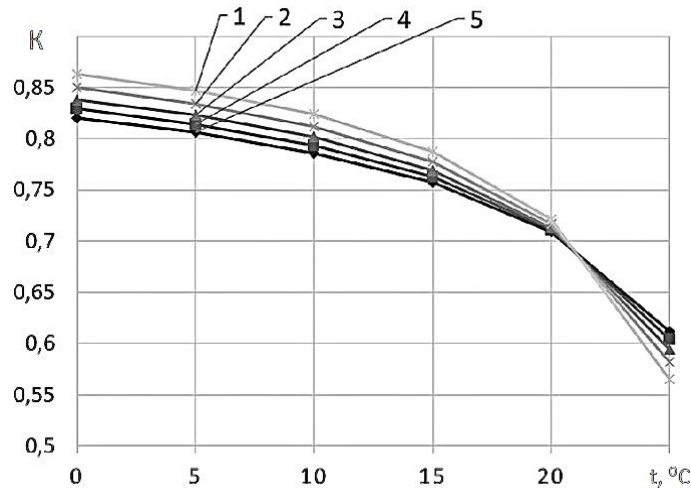


**Fig. 5.** Dependence of the recirculation coefficient on the fresh air temperature of the recuperator efficiency coefficient at a regeneration air temperature of 60 °C: 1-  $\eta_{rec} = 0.8$ ; 2-  $\eta_{rec} = 0.6$ ; 3-  $\eta_{rec} = 0.4$ ; 4-  $\eta_{rec} = 0.2$ ; 5- a system with a heat pump but without a recuperator.

The results demonstrate that at fresh air temperatures ranging from 0°C to 25°C, the recirculation coefficient in a system with a recuperator surpasses that of a system without a recuperator.

However, at higher temperatures, the recirculation coefficient declines more rapidly in a system with a recuperator compared to a system without one. Figure 6 shows graphical dependences of the overall energy efficiency coefficient of a system with a heat pump and recuperator, a system with only a heat pump, without a recuperator, and a system with an electric heater at different temperatures of regenerative air.

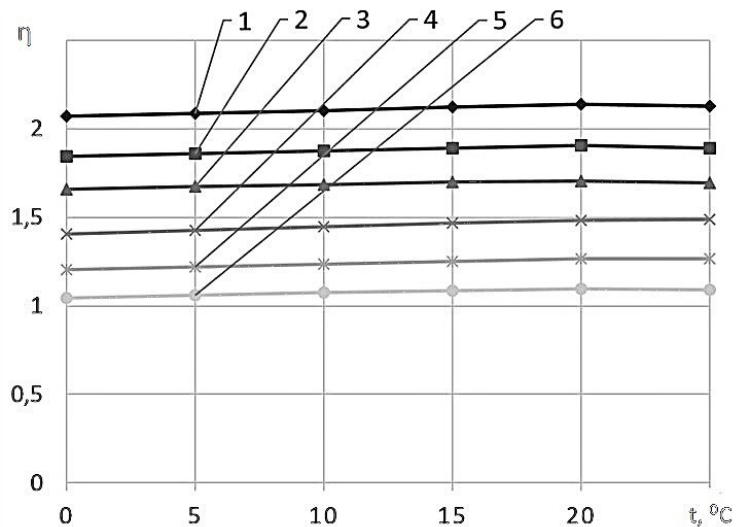


**Fig.6.** Dependence of the energy efficiency coefficient  $\eta$  on the temperature of fresh air and the temperature of regeneration air at  $\eta_{rec} = 0.6$ : 1-  $t_r = 60^\circ\text{C}$ ; 2-  $t_r = 65^\circ\text{C}$ ; 3-  $t_r = 70^\circ\text{C}$ ; and without recuperator: 4 -  $t_r = 60^\circ\text{C}$ ; 4 -  $t_r = 65^\circ\text{C}$ ; 4 -  $t_r = 70^\circ\text{C}$ .

In fig. 7 shows graphical dependences of the overall energy efficiency coefficient of a system with a heat pump and recuperator, a system with only a heat pump, without a recuperator, and a system with an electric heater.

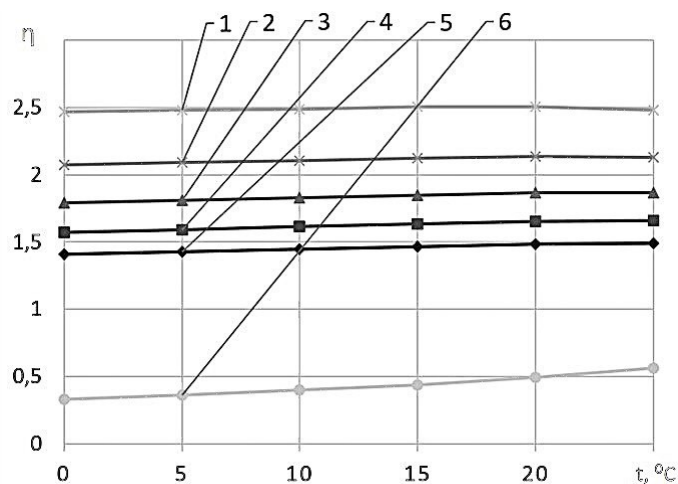


**Fig.7.** Dependence of the coefficient of energy efficiency  $\eta$  on the temperature of fresh air and the coefficient of efficiency of the recuperator at the temperature of regeneration air  $60\text{ }^{\circ}\text{C}$ : 1-  $\eta_{\text{rec}}=0.8$ ; 2-  $\eta_{\text{rec}}=0.6$ ; 3-  $\eta_{\text{rec}}=0.4$ ; 4-  $\eta_{\text{rec}}=0.2$ ; 5- a system with a heat pump but without a recuperator; 6- system without a heat pump.

It can be seen from the given graph that the energy efficiency of a system with a heat pump is 2.5-3.6 times higher than a system with an electric heater, and a system with a heat pump and recuperator can have an energy efficiency up to 6 times higher than a standard scheme with an electric heater. and 1.8 times higher energy efficiency than a scheme with a heat pump without a recuperator.

## 5. Conclusions

1. The combined use of an adsorption dehumidifier and a heat pump is a much more energy-efficient solution than the use of an adsorption dehumidifier with an electric heater, and the use of a heat pump with a recuperator in the system additionally increases the overall energy efficiency of the air drying process.

2. The overall energy efficiency of the considered air drying system largely depends on the coefficient of efficiency of the recuperator itself, and therefore the issue of selecting the type of recuperator requires special attention.

3. At the temperature of the regeneration air before the heat pump  $60\text{ }^{\circ}\text{C}$  and increasing the efficiency of the recuperator to the  $\eta_{\text{rec}}=0.8$ , the specific external energy consumption for air drying can be reduced by 1.8 times compared to the heat pump scheme without a recuperator and up to 6 times compared to the basic scheme without a heat pump and recuperator.

## REFERENCES

- 1 Maistrenko O.O., Bezrodny M.K., Shapoval B.A. Preservation of power equipment by dry air blowing method. *Energy and electrification*, 2018, No. 4, pp. 3 – 5.
- 2 Ministry of Energy and Coal Industry of Ukraine. Current industry regulatory documents on operation and repair of Power Plants and networks. [https://ua.energy/wp-content/uploads/2018/01/GID-34.01.101-2009\\_2018\\_01\\_01\\_web.pdf](https://ua.energy/wp-content/uploads/2018/01/GID-34.01.101-2009_2018_01_01_web.pdf).
- 3 Startsev V.I. Methodological instructions for conservation of thermal energy equipment. SPO ORGRES-1997, 49p. [in Russian].
- 4 Khmelnyuk M.G. Modern drying technologiesair. *Refrigeration equipment and technology*, 2014, No.3, pp.15-21.
- 5 Bezrodny M.K. Energy efficiency of the heat pump-adsorption system for the conservation of energy equipment taking into account real working processes in the adsorption rotor. *Energy: economy, technologies, ecology*, 2020, No. 4, pp. 7–19.
- 6 Ahmad A.P. *A Review of Desiccant Dehumidification Technology*. National Renewable Energy Laboratory Golden, Colorado. 1994, 9 p.
- 7 Morozyuk T.V. *Theory of refrigeration machines and heat pumps*. Odesa: Negotiant Studio. 2000, 712 p.
- 8 Oslovskiy S.A. Efficiency analysis of using a combination of air and ground heat pumps for heating and ventilation. *Eurasian Physical Technical Journal*, 2021, Vol.18, No. 1(35), pp. 57–64. doi:10.31489/2021No1/57-64

DOI 10.31489/2023No4/54-60

UDC 621.039.548

## FISSION PRODUCT RELEASE FROM HIGH AND LOW-ENRICHED URANIUM FUELS OF THE IVG.1M RESEARCH REACTOR

Medetbekov B.S., Vurim A.D., Prozorova I.V., Popov Yu.A.

Institute of Atomic Energy Branch of the National Nuclear Center of the Republic of Kazakhstan,  
Kurchatov, Abay region, Kazakhstan, medetbekov@nnc.kz

*The research involved conducting resource tests on two experimental water-cooled technological channels (WCTCs) utilizing low-enriched uranium (LEU) fuel within the IVG.1M research reactor. This testing was a crucial step in the reactor's conversion from highly enriched uranium (HEU) fuel to LEU. The research focused on two key parameters, namely the specific activity and the relative release of fission products (FPs) into the coolant, to evaluate the tightness of the fuel element cladding. A gamma-spectrometric sampling method was proposed to determine the relative release of FPs, which involved assessing the specific activity of the coolant, calculating the release rate (Release), the born rate (Born), and the R/B ratio of FPs. Comparative gamma-spectrometric measurements were conducted to analyze the content of FPs and activation products (AP) in the coolant of WCTCs utilizing both LEU and HEU during the tests. From the comprehensive list of detected radionuclides in the IVG.1M reactor coolant, well-identified reference radionuclides recommended for monitoring fuel element cladding tightness were carefully selected. The results of the study provided insights into the specific activity and relative release of FPs, demonstrating that quantitative values for the relative release of FPs from WCTCs using LEU and HEU fuel were comparable.*

**Keywords:** coolant, fuel element, fuel element cladding, fission products, relative release of fission products, gamma-spectrometry

### 1. Introduction

One of the requirements for fuel elements developed within the project's framework for converting the IVG.1M research reactor to low-enriched uranium fuel is the value of the permissible release of fission products (FP) from fuel elements into the coolant. Measuring the quantity and distribution of radioactive isotopes in reactor fuel provides a wealth of information regarding fuel behavior. This data is invaluable for studying the assessing fuel element performance during irradiation, and various aspects of nuclear fuel safeguarding. Chemical analysis of spent fuel is laborious and time-consuming, often yielding incomplete results. As a result, non-destructive techniques like passive and active neutron counting, calorimetric measurements, and gamma spectroscopy studies are gaining importance. Among these techniques, gamma scanning stands out as it is the sole non-destructive method for the quantitative measurement of gamma-emitting fission or activation products in spent fuel [1].

A suitable method for power distribution determination in the reactor core based on measurement and analysis of the short-living fission products in lightly irradiated fuel pins has been developed on the experimental facility for gamma scanning at the LR-0 experimental reactor [2-4]. The analysis of fuel rod failure character is the key to a real-time detection system for fuel rod failure in a pressurized water reactor (PWR) of great significance for the safe operation of nuclear reactors [5,6].

A mathematical treatment has been developed to predict the release of volatile fission products from operating defective nuclear fuel elements. [7-10] for type CANDU and LWR, WWER reactors.

For any nuclear reactor, the allowable release of fission products (FP) is determined with the objective of ensuring the necessary level of operational safety. This determination hinges upon the effectiveness of protective barriers against the propagation of radionuclides, as well as the reliability and accuracy of methods used to monitor FP concentrations in the reactor coolant [11-16].

One practical approach to address the challenge of monitoring FP levels in a nuclear reactor's coolant involves the implementation of Fuel Element Cladding Tightness Monitoring (CTM) systems. These systems facilitate the timely identification of cladding damage in fuel elements when FP concentrations exceed

established limits. They enable continuous monitoring of the situation's evolution and empower decision-making regarding the continued operation of compromised elements [17].

In the context of the IVG.1M reactor, FP concentrations and APs in the coolant are monitored using the CTM system. This system, established in 1990, serves as a critical component of the reactor's safety systems.

Between 2017 and 2019, the CTM system played a crucial role in verifying the cladding integrity of experimental water-cooled technological channels with low-enriched uranium fuel (WCTC-LEU) during their operational lifespan within the IVG.1M reactor [17].

This article focuses on the findings related to FP and AP concentrations in the coolant during the IVG.1M reactor startup. These measurements were comparative in nature, as samples of coolant were extracted from individual cooling paths within two WCTC-LEU systems and standard water-cooled technological channels with highly enriched uranium fuel (WCTC-HEU).

## 2. Material and methods

Within the framework of the accepted research procedure, the content of FPs and APs in the coolant samples of the IVG.1M reactor was determined. Coolant samples were taken from the WCTCs-LEU cooling paths loaded into cells No. 14 and 24 of the IVG.1M reactor core and from the WCTCs-HEU cooling paths loaded into the remaining 28 cells of the reactor core (Fig. 1).

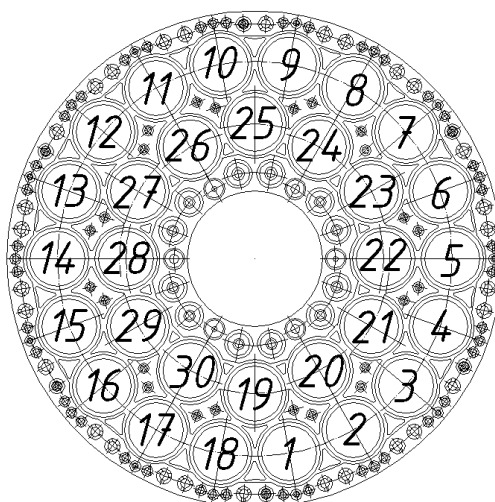


**Fig. 1.** The cartogram of the WCTC layout in the reactor core

The gamma spectra of the coolant samples were measured using an InInspector-2000 gamma spectrometer with a GC1020 coaxial detector. The spectra were processed in the GENIE-2000 environment and further analyzed using the IPF interactive peak fitting program. The values of the specific activity of AP or FP in the coolant ( $A_0$ ) at the time of sampling were calculated using Formula (1):

$$A_0 = A_i(t_1) \cdot \exp(\lambda t_1) \quad (1)$$

where:

$A(t_1)$  – represents the specific activity of AP (FP) at the time of measurement in Bq/l;

$\lambda$  – is the decay constant in  $s^{-1}$ ;

$t_1$  – represents the time elapsed from sampling to the start of measuring coolant activity in seconds.

The degree of fuel element tightness is characterized by the relative release of FP, defined as the ratio of the FP release rate into the coolant ( $R$ ) to the rate of its creation ( $B$ ). The creation rate of a B nuclide, accounting for the formation of its predecessors, is calculated as shown in Formula (2):

$$B = P_c \cdot 3,2 \cdot 10^{13} \eta \quad (2)$$

where:

$P_c$  – represents WCTC power in kW;  
 $\eta$  – stands for the relative yield of this nuclide and its predecessors per fission of  $^{235}\text{U}$  in relative units;  
 $3.2 \cdot 10^{13}$  – is the number of  $^{235}\text{U}$  fissions required to release 1 kJ (for a reactor operating for a long time at a constant power level).

The release rate of R radionuclides from FAs into the coolant per unit time is determined from their measured specific activity  $A(t_1)$  using Formula (3):

$$R = \frac{A(t_1) \cdot Q_c \cdot 10^{-3}}{\rho \cdot \lambda \cdot F} \quad (3)$$

where:

$A(t_1)$  – is the specific activity of FP during measurement in Bq/l;

$Q_c$  – is the coolant flow rate through the WCTC in g/s;

$\rho$  – represents the coolant density in g/cm<sup>3</sup>, with  $\rho = 1$  g/cm<sup>3</sup>;

$\lambda$  – is the decay constant of the measured nuclide in s<sup>-1</sup>;

$F$  – is a correction factor for decay from sampling to measurement ( $F = \exp(\lambda \cdot t_1)$  in relative units).

The relative yield of the  $i$ -th FP into the coolant ( $R/B$ ) for each WCTC is determined as shown in Formula (4):

$$(R/B)_i = \frac{A(t) \cdot Q_c \cdot 10^{-16}}{P_c \cdot 3,2 \cdot \eta \cdot \rho \cdot \lambda \cdot F} \quad (4)$$

The average relative yield for  $m$  FP analytes of the  $j$ -th WCTC is calculated using Formula (5):

$$R/B_{cp\ j} = \sum_{i=1}^m (R/B)_i / m \quad (5)$$

The arithmetic means of the relative yield of activation products for the 28 standard WCTCs is determined by Formula (6):

$$R/B_{cp} = \sum_{j=1}^n (R/B)_j / n \quad (6)$$

The root-mean-square deviation of the relative yield of FP for the 28 standard WCTCs is calculated using Formula (7):

$$\sigma = \sqrt{\frac{\sum_{j=1}^n ((R/B)_j - (R/B)_{cp})^2}{n-1}} \quad (7)$$

### 3. Results

The results of gamma-spectrometric studies of the coolant of experimental and standard WCTC are presented in [17]. Figure 2 shows a typical gamma spectrum for the IVG.1M reactor of the coolant sample taken from the WCTC-LEU cooling path after the reactor was brought to a constant power level of 6 MW.

After sampling and subsequent measurements, Ar-41 was identified in the gamma radiation spectra of the coolant. In contrast, the gamma radiation spectra of the WCTC-HEU coolant revealed the presence of AP elements that are part of the AMg6 alloy. This alloy is used in the construction of the shell, end grids of the fuel assemblies (FAs), and casing of standard WCTCs-HEU. It's worth noting that WCTC-LEU doesn't contain any parts made of aluminum alloys, which explains the significantly lower activity levels of isotopes Mg-27, Na-24, and Mn-56 in the WCTC-LEU coolant when compared to the WCTC-HEU coolant. Weighted average values of specific activity of AP in the coolant at startup of the reactor IVG.1M are given in Table 1.

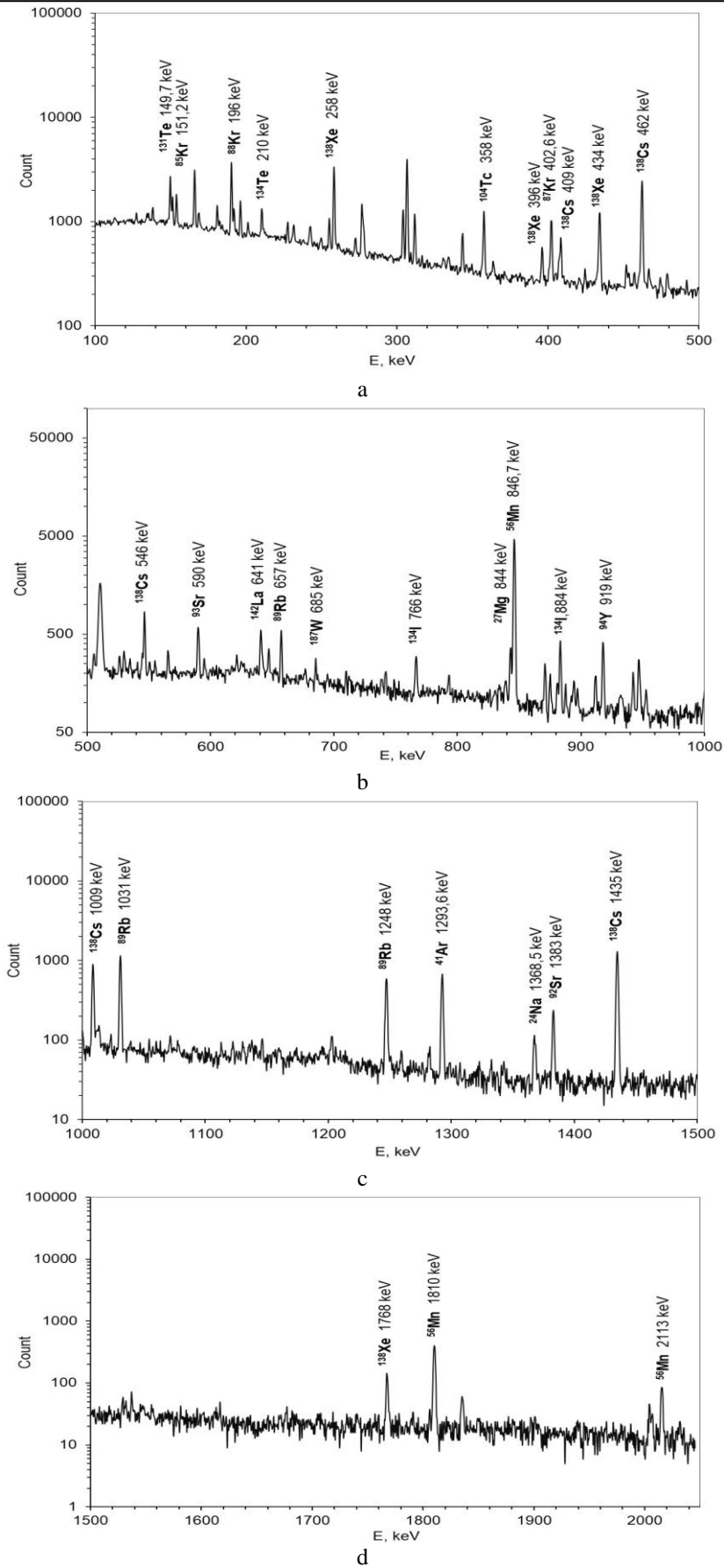


**Fig. 2.** Gamma spectrum of the IVG.1M reactor coolant:  
 a) spectral region from 100 to 500 keV; b) 500 to 1000 keV; c) 1000 to 1500 keV; d) 1500 to 2000 keV.

Table 2 summarizes the results of coolant samples analyzed during a typical reactor startup, providing information on specific activity and the relative release of FPs.

**Table 1.** Weighted average values of the AP specific activity in the coolant at the start-up of the IVG.1M reactor.

Isotope-AP	$A_0$ , Bq/l			
	WCTC-LEU #14	WCTC-HEU #18	WCTC-LEU #24	WCTC-HEU #22
Na-24	1.8E+03	5.9E+03	1.8E+03	6.9E+03
Ar-41	1.5E+04	1.4E+04	1.9E+04	2.3E+04
Mn-56	5.8E+04	9.2E+04	6.0E+04	1.0E+05
W-187	3.1E+03	5.4E+03	2.2E+03	6.9E+03
Mg-27	5.7E+04	4.1E+05	6.0E+04	5.7E+05

**Table 2.** Weighted average values of the relative release of FPs into the coolant at the start-up of the IVG.1M reactor

Isotope - FP	WCTC-LEU #14		WCTC-HEU #18		WCTC-LEU #24		WCTC-HEU #22	
	A(t), Bq/l	R/B, rel. units						
Kr-85	1.4E+03	7.8E-07	4.0E+02	2.4E-07	2.0E+03	1.1E-06	8.5E+02	4.7E-07
Kr-87	6.1E+03	7.1E-07	1.8E+03	2.1E-07	1.1E+04	1.1E-06	4.3E+03	4.5E-07
Kr-88	5.4E+03	7.7E-07	1.1E+03	1.6E-07	8.2E+03	1.0E-06	3.3E+03	4.3E-07
Rb-89	1.5E+04	9.7E-07	4.9E+03	2.8E-07	3.2E+04	1.1E-06	9.5E+03	4.4E-07
Sr-92	4.0E+03	3.3E-07	1.9E+03	1.7E-07	4.0E+03	3.0E-07	2.2E+03	1.7E-07
Y-94	4.8E+03	2.1E-07	2.3E+03	9.1E-08	7.2E+03	1.9E-07	3.1E+03	1.0E-07
Tc-104	2.3E+03	3.5E-07	1.2E+03	1.7E-07	3.6E+03	3.2E-07	1.7E+03	2.0E-07
Te-131	3.1E+03	3.1E-07	1.2E+03	1.1E-07	3.2E+03	2.1E-07	1.8E+03	1.4E-07
I-133	8.3E+02	3.8E-07	5.1E+02	2.6E-07	1.4E+03	4.1E-07	8.4E+02	5.6E-08
I-134	6.6E+03	2.5E-07	1.6E+03	6.7E-08	4.0E+03	1.3E-07	3.1E+03	1.0E-07
Te-134	4.6E+03	1.6E-07	1.1E+03	3.7E-08	4.4E+03	1.2E-07	4.3E+02	3.8E-08
Cs-138	3.0E+04	1.1E-06	8.2E+03	3.0E-07	4.8E+04	1.3E-06	1.8E+04	5.5E-07
Xe-138	1.2E+04	6.4E-07	3.9E+03	1.7E-07	3.4E+04	9.2E-07	1.0E+04	3.3E-07
La-142	5.2E+03	2.9E-07	1.8E+03	1.1E-07	5.4E+03	2.6E-07	3.4E+03	1.7E-07
$R/B$		5.2E-07		1.7E-07		6.0E-07		2.6E-07

The outcomes of assessing the average relative release of FP for all 28 WCTC-HEU are graphically represented in Fig.3.

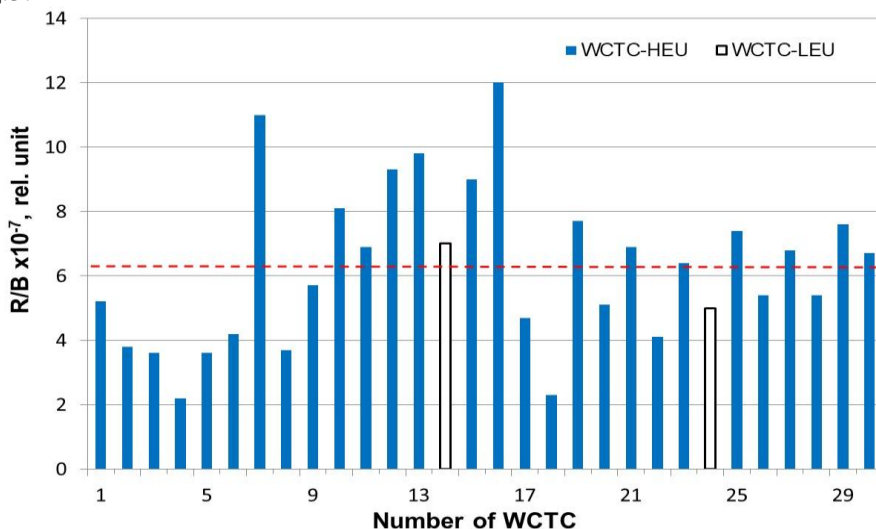


**Fig.3.** Vales of FP release from WCTC-HEU and WCTC-LEU

The same figure shows the results of R/B determination for two experimental WCTC-LEU averaged for three experiments completing the IVG.1M reactor core operation with 90% enriched fuel. The dashed line in the figure denotes the average relative FP release observed across these 28 WCTCs-HEU. Additionally, the figure depicts the relative release results for two WCTCs-LEU. For the 28 WCTCs-HEU, the average value of the relative release of FP into the coolant, as shown in Figure 3, amounted to  $6.3 \cdot 10^{-7}$ , with a corresponding standard deviation of  $2.5 \cdot 10^{-7}$ .

#### 4. Discussion

The obtained results highlight the difference between the relative release of FP for the two experimental WCTCs-LEU and the average relative FP release of standard WCTCs-HEU is within one standard deviation. This observation leads to the conclusion that these parameters closely align, indicating that the quality of fuel element cladding in WCTCs-LEU is comparable to that in WCTCs-HEU. Essentially, WCTCs-LEU exhibit cladding tightness that is on par with the quality observed in fuel elements using high-enriched uranium.

During the analysis of the coolant spectra, the activity of fourteen FPs was determined, encompassing various groups of chemical elements, including halogens, noble gases, alkali metals, metals, and non-metals. Notably, specific radionuclide analytes were carefully chosen for exclusive content measurement in the coolant. This selection enabled the comprehensive monitoring of fuel element cladding tightness concerning the parameters of FP release into the coolant.

The criteria for selecting FP-analytes were based on the presence of prominent FP gamma lines in the spectrum and the reliability of FP identification ensuring the absence of other competing lines near the gamma line of interest. Equally significant was the capability of reliably identifying these FP analytes in the spectra of coolant obtained from WCTCs with varying relative FP releases.

The analysis of measurement results emphasizes that the technique of experimental determination of FP content in samples provides reliable control of fuel element cladding tightness. This technique allows to effectively reduce the workload in the fuel element cladding tightness monitoring system (CTM) without reducing the quality of this control.

#### 5. Conclusion

In conclusion, based on the analysis of the results of measuring the release of fission products and activation products into the coolant of the IVG.1M reactor during life tests of the WCTCs with LEU fuel, the following conclusions can be drawn:

- the release of fission products from the WCTCs loaded with LEU is comparable to the release from the WCTCs loaded with HEU. This indicates that the quality of the fuel element cladding with LEU fuel is acceptable and is not different from the quality of fuel element cladding with HEU fuel in terms of fuel tightness.
- the coolant of WCTCs-LEU contains significantly lower levels of Mg-27, Na-24, and Mn-56 isotopes compared to the coolant of WCTCs-HEU. This reduction is due to the phased-out use of parts and assemblies made of aluminum alloy AMg-6 in the structure of the WCTCs-LEU.
- the tightness of the fuel element cladding in the IVG.1M reactor can be effectively monitored by conducting exceptional measurements of analyte radionuclide content in the coolant. This method is characterized by intense FP gamma lines and the absence of competing lines of other radionuclides nearby, which enhances control efficiency and reduces operational intensity.

#### Acknowledgments

This research is funded by the Committee of Science of the Ministry of Science and Higher Education of the Republic of Kazakhstan [grant No. BR21882185]

## REFERENCES

- 1 Krištof E., Pregl G. Gamma spectrometric assessment of nuclear fuel. *Nucl. Instrum. and Methods in Phys. Res. Section A: Accelerators, Spectrometers, Detectors and Associated Equip.*, 1990, Vol. 297, Is.3, pp. 507 – 513. doi:10.1016/0168-9002(90)91335-9
- 2 Švadlenková M., Heraltová L., Juříček V., Košťál M., Novák E. Gamma spectrometry of short living fission products in fuel pins. *Nucl. Instrum. and Methods in Phys. Res. Section A: Accelerators, Spectrometers, Detectors and Associated Equip.*, 2014, 739, pp. 55 – 62. doi:10.1016/j.nima.2013.12.019
- 3 Košťál M., Švadlenková M., Kolečka M., Rypar V., Milčák J. Comparison of various hours living fission products for absolute power density determination in VVER-1000 mock up in LR-0 reactor. *Appl Radiat and Isotopes*, 2015, Vol.105, pp. 264 – 272. doi:10.1016/j.apradiso.2015.08.037
- 4 Kröhnert H., Perret G., Murphy M.F., Chawla R. Gamma-ray spectrometric measurements of fission rate ratios between fresh and burnt fuel following Irradiat. in a zero-power reactor. *Nucl. Instrum. and Methods in Phys. Res. Section A: Accelerators, Spectrometers, Detectors and Associated Equip.*, 2013, Vol. 698, pp. 72 – 80. doi:10.1016/j.nima.2012.09.008
- 5 Qin G., Wang Q., Chen X., Li F., Li W., Guo X. Development of fuel rod failure character analysis code for pressurized. *Nucl. Engineering and Des.*, 2020. Vol. 361(15):110515. doi:10.1016/j.nucengdes.2020.110515
- 6 Kim K. Relation between a fuel rod failure cause and a reactor coolant radioactivity variation. *Nucl. Engineering and Des.*, 2012, Vol. 248, pp. 156 – 168. doi:10.1016/j.nucengdes.2012.03.051
- 7 El-Jaby A., Lewis B.J., Thompson W.T., Iglesias F., Ip M. A general model for predicting coolant activity behavior for fuel-failure monitoring analysis. *Journal of Nucl. Mater.*, 2010, Vol. 399, Is.1, pp 87 – 100. doi:10.1016/j.jnucmat.2010.01.006
- 8 Parrat D., Genin J.B., Musante Y., Petit C., Harrer A. Failed rod diagnosis and primary circuit contamination level determination thanks to the DIADEME code - fuel failures in water reactors: causes and mitigation. *Proceedings of a Technical Meeting*, 2002. Bratislava, Slovakia, 17–21 June, IAEA-TECDOC-1345, Part II, 265 p. [https://inis.iaea.org/collection/NCLCollectionStore/\\_Public/34/028/34028202.pdf?r=1](https://inis.iaea.org/collection/NCLCollectionStore/_Public/34/028/34028202.pdf?r=1)
- 9 Likhanskiy V., Yevdokimov I., Khoruzhy O., Sorokin A., et al. Modelling of fission product release from defective fuel under WWER operation conditions and in leakage tests during refuelling. *Proc. Int. Top. Mtg LWR Fuel Performance*, 2004. Florida, pp. 798 – 812. <https://elibrary.ru/item.asp?id=15039948&pf=1>
- 10 Likhanskiy V., Yevdokimov I., Sorokin A.A., Khramov A.G., Kanukova V.D., Apollonova O.V., Ugryumov A.V. WWER Expert system for fuel failure analysis using data on primary coolant activity. *Proceeding of the 2007 Intern. LWR Fuel Performance Meeting*, 2007. San Francisco, California, 237 p. [https://www.researchgate.net/publication/236399850WWER\\_Expert\\_System\\_for\\_Fuel\\_Failure\\_Analysis\\_Using\\_DataonPrimary\\_Coolant\\_Activity](https://www.researchgate.net/publication/236399850WWER_Expert_System_for_Fuel_Failure_Analysis_Using_DataonPrimary_Coolant_Activity)
- 11 Bakhmetyev A.M., Samoilo O.B., Usynin G.B. *Methods for assessing and ensuring the safety of Nucl. power plants*. Energoatomizdat, 1988, 136 p. [in Russian]
- 12 Berlizov A.N., Malyuk I.A., Rudyk O.F., Trishin V.V., Chizh R.V. Continuous monitoring of the state of safety barriers of water-moderated reactors using high-resolution gamma spectrometry. *Yaderna Fizika Ta Energetika*, 2009, Vol.10, No. 4, pp. 387 – 394. [http://jnpae.kinr.kiev.ua/10.4/Articles\\_PDF/jnpae-2009-10-0387-Berlizov.pdf](http://jnpae.kinr.kiev.ua/10.4/Articles_PDF/jnpae-2009-10-0387-Berlizov.pdf) [in Russian]
- 13 Kurskiy A.S., Kalygin V.V., Semidotsky I.I. Methods for monitoring the tightness of the fuel element cladding in a pressure vessel boiling water reactor VK-50. *Bulletin of Ivanovo State Power Engineering University*, 2014, Edit. 1, pp. 1 – 6. [in Russian] [https://elibrary.ru/download/elibrary\\_21378648\\_79721658.pdf](https://elibrary.ru/download/elibrary_21378648_79721658.pdf)
- 14 Agulnik M.A., Bylkin B.K., Momot G.V., Morgunova V.A. Method for non-destructive testing of fuel element tightness. *Atomic Energy*, 2010. Vol. 109, № 4, pp. 229 – 233. <https://www.j-atomicenergy.ru/index.php/ae/article/view/1520/1501>. [in Russian].
- 15 Kudrin Yu.S., Ilyienko S.A., Kiseleva I.V. Investigations in the loop installation of the MIR reactor of fission product release from the fuel elements of the WWER-1000 reactor with artificially Appl. cladding defects. *Proceedings of “SSC RIAR” JSC* (collection of scientific articles). Dimitrovgrad, 2017. pp. 14 – 26. [https://elibrary.ru/download/elibrary\\_30627971\\_15926797.pdf](https://elibrary.ru/download/elibrary_30627971_15926797.pdf)
- 16 Tarasov V.I. Modeling of the diffusion release of radioactive fission products from uranium dioxide fuel. *Atomic Energy*, 2009. Vol. 106, Edit. 6, pp. 315 – 328. <https://www.j-atomicenergy.ru/index.php/ae/article/view/1681/1661>
- 17 Medetbekov B.S., Popov Yu.A., Zhmuk D.V. Estimation of the yield of fission products from the fuel elements of the experimental LEU WCTC into the coolant of the IVG.1M reactor. *Bulletin of the NNC RK*, 2019, Is.3 (79), pp. 81 – 87. <https://www.nnc.kz/media/bulletin/files/VgIusNp2RU.pdf>

DOI 10.31489/2023No4/61-66

UDC 531.43; 620.178.179.119

## ACCELERATED TESTING OF MECHANICAL AND CHEMICAL EFFECT OF THE ENVIRONMENT ON WEAR RESISTANCE OF PARTS OF TRIBOCOUPLES UNDER COMPLEX DYNAMIC LOADING

Tsyganov V.V.<sup>1\*</sup>, Sheyko S.P.<sup>2</sup>, Shalomeev V.A.<sup>1</sup>, Vodennikova O.S.<sup>2</sup>, Kulabnieva O.A.<sup>1</sup>

<sup>1</sup> National University Zaporizhzhia Polytechnic, Zaporizhzhia, Ukraine, tsyganov705@gmail.com

<sup>2</sup> Zaporizhzhia National University, Zaporizhzhia, Ukraine, ss6309113@gmail.com

*The wear of tribocouplings parts under complex dynamic loading conditions is considered. A methodology for accelerated testing of friction pairs under multi-component dynamic loading is offered. The designs stand for modeling the processes of contact interaction, and studies of the wear resistance of tribocouplings, which operate under complex dynamic loading conditions with various lubricating and cooling media, are presented. The results of the impact assessment of mechanic and chemical transformations in the contact zone of tribological interfaces for wear resistance according to the developed method are presented. The variable effectiveness evaluation of the degradation influence products of macromolecular compounds in the composition of cutting fluid on wear resistance of metals in the contact zone of tribocouplings are analysed. The use of the presented materials allows rationally selecting friction pair materials for given operating conditions, developing new wear-resistant materials and coatings, lubricant composition and cooling mediums.*

**Keywords:** wear, complex loading, friction, stand, polymer.

### 1. Introduction

Metal deformation during friction with different loading schemes leads to structural rearrangements of the surface layer, changes in the energy relief of the surface, which is inextricably linked with the wear resistance of the tribocoupling. A promising direction for changing the loading conditions in the contact zone and controlling the wear resistance of the tribocoupling is the use of lubricating and cooling technological media of various characteristics.

From a physical point of view, the surface of metals is an atomic plane with an incomplete crystal lattice, which leads to a high sorption activity of the surface layer. This, in particular, leads to the Rebinder effect (external and internal), which consists in adsorption processes, primarily the plasticization of the metal in the contact zone with the transfer of plastic deformations to a thin surface layer and the wedging action of surfactants when they enter the cavity of surface cracks [1]. Various effects produced by the lubricating medium on rubbing surfaces can lead to both an increase in the resistance of the material to destruction and to the weakening of the material.

Multi-component loading initiates mechanic and chemical phenomena in the tribe-conjugation contact zone. Mechanic and chemical transformations differ from other chemical reactions initiated by physical methods in that they can develop at a relatively low average energy level per unit volume of matter. In alternating mechanical fields, the efficiency of the mechanic and chemical process sharply increases with increasing intensity of exposure and has the highest value under conditions of maximum concentration of mechanical energy per unit volume of a substance per unit time [2-4].

When studying processes in the zone of contact interaction of solids, one usually encounters difficulties associated with conflicting data on the wear resistance of tribocouplings and the impossibility of comparing different research methods. A number of authors to a greater extent carried out studies of the wear resistance of friction pairs using standard or modernized friction machines in the process of rolling or sliding samples. The research results obtained in this case do not allow creating a picture of the wear process that corresponds to the real process, since most of the tribocouplings operate under more complex loading conditions [5-7].

## 2. Research method and experimental technique

Most of the tribocoupling parts of various machines and mechanisms are under three-component dynamic loading during operation (shock and slip in two mutually perpendicular directions), due to functional mutual movements in different directions, the presence of vibrations or their combinations. Their wear resistance is significantly different from that which occurs under unidirectional or two-component loading [8, 9].

Given the complexity of the phenomena occurring in the contact zone of tribocouplings, methods of accelerated testing of friction pairs are of great importance, in which the necessary amount of information on wear resistance is obtained in a shorter time. The most acceptable is the test method based on the simulation of natural conditions on a special dynamic stand. In this case, the tests are carried out with a cyclically changing amplitude of displacements, contact pressure, and temperature. This makes it possible to reproduce test conditions for samples and full-scale parts close to operational ones, as well as to carry out programs of accelerated wear resistance tests, conducting them, for example, in the most severe modes, or in modes corresponding to the greatest accumulation of damage in the surface layer of rubbing parts [10 - 12].

A device for the study of friction with increased research productivity was developed. It allows testing simultaneously two contact pairs of specimens under three-component loading conditions with the possibility of providing the same contact load conditions, slipping in two mutually perpendicular directions and supplying a liquid or gas lubricating-cooling technological medium to the contact zone. The device has one holder with a fixed sample and two spring-loaded counter samples. The holder has the ability to move relative to the ball bearing in two mutually perpendicular directions under the action of the units for setting the transverse displacement, longitudinal displacement and impact energy. Variable loading conditions and longitudinal displacement parameters are set using a conical eccentric (Fig. 1).

In this case, the three-component loading of samples (impact and slip in two mutually perpendicular directions) is provided by the corresponding nodes. The energy (impulse) of impacts, as well as the amplitude and frequency of slips in the plane of impact, is controlled by means of a conical eccentric, by changing the rotational speed of the motor shaft, as well as by the springs of counter samples and the size of the gaps between the sample and counter samples.

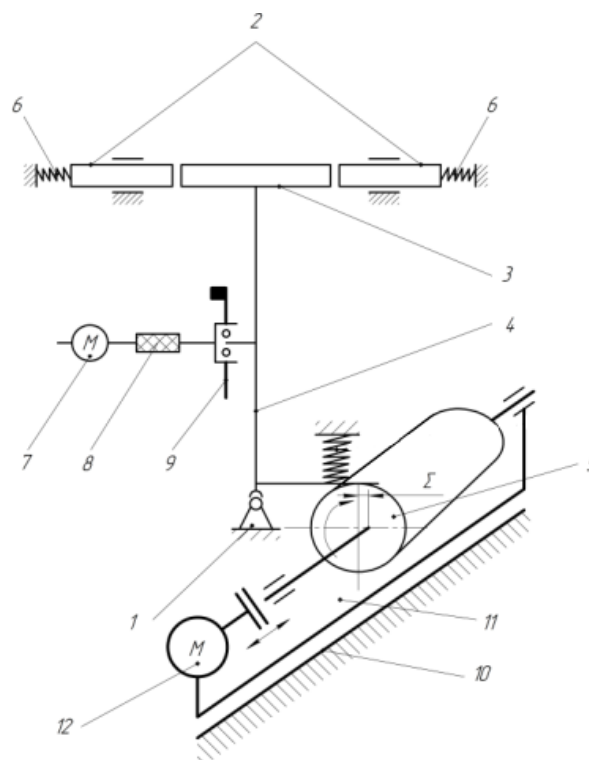


**Fig.1.** Scheme of the installation for studying the wear of a sample under complex three-component loading with two contact pairs: 1 - ball bearing; 2 — counter sample; 3 - sample; 4 - holder; 5 - conical eccentric; 6 - spring; 7 - electric motor; 8 - flexible shaft; 9 – disc with unbalanced mass; 10 - guide; 11 - carriage; 12 - electric motor

The relative motion of the sample and the counter-sample in two mutually perpendicular directions is provided by one holder, which simplifies the design of the device and increases the constancy of contact conditions. The use of two counter samples makes it possible to simultaneously study the wear of two contact pairs from the same or different materials. Preliminarily, in the neutral position of the eccentric, its conical surface is set, and in the process of wear studies, an equal gap is maintained between the sample and the counter-sample to ensure the same contact conditions. The amplitude of slips in the direction perpendicular to the plane of impacts is controlled by changing the position of the unbalanced mass relative to the axis of its rotation, the frequency (speed) of slips is controlled by changing the speed of the motor shaft.

The installation works as follows. In the neutral position of the eccentric 5, its conical surface sets an equal gap between the sample 3 and the counter samples 2 to ensure the same contact conditions. The conical eccentric 5 receives rotational motion from the electric motor 10 and carries out kinematic excitation of the holder 4 with the sample 3, which leads to the collision of the sample 3 and the counter-samples 2 and their slipping in the perpendicular direction to the collision plane due to the compression of the springs 6. The disk with an unbalanced mass 9 has an adjustable unbalanced mass to the axis of its rotation and receives a rotational movement from the electric motor 7, which leads to the movement of the holder 4 relative to the ball supports 1 and slippage of samples in the direction opposite to the collision plane.

If it is necessary to evaluate the effect of shock loading separately on the wear resistance of tribocouplings, a special setup was developed that allows testing two contact pairs of specimens simultaneously under shock loading conditions while ensuring the same contact conditions. This is achieved due to the fact that counter samples are installed with a gap relative to the sample in the device, the load creation mechanism has a conical eccentric, and the variable loading conditions are set using the loading creation mechanism and the registration and control system (Fig. 2).

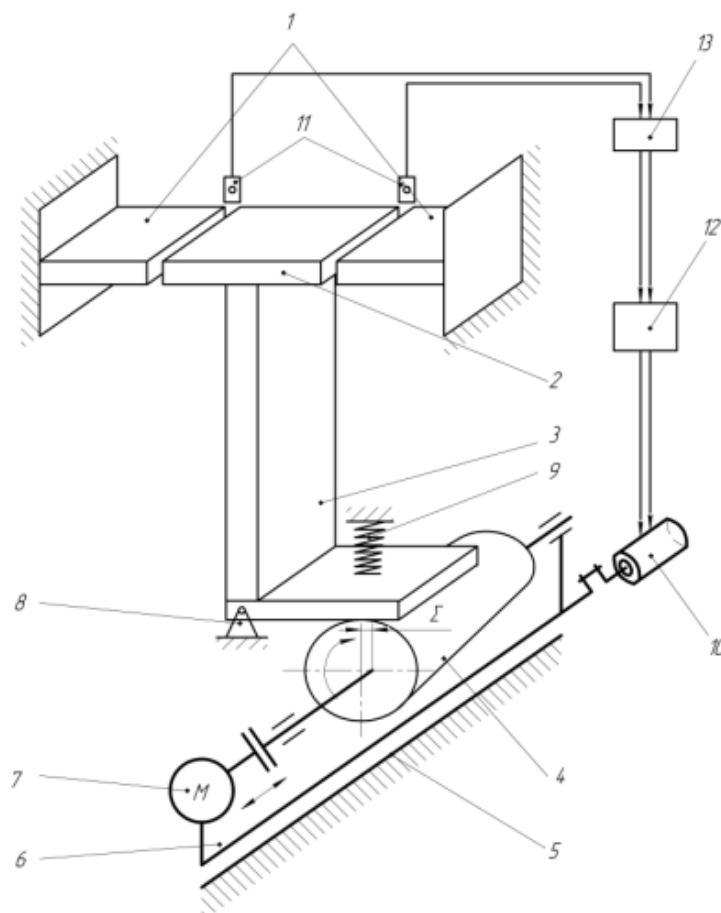


**Fig.2.** Scheme of installation for studying the wear of a sample under shock loading with two contact pairs:  
 1 — counter sample; 2 - sample; 3 - holder; 4 - conical eccentric; 5 - guide; 6 - carriage; 7 - electric motor; 8 - hinged support; 9 - spring; 10 - stepper motor; 11 - sensor; 12 - computer; 13 - analog-to-digital converter.

Impact loading is provided by the mechanism for creating loading in the process of swinging the sample holder relative to the hinged support due to the presence of gaps between the sample and the counter-sample. The energy (impulse) of impacts, the amplitude and frequency of impacts are controlled by means of a conical eccentric and by changing the rotational speed of the motor shaft, as well as by the size of the gaps between the sample and counter samples. Preliminarily, in the neutral position of the eccentric, its conical surface is set, and in the process of wear studies, an equal gap is maintained between the sample and the counter-sample to ensure the same contact conditions.

The use of two counter samples makes it possible to simultaneously study the wear of two contact pairs from the same or different materials. At the same time, in order to ensure the same contact conditions in the process of research, the possible uneven wear of the contact pairs is compensated by maintaining the same gap in the contact pairs. The same gap in the contact pairs is maintained by the registration and control system, which includes two sensors for measuring the gaps. The signal from the sensors using an analog-to-digital converter is recorded by a computer.

In the case of obtaining data on the difference in the size of the gaps, they are automatically corrected by the stepper motor of the conical eccentric according to the program from the computer. The installation works as follows. In the neutral position of the eccentric 4, its conical surface sets an equal gap between the sample 2 and the counter-samples 1 to ensure the same impact contact conditions. The conical eccentric 4 receives a rotational movement from the electric motor 7 and performs kinematic excitation of the holder 3 with the sample 2, which leads to the collision of the sample 2 and counter samples 1. In the process of research, two sensors 11 measure the gaps. The signal from the sensors using an analog-to-digital converter 13 is recorded by the computer 12. If differences in the gaps are determined, they are corrected by the stepper motor 10 of the conical eccentric.

### 3. Results and discussion

To check the degree of influence of mechanic and chemical transformations on wear resistance, according to the considered research method, a comparative assessment of the change in the intensity of wear of the samples was carried out when the polymer was introduced into the contact zone [13].

The wear intensity of 40Kh steel samples was studied under three-component loading conditions (impact and slip in two mutually perpendicular directions) with poly-methyl methacrylate (PMMA) being fed into the contact zone. The tests were carried out in the mode of boundary and semi-liquid friction with the supply of acetone and a solution of PMMA in acetone (1 g of PMMA powder per 200 ml of acetone) to the contact zone of the studied samples. At the same time, preliminary grinding of the polymer to a powder state contributed to the additional initiation of mechanical destruction and an increased content of free macro radicals in the solution.

Testing conditions: transverse slip amplitude 0.25 mm; longitudinal slips 0.15 mm; cross slip frequency 30 Hz; longitudinal slip frequency 66 Hz; normal load 20 N, test time 4 hours. The test results are shown in Figure 3. As follows from the results obtained, the introduction of PMMA into the contact zone leads to a significant increase in the wear rate of steel.

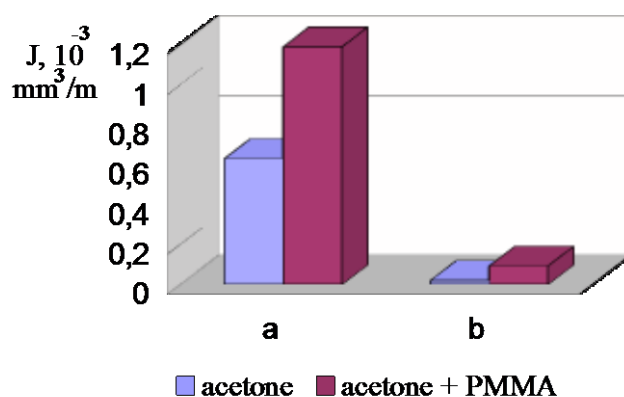


**Fig.3.** The intensity of wear of samples with the supply of acetone and acetone solution with PMMA to the contact zone: a – boundary friction; b - semi-fluid friction

Moreover, the more the solution is supplied, and, accordingly, the greater the amount of PMMA enters the contact zone, the greater the change in wear intensity is observed. The marked significant decrease in wear resistance is a positive factor for facilitating surface running-in and reducing cutting forces during processing.

Destructible polymers activate the destruction of iron particles similarly to low molecular weight surfactants [14-16]. When processing with the use of polymers, an increased destruction of metals is observed due to the formation of products of mechanical destruction of the molecular chains of polymers - free macro radicals. The lower the activation energy of polymer destruction, the higher metal destruction degree. Thus, phenol-formaldehyde resin has a three-dimensional structure, therefore, its destruction activation energy is higher than, for example, that of polyethylene, a polymer of a linear structure, and, moreover, of poly-methyl methacrylate. The activation energy of polyethylene is 60-70 kcal/mol, PMMA is 27 kcal/mol.

#### 4. Conclusions

Varying the conditions for the occurrence of mechanic and chemical reactions in the contact zone of tribocoupling in the presence of polymer degradation products opens up great prospects for controlling the wear resistance of contacting parts. Optimization of these conditions, taking into account the dynamics of loading, makes it possible to expand the technological possibilities for ensuring the durability of tribocouplings both in the process of manufacturing parts of machines and mechanisms, and during their operation.

The presented stands can be used to assess the performance of friction materials in the nodes of real structures. When testing friction units on stands in a wide range, the main operating parameters are implemented, which ensure testing by the method of full-scale simulation and the method of accelerated tests for wear resistance of a large number of real tribocouples. It becomes possible to provide the necessary set of mechanical loading factors - a three-dimensional dynamic load, to separate the load factors, and also to combine them in different combinations, to regulate and control the loading parameters, including during the test cycle (this is impossible in natural conditions).

Test benches can be recommended for obtaining and studying the functional dependencies of the friction and wear characteristics of pair materials, comparative evaluation of friction pairs, physical modeling of real tribocouples, and assessment of the effect of mechanic and chemical phenomena in the contact zone on wear resistance. The proposed methods for accelerated testing of the wear resistance of tribocouplings will significantly reduce the cost of developing promising anti-friction materials and designs of new friction devices, selecting a lubricating-cooling technological medium and significantly reducing the time for their introduction into production. The test results will create prerequisites for a reasonable choice of materials for friction pairs for given operating conditions and can be used in the development of new wear-resistant materials and coatings.

#### REFERENCES

- 1 Ryzhov E.V. *Contacting solid bodies under static and dynamic loads*. Moscow, Mashinostroenie, 1988, 303p. [in Russian]
- 2 Butyagin P.Yu. Kinetics and nature of mechanochemical reactions. *Advances in Chemistry*. 1971. Vol. XL, No.11, pp. 1935-1959. doi:10.1070/RC1971v040n11ABEH001982 [in Russian]
- 3 Belikov S., Shalomeev V., Tsivirko E. Microalloyed magnesium alloys with high complex of properties. *Mater. Sci. Technol. Conf. Exhib., 2017, MS and T*, 2017. Vol. 1, pp. 84-91. doi:10.7449/2017/mst\_2017\_84\_91
- 4 Sheyko S., Mishchenko V., Matiukhin A. Universal Equation of Metal Resistance Dependence To Deformation On Conditions Of Thermoplastic Processing. *METAL 2021 - 30th Anniversary International Conference on Metallurgy and Materials*, 2021, pp. 329–334. doi.org/10.37904/metal.2021.4121
- 5 Belodedenko S., Hrechanyi O., et al. Development of a methodology for mechanical testing of steel samples for predicting the durability of vehicle wheel rims. *Results Eng.*, 2023, Vol.18, pp. 101117. doi:10.1016/j.rineng.2023.101117
- 6 Vasilchenko T., Hrechanyi O., Shevchenko I. The Influence of Configuration Parameters of the Planetary Drive of Crank Presses on its Dynamic and Energy-Consumption Characteristics. *Sci. Innov*, 2023, Vol. 19(2), pp. 67-72. doi:10.15407/scine19.02.067

- 7 Frolov M. Variation coefficient and some distribution laws in the context of cutting tools and other technical objects reliability modeling. *Lecture Notes in Mechanical Engineering*, 2019, pp. 13-22. doi:10.1007/978-3-319-93587-4\_2
- 8 Tsyganov V.V., Sheyko S. Features of engineering the wear-resistant surface of parts with the multicomponent dynamic load. *Wear*, 2022, pp. 494 – 495, 204255. doi:10.37904/metal.2021.4121
- 9 Tsyganov V.V., Sheiko S.P., Sakipov K.E. Features of estimation wear proofness tribojoints by work of electron output. *Eurasian phys. tech. j.*, 2022, Vol.19, No.3 (41), pp.78 – 83. doi:10.31489/2022No3/78-83
- 10 Yurov V.M., Oleshko V.S. The impact of the environment on the contact potential difference of metal machine parts. *Eurasian phys. tech. j.*, 2019, Vol. 16, No.1 (31), pp. 99 – 108. doi:10.31489/2019No1/99-108.
- 11 Tsyganov V.V. Features of mechanics destruction tribounits at difficult dynamic loading. *Eurasian phys.tech. j.*, 2023, Vol.20, No. 2 (44), pp. 99 – 105. doi.org/10.31489/2023NO2/99-105
- 12 Ivschenko L.Y., Tsyganov V.V., Adjerid S. Influence des conditions de chargement dynamique sur la resistance al'usure des tribocontacts. *Journal Materiaux & Techniques*, 2013. Vol. 4, pp. 403. doi:10.1051/mattech/2013075
- 13 Kindrachuk M.V., et al. Electrodynamics of the Thermal Contact Friction Interaction in Metal-Polymer Friction Couples *Material Science*, 2018, Vol. 54, No. 1, pp. 69 – 77. <https://www.researchgate.net/publication/328675084>
- 14 Gorokhovskiy G.A. *Polymers in metal processing technology*, Kyiv, Naukova Dumka, 1975, 224 p. [in Russian]
- 15 Belodedenko, S., Hrechanyi, O., Vasilchenko T. Determination of the critical cyclic fracture toughness for the II mode in mixed fracture of structural steels. *Forces in Mechanics*, 2023, Vol. 13, pp. 100236. doi:10.1016/j.finmec.2023.100236
- 16 Belodedenko S.V., Hanush V.I., Hrechanyi O.M. Experimental Verification of the Survivability Model Under Mixed I+II Mode Fracture for Steels of Rolling Rolls. *Structural Integrity*, 2022, Vol. 25, pp. 3 – 12. doi:10.1007/978-3-030-91847-7\_1

Article received: 04.07.2023  
Article accepted: 26.11.2023

DOI 10.31489/2023No4/67-73

UDC 539.8; 53.097; 537.523.5; 621.791.927.5

## INVESTIGATION OF THE PROCESS OF ELECTRIC ARC METALIZATION OF COATINGS FROM STEEL 30KhGSA

Shynarbek A.B.<sup>1\*</sup>, Rakhadilov B.K.<sup>2</sup>, Stepanova O.A.<sup>1</sup>, Kusainov R.K.<sup>1</sup>,  
Zhassulan A.Zh.<sup>1</sup>, Daumova G.K.<sup>3</sup>

<sup>1</sup> SC "Modification of the surface of materials" Shakarim University of Semey, Semey, Kazakhstan,  
shinarbekov16@gmail.com

<sup>2</sup> Plasma Science LLP, Oskemen, Kazakhstan

<sup>3</sup> D. Serikbayev East Kazakhstan Technical University, Oskemen, Kazakhstan

*The article considers the electric arc metallization technological modes of steel 30KhGSA wires, which affect the structure formation and properties of coatings. Electric arc spraying was carried out using an SX-600 electric arc metallizer. The properties and characteristics of the resulting coatings depend on several plating parameters such as wire feed speed, voltage, and amperage. The coating structure was studied by electron microscopy and metallographic analysis. The coating has a layered structure, which consists of frozen convective metal flows, micro-welded small metal particles and oxides. The results of the study show that an increase in the wire feed speed during metallization leads to an increase in the resulting coating thickness per unit time. On the surface of steel 45, depending on the selected mode, coatings were formed from steel 30KhGSA with a thickness in the range from 50 μm to 370 μm. It has been established that when electric arc metallization coatings are sprayed with 30KhGSA wire, the microhardness of the surface layer increases by a factor of 2 relative to the microhardness of 45 steel. Based on studies investigating the impact of various factors in the electric arc spraying process on the formation of coating structures and properties, it can be deduced that utilizing electric arc metallization on steel 30KhGSA substrates allows for the production of coatings with enhanced hardness.*

**Keywords:** arc metallization, wire, coating, steel, structure, microhardness, wear resistance.

### 1. Introduction

Electric arc metallization (EAM) is a surface coating process that involves using an electric arc to melt a metal wire or powder and apply it to a substrate. The process usually includes the following main steps: surface preparation and metal plating. During the process, metal wire or powder is fed into an electric arc torch that creates a high-temperature arc that melts the material. The molten material is then sprayed onto the surface of the substrate using compressed air or an inert gas. The droplets of molten material solidify upon impact with the substrate, forming a coating. The properties of the resulting coatings depend on several plating parameters such as wire or powder feed speed, voltage, current, withdrawal distance and nozzle geometry. Arc plating has a number of advantages over other coating processes [1-2]. It is a relatively inexpensive and fast process that can be used to coat large surfaces. It can also be used to coat a wide range of materials including metals, ceramics and plastics. The resulting coatings are usually dense, uniform and have good adhesion to the substrate. They also have good resistance to wear, corrosion and high temperatures [3-5]. Coatings can be applied to improve the surface properties of a material for a variety of applications, including aerospace, automotive, and industrial applications [6-8].

One of the applications of EAM is the repair of crankshafts after wear exceeding tolerance values, which are considered to be one of the most loaded and critical parts of internal combustion engines and rotation mechanisms. Their reliability and durability play a decisive role in ensuring the safe and efficient operation of vehicles and machines. Research into the influence of EAM modes is an urgent task, and the results of the study will optimize the modes of electric arc metallization when restoring the surfaces of crankshafts made of steel 45. This can lead to an increase in the efficiency and durability of restored crankshafts, as well as improve their mechanical properties. These results have important practical applications in the automotive and industrial sectors, where crankshafts play a critical role in the operation of various mechanisms and equipment. Many researchers have studied the effect of a wide range of deposition parameters on the performance of arc-sprayed metal coatings, for example, [9] reported the effect of deposition parameters on the performance of arc-sprayed zinc coatings. The study showed that the characteristics of the resulting surface layer, such as

microstructure, porosity and hardness, correlate well with the input parameters of the deposition. The authors of [10] optimized the process parameters such as current, voltage, spray distance and gas pressure in two-wire arc spraying of aluminum coating to obtain the desired microstructure, physical and mechanical properties.

As is known from works [11], during electric arc metallization during sputtering, particles from the sprayed material are subject to changes in the environment and due to the thermal effect on its morphological structure. These changes accordingly affect the mechanical properties of the resulting coating. The structural criteria responsible for the mechanical and tribological characteristics of coatings obtained by electric arc metallization from 30KhGSA steel have not been fully studied.

In this regard, this article proposes to carry out comprehensive experimental work aimed at understanding the influence of spraying parameters on the structure and properties of coatings based on grade 45 steel.

The purpose of this work is to study the influence of operating parameters, such as voltage, current and wire feed speed of electric arc metallization on the mechanical properties of the resulting coating of 30KhGSA steel on a substrate of grade 45 steel.

## 2. Research method

The formation of coatings was carried out on a supersonic electric arc metallizer SX-600 (Fig.1.). The complex consists of a power source, a supersonic arc atomizer, a control system and a compressed air system.

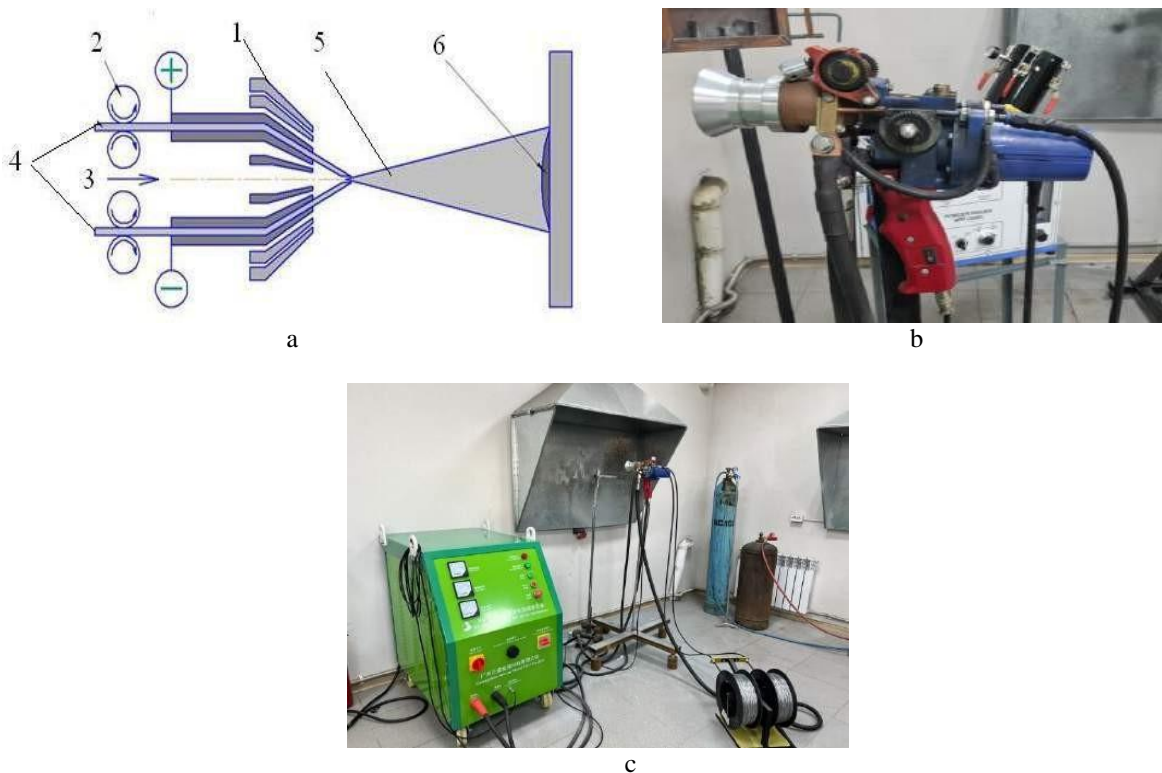


**Fig.1.** a) Process diagram SX-600: (1 – metallizer body; 2 – wire feeder; 3 – air supply channel; 4 – electrode wires; 5 – electric arc with sprayed wire particles; 6 – sprayed coating; b) appearance of the pistol; c) appearance of the complex for supersonic electric arc metallization.

The process of electric arc plating involves melting the wire with an electric arc and spraying it onto the surface of the steel with compressed air. The molten wire solidifies on the surface of the substrate, creating a coating characterized by high hardness. Coating thickness can be controlled by adjusting the wire feed speed and the distance between the wire and the surface of the sprayed sample. The properties of the resulting coatings depend on several plating parameters, such as wire feed speed, voltage, current, and withdrawal distance. The coatings were obtained with the selected parameters, which are shown in Table 1. The metallization modes in the experiments have been changed within the limits that made it possible to obtain a coating without cracks and delaminations. Steel grade 30KhGSA was used as the welding wire. The samples

were cut in the form of a disk segment of one quarter from a disk 65 mm in diameter and 10 mm thick from a bar of steel grade 45 (GOST 1050- 2013). Before the EAM, samples were prepared by mechanical (grinding) and sandblasting (quartz sand). The roughness of steel 45 after sandblasting was determined using a Model 130 profilometer.

**Table 1.** Modes of coating 30KhGSA by electric arc metallization.

Sample name	Voltage, V	Current, A	Wire feed Speed in percentage scale of the SX-600 metallizer	Wire feed speed, cm/s	Compressed air pressure, bar	Spraying distance, mm	Application time, s
No.1	31	120	25%	1	9	350	10
No.2	37	120	25%	1			
No.3	43	125	25%	1			
No.4	43	150	50%	3.4			
No.5	45	300	100%	12.8			

The microstructure of the coatings was studied using a JSM-6390LV scanning electron microscope and an ALTAMI-MET-5C metallographic microscope. The microhardness of the formed coatings was determined on a Vickers microhardness tester HLV-1DT, with a load on the indenter  $P=2H$  and a holding time at this load of 10 s. An Anton Paar TRB3 tribometer was used to measure the tribological properties of the coatings. In this study, the sample was placed in the holder in such a way that the surface of the coating was perpendicular to the plane of the rod trajectory. A ball 3 mm in diameter, made of 100Cr6 steel (similar to ShKh15), was attached to the end of the rod. By adjusting the displacement sensor, the radius of curvature of the wear surface of the sample was selected. A friction force compensation sensor was also used, which made it possible to determine the value of the friction coefficient at a given point in time. The tests were carried out in the open air at a load of 6 N and a speed of 2 cm/s. The radius of curvature of the wear surface ranged from 1.5 mm, and the length of the friction path was 60 m.

Thus, the selection of optimal parameters for arc plating is crucial to achieve the desired properties of the coating, and research is needed to determine other mechanical and tribological characteristics of coatings.

### 3. Results and discussion

Fig. 2 shows SEM images of cross-sections of coatings obtained by arc metallization. The EAM coating has a dense lamellar structure (Fig.2 d, e) with low porosity. The formation of the lamellar structure of the coatings is associated with a high compressed air pressure of 9 bar (0.9 MPa). In a jet of compressed air, droplets of a metal melt hit the sprayed surface with greater force, are strongly flattened and form lamellae. And also, with an increase in the wire feed speed, the value of the current strength increases, which leads to the release of more thermal energy in the electric arc for melting the wire and, accordingly, contributes to the formation of dense coatings with low porosity [12,13]. The welding wire feed speed of the deposition directly affects the thickness of the resulting coating with the same duration of metallization. However, this dependence is non-linear, which can also be explained by the fact that with an increase in the wire feed speed, the amperage in the electric arc increases accordingly, which led to the coating compaction. This statement can be confirmed by the fact that a study on a scanning electron microscope showed that at high values of amperage, porosity decreases, leading to a compaction of the resulting layer.

The surface layer differs in structure from the substrate, however, there is no clearly defined interface between the coating and the substrate, which indicates the high adhesive strength of the EAM coatings. The adhesion strength of the coating to the base depends on the distance of spraying and the speed of particles before impact, which is controlled by compressed air pressure [14].

An increase in the speed of metal particles during EAM contributes to their deeper penetration into microroughnesses on the surface, the destruction of the oxide film, and enhances adhesive and chemical bonds. The main condition necessary for the strength adhesion of the coating to the base is surface activity, which largely depends on the nature of the surface roughness and the method of its preparation. To increase the adhesion strength, the surface of grade 45 steel was sandblasted with corundum. The surface roughness of steel 45 was 5–6  $\mu\text{m}$ .

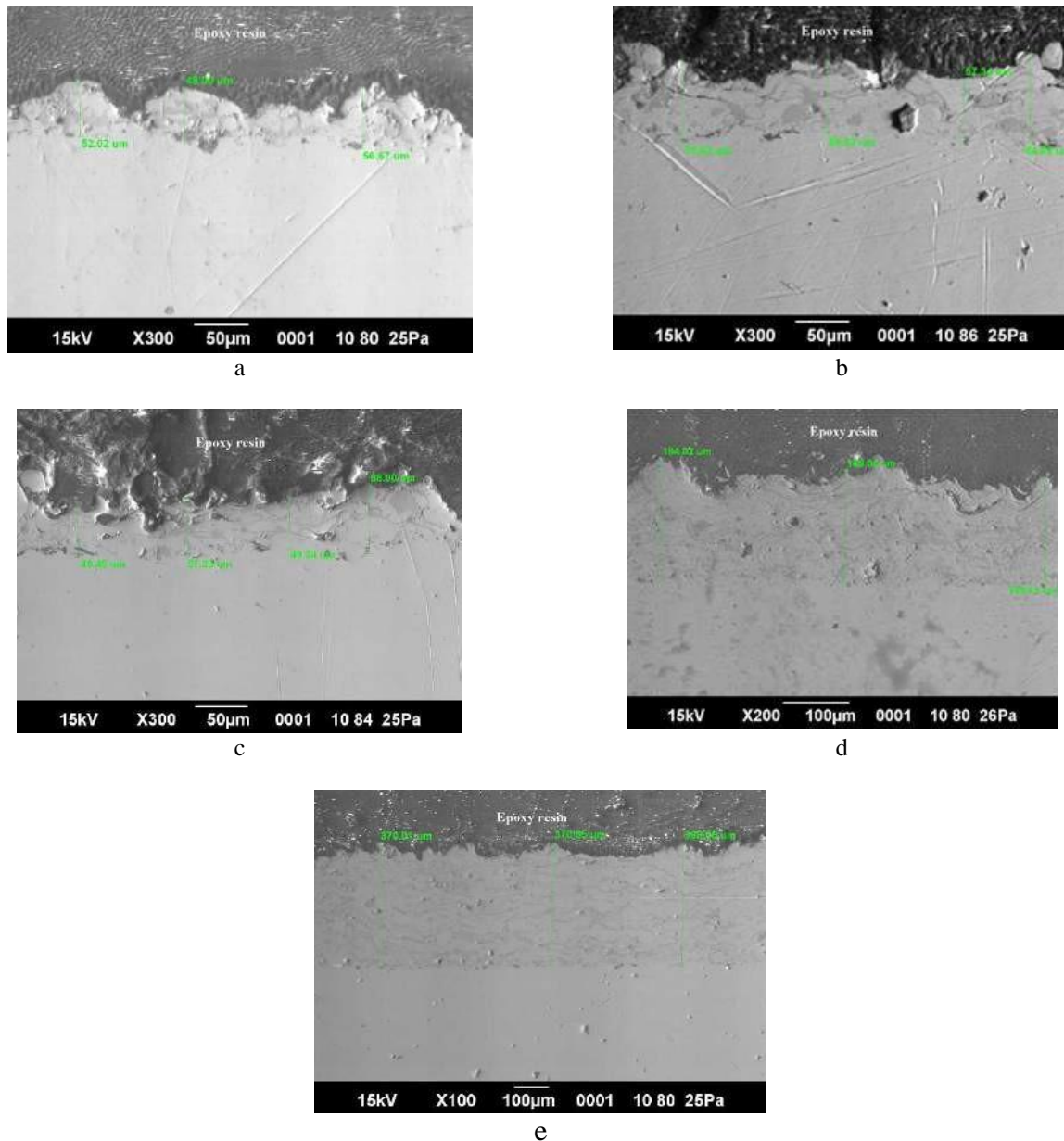


**Fig.2.** SEM images of the cross section of 30KhGSA coatings on steel 45 obtained under different spraying modes: a) No.1; b) No.2; c) No.3; d) No.4; e) No.5

Fig. 3 shows the structure of the coating obtained by electric arc metallization (sample No. 5, table 1). The shape of the flattened metal particles allows us to conclude that at the moment of impact they were in a plastic state, in which they are easily deformed. In [15], the mechanism of coating formation during electric arc metallization was shown and it was found that large metal particles reach the surface mainly in the liquid state, while smaller ones in the plastic and even solid state. Liquid metal wets the surface and fills in irregularities, while colder (semi-liquid) metal particles are deformed upon impact and mixed with hotter ones, forming a single coating layer. The result of a metallographic study of the structure of the coatings shows that the coating consists of a mixture of phases of different densities. In the applied surface layer, frozen convective metal flows, microwelded small metal drops and oxides are observed in the liquid metal (Fig. 3). At high pressures of compressed air up to 0.9 MPa, the size of liquid metal droplets may decrease, and during crystallization, they are partially microwelded.

Table 2 shows the characteristics of 30KhGSA coatings on steel 45 obtained by EAM. After spraying, the roughness of the coatings was 9–11  $\mu\text{m}$ . To measure the hardness of the coatings by the Vickers method, the surface was polished to a value of  $\leq 0.23 \mu\text{m}$ . The study of coatings from steel grade 30KhGSA on a steel substrate 45 showed that an increase in the wire feed speed leads to an increase in the thickness of the resulting

coating with the same duration of the deposition process of 10 s (Fig. 2 d, e), while varying the voltage value does not lead to significant changes in thickness obtained coatings (Fig. 2 a-c). Depending on the deposition parameter, the thickness of 30KhGSA coatings can reach a maximum of 370  $\mu\text{m}$  in 10 seconds of deposition.

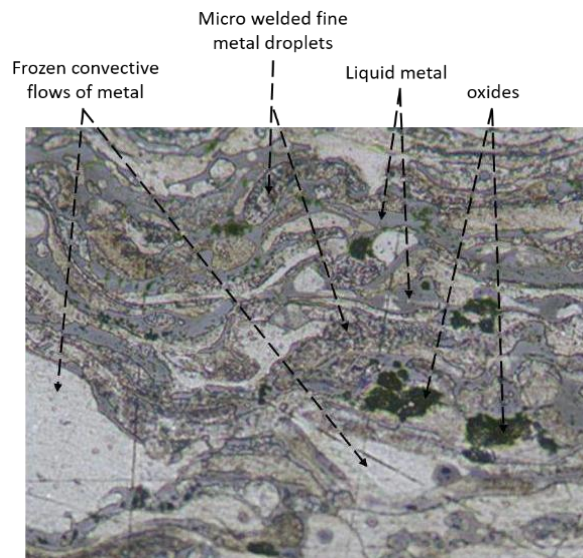


**Fig.3.** The structure of the coating of steel 30 KhGSA, obtained by the method of electric arc metallization

The hardness of coatings obtained by arc plating depends on several factors, including the material used for coating, the plating process and application conditions. The hardness of the coating 30KhGSA is much higher compared to the material of steel grade 45 and has a value of 380-420 HV0.2. The increase in the hardness of the EAM coating is explained by the fact that at the moment of impact on the substrate, the metal particles, simultaneously with deformation, undergo a sharp cooling by a cold jet of compressed air, which causes their instantaneous hardening.

The results of testing the wear resistance of 30KhGSA coatings according to the standard “ball-disk” test scheme showed that despite a significant increase in hardness, its wear resistance decreases compared to steel45. For a sample of steel 45, the average value of the friction coefficient is 0.45 (Table 2) at a distance of 60 m (Fig. 4). After coating, the average value of the friction coefficient varied from 0.48 to 0.63 depending on the EAM coating parameter. Table 1 shows that the coefficient of friction for coatings No. 3, obtained at a voltage of 43 V and a current of 125A, corresponds to the value of the original sample, which is equal to  $\mu = 0.454$ . A factor of high tribological properties of the coating is its higher plasticity index [16]. However, with an increase in the amperage at EAM, a denser coating is formed and the heterogeneity of the coating decreases. Due to the difference in the wear mechanism of the coatings under consideration, a more detailed tribological study is required.

**Table 2** - Thickness and properties of 30KhGSA coatings on steel 45 obtained by EAM

Sample name	Wire feed speed, cm/s	Coating thickness, $\mu\text{m}$	Coating hardness, HV0,2	The average value of the coefficient of dry friction (counterbody steel ShKh15)
No.1	1	52.2±3.2	404.50±25.37	0.630
No.2	1	72.3±2.7	388.16±31.58	0.571
No.3	1	56±2.5	417.27±24.983	0.482
No.4	3.4	170.7±4.7	401.83±26.91	0.555
No.5	12.8	369.7± 7.3	400.88±34.86	0.594
Steel 45 uncoated	-	-	190.00±19.25	0.454

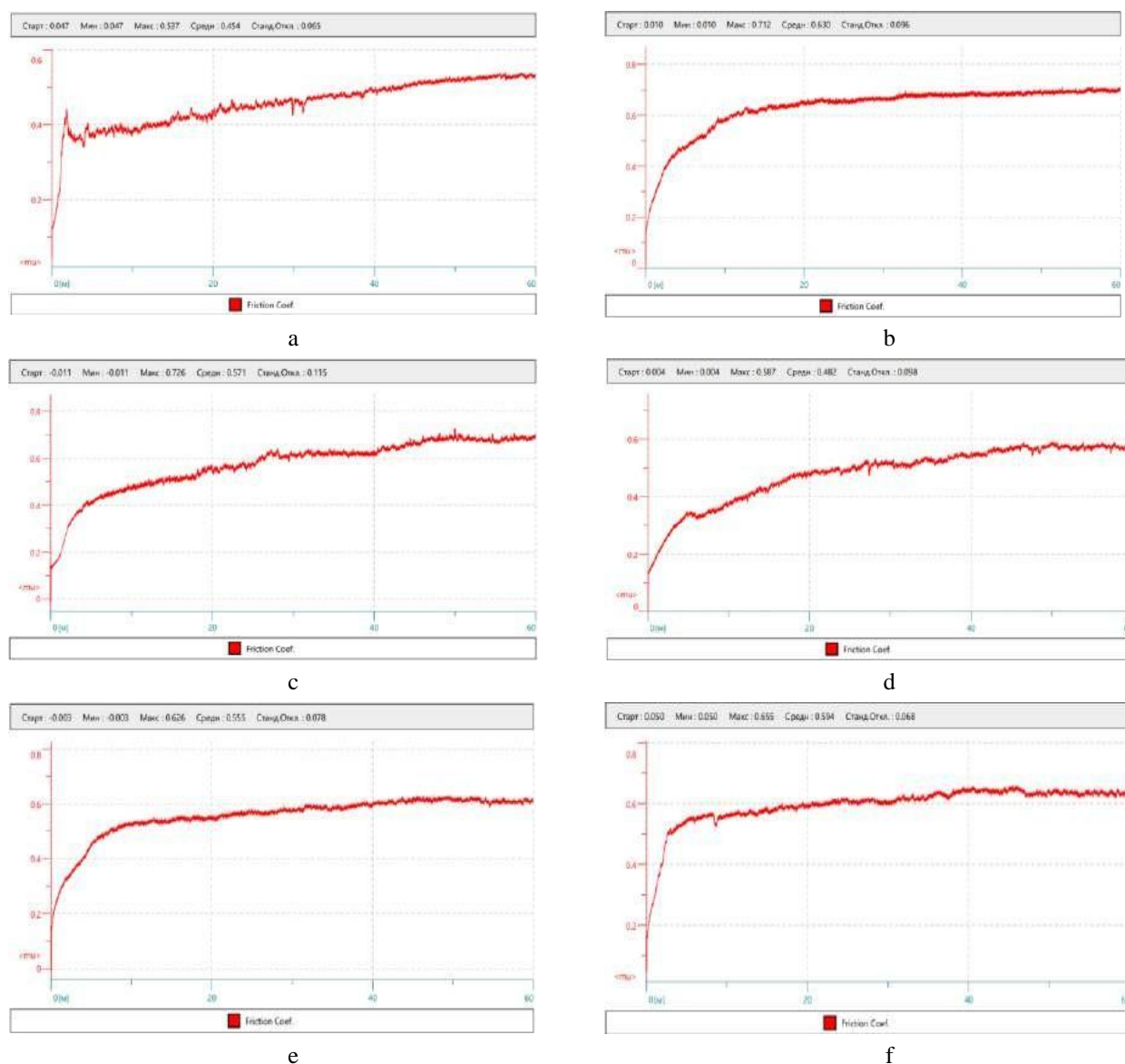


**Fig.4.** Results of tribological tests of 30KhGSA coatings: a) steel 45; b) No.1; c) No.2; d) No.3; e) No.4; f) No.5.

#### 4. Conclusion

The work investigated the influence of the operating parameters of electric arc metallization on the structure, hardness and coefficient of friction of the resulting coating made of 30KhGSA steel on a substrate of grade 45 steel. The relationship between these characteristics of the resulting surface layer and voltage, current strength and wire feed speed was comprehensively studied.

It has been established that the coating has a lamellar structure, which consists of frozen convective flows of metal, micro-welded small metal particles and oxides. This structure is explained by the formation of the coating as a result of successive impacts of particles from the 30KhGSA metal and their severe deformation, which in turn are formed under the influence of melting and dispersion of the metal during the metallization process.

The conducted studies revealed that an increase in the wire feed speed (steel 30KhGSA) leads to an increase in the thickness of the resulting coating. The results of a study of the cross-section of the coatings showed that the thickness of the coating varies from 50 to 370 microns. Also, as the wire feed speed increases, the current increases. When analyzing SEM images of cross sections of the samples under study, it was revealed that samples No. 4 and No. 5 have a more homogeneous structure and include a small number of pores.

When studying the hardness of sprayed samples, it was shown that the values of this parameter do not differ much (average hardness value  $402.53 \pm 10.38$  HV). It has been shown that samples made of steel 45 with a 30KhGSA coating have improved surface hardness by a factor of 2 compared to the uncoated sample. Despite the fact that the hardness of the surfacing material does not greatly exceed the hardness of steel 45, this result was obtained due to the hardening of the particles after their rapid cooling with an air jet. Hardness at given metallization parameters showed high properties for all studied samples.

### Acknowledgements

This research has been funded by the Science Committee of the Ministry of Science and Higher Education of the Republic of Kazakhstan (Grant No. AP14871373).

### REFERENCES

- 1 Matyushkin, B.A., Denisov V. I., Tolkachev A.A. Technological features of electric arc metallization in the agricultural sector. *Welding production*, 2016, No.12, pp. 46 – 50. [in Russian]
- 2 Kolomeichenko A.V., Sharifullin S.N., Logachev V.N., Izmalkov A.A. Investigation of properties of electro-metallized coatings deposited by supersonic air stream with aerosol fluxing. *IOP Conf. Ser.: Mater. Sci. Eng.*, 2019, 570, 012059. doi 10.1088/1757-899X/570/1/012059. [in Russian]
- 3 Kolomeichenko A.V., Kravchenko I.N., Logachev V.N. Improvement of the physical and mechanical properties of coatings obtained by electric arc metallization. *Construction and road machines*, 2015, No.7, pp. 25 – 29. [in Russian]
- 4 Logachev V.N. Improving the physical and mechanical properties of coatings obtained by electric arc metallization. *Equipment and equipment for rural areas*, 2017, No. 3, pp. 28-31. [in Russian]
- 5 Kolomeichenko A.V., Gorlenko A.O., Logachev V.N., Titov N.V. Equipment and technological recommendations for application of coatings by electric arc metallization. *Transport engineering*, 2022. No. 4. pp. 44-50. doi:10.30987/2782-5957-2022-4-44-50. [in Russian]
- 6 Tolkachev A.A., Denisov V. I., Matyushkin B. A. Application of electric arc metallization for the restoration of cylinder liners of diesel engines of agricultural machinery. *Proceedings of SSRTI*, 2017, No. 126, pp. 179-182. [in Russian]
- 7 Royanov V.A., Zakharova I. V. From the experience of using electric arc spraying for the restoration and repair of parts of metallurgical equipment. *Bulletin of the Azov State Technical University. Series*, 2015. No. 31, pp. 93 – 97. [in Russian]
- 8 Radyuk A.G., Gorbatyuk S.M., Gerasimova A.A. Use of electric-arc metallization to recondition the working surfaces of the narrow walls of thick-walled slab molds. *Metallurgist*, 2011, Vol.55, pp. 419. doi: 10.1007/s11015-011-9446-y.
- 9 Johnston A.L., Hall A.C., McCloskey J.F. Effect of process inputs on coating properties in the twin-wire arc zinc process. *Journal of Thermal Spray Technology*, 2013, 22(6), pp. 856 – 863. doi: 10.1007/s11666-013-9949-0
- 10 Kumar D., Murtaza Q., Singh R.C. Sliding wear behavior of aluminum alloy coating prepared by two-wire electric arc spray process. *International Journal of Advanced Manufacturing Technology*, 2016, No. 85, pp.237-252. doi: 10.1007/s00170-015-7920-6
- 11 Vinokurov G.G., Struchkov N.F. The influence of heat treatment on the wear resistance of sprayed coatings made of flux-cored wires with refractory additives. *Hardening technologies and coatings*, 2009, No. 11, pp. 21-24. [in Russian]
- 12 Newbery A.P., Grant P.S. Arc Sprayed Steel: Microstructure in severe substrate features. *Journal of thermal spray technology*, 2009, No.18, pp. 256 – 271. doi: 10.1007/s11666-009-9300-y
- 13 Ageev M., et al. Study influence factors of the spraying process on the properties of electric arc spraying coatings. *Problems of Tribology*, 2021, Vol. 26, No.1/99, pp. 74-83. doi: 10.31891/2079-1372-2021-99-1-74-83
- 14 Gusev V.M., Buklakov A.G. Influence of air flow on the quality of electric arc spraying. *Quality Management in the Oil and Gas Complex*, 2010, Vol. 3, pp. 34-38. <https://cyberleninka.ru/article/n/sposoby-sovershenstvovaniya-tehnologii-elektrodugovoy-metallizatsii>. [in Russian]
- 15 Kolomeichenko A.V., Logachev V.N., Deev V.B., Dudareva N.Yu. Properties of coatings obtained by supersonic electric arc metallization with aerosol fluxing. *News of higher educational institutions. Ferrous Metallurgy*, 2022, Vol. 65(9), pp. 637-643. doi: 10.17073/0368-0797-2022-9-637-643. [in Russian]
- 16 Pokhmursky V.I., Studen M.M., Ryabtsev I.A., Sidorak I.I., Dzioba Yu.V., Dovgunyk V.M., Formanek B., Influence of electric arc metallization modes and the composition of the applied flux-cored wires on the structure and abrasive wear resistance of coatings. *Automatic welding: intern. scientific, technical and industrial journal*, 2006, No.7, pp.31-36. [in Russian]

Article received 17.07.2023

Article accepted 09.12.2023

## IMPLEMENTATION OF FUNCTIONAL BLOCK RADIO UNIT BASED ON SYSTEM-ON-CHIP

Ibraimov M.K., Kozhagulov Y.T., Zhexebay D.M., Sarmanbetov S.A\*.

Al-Farabi Kazakh National University, Almaty, Kazakhstan, sarmanbetov.sanzhar@gmail.com

*This article discusses the implementation of the Radio Unit functional block based on the System-on-Chip. The primary focus was on integrating Radio Unit blocks such as modulation and Fast Fourier Transform on Field-Programmable Gate Array. Technical aspects of design, module testing, and Radio Unit block performance optimization are thoroughly examined. The results demonstrate that when separating the functionality of the 7.3 technology Fifth Generation (5G) radio block, the modulation module uses the minimum Field-Programmable Gate Array resources compared to other blocks. The Fast Fourier Transform block can meet delay requirements at the maximum Field-Programmable Gate Array size and clock frequency of 250 MHz. This article serves as a resource for engineers and researchers interested in optimizing the development and integration process of high-performance functional blocks in modern radio systems.*

**Keywords:** Field-Programmable Gate Array, Zynq, Fifth Generation New Radio, Radio Unit, Orthogonal Frequency-Division Multiple Access.

### 1. Introduction

5G (Fifth Generation) technology is transitioning from promise to reality in mobile communication, playing a crucial role in ensuring outstanding performance and ultra-reliable communication services. This article focuses on research efforts aimed at implementing 5G technology, with a particular emphasis on the use of Field-Programmable Gate Arrays (FPGAs) in this exciting context. Today, the challenge is not only to provide uninterrupted connectivity in the face of society's growing dependence on data transmission but also to meet the increasing demand for higher data transfer speeds and service reliability. In this regard, 5G emerges as a kind of backbone, opening new horizons in the realm of mobile communications.

The investigation of the architectural framework of this state-of-the-art technology precedes the exploration of the role of FPGAs in the implementation of 5G. The organizational structure of the 5G network revolves around three distinct functional blocks, namely the Centralized Unit (CU), Distributed Unit (DU), and Radio Unit (RU). Each of these blocks performs specific functions, ensuring synergy in the overall network operation. When designing RUs, critical considerations include size, weight, and power consumption. The efficiency of these parameters is essential to ensure the seamless operation of the network and, consequently, to create the best conditions for end-users.

FPGAs serve as a key tool in providing high-speed data processing in light of the aforementioned design requirements for RUs. The flexibility, energy efficiency, and parallel processing capabilities make FPGAs an ideal choice for the efficient implementation of 5G NR (New Radio) functions. As early as now, we witness the results of these studies in works [1-5], where the implementation of certain 5G NR functions on FPGAs is comprehensively described. This not only demonstrates the relevance of using FPGAs in this field but also underscores their ability to adapt to the requirements of high-speed data processing and parallel processing.

Thus, our article aims not only to uncover the fundamental aspects of designing RUs within 5G networks but also to conduct a detailed examination of the role of FPGAs in this context. The past years attest that FPGAs are not merely a theoretical proposition but a concrete tool that can effectively impact the development of key components of 5G technology. We will delve deeper into the influence of FPGAs on data transfer speed, power consumption, and overall reliability of 5G networks, opening new perspectives for the further advancement of mobile communications in the following sections of our article.

---

## 2. Statement of the problem

The work [6] provides a review of the current state of 5G technology, presenting fundamental concepts and explaining the construction of physical channels. Research by [7] suggests detailed descriptions of the functional division of the 5G network. It is demonstrated that performance optimization can be achieved through functional separation of 5G technology blocks.

Results of implementing the 5G DU Low-PHY function on SmartNIC based on FPGA are presented in the work [8]. Moreover, it is shown that FPGA-based implementations exhibit lower processing time and energy consumption compared to CPU-based implementations by up to two cores. The work [9] reveals that the research results of implementing the 5G-NR DU receiver based on Matlab/Simulink using HDL Coder are presented. Various constructive parameters are evaluated, including EVM, resource utilization, power, throughput, maximum operating frequency, and delay for different modulation schemes. There is a direct correlation between the type of input data and these constructive parameters, with the modulation scheme being practically independent of the model.

The research results on the implementation of a transceiver on FPGA for 5G PDSCH in the FR 28 GHz frequency band are presented in a study [10]. The Xilinx RFSoc platform and the Python Productivity for Zynq (PYNQ) software environment are utilized. The RFSoc platform is scalable to provide multiple T/R channels for high-speed data transmission and can be integrated with the active antenna array radio frequency subsystem to format the base radio unit (RU) of the O-RAN system.

The research results on the implementation of 5G-NR DU and RU on FPGA are outlined in an article by [11]. The 5G-NR DU receiver, combined with the RU receiver, was implemented in the ZCU102 evaluation kit with the integrated AD9371 transceiver. Resource utilization is at 25.7%, with 4.4% allocated to the 5G DU receiver and 21.3% to the AD9371 reference project, operating at a maximum frequency of 245.76 MHz [12] presents the implementation of a multimode DU transmission chain on FPGA. A comparative analysis of physical layer differences between 4G-LTE and 5G-NR mobile networks was conducted to determine fundamental changes in the architecture of each generation's DU. The FPGA implementation has an EVM of 0.24% for 4G and 1.60% for 5G.

Various applications of FPGA in the 5G network are presented in the work [13]. Several more works [14-16] are devoted to the implementing computational blocks of the 5G network on FPGA. Considering the aforementioned works, it is deemed advisable to conduct research on the implementation of physical radio modules of 5G technology on FPGA to reduce processing time with minimal energy consumption.

## 3. Methods

This study implemented a functional RU block based on FPGA. The transmitter-receiver processing module was realized on the ZedBoard evaluation kit with the AD-FMCOMMS3-EBZ board. ZedBoard is used for designing digital circuits using the programmable AMD Xilinx Zynq-7000 SoC. This device includes all the necessary interfaces for versatile applications. The data processing module of the RU block was developed and tested in the Vivado 2017.4 software environment using the Hardware Description Language (HDL) Verilog. There are several methods of functional partitioning for 5G networks [17-18]. Partitioning 7 is considered optimal in terms of simplicity and cost-effective RU design. Therefore, in this work, an RU block with functional partitioning 7 was implemented. However, there are several variants of partitioning 7.

Figure 1 illustrates these partitioning options for 5G networks. The partitionings 7.2 and 7.3 was chosen within the framework of this study.

## 4. Results and Discussion

The QPSK, 16QAM, 64QAM, and 256QAM modulators were implemented based on FPGA using the Verilog language. The modulation QPSK signal constellation is shown in Figure 2 for comparison with FPGA results. The results are shown in Figure 3 and are in complete accordance with the theoretical expectations.

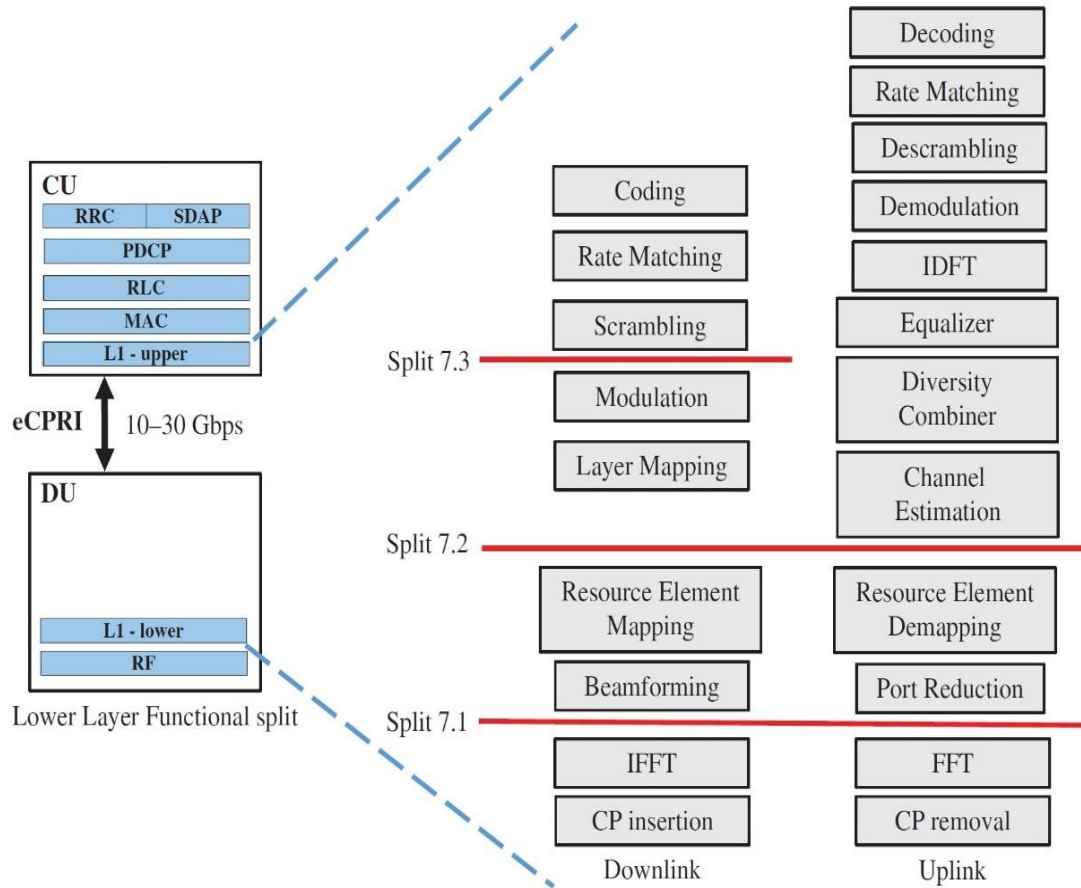


**Fig.1.** Options for Functional Partitioning 7 [19]

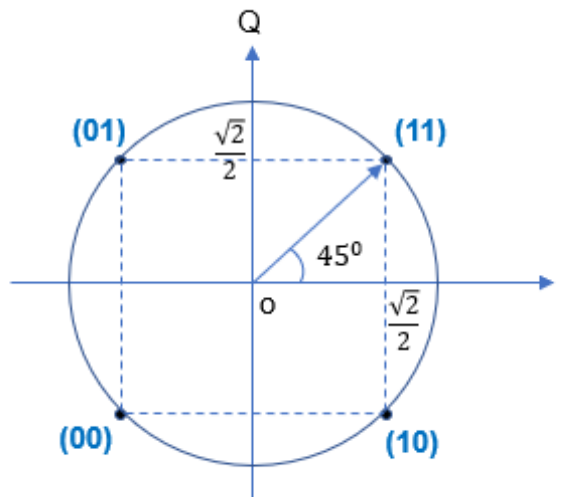
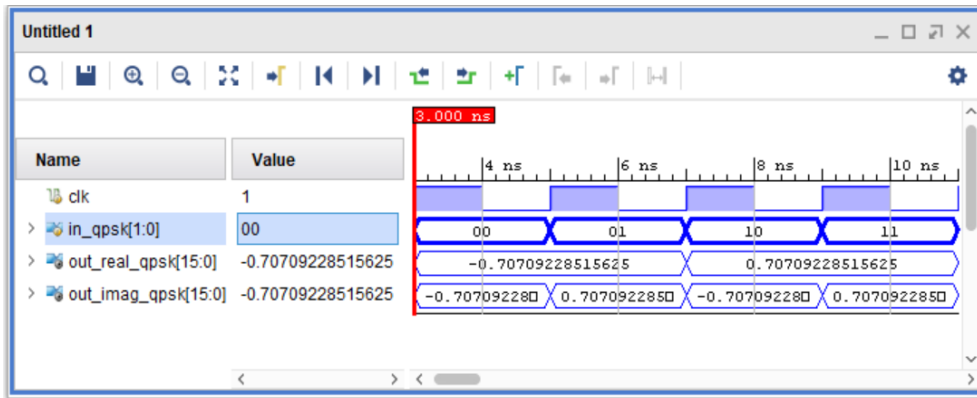
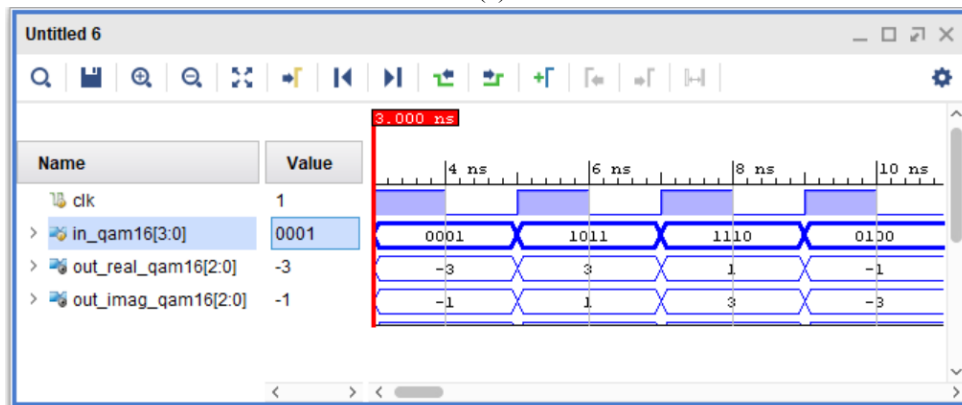


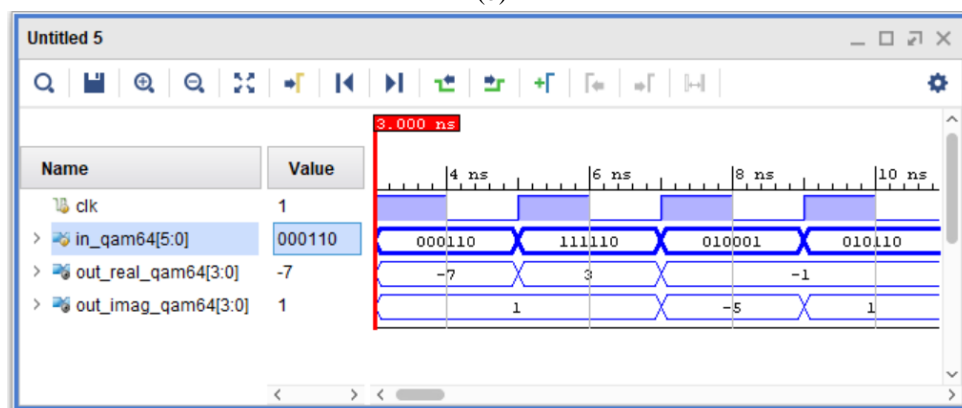
**Fig.2.** QPSK Constellations



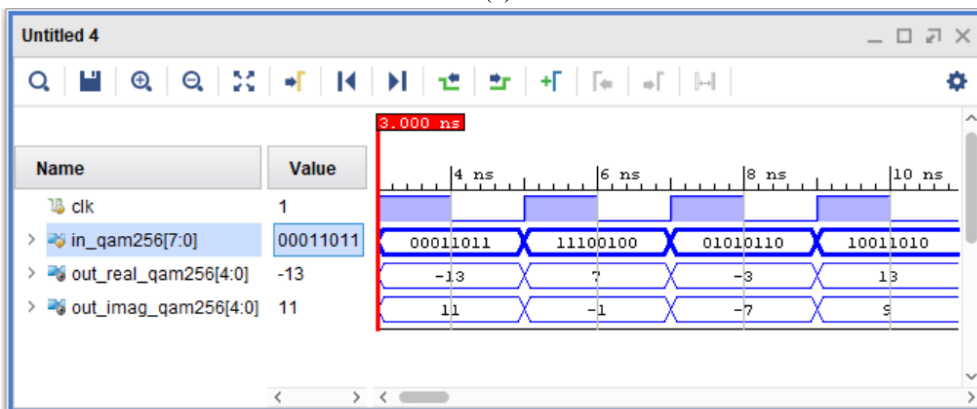
(a)



(b)



(c)



(d)

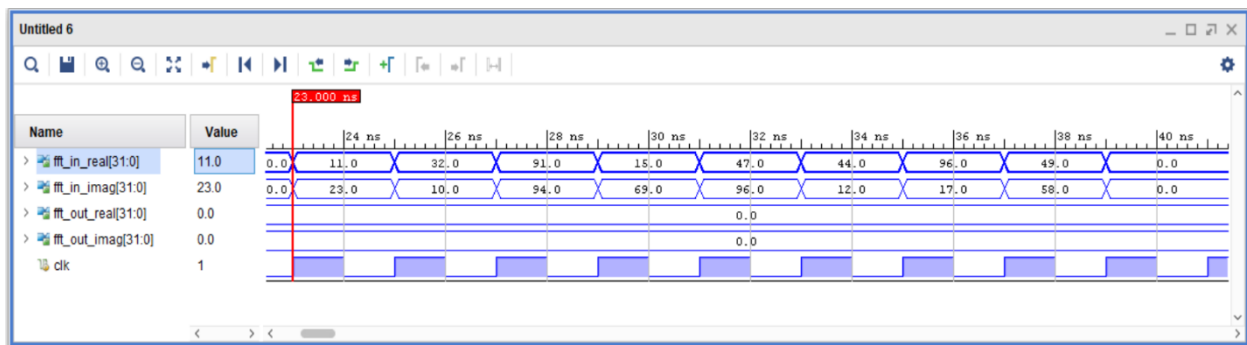
Fig.3. Results of ...QPSK (a), 16QAM (b), 64QAM (c), 256QAM (d) Modulation for RU.

The execution time of this module is 0.01 microseconds at a frequency of 100 MHz. The resources utilized for the execution of this module are presented in Table 1. The results show that only the 256QAM modulation utilizes the BRAM (Block RAM) block, while the others utilize logical blocks. As the modulation complexity increases, the resources used also increase.

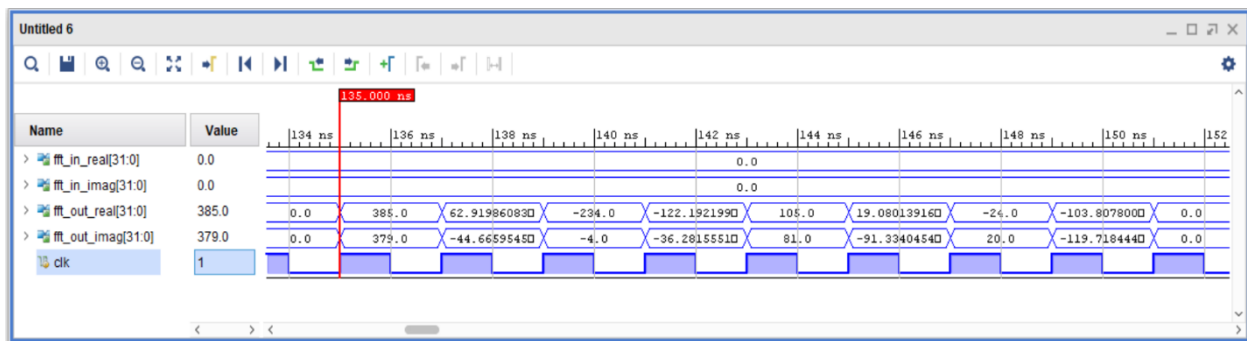
**Table 1.** FPGA Resource Utilization According to Modulation Types.

	QPSK	16QAM	64QAM	256QAM
LUT	2	2	4	0
FF	4	4	6	0
BRAM	0	0	0	1

However, QPSK and 16QAM exhibited identical resource utilization values. This could be attributed to the fact that QPSK employs fractional numbers, while 16QAM uses only integers. Additionally, a FFT/IFFT module was implemented, and the correctness of its operation was verified, as shown in Figure 4.



a



b

**Fig.4.** FFT Module Results for RU: (a) input data, (b) output data

The delay increases as the size of the transformation data grows. The results are shown in Figure 5 at a clock frequency of 100 MHz. However, the conversion frequency can be increased to 250 MHz. In that case, the delay time can be reduced by a factor of 2.5. The resources used for the execution of this module are presented in Figure 6.

It can be noted that the number of DSPs increases linearly with the growth of the transformation data size based on the obtained results of resource utilization. On the other hand, BRAM exhibits a non-linear dependence, meaning it increases exponentially with the growth of data size. This may be attributed to the fact that the computational complexity changes linearly while the memory used for computation increases exponentially.

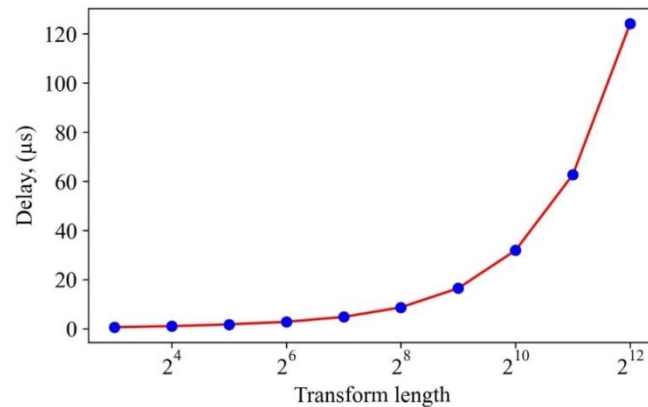


**Fig.5.** Dependence of Delay on FFT Module Size

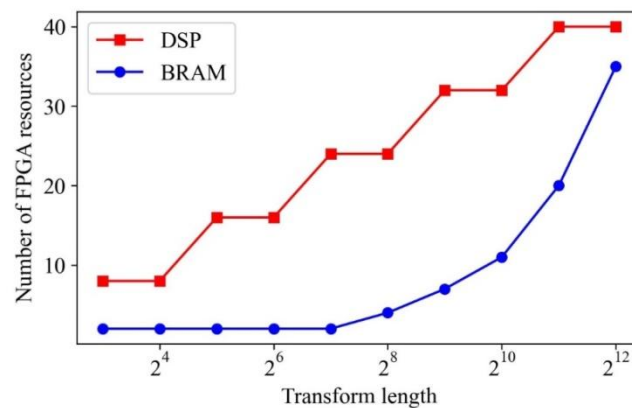


**Fig.6.** Dependence of FPGA Resources on FFT Module Size

## 5. Conclusion

In conclusion of this scientific work, it is noteworthy to highlight the successful implementation of a signal modulator supporting QPSK, 16QAM, 64QAM, and 256QAM on an FPGA platform using the Verilog programming language. The modulation results have confirmed the conformity of signal constellations and output data to theoretical expectations, emphasizing the reliability and efficiency of the proposed solution.

The execution time of the modulator was investigated, revealing a duration of 0.01 microseconds at a frequency of 100 MHz. Analysis of FPGA resource utilization allows for the identification of distinctive features associated with each modulation type, with resource consumption increasing in tandem with complexity. An interesting observation is that QPSK and 16QAM modulations exhibit identical resource usage, potentially explained by peculiarities in their numerical representations.

Additionally, an FFT/IFFT module was implemented and verified, featuring a delay dependent on the size of the transformation data. Increasing the transformation frequency can lead to a reduction in delay time. Resource utilization analysis also revealed that the number of DSP units increases linearly, while the usage of BRAM exhibits a nonlinear dependence, growing exponentially with the size of the data. This cautions against potential challenges related to memory volume in future expansions and optimizations.

Thus, the outcomes of this research not only affirm the effectiveness of implementing the FPGA-based modulator but also provide a foundation for further investigations into resource optimization and functionality expansion in communication systems.

## Funding

This research was funded by the Committee of Science of Ministry of Science and Higher Education of the Republic of Kazakhstan, grant AP09058525.

## REFERENCES

- 1 Bishop J., Chareau J. M., Bonavitacola F. Implementing 5G NR features in FPGA. *IEEE, Proceeding of the European Conference on Networks and Communications (EuCNC)*, 2018, pp. 373 – 379. doi:10.1109/EuCNC.2018.8443214.
- 2 Ricart-Sanchez R., Malagon P., Salva-Garcia P., Chirivella-Perez T., Wang Q., Alcaraz-Calero J. M. Towards an FPGA-Accelerated programmable data path for edge-to-core communications in 5G networks. *Journal of Network and Computer Applications*, 2018, Vol. 124, pp. 80 – 93. doi:10.1016/j.jnca.2018.09.012.
- 3 Visconti P., Velazquez R., Del-Valle C.S., Fazio R. FPGA based technical solutions for high throughput data processing and encryption for 5G communication: A review. *Telecommunication Computing Electronics and Control*, 2021, Vol. 19, Part 4, pp. 1291 – 1306. doi:10.12928/telkomnika.v19i4.18400.
- 4 Kumar V., Mukherjee M., Lloret J. Reconfigurable architecture of UFMC transmitter for 5G and its FPGA prototype. *IEEE, Systems Journal*, 2019, Vol. 14, Part 1, pp. 28 – 38. doi:10.1109/JSYST.2019.2923549.
- 5 Ferreira M.L., Ferreira J.C. An FPGA-oriented baseband modulator architecture for 4G/5G communication scenarios. *Electronics*, 2018, Vol. 8, Part 1, pp. 2. doi:10.3390/electronics8010002.
- 6 Lin X. Li J., Baldemair R., Cheng JF. T., Parkvall S., Larsson D.C., Koorapaty H., Frenne M., Falahati S., Grovlen S., Werner K. 5G new radio: Unveiling the essentials of the next generation wireless access technology. *IEEE, Communications Standards Magazine*, 2019, Vol. 3, Part 3, pp. 30 – 37. doi:10.1109/MCOMSTD.001.1800036.
- 7 Larsen L.M.P., Checko A., Christiansen H.L. A survey of the functional splits proposed for 5G mobile crosshaul networks. *IEEE, Communications Surveys & Tutorials*, 2018, Vol. 21, Part 1, pp. 146 – 172. doi:10.1109/COMST.2018.2868805.
- 8 Borromeo J.C., Kondepu K., Andriolli N., Valcarengi L. FPGA-accelerated SmartNIC for supporting 5G virtualized Radio Access Network. *Computer Networks*, 2022, Vol. 210, pp. 108931. doi:10.1016/j.comnet.2022.108931.
- 9 Coutinho F.D.L., Silva H.S., Oliveira A.S.R. FPGA-based Design and Optimization of a 5G-NR DU Receiver. *IEEE, Telecoms Conference*, 2021, pp. 1 – 6. doi:10.1109/ConfTELE50222.2021.9435579.
- 10 Chang C.Y., Chou H.T. FPGA Implementation of 5G NR PDSCH Transceiver for FR2 Millimeter-wave Frequency Bands. *Proceeding of the IEEE 4th Eurasia Conference on IOT, Communication and Engineering (ECICE)*, 2022, pp. 60 – 63. doi:10.1109/ECICE55674.2022.10042864.
- 11 Coutinho F.D.L., Domingues J.D., Marques P.M.C., Pereira S.S., Silva H.S., Oliveira A.S.R. Towards the flexible and efficient implementation of the 5G-NR RAN physical layer. *IEEE, Radio and wireless symposium (RWS)*, 2021, pp. 130 – 132. doi:10.1109/RWS50353.2021.9360353.
- 12 Domingues J.D., Silva H.S., Oliveira A.S.R. FPGA Implementation of a 4G/5G Multimode DU Downlink Transmission Chain. *IEEE, Telecoms Conf.*, 2021, pp. 1 – 5. doi:10.1109/conftele50222.2021.9435553.
- 13 Chamola V., Patra S., Kumar N., Guizani M. FPGA for 5G: Re-configurable hardware for next generation communication. *IEEE, Wireless Communications*, 2020, Vol. 27, Part 3, pp. 140 – 147. doi:10.1109/MWC.001.1900359.
- 14 Nadal J., Baghdadi A. Parallel and flexible 5G LDPC decoder architecture targeting FPGA. *IEEE, Transactions on Very Large Scale Integration (VLSI) Systems*, 2021, Vol. 29, Part 6, pp. 1141 – 1151. doi:10.1109/TVLSI.2021.3072866.
- 15 Shah N. A., Lazarescu M. T., Quasso R., Scarpina S., Lavagno L. FPGA Acceleration of 3GPP Channel Model Emulator for 5G New Radio. *IEEE, Access*, 2022, Vol. 10, pp. 119386 – 119401. doi:10.1109/ACCESS.2022.3221124.
- 16 Papatheofanous E.A., Reisis D., Nikitopoulos K. LDPC hardware acceleration in 5G open radio access network platforms. *IEEE, Access*, 2021, Vol. 9, pp. 152960 – 152971. doi:10.1109/ACCESS.2021.3127039.
- 17 Kim J., Kim D., Choi S. 3GPP SA2 architecture and functions for 5G mobile communication system. *ICT express*, 2017, Vol. 3, Part 1, pp. 1 – 8. doi:10.1016/j.ict.2017.03.007.
- 18 Wypiór D., Klinkowski M., Michalski I. Open ran-radio access network evolution, benefits and market trends. *Applied Sciences*, 2022, Vol. 12, Part 1, pp. 408. doi:10.3390/app12010408.
- 19 Holma H., Toskala A., Nakamura T. 5G technology: 3GPP new radio. *John Wiley & Sons*, 2020.

Article received 14.10.2023  
 Article accepted 22.11.2023

DOI 10.31489/2023No4/81-89

UDC 53.072; 681.5.075

## STUDYING THE PHYSICAL CHARACTERISTICS OF THE SNAKE ROBOT MOTION BASED ON THE “BIOLOID PREMIUM KIT” CONSTRUCTION

Loboda Yu.<sup>1</sup>, Galtseva O.<sup>1,2</sup>, Biryukova N.<sup>1</sup><sup>1</sup> Tomsk State University of Control Systems and Radioelectronics, Tomsk, Russia<sup>2</sup> National Research Tomsk Polytechnic University, Tomsk, Russia

*This article examines the physical characteristics of the movement of a snake robot. The main purpose of this work is to develop an algorithm based on the study of the physical characteristics of the movement of a snake robot, which will allow movement in various environmental conditions, both an industrial robot manipulator and a mobile robot. In the course of the work, the equations of motion of the snake robot on various surfaces were obtained. It is established that the snake robot is an open kinematic chain, the elements of which are interconnected by five or more kinematic nodes of rotation based on solving direct and inverse kinematics problems and calculating the position of the robot block in a given orientation. Based on the study of the physical movements of snakes, a proprietary algorithm for the movement of a snake robot has been developed. A prototype snake robot based on the ROBOTIS BIOLOID Premium Kit was assembled and tested on seven different surfaces. The created high-speed prototype consists of eleven blocks and a CM-530 controller without wheels and ensures high smoothness of movement compared to analogues thanks to the use of the developed algorithm.*

**Keywords:** snake robot algorithm, snake movement, serpentine robot, physical characteristics, control, RoboPlus.

### 1. Introduction

Useful characteristics of snake-like robots (stability, permeability, good adhesion to the surface) allow them to move easily in unpredictable conditions that are problematic for traditional wheeled or humanoid robots. The snake can distribute the weight of its body over a large area at the risk of subsidence of the ground; the snake robot can continue to move even when a part of the ground falls or hangs in the air. The authors see the following possibilities of using a snake robot, based on this.

Such a robot can also be used as an in-line flaw detector to check the condition of the walls of main pipelines without opening it in the oil and gas industry [1]. Snake robots could solve the problem of laying cables and electrical equipment lines in a wall or in a pipe, as well as at various distances [2-3]. It is also possible to use serpentine robots in minimally invasive surgery to eliminate the need to make large incisions in the skin and body tissues. When the size of the wound decreases, it is less traumatic for the body, resulting in an easier postoperative period, a reduction in the cost of postoperative care, etc. [4].

In addition, coil robots can manifest themselves in the best way in areas of natural disasters, be it earthquakes, landslides, explosions, hurricanes, fires. The ability to control a small mobile device with a camera and microphone opens up attractive opportunities for law enforcement agencies. If necessary, the robot can work in the autumn-spring period as a lifeguard on ice river crossings [5]. Many tracked and wheeled vehicles (at movement limitation of them) are used in conditions where human activity is unsafe, for example, where there is a danger of radiation, temperature restrictions, chemical toxicity, pressure, weakening of structures, etc. Snake-like robots are devoid of many disadvantage characteristics of wheeled structures [6].

The movement of the robot with the help of wheels is easier to understand than with the help of the musculoskeletal system; the movement of the snake is not so obvious at the same time. It is the understanding of the laws of motion when modeling a snake robot that will help to apply widely this robot in various fields. One of the main issues in the modeling of serpentine robots is their management. Servo engines fixed on special units are used in this snake. It allows the robot to move according to almost any algorithm, similar to the real snake motion. The robot possesses a camera taking the picture in the FullHD format (standard in accordance with matrix resolution 1920×1080 pixels), as well as a number of sensors,

which make it possible to orientate. The fastest natural snakes can move with the speed 3m/s in ideal conditions. It seems unlikely that robotic systems will move with the same speed in the nearest future as the majority of snakes move rather slow. Feedback control approach is used in the servo-engines Dinamixel AX-12A, due to this high accuracy of positioning has been achieved. One of the main questions under modeling serpentine robots is a control by them. Motion of robot using wheels is easier to understand than that by locomotor system; wherein, the snake motion is not so obvious. As it is known, a snake body is rather long and can consist of 200÷400 spinal bones [7]. This provides multitude of snake motions; there are several possible ways to control a snake robot. The research shows that snakes move along the surface by deforming their bodies. Typical snake motions are forward, serpentine, lateral and crawler. A snake body takes the S-shape at concertina motion; its front part moves forward while its back part constricts.

Consider in detail the typical movements of a snake to understand the laws of motion for modeling a snake robot [8-9]. A snake moves due to friction between the side surface and the ground at serpentine motion. The body bends and waves would run along the body from head to tail when the type of motion is snake-like. A bending part of the body that is set obliquely to the direction of its motion rests on the surface and creates a pushing force. This force is directed at an angle to the movement, but can be decomposed into two components: perpendicular and parallel to the line of motion. The resistance of the support dampens the first component, and the second pushes the body forward. Thus, the more bends, the more the total driving force. Almost all mobile vehicles designed by the human to use on land, are either wheel or foot driven. Wheeled vehicles started to be used several thousand years. Vehicles, which use steps to move, appeared later. Other driving mechanisms – chain tracks and feet were introduced in the twentieth century, in 1920 in particular, since then the first prototypes of snake-like robots appeared. There are various models of snake robots [10]: waver; active cord mechanisms; manipulator without support; shan; the quake snake, etc.

Nowadays, the snake-like robot “Uncle Sam snake” is the most advanced technical and software product [11]. The mentioned robot is able to climb a tree easily, crawl cross-country, and, most significantly, change from one motion mode to another in a matter of seconds. Servo engines fixed on special units are used in this snake. It allows the robot to move according to almost any algorithm, similar to the real snake motion. The robot possesses a camera taking the picture in the FullHD format (standard in accordance with matrix resolution 1920×1080 pixels), as well as a number of sensors, which make it possible to orientate. The fastest natural snakes can move with the speed 3m/s in ideal conditions. It seems unlikely that robotic systems will move with the same speed in the nearest future as the majority of snakes move rather slow. Feedback control approach is used in the Dinamixel AX-12A servo-engines, due to this high accuracy of positioning has been achieved.

## 2. Methodical part

Kinematics is a section of mechanics, which investigates mathematical description of idealized moving objects without considering the reasons for movement. The target of kinematics is geometry analytical description of an absolute robot motion apart from considering the forces affecting it. The problem of kinematics is analytical description of kinematic pairs spatial arrangement depending on time. An analytical mathematical robot model for kinematics problems statement and calculation is made, which is based on types and number of units; geometrical sizes of units; kinematic pairs distribution [12-13]. Each part or several parts joined in a stationary position are called a kinematic unit. Some parts are in motion during the device operation. Movable joint of two parts providing a certain movement of one part in relation to another one is called a kinematic pair [14]. A number of kinematic pairs joined to one another form a kinematic chain [15]. Kinematic chains classification is shown in Figure 1.

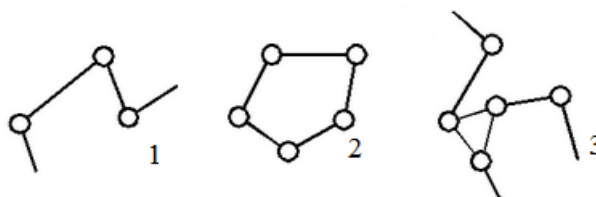


**Fig. 1.** Types of kinematic chains, where 1 is open kinematic chain; 2 is closed kinematic chain; 3 is complex open kinematic chain.

Now snake robot kinematics has been calculated and can be realized based on an industrial manipulator. It will be discussed further. Due to the presence of several kinematic pairs for the robot transfer, the units must move in the defined sequence.

Figure 2 shows the fixed positions of the linear robot motion phase. The snake robot is supposed to perform one “step” within time  $T$ , and then each of the intermediate state must be performed within  $1/8T$ . In order to ensure stability at the beginning of motion, the head and tail remain on the surface, whereas the media bend. The snake robot moves due to the unit bends, the direction of its head and tail is unchanged. In order to perform various tasks, for example, obstacle avoidance, it is necessary to change motion directions of the definite robot unit.

The consequential phases possess a number of characteristics, when the robot linearly moves on the surface. The head position is unchanged in positions 1, 2, 3 and 5, 6, 7, and the robot tail position is fixed in positions 3, 4, 5, 7, 8, 9 (Fig. 2).

We will define the relation between the transfer point  $O$  and time transfer  $F$  and time  $t$ , according to the phases of linear robot motions:

$$\{F(a, t) = x \cdot n + d_f \cdot t = n \cdot T + \tau, \tag{1}$$

$$x = 8L(1 - \cos \cos \alpha), \tag{2}$$

where  $x$  is the robot transfer within one cycle;  $n$  is number of the total cycles;  $d_f$  is robot transfer within one cycle

$$\begin{aligned} d_f = \{ & 2L(1 - \cos \cos(\omega\tau)), 0 \leq \tau \leq \frac{T}{8} 2L(1 - \cos \cos \alpha + 2L(1 - \cos \cos(\omega(\tau - \frac{T}{8}))), \\ & \frac{T}{8} < \tau \leq \frac{T}{4} 4L(1 - \cos \cos \alpha), \frac{T}{4} < \tau \leq \frac{T}{2} 4L(1 - \cos \cos \alpha) - 2L(1 - \cos \cos \omega(\tau - \frac{T}{2})), \\ & \frac{T}{2} < \tau \leq \frac{5T}{8} 6L(1 - \cos \cos \alpha) - 2L(1 - \cos \cos \omega(\tau - \frac{5T}{8})), \\ & \frac{5T}{8} < \tau \leq \frac{3T}{4} 4L(1 - \cos \cos \alpha), \frac{3T}{4} < \tau \leq T, \end{aligned} \tag{3}$$

where  $\tau$  is time within which the transfer  $d_f$  is performed;  $\omega$  is angular velocity of a robot unit.

Figure 2 shows that the robot can only move forward, which is not sufficient for a mobile robot. Changes in motion directions provide the robot with access to any point in the horizontal plane.

Figure 3 shows changes in directions of the robot motion. It is necessary to plot the time function  $G(\beta)$  to change the snake robot motion direction

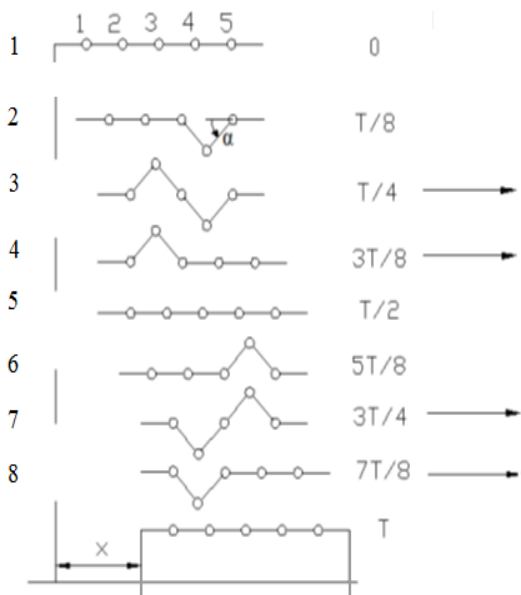


Fig. 2. Linear motion phases of the robot

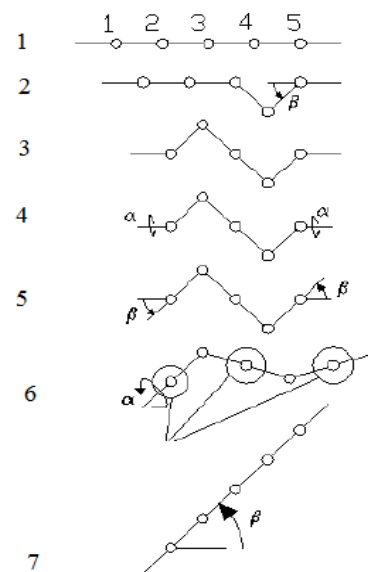


Fig. 3. Changes in the robot motion direction on the horizontal plane, where  $\alpha$  is angle in the vertical plane;  $\beta$  is angle in the horizontal plane

$$G(\beta) = \sum t_i (i = 1, \dots, 6), G(\beta) = \sum t_i \quad (i = 1, \dots, 6) \quad (4)$$

where  $G(\beta)$  is time needed for changes in motion direction of at an arbitrary angle  $\beta$ .

A robot turn by an angle  $\beta = 45^\circ$  is performed within time  $T_H$ .

$$T_H = \sum_{i=1}^6 T_i, \quad (5)$$

where  $T_i$  is time for transfer from phase  $i$  to  $i+1$ .

If parameters  $\alpha$ ,  $\beta$  and  $t$  are given, the robot head position coordinates can be determined:

$$x = \cos \cos \beta_1 F(\alpha_1, t_1) + \dots + \cos \cos (\sum \beta_1) F(\alpha_1, t_i), \quad (6)$$

$$y = \sin \sin \beta_1 F(\alpha_1, t_1) + \dots + \sin \sin (\sum \beta_1) F(\alpha_1, t_i), \quad (7)$$

$$T_m = \sum t_i \Sigma G(\beta_i), \quad (8)$$

where  $T_m$  is time of mobile robot motion.

The robot moves due to the unit winding and can bypass obstacles; the problem of the robot body transfer from one position to another has been solved.

Thus, it is necessary to know to design a kinematic model:

- types and number of units;
- geometrical dimension of units;
- distribution of kinematic pairs;

and to solve the direct and inverse problems of the robot spatial positioning.

### 3. Results and discussion

Robotis Bioloid is a kit for constructing a robot. Robotis Korean firm produces it. The kit is intended for educational purposes, as well as for those interested in robotics. The kit Bioloid is similar to LEGO Mindstorms kit by the company LEGO and Vex Robotics Design System by the company VEX Robotics (Werter Technology, 2015). The kit Bioloid contains servos Dynamixel, a set of sensors, software including 3D modeling environment and programming environment in C-like language (Table 1). The number of actuators is enough to produce a mechanism with eighteen degrees of freedom.

**Table 1.** List of parts in ROBOTIS BIOLOID Premium Kit

Servo Dynamixel AX-12 +, pcs.	18
Two-axial gyroscope, pcs.	1
IR finder, pcs.	1
IR obstacle sensor, pcs.	2
Remote control RC-100, pcs.	1
Set of robot trunk covering, pcs.	1
Li-Po battery, pcs.	1
Charging unit, pcs.	1
CD, pcs.	1
Screwdriver, pcs.	1
Cable clamp, pcs.	1

Eighteen Robotis Dynamixel AX-12A servomotors (Robotis e-Manual, 2015) are used to perform motions. The servomotors are capable of working in the positioning mode (in this mode each servo has 1024 possible positions) and in the rotation mode.

The servomotors maintain the joint through half duplex asynchronous protocol (Avage Robotics, 2015) (used with controller CM-530), RS485. The communication between the servomotors and the operator is obtained with the help of data package exchange. The servos are connected to the operator in sequence. As a matter of convenience in designing robot models, several servo-motors lines can be connected to the operator.

It is recommended to use four lines to connect servomotors, for example, when a humanoid is constructed: one line for each extremity. A maximum number of lines available for controller CM-530 are five pieces. Robots of various structures can be assembled with the help of the Dynamixels actuators in the form of instantiated units. Construction mobility is provided due to application of joint for joining actuators to one another. A snake robot is a ground multi-unit mobile robot, which can move in the restricted space, bypass obstacles and move on the surface. It is possible to design a robot structure, having identified the number of units, are knowing their geometrical sizes and made kinematic pairs distribution. We can conclude that the snake robot is an open kinematic chain the elements of which are connected with one another by five or more rotation kinematic units, based on the solutions of the direct and inverse problems. A crawling robot structure consists of five units with the total length of 0.44 m (Fig. 4a). It can be modernized up to eighteen units, depending on its execution. The units are connected with one another with the help of joints so that the turns around horizontal axis provided for each of them. A five-unit robot could not move due to its heavy head, servos did not have enough capability for moving. The snake moved on-the-site. That is why it was decided to add six units more. An eleven-unit snake structure consists of eleven units (Fig. 4b) with the total length of 0.91 m. A snake robot moves on the smooth surface with some is sliding, therefore, rubber “footing” can be attached to the unit bottom part to ensure necessary robot traction coefficient. All possible ways of snake motions have been studied before writing the motion algorithm. As a result, the algorithm of the direct snake motion (Fig. 5a) and the algorithm of the reverse snake motion (Fig. 5b) have been written.



Fig. 4. A snake robot structure with different number units, where a is with five chains; b is with eleven units

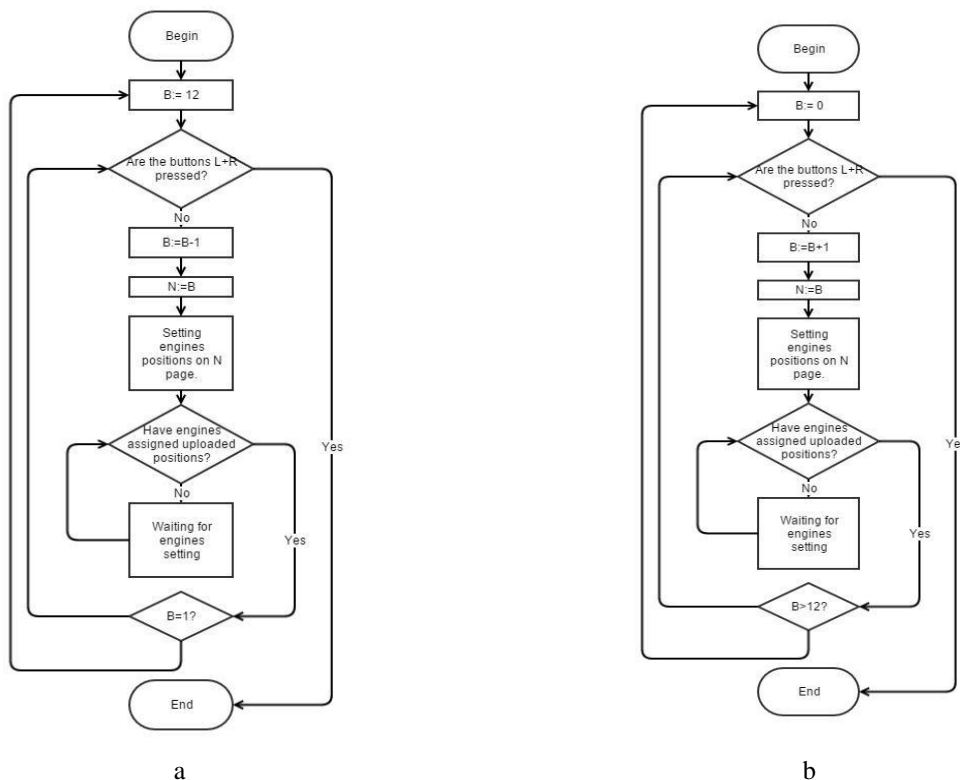


**Fig.5.** Algorithm of a snake robot motion, where a is direct algorithm, b is reverse algorithm.

Programming the snake-like robot designed on the basis of Bioloid Premium Kit was carried out with the help of the problem-oriented software system RoboPlus. The snake robot control program was created with the help of the programming environment RoboPlus Task as well as the programming environment RoboPlus Motion. Initially, positions of all eleven engines were selected, thereby the shape of the snake robot was comparable with the real snake when it moves. Initial position of a snake-like robot is illustrated in Figure 6a. A number of engines starts from the head and takes place towards the tail. It is shown in Figure 6b.



a

	Value	
ID[1]	647	<input checked="" type="checkbox"/>
ID[2]	678	<input checked="" type="checkbox"/>
ID[3]	628	<input checked="" type="checkbox"/>
ID[4]	387	<input checked="" type="checkbox"/>
ID[5]	379	<input checked="" type="checkbox"/>
ID[6]	400	<input checked="" type="checkbox"/>
ID[7]	364	<input checked="" type="checkbox"/>
ID[8]	392	<input checked="" type="checkbox"/>
ID[9]	661	<input checked="" type="checkbox"/>
ID[10]	658	<input checked="" type="checkbox"/>
ID[11]	642	<input checked="" type="checkbox"/>

b

**Fig. 6.** The initial position, where a is of a snake robot, b is of engines/

There is an impression that a snake does not crawl but floats like a wave when we observe moving snakes. The basis for creating this algorithm has been invented due to this observation. The position of each following engine was transmitted to the previous one. For example, number 11 engine transmits its location to number 10 engine at the first locomotion, while number 10 engine transmits its location to number 11 engine. After the last unit, the location of number 1 engine is transmitted to number 11 engine, and the cycle starts again. Eleven positions of the snake had to be created for functioning of the set algorithm; they were in-series shifted onto one position of engines relative to the previous one (Fig. 7).

Consequently, locomotion has been created which enables a snake robot repeat a real snake motion. The following characteristics have been improved after testing the snake motion algorithm: smoothness and speed of snake motions. Such parameter as Joint Softness is responsible for smoothness of engines motion (Fig. 8). The greater value Joint Softness for a certain engine is, the smoother a robot will move.

	Name	Next	Exit
▶ 1	1	0	0
2	2	0	0
3	3	0	0
4	4	0	0
5	5	0	0
6	6	0	0
7	7	0	0
8	8	0	0
9	9	0	0
10	0	0	0
11	11	0	0
12		0	0

**Fig. 7.** Eleven positions of the snake written in RoboPlus Motion

[Joint Softness]	
	Level
ID[1]	7
ID[2]	7
ID[3]	7
ID[4]	7
ID[5]	7
ID[6]	7
ID[7]	7
ID[8]	7
ID[9]	7
ID[10]	7
ID[11]	7

**Fig. 8.** The controller of engine operation smoothness

Moreover, RoboPlus Motion programme software makes it possible to set a quantity of motion repeats, speed of engine work, as well as inertial force after finishing engines operation (Figure 9). It was necessary to fully assemble all parts of the program after setting all possible parameters of engines. In order to do it, the

RoboPlus Task programme software was applied. C-like language, intended for the work with Bioloid products was used in the programming environment. It is necessary to download the program onto the inner memory of the robot with the help of the "Download Program" button after writing the software code (Fig. 10). Motion algorithms were tested on eleven various surfaces.

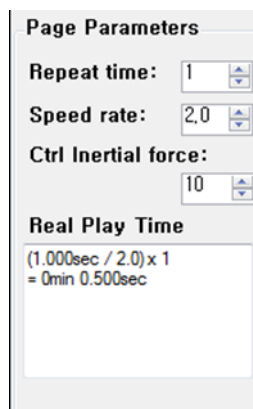


**Fig. 9.** Form for changing speed of engine work

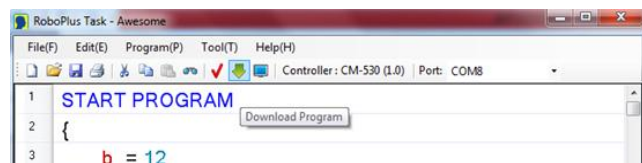


**Fig. 10.** Uploading files on the inner memory controller in the programming environment RoboPlus Task

The main point of tests was indicating the most favorable surfaces for prototype movement by measuring the motion speed of a snake robot. The length of the snake-like robot assembled on the basis of Bioloid premium kit which includes eleven units being stretched is 88 cm. Tests involved accomplishing the given distance, i.e. a distance was considered covered at the moment when the snake tail crossed the initial position of its head. Ten experiments have been conducted on each surface; the overall average has been calculated. The most common surfaces were selected such as paving slab, asphalt, linoleum, plastic, ground, carpeted floor and grass. Results of all experiments of eleven various surfaces were obtained and results of one experiment is presented below as example.

The snake moved on asphalt with approximately the same speed as that on paving slab (Fig. 11). Data about the time spent on accomplishing the distance are presented in Table 2.



a



b

**Fig. 11.** Position of the snake robot, where a is an initial position, b is a final position

The following is a comparative analysis of the robot under study with other existing robots of this type.

Since 1920, the first prototypes of serpentine robots began to appear. The first prototype of the snake-like robot was presented by Peter Míturich, who developed a number of designs called "Waveguides". Nine technical ways of solving the principle of undulating motion on the earth were proposed. In 1970, a legless robot "Active Cord Mechanisms or ACMs" was built. It was aimed at performing a lateral type of movement and moved due to the existing wheelbase. At the beginning of the XXI century, Joel Burdick and his students from the California Institute of Technology developed a VGT manipulator that could repeat the movements of snakes. Later, the Shan robot was developed, which differed from the others in that it used solenoids to contact the surface, which allowed at a certain moment to fix the desired part of the snake on the surface,

while the rest of the snake was moving. Due to the configuration, the robot's movement was limited on a flat floor and with a tortuous type of movement when a large space is required.

**Table 2.** Timed consumed for movement on asphalt

Experiment number	Surface used	Operating time, sec	Average value, sec
1	asphalt	58	63
2		65	
3		68	
4		60	
5		57	
6		63	
7		69	
8		66	
9		72	
10		55	

The giant Japanese electronics company NEC has developed a robot snake "The Quake Snake". The device used a universal Hook joint, which was designed specifically for use in the construction of a snake robot. This snake-like robot is not a promising because of such a hinge, the design turned out to be very flexible and versatile. The robot was controlled manually by means of a special remote control and a video camera.

GMD snake was developed by a working group working in Germany: the serpentine robot was a development for real-time control. The device consisted of short sections connected by cables.

IS robotics has built a small Kaa snake designed for grabbing pipes, branches, etc., as well as for moving along the surface with a tortuous type of movement. The robot was not the most effective in terms of wriggling crawling on the floor due to the large processor unit located in the middle of the robot. The "Kaa snake" managed to move more efficiently in the pipeline networks. It was the first fully autonomous snake robot. Comparative analysis has shown that the presented project uses lateral movement, which distinguishes our development from most other developments of snake robots. According to the presented hypothesis, which was later confirmed experimentally, the snake robot demonstrates the best speed with lateral movement on moderately fleecy surfaces.

#### 4. Conclusion

Algorithm, based on the studying the physical characteristics of the snake robot movement, which takes into account the interaction and position of neighboring links of the snake robot, was created and it ensures the smooth of the snake robot movement. Test results showed that it is possible to control the robot's movement on seven different types of surfaces thanks to this algorithm. The advantage of this development compared to other analogues is to ensure smooth movement of the snake robot on various surfaces, in particular, with moderate hairiness, while most such robots move using a worm-like method or jerks. In addition, the required minimum (eleven) positions of the snake was studied for the functioning of the given algorithm with using the created robot system with motors sequentially shifted by one position relative to the previous one and transmitting the position of each subsequent motor to the previous one. Thus, a hardware and software complex was obtained that simulates also the lateral movements of sand snakes with the best movement performance on moderately fleecy surfaces. Now it has become possible to control the movement of robots of this type when using them in different life situations in various fields of application, using the developed algorithm for the movement of a snake robot. An experimental snake robot powered by DYNAMIXEL motors, in the presence of a protective casing, can be used in the field of extreme robotics in conditions where it is difficult for a person to stay: for example, in a situation with bad weather conditions or in an aggressive environment inaccessible to humans.

#### REFERENCES

1 Kesteloo T.V. Autonomous navigation for the pipeline inspection robot "Pirate". 2020. Available at: [http://essay.utwente.nl/85373/1/85373\\_Kesteloo\\_MA\\_EEMCS.pdf](http://essay.utwente.nl/85373/1/85373_Kesteloo_MA_EEMCS.pdf)

- 
- 2 Borikov V.N., Galtseva O.V., Filippov G.A. Method of Non-contact Calibration of the Robotic Ultrasonic Tomograph. *IOP Conference Series: Materials Science and Engineering*, 2016, Vol. 671, 012014. doi: 10.1088/1742-6596/671/1/012014.
  - 3 Trebuña F., Virgala I., Pástor M., Lipták T., Miková L. An inspection of pipe by snake robot. *International Journal of Advanced Robotic Systems*, 2016. Vol. 13, No. 5. doi: 10.1177/1729881416663668.
  - 4 Runciman M., Darzi A., Mylonas G.P. Soft Robotics in Minimally Invasive Surgery. *Soft Robot*, 2019, Vol. 6, No. 4, pp. 423–443. doi: 10.1089/soro.2018.0136.
  - 5 NASA shows a snake robot to explore planets. 2023. Available at: <https://universemagazine.com/en/nasa-shows-a-snake-robot-to-explore-planets-video/>
  - 6 Sanfilippo F., Azpiazu J., Marafioti G., Transeth A.A., Stavadahl Ø., Liljebäck P. Perception-Driven Obstacle-Aided Locomotion for Snake Robots: The State of the Art, Challenges and Possibilities †. *Applied Sciences*, 2017, Vol. 7, No. 4, 336. doi: 10.3390/app7040336.
  - 7 Matthews T. *Do Snakes Have Bones?* Information and Facts, 2021. Available at: <https://pestsamurai.com/do-snakes-have-bones/>
  - 8 Ali Sh. *Newton-Euler approach for bio-robotics locomotion dynamics: from discrete to continuous systems*. Automatic. France: Ecole des Mines de Nantes, 2011, 251 p.
  - 9 Rollinson D. *Control and Design of Snake Robots*. Pennsylvania: Carnegie Mellon University, 2014, 203 p.
  - 10 Zhang J., Chen Y., Liu Y., Gong Y. Dynamic Modeling of Underwater Snake Robot by Hybrid Rigid-Soft Actuation. *Journal of Marine Science and Engineering*, 2022. Vol. 10, No. 12, 1914. doi: 10.3390/jmse10121914.
  - 11 Wright C., Buchan A., Brown B., Geist J., Schwerin M., Rollinson D., Tesch M., Choset H. Design and architecture of the unified modular snake robot. *Proceedings of the 2012 IEEE International Conference on Robotics and Automation*, 2012, 4347. doi:10.1109/ICRA.2012.6225255.
  - 12 Shumilin N.A., etc. Kinetic robot programming. *Proceedings of the 2014 All-Russian Scientific and Technical Conference “TUSUR Scientific Session”*, 2014, pp. 155–157. [https://storage.tusur.ru/files/43235/2014\\_3.pdf](https://storage.tusur.ru/files/43235/2014_3.pdf) [in Russian]
  - 13 Iurevich E.I. *Basics of Robotics*. Sankt-Peterburg: BKhV-Peterburg, 2010, 252 p. [in Russian]
  - 14 Frolov K.V., Vorobev E.I. *Industrial Robot Mechanics*. Moskva: Vysshaya shkola, 1989. 383 p. [in Russian]
  - 15 Chang K.H. *Chapter 8-Motion Analysis*. Academic Press, 2015, pp. 391–462. doi: 10.1016/B978-0-12-382038-9.00008-9.

Article received 12.10.2023

Article accepted 05.11.2023

## ROUTING METRIC AND PROTOCOL FOR WIRELESS MESH NETWORK BASED ON INFORMATION ENTROPY THEORY.

Turlykozhasheva D.<sup>1</sup>, Ussipov N.<sup>1</sup>, Baigaliyeva A.<sup>1</sup>, Temesheva S.<sup>1</sup>, Bolysbay A.<sup>1</sup>,  
Abrahmatova G.<sup>2</sup>, Akhtanov S.<sup>1\*</sup>

<sup>1</sup> Al-Farabi Kazakh National University, Almaty, Kazakhstan, ahtanov.saiyat1@kaznu.kz

<sup>2</sup> Almaty University of Power Engineering and Telecommunications named after G. Daukeev, Almaty, Kazakhstan,  
G.abrahmatova@aes.kz

*In this work, the authors propose a routing algorithm based on information entropy theory for calculating the metric, considering the probability of packet loss. Information entropy theory serves as a robust foundation for evaluating uncertainty and disorder in data transmission, facilitating the development of a more resilient and intelligent routing strategy. In contrast to existing algorithms, the proposed approach enables a more accurate assessment of data transmission quality within the network, optimizing the routing process for maximum efficiency. The experimental results demonstrate a significant enhancement in network service quality while maintaining high performance. To validate the algorithm's effectiveness, a series of experiments were conducted, evaluating key performance metrics such as throughput, delay, and packet loss. A comparative analysis with established routing algorithms was also carried out, allowing for the assessment of advantages and drawbacks in relation to well-known algorithms. The findings suggest that the proposed algorithm surpasses traditional routing methods in optimizing data transmission quality and overall network efficiency.*

**Keywords:** Routing, entropy, information, wireless mesh network.

### 1. Introduction

In the present day, wireless mesh networks (WMNs) are emerging as a rapidly deployed communication technology. This swift adoption can be attributed to several advantages, including easy and quick implementation, automatic self-recovery, dynamic self-organization, self-configuration, extensive network coverage, and cost-effectiveness. Furthermore, the versatility of WMNs makes them suitable for a wide range of applications, including broadband home networking, education, healthcare, building automation, disaster management, rescue operations, and military applications [1-4].

The WMN architecture consists of three carefully structured node layers. In the first layer, gateway nodes (GWs/Gws) are linked to the physical layer. Moving to the second layer, quasi-static wireless mesh routers (MRs/APs) fulfill the role of transmitting packets to and from mesh gateways. Finally, the third layer comprises mesh clients (MCs), including devices such as desktop computers, mobile phones, laptops, and various other wireless devices.

In general mesh routers have more sophisticated capabilities than mesh clients, such as multiple receive/transmit interfaces, higher transmitting power, infinite power supply. The data traffic in WMNs comprises gateway-oriented traffic and client-oriented traffic. In gateway-oriented traffic, data is transferred through a gateway to the Internet. In client-oriented traffic, the data packets are transmitted to the destination mesh client by multiple hops [5-6]. Currently, a lot of research has been done on routing issues in WMNs [7-15]. Routing protocol design is essential for the performance and reliability of WMNs. The primary goal of the routing protocols is to find reliable routes in multi-hop WMN that is deals with the highly unstable wireless medium. These days, more and more communication services require high throughput and little delay, so it is crucial to tackle the problem of traffic routing for throughput optimization and delay minimization in WMNs [11, 12]. In recent times, there has been a rising interest in the application of information entropy theory in routing for wireless networks [13, 14]. Information entropy methods offer a valuable framework to assess and improve the efficiency and reliability of data transmission in wireless networks. By quantifying uncertainty and disorder in network communication, these methods allow for a more comprehensive understanding of network dynamics, error detection, and quality of service

optimization. Information entropy theory aids in identifying and mitigating potential vulnerabilities in routing protocols while enhancing the accuracy of performance metrics, such as throughput and overall network performance. Its adoption represents a promising direction for enhancing WMN routing in an era of growing data demands and network complexity [15-18].

In this work, a new algorithm, named Information entropy-based routing algorithm (IER), is proposed to calculate the routing metric based on information entropy theory. The method considers vulnerabilities observed in Dijkstra's algorithm, where an increase in complexity correlates with a higher probability of errors. For a more accurate assessment of errors in the communication channel, it is proposed to use the entropy method. Additionally, routing algorithms developed for WMNs, such as Optimized Link State Routing (OLSR) and Better Approach to Mobile Adhoc Networking (BATMAN), use broadcasting techniques to discover pathways. However, this approach often leads to network congestion, which, in turn, reduces throughput. It's also important to note that current routing algorithms designed for wireless ad hoc networks are not directly applicable to WMNs, as they haven't been optimized for the specific requirements of WMNs.

## 2. Routing Protocols

This section presents a concise overview of several prominent routing protocols developed for WMNs, with the aim of identifying vulnerabilities and strengths as a preliminary step before creating a new routing algorithm. Furthermore, the discussion of Dijkstra's algorithm is delved into as a benchmark for comparison with more specialized WMN routing protocols, enabling the evaluation of its applicability and constraints [19].

Numerous routing protocols have been proposed for wireless mesh networks, including Dynamic Source Routing (DSR), Ad-hoc On-Demand Distance Vector (AODV), Destination-Sequenced Distance Vector (DSDV), Optimized Link State Routing (OLSR), Better Approach to Mobile Adhoc Networking (BATMAN), Software-Defined Networking for Mesh Networks (SDNMesh), and Three-Stage Routing Algorithm (Three-Stage). Many of these protocols use broadcasting techniques to establish communication pathways, but this approach can be energy-consuming and lead to unnecessary overhead.

The OLSR protocol is a proactive, table-driven routing protocol designed for use in mobile ad-hoc networks (MANETs) and wireless mesh networks (WMNs). OLSR aims to efficiently determine and maintain routes in a network where nodes can move and change their connections frequently. It was developed to address the challenges of routing in dynamic, self-organizing, and multi-hop wireless networks. OLSR represents an enhancement of the traditional link state protocol, designed specifically for mobile ad hoc networks and wireless networks.

First, OLSR is a proactive routing protocol, which means it maintains routes at all times. This proactive nature reduces route discovery latency, making it suitable for applications that require low-latency communication. Secondly, OLSR optimizes control message overhead using Multipoint Relays (MPRs), reducing the number of nodes that need to rebroadcast control messages. This optimization reduces the impact on the available network bandwidth and power resources.

Also, OLSR is well-suited for multi-hop wireless networks, making it ideal for wireless mesh networks, ad-hoc networks, and other scenarios where nodes need to relay data across multiple hops. OLSR also can work with existing IP networks and can be easily integrated with the Internet Protocol (IP), enabling seamless communication with other IP-based devices. However, it comes with certain vulnerabilities and limitations such as limited scalability, resource consumption, static MPR selection, security concerns, inapplicability for all scenarios, and lack of QoS Guarantees. OLSR can face scalability issues in large networks due to its proactive nature. Maintaining routing information for all nodes in the network can lead to excessive control overhead, which may not be practical in highly dynamic and large-scale environments.

The proactive approach of OLSR results in higher resource consumption, both in terms of memory and processing power. This can be a concern in resource-constrained devices, such as sensor nodes. Also, OLSR's Multipoint Relay (MPR) selection is typically static, meaning that MPRs are selected during the initial setup and do not adapt to changing network conditions. This can lead to suboptimal routing in dynamic networks. (OLSR) protocol faces security vulnerabilities as it lacks robust built-in security mechanisms, making it susceptible to attacks such as spoofing, eavesdropping, and denial of service. To ensure secure operation, additional security mechanisms like encryption and authentication must be added. Furthermore, OLSR may not be the optimal choice for all types of wireless networks. In scenarios involving

highly mobile networks or rapidly changing network topologies, alternative routing protocols like AODV (Ad Hoc On-Demand Distance Vector) might be more suitable due to their adaptability and responsiveness to dynamic network conditions. Moreover, while OLSR can be extended to consider Quality of Service (QoS) metrics, it does not inherently provide strong QoS guarantees. This limitation makes it less suitable for applications with stringent QoS requirements, where the assurance of specific performance characteristics is of utmost importance [20-22].

The BATMAN is a proactive, table-driven routing protocol designed for wireless ad-hoc networks and mobile mesh networks. BATMAN aims to provide efficient and reliable communication in scenarios where nodes can move, and the network topology changes frequently. BATMAN (Better Approach to Mobile Ad-Hoc Networking) offers numerous advantages in wireless mesh and ad-hoc networks. It is a proactive routing protocol that maintains up-to-date routing information, reducing route discovery latency and facilitating low-latency communication. BATMAN excels in multi-hop environments, making it ideal for wireless mesh networks, where data must traverse multiple nodes to reach their destination. Its innovative Originator-based routing approach minimizes control message overhead by allowing nodes to select Originators that relay information, enhancing network efficiency.

BATMAN is known for its ease of use with minimal configuration requirements, making it accessible to a broad range of users and applications. Additionally, it provides adaptability to various wireless environments, supports mesh networking, and can be integrated with the Internet Protocol (IP) for broader internet connectivity. Extensions such as BATMAN-ADV can enhance security with features like encryption and authentication, adding to its versatility and robustness. BATMAN (Better Approach to Mobile Ad-Hoc Networking) has notable limitations. While it offers proactive routing, it can encounter scalability issues in large networks due to control message overhead, potentially affecting network performance. Its resource consumption, including memory and processing power, can be demanding and may not be suitable for resource-constrained devices. Security concerns are a drawback, as BATMAN lacks strong built-in security mechanisms by default, leaving it vulnerable to various attacks. Moreover, it may not be the optimal choice for highly mobile or rapidly changing network scenarios, where other routing protocols might provide more adaptability and responsiveness. Lastly, BATMAN does not inherently guarantee Quality of Service (QoS), making it less appropriate for applications requiring strict QoS requirements, which need assurance of specific performance characteristics. Consideration of these limitations is essential when selecting BATMAN as a routing protocol in various network deployments [23, 24].

SDNMesh is a routing protocol designed to enhance the capabilities of the OpenFlow protocol, enabling its application in Wireless Mesh Networks (WMNs) with their dynamic characteristics. It involves the modification of the OpenFlow client to align with the proposed routing architecture. SDNMesh operates in two phases: the first phase establishes routes from the controller to switches, which may not be optimal in terms of latency, while the second phase optimizes these initially inefficient routes, introducing some additional delay. This protocol addresses challenges like link or node failures, which are common in wireless environments. To support its functionalities, an OpenDaylight controller is integrated into the network, enabling the controller to gather information from Mesh Access Points (MAPs) and form a global network view. SDNMesh provides a stepwise approach to routing, focusing initially on establishing connections between the controller and all the switches in the network, followed by setting up routing paths between the SDN controller and connected switches, ultimately ensuring efficient data transmission between switches.

The Three-Stage routing algorithm is a specialized approach designed to address routing challenges within Software-Defined Networking (SDN)-based Wireless Mesh Networks (WMNs), particularly in the context of Smart Grid communication and power grid management. This algorithm extends the capabilities of the OpenFlow protocol to adapt to the dynamic nature of WMNs. It operates in three key stages: First, it focuses on establishing connections between all switches in the SDN-based wireless mesh network and at least one controller, utilizing an OpenFlow-based routing algorithm and network flooding. Once initial connections are established, the second stage optimizes routing paths, introducing new alternatives, including shortest and load-balanced routes. Finally, the third stage addresses routing among switches, ensuring efficient data transmission. The Three-Stage routing algorithm emphasizes cost-effectiveness, low latency, and network-aware communication, making it well-suited for providing coverage in challenging environments, such as power systems in rural and disaster-prone areas [25, 26].

Dijkstra's algorithm is an algorithm used to find the shortest path between two nodes in a weighted graph. It was developed by Dutch computer scientist Edsger Dijkstra and is one of the most widely used methods in networking and telecommunications. Dijkstra's algorithm operates on the principle of finding the

shortest path in a weighted graph. It begins with an initial node, setting its distance to itself as zero and all other nodes as distances to infinity. The algorithm iteratively selects the unvisited node with the smallest known distance, evaluates the distances to its adjacent nodes, and updates them if a shorter path is found. This process continues until all nodes are marked as visited or until the shortest path to a specific destination node is discovered. Once completed, the algorithm allows for determining the shortest path to any node by tracing the sequence of nodes and their distances from the initial node. Dijkstra's algorithm offers several key advantages, making it a valuable tool in various applications. It guarantees the discovery of the shortest path in graphs with non-negative edge weights, ensuring optimal route selection. Its versatility allows it to be applied to a wide range of real-world problems, from transportation and logistics to computer network routing. The algorithm excels in providing accurate results, making it suitable for critical applications where precision is essential. Also, Dijkstra's algorithm is relatively simple to understand and implement, making it accessible to a broad audience of users, from novice programmers to experts in route optimization. Despite its effectiveness, Dijkstra's algorithm has notable vulnerabilities that must be considered when applying it to certain scenarios.

First and foremost, it cannot handle graphs with negative edge weights, as it assumes non-negativity, and attempting to use it in such cases can result in incorrect results. Additionally, the algorithm focuses on finding the shortest path from a single source node to all other nodes, making it less suitable for problems that require simultaneous determination of multiple sources or destinations. While its time complexity can be improved with the use of a priority queue, Dijkstra's algorithm remains inefficient for large graphs, leading to increased computational demands. Furthermore, its memory usage can be high in large-scale applications, as it requires storing and updating distances for all nodes. Lastly, the algorithm is not suitable for graphs with negative weight cycles, as it may get stuck in an infinite loop in such scenarios [27, 28].

### 3. The proposed routing method

The fundamental principle of the Information entropy-based routing algorithm (IER) centers on channel multiplication, providing it with the capability to adeptly manage errors and efficiently handle packet loss during data transmission. To implement the proposed routing algorithm, the initial step involves calculating the distance between nodes, defined as the shortest length between the nodes  $u$  and  $v$ . Consider Fig. 1 which illustrates a cascade-connected network configuration featuring routers  $R1$ ,  $R2$ , and  $R3$ , interconnected through channels (ch1 and ch2), where potential errors can occur. This diagram visually portrays the sequential connections between the routers, underscoring the cascading nature of their arrangement.

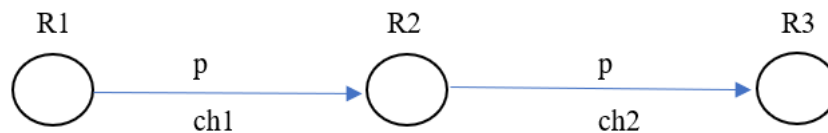


**Fig.1.** An example of cascade-connected routers.

Each channel has error probabilities that depend on the distances between routers (Fig. 1). To find the distances, the following equation is used:

$$d = \sqrt{(x_1 - x_2)^2 + (y_1 - y_2)^2}, \quad (1)$$

where  $d$  represents the distance between the two routers,  $(x_1, x_2)$  are the coordinates of the first router,  $(y_1, y_2)$  are the coordinates of the second router.

The calculation of received power ( $P_r$ ) is crucial for assessing the quality of the received signal in communication networks. It helps in determining whether the signal is strong enough to ensure reliable communication and to identify potential issues such as signal degradation or interference. The received power ( $P_r$ ) can be calculated using the Friis transmission equation. It is expressed as:

$$P_r = \frac{P_t G_t G_r (\lambda^2)}{(4\pi d)^2}, \quad (2)$$

where  $P_r$  is the received power,  $P_t$  is the transmitted power,  $G_t$  is the gain of the transmitting antenna,  $G_r$  is the gain of the receiving antenna,  $\lambda$  is the wavelength of the signal,  $d$  is the distance between the transmitter and receiver.

The free-space path loss equation, also known as the Friis transmission equation, is used to calculate the loss of signal power as it propagates through free space.

$$\frac{P_r}{P_t} = D_t D_r \left(\frac{\lambda}{4\pi d}\right)^2, \tag{3}$$

where  $D_t$  is the directivity of the transmitting routers antenna,  $D_r$  is the directivity of the receiving routers antenna,  $\lambda$  is the signal wavelength,  $d$  is the distance between the antenna routers.

Next, both the Signal-to-Noise Ratio (SNR) and the Bit Error Rate (BER) can be derived. SNR is a ratio that compares the strength of the received signal to the background noise, while BER quantifies the likelihood of errors in the received data. Since  $p$  represents the probability of an error, it is indeed equal to the BER. The equation for BER depends on the modulation scheme and channel model but can generally be expressed as:

$$p = BER = \frac{1}{2} \operatorname{erfc}\left(\frac{Q}{\sqrt{2}}\right), \tag{4}$$

where  $\operatorname{erfc}$  is the complementary error function.

Next, cascade-connected channels are examined, and their error probabilities (Fig. 2) are calculated. The model and analysis of cascade-connected channels are presented in [29].

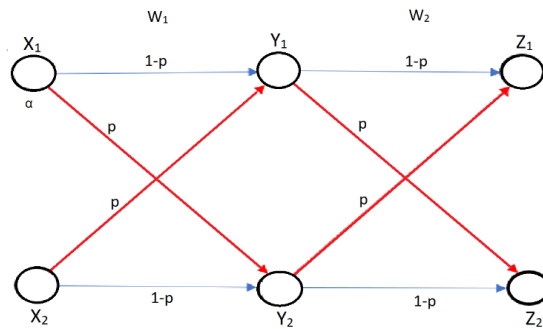


**Fig.2.** Cascading channels.

The channels are considered as matrices and multiplied accordingly. The matrix representing the conditional probabilities for this model is provided below:

$$P(R_3/R_1) = \begin{bmatrix} 1-p & p \\ p & 1-p \end{bmatrix} \begin{bmatrix} 1-p & p \\ p & 1-p \end{bmatrix}, \tag{5}$$

where  $p$  is probability of error.

The total probability  $n$  cascade-connected channels are defined as follows:

$$P = P\left(\frac{R_N}{R_1}\right) = \prod_{i=1}^N \begin{bmatrix} 1-p & p \\ p & 1-p \end{bmatrix} = \begin{bmatrix} 1-p_N & p_N \\ p_N & 1-p_N \end{bmatrix}, \tag{6}$$

where,  $p$  is probability of error of each cascade,  $p_N$  – total probability of  $N$  cascade-connected channels.

In the following step the total entropy of the channel path is calculated. The total entropy of the channel path characterizes the degree of uncertainty or information content associated with the transmission through a particular route. The total entropy of the channel path is defined as:

$$H_N(p) = -p_N \ln p_N - (1 - p_N) \ln(1 - p_N), \tag{7}$$

The subsequent step involves selecting the path with the minimum entropy among calculated entropies. This decision-making process is guided by the principle of minimizing unpredictability or disorder in the information associated with the chosen path. By prioritizing paths with minimized uncertainty, the algorithm is designed to optimize the flow of data, leading to higher throughput, and improved overall network performance. In the final step we defined throughput according to the following equation:

$$C = 1 - H_N(p_N), \quad (8)$$

where  $C$  is throughput,  $p_N$  is total probability of  $N$  cascade-connected channels and  $H_N$  is total total entropy of the channel path.

Here, a brief description of the proposed method is presented. To implement the IER, the following steps need to be performed:

- 1) Find distance ( $d$ ) between routers;
- 2) Define received power ( $P_r$ );
- 3) Find SNR and BER of each channel;
- 4) Choose 10 random paths between source and target;
- 5) Define entropy of each path;
- 6) Choose path with minimum entropy;
- 7) Determining the throughput of the route.

#### 4. Experimental evaluation

To assess the effectiveness of the IER algorithm, a simulation model of a WMN with 200 nodes was constructed using Python. The performance of the IER algorithm was benchmarked against several established routing protocols, including OLSR, BATMAN, and SDN based routing, Three-Stage algorithm, and the classic Dijkstra's algorithm. This comparative analysis was focused on key performance metrics: throughput, as illustrated in Figure 3 (a, b); Packet Loss Ratio, depicted in Figure 4; and Delay, shown in Figure 5. The simulations were carried out under varying network sizes, with WMN node counts of 10, 50, 100, 150, and 200, to obtain a comprehensive set of data on the three-performance metrics of interest: throughput, packet loss ratio, and average delay.

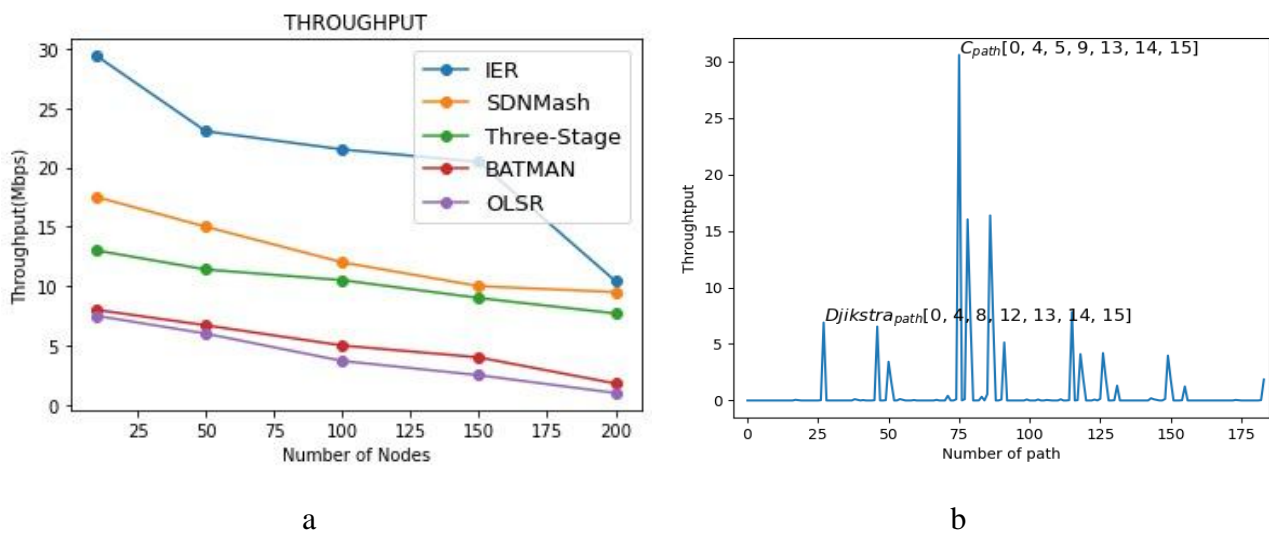


**Fig.3.** Throughput: a) of IER, SDNMash, Three-Stage, BATMAN and OLSR algorithms; b) of Dijkstra's algorithm

Figure 3 (a) presents the throughput measurements for each of the evaluated protocols – IER, OLSR, BATMAN, Three-Stage, and Dijkstra's across different network sizes. The data indicates that the IER algorithm consistently achieves higher throughput than the other protocols, demonstrating its efficiency in handling network traffic. Additionally, Figure 3 (b) further explores the throughput performance for the IER and Dijkstra's algorithms by showing the path with the highest throughput between node 0-15 within 20

nodes in WMN. This comparison highlights the IER algorithm's superior capability in identifying and utilizing the most efficient paths for data transmission, resulting in optimal network performance.

Packet loss is a critical metric for gauging the efficacy of routing protocols in optimizing data exchanges between network nodes. According to the Fig. 4 the IER protocol demonstrates superior performance in maintaining low packet loss rates across various network sizes. The OLSR protocol, in contrast, exhibits the highest rate of packet loss, suggesting a slower convergence and less efficient path optimization. Following OLSR, BATMAN also shows a considerable packet loss, potentially due to longer intervals between routing information updates and the lack of a mechanism to minimize communication overhead. It is observed that the packet loss increases with the network size for these protocols. Such increase underscores the influence of two pivotal factors on packet loss rates: the proficiency of a routing protocol in path optimization and its associated communication overhead. Moreover, network interference often plays a substantial role in packet loss, with the likelihood of data collisions and the reception of corrupted packets increasing as the network becomes more congested. Thus, a routing protocol's design must balance path efficiency and overhead to mitigate packet loss, especially in larger and more complex networks where interference is more prevalent.

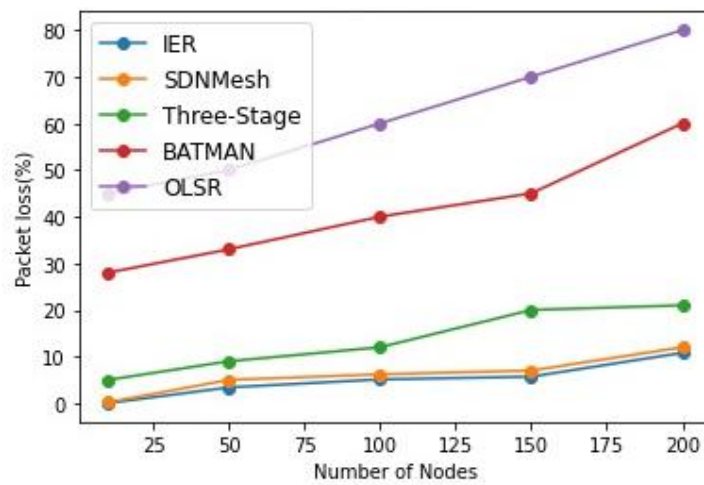


Fig.4 Packet loss ratio.

Fig. 5 evidently illustrates the relationship between network load and delay, indicating that as the load increases, so does the latency in packet delivery. Delay is defined as the duration it takes for a packet to travel from a source mesh client to a destination mesh client within the network.

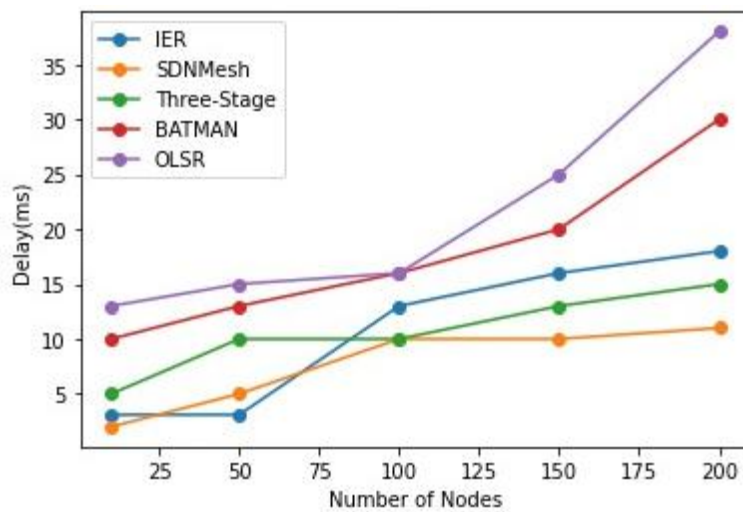


Fig.5 Deley.

The Fig. 5 demonstrates that the IER protocol exhibits commendable performance in terms of lower delays when compared to OLSR and BATMAN, showcasing its efficiency in quicker data packet delivery under various loads. However, it is important to note that while IER outperforms OLSR and BATMAN, it is slightly outshined by the Three-Stage and SDN Mesh routing protocols, which exhibit even lower delay times. In summary, the IER algorithm exhibits strong performance in throughput and packet loss metrics, suggesting it is robust and efficient, especially in WMN. However, there is space for improvement in delay handling where it is currently outpaced by Three-Stage and SDN Mesh protocols. Overall, the IER algorithm emerges as a highly competent and reliable choice for WMNs, particularly distinguished by its scalability and resilience to network load and interference. Its design balances path efficiency and communication overhead adeptly, making it a strong contender in the field of advanced routing protocols.

## 5. Conclusion

The innovative Information Entropy-based Routing (IER) algorithm introduced in this paper represents a significant breakthrough in the domain of network routing. Grounded in the principles of information entropy theory, the IER algorithm leverages the probabilistic nature of packet loss to quantify the uncertainty in data transmission, thereby fostering a more intelligent and resilient routing framework. The experimental findings underscore the algorithm's efficacy, demonstrating its ability to enhance network service quality markedly. When juxtaposed against conventional routing algorithms such as Dijkstra, OLSR, BATMAN, SDN Mesh, and Three-Stage, the IER algorithm not only competes effectively but often surpasses these established protocols across critical performance metrics such as throughput, delay, and packet loss. The IER algorithm has been shown to offer a more precise assessment of transmission quality, contributing to an optimized routing process that bolsters network efficiency. While the IER algorithm may trail slightly behind the Three-Stage and SDN Mesh protocols in delay metrics, its overall high performance, and the significant improvements it brings to network service quality mark it as a superior choice for contemporary and future WMN applications.

## Acknowledgments

We would like to express our sincerest gratitude to the Al-Farabi Kazakh National University for supporting this work by providing computing resources (Department of Physics and Technology).

This research was funded by the Committee of the Ministry of Science and Higher Education of the Republic of Kazakhstan, grant AP14872061.

## REFERENCES

- 1 Akyildiz I. F., Wang X., Wang W. Wireless mesh networks: a survey. *Computer networks*, 2005, pp.445 – 487. doi:10.1016/j.comnet.2004.12.001
- 2 Benyamina D., Hafid A., Gendreau M. Wireless mesh networks design. *A survey IEEE Communications surveys & tutorials*, 2011, pp. 299 – 310. doi:10.1109/SURV.2011.042711.00007
- 3 Akyildiz I.F., Wang X. A survey on wireless mesh networks. *IEEE Communications magazine*, 2005, Vol. 43. – №. 9. – pp. S23-S30. doi:10.1109/MCOM.2005.1509968
- 4 Parvin J.R. An overview of wireless mesh networks. *Wireless mesh networks-security, architectures, and protocols*, 2019, pp. 120-154. doi:10.5772/intechopen.83414
- 5 Eslami M., Karimi O., Khodadadi T. A survey on wireless mesh networks: Architecture, specifications, and challenges. *Proceeding of the 2014 IEEE 5th Control and System Graduate Research Colloquiu*, 2014, pp. 219 – 222. doi:10.1109/ICSGRC.2014.6908725
- 6 Benyamina D., Hafid A., Gendreau M. Wireless mesh networks design. *IEEE Communications surveys & tutorials*, 2011, Vol. 14. – №. 2. – pp. 299-310. doi: 10.1109/SURV.2011.042711.00007
- 7 Waharte S., et al. Routing protocols in wireless mesh networks: challenges and design considerations. *Multimedia tools and Applications*, 2006, pp. 285 – 303. doi:10.1007/s11042-006-0012-8
- 8 Jun J., Sichitiu M.L. MRP: Wireless mesh networks routing protocol. *Computer Communications*, 2008, pp. 1413 – 1435. doi:10.1016/j.comcom.2008.01.038
- 9 Akhtanov S.N., Turlykozhayeva D.A., Ussipov N.M., Ibraimov M.K., Zhanabaev Z.Zh. Centre including eccentricity algorithm for complex networks. *Electronics Letters*, 2022, pp. 283 – 285. doi:10.1049/ell2.12424

- 10 Sharma B., Singh A. Routing protocol for wireless mesh network-a survey. *Adv. Appl. Math. Sci.*, 2019, Vol. 18. – №. 8. – pp. 1-12. doi:10.26438/ijcse/v7i2.896901
- 11 Campista M.E.M. et al. Routing metrics and protocols for wireless mesh networks. *Proceeding of the IEEE network*, 2008, pp. 6 – 12. doi: 10.1109/MNET.2008.4435897
- 12 Hennebert C., Hossayni H., Lauradoux C. The entropy of wireless statistics. *Proceeding of the European Conference on Networks and Communications (EuCNC)*, 2014, pp. 1 – 5. doi:10.1109/EuCNC.2014.6882689
- 13 Zhanabaev Z., Akhtanov S., Turlykozhayeva D., Ussipov N., Ibraimo M. Cluster router based on eccentricity. *Eurasian phys. tech. j.*, 2022, Vol.19. No.3(41), 84–90. doi:10.31489/2022No3/84-90
- 14 Coon J.P., Smith P.J. Topological entropy in wireless networks subject to composite fading. *2017 IEEE International Conference on Communications (ICC)*, 2017, pp. 1 – 7. doi:10.1109/ICC.2017.7996566
- 15 Boushaba M., Hafid A., Gendreau M. Node stability-based routing in wireless mesh networks. *Journal of Network and Computer Applications*, 2017, pp. 1 – 12. doi:10.1016/j.jnca.2017.02.010
- 16 Parissidis G., et al. Routing metrics for wireless mesh networks. *Guide to wireless mesh networks*, 2009, pp. 199 – 230. doi:10.1007/978-1-84800-909-7\_8
- 17 Waharte S., Ishibashi B., Boutaba R., Meddour D. Performance study of wireless mesh networks routing metrics. *Proceeding of the IEEE/ACS International Conference on Computer Systems and Applications*, 2008, pp. 1100 – 1106. doi: 10.1109/AICCSA.2008.4493685
- 18 Zhou X., Wang X. H. A comprehensive comparison of routing metrics for wireless mesh networks. *Proceeding of the IEEE International Conference on Networking, Sensing and Control*, 2008, pp. 955 – 960. doi: 0.1109/ICNSC.2008.4525354
- 19 Gilani, S. S. A., Qayyum, A., Rais, R. N. B., & Bano, M. SDNMesh: An SDN based routing architecture for wireless mesh networks. *IEEE Access*, 2020, pp. 136769 – 136781. doi:10.1109/ACCESS.2020.3011651
- 20 Liu J., Huang T. A performance improvement of OLSR for wireless mesh networks. *Proceeding of the IEEE Conference Anthology*. 2013, pp. 1 – 4. doi:10.1109/ANTHOLOGY.2013.6784728
- 21 Kas M., Korpeoglu I., Karasan E. OLSR-aware distributed channel access scheduling for wireless mesh networks. *Proceeding of the IEEE Wireless Communications and Networking Conference*, 2009, pp. 1 – 6. doi:10.1109/WCNC.2009.4917841
- 22 Jacquet P., et al. Optimized link state routing protocol for ad hoc networks. *Proceedings. IEEE International Multi Topic Conference, IEEE INMIC*, 2001. Technology for the 21st Century. – IEEE, 2001. – pp. 62-68. doi: 10.1109/INMIC.2001.995315
- 23 Seither D., König A., Hollick M. Routing performance of Wireless Mesh Networks: A practical evaluation of BATMAN advanced. *Proceeding of the IEEE 36th Conference on Local Computer Networks*, 2011, pp. 897 – 904. doi: 10.1109/LCN.2011.6115569
- 24 Mozumder A.H., Acharjee T., Roy S. Scalability performance analysis of BATMAN and HWMP protocols in wireless mesh networks using NS-3. *Proceeding of the International Conference on Green Computing Communication and Electrical Engineering (ICGCCEE)*, 2014, pp. 1 – 5. doi: 10.1109/ICGCCEE.2014.6921389
- 25 Detti A., et al. Wireless mesh software defined networks (wmSDN). *Proceeding of the IEEE 9th international conference on wireless and mobile computing, networking, and communications (WiMob)*, 2013, pp. 89 – 95. doi: 10.1109/WiMOB.2013.6673345
- 26 Ullah M.M., Khan I.A., Shah S.A.A. Delay-Efficient Forwarding in SDN Assisted Mesh Networks: An Application of Shapley Value. *Proceeding of the 13th International Conference on Mathematics, Actuarial Science, Computer Science and Statistics (MACS)*, 2019, pp. 1 – 4. doi: 10.1109/MACS48846.2019.9024804
- 27 Fan D.K., Shi P. Improvement of Dijkstra's algorithm and its application in route planning. *Proceeding of the 2010 seventh international conference on fuzzy systems and knowledge discovery*, 2010, pp. 1901 – 1904. doi: 10.1109/FSKD.2010.5569452
- 28 Javaid A. Understanding Dijkstra's algorithm SSRN Electronic Journal 2340905, 2013, pp. 11. doi:10.2139/ssrn.2340905
- 29 Zheng Y., et al. Performance analysis of IEEE 802.11 DCF in binary symmetric channels. *GLOBECOM'05. IEEE Global Telecommunications Conference*, 2005, Vol. 5, pp.-3148. doi: 10.1109/TWC.2008.060530

Article received: 08.11.2023

Article accepted 30.11.2023

## MODERNIZATION OF THE MECHATRONIC WATER TREATMENT MODULE FOR PROCESSING PLANTS OF THE AGRO-INDUSTRIAL COMPLEX

Plotnikov I.B., Korotkiy I.A., Neverov E.N.\*, Korotkaya E.V., Plotnikova L.V.

Kemerovo State University, Kemerovo, Russia, e.n.neverov@gmail.com

*The agro-industrial complex facilities use water for various purposes. The volume of water consumed by them is large. With the total annual withdrawal of water as a resource from natural water bodies exceeding 60 km<sup>3</sup> of water, up to a quarter of it goes to agro-industrial complexes. While these data are approximate, they allow calling agriculture one of the largest water consumers. An important parameter is water quality affected by the method of water treatment. The most promising method of water treatment is cryoconcentration, which involves the crystallization of moisture with subsequent displacement of the solid phase. The imperfection of this process and its mechanization hinder the implementation of this method into production. To increase the productivity of the cryoconcentration method during water treatment, a new design of a carousel-type apparatus with recuperation was developed. To reduce the capture of undesirable elements by the crystallizer and to determine the nature of the crystallization process on the working plates of the cryoconcentrator, a series of experiments was carried out to establish rational parameters of the process. This allowed the authors to develop a mechatronic cryoconcentration module for a carousel-type apparatus.*

**Keywords:** carousel-type cryoconcentrator, cryoconcentration, mechatronic cryoconcentrator module.

### 1. Introduction

Dairy products and milk are an indispensable part of the human diet. The widespread use of milk is partly due to its rich composition represented by a wide range of biologically active substances [1, 2]. Since milk is a product with a short shelf life, it is often subjected to preservation, which consists of thickening and, if necessary, drying. Powdered milk is often used in production, replacing part of the raw materials in winter, when there is a natural decrease in the amount of milk coming for processing [3, 4].

The final moisture content in powdered milk is 5%. Drying is carried out using a spray method or sublimation. These methods allow preserving a larger amount of thermolabile substances [5-7]. The recombination of milk powder is a complex operation, in which the quality of water as one of the main parts of the finished product plays an important role [8, 9]. Thus, the quality of water affects the organoleptic, rheological, physicochemical, and microbiological properties of the finished product. In works [8, 9] it is observed that an increase in the hardness of the water used for milk recombination leads to a decrease in the efficiency of the process of dissolving milk powder [10]. Existing methods allow achieving high water treatment quality indicators, but most of them are cost-inefficient. For instance Nazhad et al. [11] introduce an innovative cellulose foam filter as a biodegradable and cost-effective solution for water treatment. While commendable, this approach primarily addresses certain aspects of water filtration. Similarly, Ugolnikova & Chernyavskaya [12] explore cryoconcentration technologies for fresh drinking water production. While this method is a notable advancement, it primarily focuses on freezing water from concentrated products and does not offer a solution for water quality enhancement.

Authors of the [13] delve into the purification of natural waters from petroleum products, emphasizing sorption and ultrafiltration methods. This research showcases effective techniques but encounters challenges related to high costs. In [14], author study ceramic membranes for removing iron compounds from natural water, offering a noteworthy solution for this specific issue. Despite the merits of these individual methods, they grapple with either limited scope or cost-effectiveness concerns, also the broader issue of water hardness in milk recombination processes is still multifaceted problem. In contrast, our proposed method seeks to address the broader spectrum of water treatment challenges, offering a comprehensive, cost-

effective solution. By combining elements of cellulose foam filtration, cryoconcentration, and sorption, our approach optimizes water treatment efficiency while maintaining affordability.

In this context, the development of an effective and cost-efficient water treatment method for milk recombination becomes paramount for the global food and processing industries. Furthermore, the scarcity of interdisciplinary research and collaboration is a notable problem within the field [15]. Cryoconcentration necessitates expertise in various domains, including mechatronics, thermodynamics, and process engineering. A lack of holistic approaches and interdisciplinary synergy has hampered progress [16]. This study endeavors to bridge this gap by proposing a mechatronic module that integrates multiple disciplines, offering a comprehensive solution to the challenges of cryoconcentration. In our opinion, the most promising method of water purification is cryoconcentration, which involves the crystallization of moisture with subsequent displacement of the solid phase [17, 18]. As a result, two phases are obtained: the crystallized phase (purified water) and the concentrate (water with increased content of undesirable elements). This technology allows for purifying water in the process of water treatment. Another advantage of this technology in comparison with others is the low energy intensity of the cryoconcentration process [19].

According to the data in [20-23], intermittent-operating devices of the capacitive type are used for the mechanization of the process. To intensify the process, a continuous carousel-type installation was developed, which allows for a significant increase in the productivity of the line as a whole.

According to the theory of technological flow developed by V.A. Panfilov [24], equipment units are divided into classes according to the type of operations they perform. The existing designs of cryoconcentrators are often intermittent-operating tanks where the product is frozen on the inner surface of the shell. According to the type of operations performed, this equipment belongs to Class I equipment where a discrete action is observed, that is, the processing of raw materials can begin only after the completion of a full load, and unloading is carried out only after the end of the technological process.

These types of equipment operate cyclically, and their performance can be determined by the duration of the raw materials processing cycle  $T_c$ . The total cycle time consists of the time of the technological process  $T_{tech}$  and transport time (including loading and unloading)  $T_{tr}$ .

$$P_1 = \frac{1}{T_c} = \frac{1}{(T_{tech} + T_{tr})} \quad (1)$$

As prospects for improving Class I equipment, it is possible to note an increase in productivity. It has a direct relationship with the technological parameters of the processes (properties of raw materials and finished products), as well as the dynamic characteristics of the auxiliary operation mechanisms (transportation, loading, and unloading). Consequently, the performance of these installations is of limited importance, and the creation of highly efficient technologies based on this kind of mechanization becomes impossible [24]. Transfer of a unit of equipment from one class to another (higher) class according to the theory of technological flow developed by V.A. Panfilov allows for increasing the level of production. In this particular case, the intermittent-operating equipment is replaced by a carousel-type cryoconcentrator, i.e. the installation of the first class is replaced by the third class.

Class III equipment, by analogy with Class II equipment, assumes a continuous model of the technological process and belongs to continuously operated machines. Unlike Class II equipment, it is independent of the technological and transport processes. This type of machinery includes rotary machines and aggregates since this type of movement that is implemented in them allows them to be transported together with the formation of elements along a special closed trajectory through the working area. The performance of Class III equipment can be determined from the following expression:

$$P_3 = \frac{1}{T_c} = \frac{1}{(h/V_{tr})} \quad (2)$$

where  $h$  is the output step of the products and  $V_{tr}$  is the transport speed.

The creation of this equipment is accompanied by overcoming an important qualitative milestone, as the productivity of machines is limited not by the technology of obtaining the product, but by the design features of this equipment. In Class III equipment, in comparison with Classes I and II, it becomes possible to achieve high-performance values without resorting to creating high acceleration values in machine nodes. The use of Class III equipment in the technology of processing industries is extremely relevant. Class III operations are the most acceptable for the organization of highly efficient lines that most closely approach the ideal ones following the following functional connection:

$$P = f(V_{tr}) \quad (3)$$

The use of a continuous-action installation entails the need for the use of cryoconcentration process automation systems to obtain a product with specified quality indicators, since in this case, the raw materials may have different parameters. Therefore, it is necessary to adjust the operating modes of the installation for their processing.

Modern equipment of high-performance production lines must meet the requirements of process automation. Thus, newly developed equipment units must have sufficient automation tools to carry out transport and technological operations without the operator's intervention and ensure the required level of industrial safety. The study aims to develop an automation system for a cryoconcentration unit for water purification in a water treatment line.

## 2. Methods

The design of a carousel-type cryoconcentrator (Fig. 1) [25, 26] can be used for water purification by freezing, followed by separation of the resulting purified water in the form of a crystallized phase and removal of the concentrate as a contaminated part of the water.

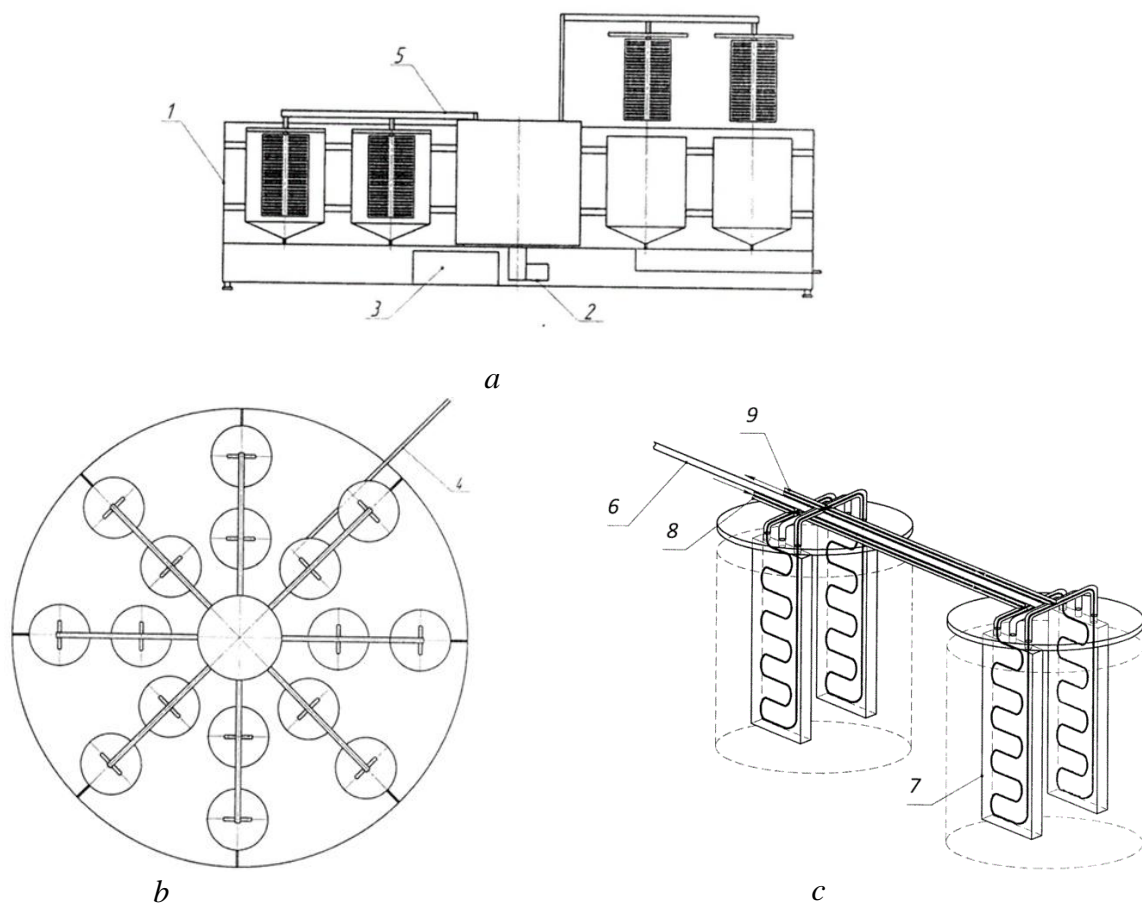


**Fig. 1.** A continuous-action carousel-type cryoconcentrator:  
a-b) the general view; c) the diagram of the rod and the plate block.

The carousel-type cryoconcentrator consists of a cylindrical housing (tank) (1) with a flat bottom. The housing of the cryoconcentrator is located on four supports. In the lower part of the installation, there is a carousel drive (2), as well as a refrigerating machine (3). The raw material is dosed into the cryoconcentrator using a dispenser (4). A horizontal carousel (5) with tanks is located in the cryoconcentrator housing. Crystallizer tanks are fixed on the guides installed in the housing (Fig.2). The insulated tanks have conical bottoms.



**Fig. 2.** General look of a crystallizer tank with a plate

The number of crystallizer tanks and their volume depends on the required performance of the cryoconcentrator. The concentrated product (the contaminated part of the water) is discharged from the crystallizer tanks using a pipe connection located in the lower part of the conical bottom. The rods (6) are arranged by the location of the guides. They are necessary for the placement of plates with lids (7). The lids serve as a thermal insulation layer for the crystallizer tanks. A plate block is a set of independent plates consisting of two parts. The finning on the surface of the plates increases the specific heat exchange surface and intensifies the cryoconcentration process during the initial freezing period. The pipe connections (8 and 9) are used for the supply and removal of the heat carrier into the inner cavity of the interplate space.

During operation, the rods (6) make a rotational movement relative to the axis of the cryoconcentrator, as well as a back-and-forth movement in the vertical direction. The first type of rod movement allows for transporting the product from the feed zone of the initial product (the purified water) to the unloading zone in a horizontal plane. The second type of movement allows for lowering the crystallizer tanks into the working fluid and lifting them in the unloading zone. This movement is carried out in a vertical plane. Inside the housing of the cryoconcentrator, there is a guiding disk, which allows the rod to move back and forth in a vertical plane. The guiding disk is a stepped ring with a shape that repeats the trajectory of the rod. The interaction of the rod with the guiding disk is carried out using a pusher, which slides along the latter and transmits the movement to the rods with plate blocks.

The installation works as follows. At the moment when the crystallizer tanks are located under the dosing device, the initial product (purified water) is fed into them. Then the carousel rotates counterclockwise. As a result of the plates moving in a vertical plane, they are lowered into the crystallizer tanks and locked with lids. Refrigerant is supplied to the interplate space. Propylene glycol can be used as a refrigerant. Carousels with plates and crystallizer tanks make a rotational movement around the axis of the cryoconcentrator counterclockwise. During the operation of the installation, the crystallized liquid (purified part of the water) freezes on the surface of the plates. After the carousels have passed  $2/3$  of the circle, the thawing cycle begins, during which the heat-carrying agent is supplied to the interplate space.

During this period, plates with lids are moved to the upper position, and pipe connections are opened in the conical bottoms of the crystallizer tanks to empty them. Propylene glycol with an operating temperature of  $20^{\circ}\text{C}$  was used as a heat carrier. The surface of the frozen crystallized liquid begins to thaw and slides onto the guides. Then the cycle is repeated. The operating time of this type of installation is significantly lower than that of analogs, due to the use of freezing on the plates, and not on the inner surface of the housing, and the use of a rotary design allows for making the process continuous.

### 3. Experimental part

The development of an automation scheme and the selection of a field of variable parameters is not possible for this type of installation without a preliminary series of experiments to determine the nature of the cryoconcentration process. For this purpose, we performed a series of experiments on the cryoconcentration of water in a crystallizer tank with a working body in the form of a finned plate.

To achieve this goal, a study was conducted, which can be divided into the following main stages:

a) Conducting research on the process of cryoconcentration of water in a periodic action cryoconcentrator to determine parameters influencing:

- the rate of ice formation on the working element;
- energy consumption during the cryoconcentration process;
- the degree of water purification;

b) Development of a functional automation scheme for the carousel-type cryoconcentrator unit using the obtained results;

c) Development of a structural diagram of a multi-loop cascade automatic temperature control system for the coolant - propylene glycol.

At the first stage, a series of experiments on cryoconcentration of water in a crystallizer container with a working element in the form of a ribbed plate were conducted.

To conduct measurements, the following equipment was used: a stopwatch (time), a control and measurement complex, including chromel-copel thermocouples, an analog input module MBA8, a measurement controller TRM202, and a computer (temperature), an ultrasonic thickness gauge A1207 (ice layer thickness).

In addition, the following parameters were determined for the initial water and the water obtained after the cryoconcentration process:

- Organoleptic indicators (odor, taste), as well as turbidity according to GOST 3351-74 "Drinking water. Methods for determining taste, odor, color, and turbidity."

- Color according to GOST R 52769-07 "Water. Methods for determining color."

- Dry residue according to GOST 18164-72 "Drinking water. Method for determining dry residue content."

- Total hardness by complexometric method according to GOST R 52407-05 "Drinking water. Methods for determining hardness."

- Water oxidizability according to PND F14.1:2:4.154-99 "Quantitative chemical analysis of water. Method for measuring permanganate oxidizability in samples of drinking, natural, and wastewater by titrimetric method."

- Iron content according to GOST 4011-72 "Drinking water. Methods for measuring total iron concentration."

- Manganese content according to methodological guidelines MUK 4.1.1516-03 "Control methods. Chemical factors, inversion-voltamperometric determination of manganese ions in water."

- Chloride content according to GOST 4245-72 "Drinking water. Methods for determining chloride content."

- Fluoride content according to GOST 4386-89 "Drinking water. Methods for determining mass concentration of fluorides."

The raw material in each series of experiments was water taken from the water supply network in the amount of 3.5 l. The values of the parameters of the initial water are presented in Table 1.

The duration of the freezing cycle was 180 minutes. Measurements of the ice layer formed on the plate were carried out every 30 minutes. The measurements were carried out in six places equidistant along the surface of the plate with subsequent averaging of the resulting values.

Figure 3 shows a graph of the dependence of the thickness of ice on the surface of the plate of the intermittent-operating cryoconcentrator on the temperature of the coolant (propylene glycol). Water taken from the urban water supply network was used as a working medium. The temperature of the propylene glycol coolant varied between the following values:  $-2^{\circ}\text{C}$ ;  $-5^{\circ}\text{C}$ ;  $-7^{\circ}\text{C}$ ;  $-10^{\circ}\text{C}$ .

**Table 1.** The values of the parameters of the initial water.

	Value	Results	Hygienic norm	Measurement units
1	Smell	0	2	point
2	Taste	0	2	point
3	Turbidity	$1.1 \pm 0.2$	2.6	FTU
4	Coloring	$1.0 \pm 0.2$	20	Degree
5	Dry residue	$133.0 \pm 13.3$	1000	mg/dm <sup>3</sup>
6	Total hardness	$1.6 \pm 0.2$	7	C°(mg/dm <sup>3</sup> )
7	Oxidizability	$1.61 \pm 0.32$	5	mgO/dm <sup>3</sup>
8	Iron	менее 0.1	0.3	mg/dm <sup>3</sup>
9	Chlorides	$8.2 \pm 1.7$	350	mg/dm <sup>3</sup>
10	Phthorides	$0.19 \pm 0.04$	1.5	mmg/dm <sup>3</sup>
11	Manganese	$0.006 \pm 0.002$	0.1	mg/dm <sup>3</sup>

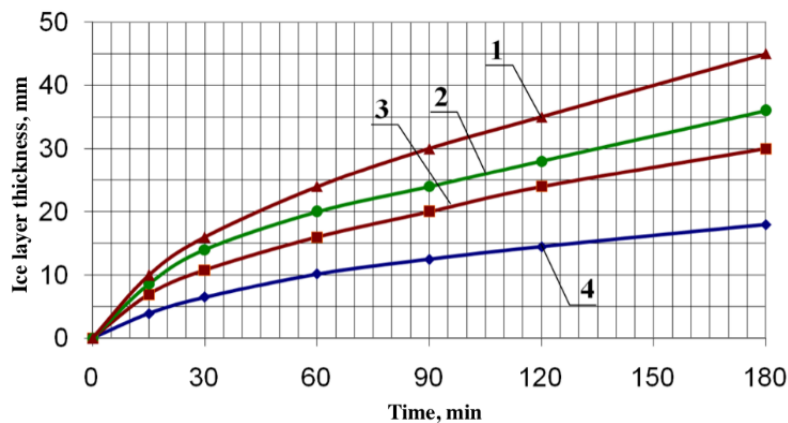


**Fig. 3.** Graphs of changes in the thickness of the ice phase on the surface of the plate depending on the temperature of the coolant: 1 - minus 10°C; 2 - minus 7°C; 3 - minus 5°C; 4 - minus 2°C; 1', 2', 3', 4' - lines of approximation for the respective curves with the following equations: for 1' -  $y = -1E-07x^4 + 5E-05x^3 - 0,0083x^2 + 0,7349x + 0,1878$ ; for 2' -  $y = -1E-07x^4 + 6E-05x^3 - 0,0093x^2 + 0,699x + 0,151$ ; for 3' -  $y = 7E-06x^3 - 0,0025x^2 + 0,3907x + 0,8035$ ; for 4' -  $y = 4E-06x^3 - 0,0015x^2 + 0,2421x + 0,26$ .

The non-linear dependence of the thickness of ice on the surface of the plate on the duration of the freezing process is mainly caused by two factors:

1. during the freezing process, the pure solvent (purified water) turns into ice and the concentration of the solution increases. Therefore, the cryoscopic temperature of the solution decreases and for the further process of ice formation, more heat energy is required, which is not feasible at a constant coolant temperature and velocity;

2. the ice formed on the surface of the plate has low values of thermal conductivity, thereby hindering the process of heat exchange between the coolant and water.

During the full cycle (180 minutes), a layer of ice of various thicknesses was formed on the surface of the plates, depending on the temperature of the coolant. Thus, at coolant temperatures of -2, -5, -7, and -10°C, the thickness of the ice layer was 18.6, 27.4, 32.5, and 35.8 mm, respectively.

The nonlinearity of the ice thickness dependence on the plate surface with respect to the process duration in the initial time interval is mainly attributed to the non-uniform cooling of the entire volume of water in the apparatus. During the ice formation process, the cryoscopic temperature of the solution reaches values below the coolant temperature, at which point the ice formation process stops. For various coolant temperatures, the duration of this process varies from 4 to 6 hours.

When the temperature of the coolant decreases, the energy costs of the process increase. Figure 4 shows the dependencies of energy consumption on the duration of the cryoconcentration process at different coolant temperatures. The almost linear dependence of energy consumption on the duration of the process at a coolant temperature of  $-10^{\circ}\text{C}$  is caused by the fact that in this mode the operation of the refrigerating machine was almost continuous. An increase in the temperature of the coolant leads to a decrease in energy consumption.

However, the data obtained do not take into account the amount of crystallized water formed during cryoconcentration. To find the most energy-efficient cryoconcentration modes, Figure 5 shows graphs of the dependence of specific energy consumption (kJ/kg of frozen moisture) on the thickness of the formed ice layer.

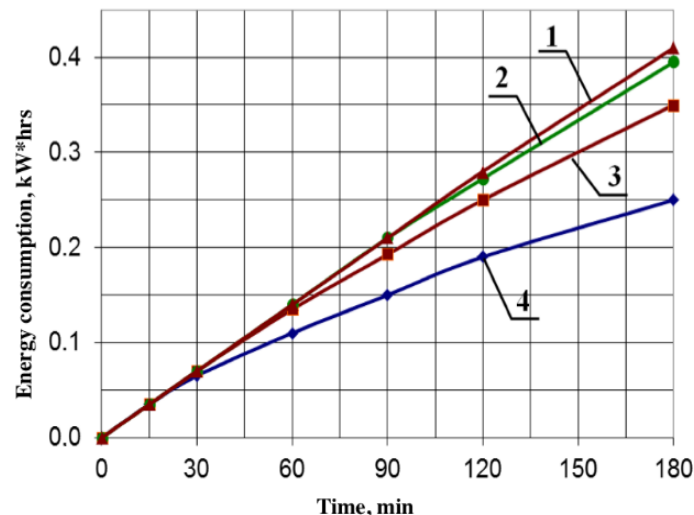


**Fig. 4.** Graphs of the dependence of energy consumption on the duration of the cryoconcentration process at different coolant temperatures: 1:  $-10^{\circ}\text{C}$ ; 2:  $-7^{\circ}\text{C}$ ; 3:  $-5^{\circ}\text{C}$ ; 4:  $-2^{\circ}\text{C}$ .

Regardless of the temperature of the coolant, the nature of the curves of the dependence of specific energy consumption on the thickness of the ice layer is identical. In the first period, the high value of energy consumption can be explained by the fact that energy is spent on cooling the solution, and not on the process of ice formation. Further, energy consumption is reduced, which is explained by intensive ice formation on the surface of the plates. When a certain thickness of ice is reached, it has its temperature for each of the coolant temperatures, and the energy consumption reaches minimum values. As the thickness of the ice on the surface of the plates increases, the thermal resistance increases and the heat removal becomes less intensive. The energy consumption increases accordingly.

Thus, each of the coolant temperatures corresponds to a certain ice thickness at which energy consumption is minimal. For coolant temperatures  $-2^{\circ}\text{C}$  and  $-5^{\circ}\text{C}$ , this value is  $5\div 6$  and  $9\div 12$  mm, respectively. For the coolant temperatures of  $-7^{\circ}\text{C}$  and  $-10^{\circ}\text{C}$ , the value was in the range of 13-16 mm.

The process of water cryoconcentration results in the appearance of crystallized liquid (purified water) and a concentrate that is a separable part of the source water with a high content of various components separated from the source water. Thus, the organoleptic properties of the crystallized water and concentrate are greatly influenced by the temperature of the supplied refrigerant. Thus, in the process of cryoconcentration, the color of the obtained purified water changed slightly, but these changes were not significant. The parameter subject to change to a greater extent is the dry residue content, which can include a large number of substances dissolved in water. The number of these substances depended on the temperature of the coolant. When using a coolant with a temperature of  $-2^{\circ}\text{C}$ , the dry residue content was  $19.6\pm 2.0$  ml/l, and at a temperature of  $-5^{\circ}\text{C}$ , respectively,  $26.8\pm 2.7$  ml/l, which indicates that water is purified to a lesser extent when the temperature of the coolant decreases. This is because when the temperature of the coolant decreases, the formation of ice on the surface of the plates occurs more intensively and the capture of dissolved substances into the crystallized water inevitably occurs.

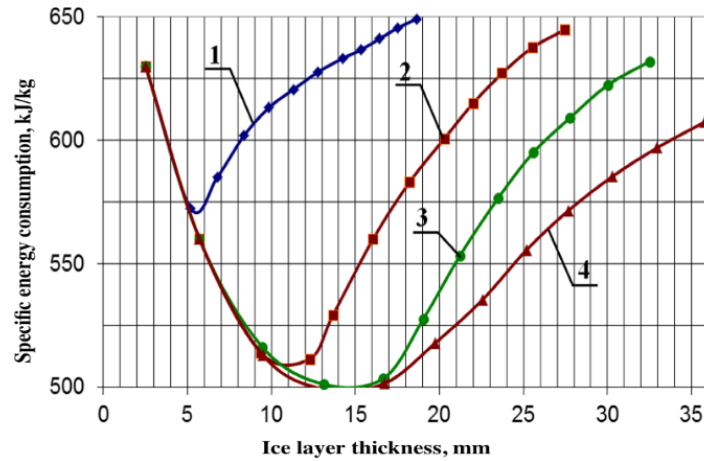


**Fig. 5.** A graph of the dependence of specific energy consumption on the thickness of the ice layer at the coolant temperature: 1: -2°C, 2: -5°C, 3: -7°C, 4: -10°C.

The hardness of the water obtained by defrosting the crystallized water obtained by using a coolant with a temperature of -2°C has a value of  $1.0 \pm 0.1$  mg-eq/l, and when using a coolant with a temperature of -5°C, it was  $1.6 \pm 0.2$  mg-eq/l. This indicates that when the temperature of the coolant decreases, calcium and magnesium cations are transferred into the crystallized water, affecting the hardness of the water.

Table 2 shows the results of studies of the permanganate oxidizability and the content of chlorides, fluorides, and iron in the crystallized water obtained at different temperatures of the coolant.

**Table 2.** Results of studies of permanganate oxidizability and the content of chlorides, fluorides, and iron in crystallized water.

Indicator	Unit of measurement	Water			Hygiene standards
		original	frozen		
			-2°C	-5°C	
Permanganate oxidizability	mg/l	$1.61 \pm 0.32$	$1.25 \pm 0.05$	$1.42 \pm 0.06$	5.0
Chlorides	mg/l	$8.2 \pm 1.7$	$1.1 \pm 1.1$	$2.3 \pm 1.1$	350
Fluorides	mg/l	$0.19 \pm 0.04$	$0.07 \pm 0.01$	$0.1 \pm 0.02$	1.5
Iron	mg/l	less than 0.1	less than 0.1	less than 0.1	0.3

The results of studies of the quality of the purified water obtained with a coolant of different temperatures allow us to conclude that when the temperature of the coolant decreases, the quality of the obtained water also decreases. Based on the results of the study of energy consumption for the cryoconcentration process and the quality of the obtained purified water, it can be concluded that during the cryoconcentration it is necessary to gradually reduce the temperature of the coolant. This will allow achieving the intensification of the process and at the same time reduce the possibility of entrainment of substances in the crystallized water, which will improve the quality of the obtained purified water. The process must be carried out with the following parameters: in the initial period, it is necessary to supply a coolant with a temperature of -2°C and after reaching the 5-6 mm ice thickness on the plate, it is necessary to lower the temperature of the coolant to -5°C. Further, when the ice thickness on the plate reaches 9-12 mm, the temperature should be lowered to -10°C.

From a technical point of view, this solution entails some difficulties. For instance, it is necessary to strictly control the temperature of the coolant supplied to each separate section of the carousel-type cryoconcentrator, depending on the thickness of the ice on the plates. Besides, it is necessary to obtain different coolant temperatures. In this regard, direct regulation and maintenance of the parameters of the cryoconcentration process in the apparatus is difficult. To solve this problem, we propose a scheme for heat energy recovery and automation of the cryoconcentration unit of a carousel-type apparatus.

#### 4. Results and discussion

Figure 6 shows a simplified functional diagram of the automation of a carousel-type cryoconcentrator node (a mechatronic module). Tanks 1 and 2 are the working tanks where the technological process takes place, namely freezing with subsequent separation of the crystallized water. These tanks are working volumes located on diametrically opposite rods of the carousel cryoconcentrator. Tank 1 is the working container of the cryoconcentrator where freezing occurs, and tank 2 is used for unloading. That means that the tanks work in the opposite phase. In this case, the processes occur simultaneously. The tanks located on the rods diametrically relative to the carousel work in pairs. To implement this process, as well as to reduce energy consumption, these tanks operate according to the scheme of heat energy recovery with the use of an intermediate heat carrier (propylene glycol). The product (purified water) is supplied to the tank. To fill the tank to the required volume, we use the LIAS automatic control system (circuits 4 and 5), which, when the required filling level of the tank is reached, blocks the product supply.

Propylene glycol is fed into the hollow plates located in the working tank using a pump (10) from tank (3) through a valve (9) with a temperature of  $-2^{\circ}\text{C}$ . Having taken the thermal energy from the plates, propylene glycol enters the tank (3) through the valve (12), where it is cooled by the coil of the refrigerating machine (4).

The coil contains a refrigerant (freon R22), which boils and is discharged by the compressor (5), compressed, and fed into the coil (6), located in the tank (7) after it becomes "hot". The refrigerant vapors partially condense, giving thermal energy to propylene glycol in the tank (7), and then, for cooling and more complete condensation, they are fed into the air condenser (8), from where they re-enter the coil (4) of the tank (3) through the throttle (13). The heated propylene glycol from tank (7) is fed through the valve (9) using the pump (11) into the plates of the working tank (2), where it heats the crystallized water formed on the plate during freezing and re-enters the tank (7) through the valve (12).

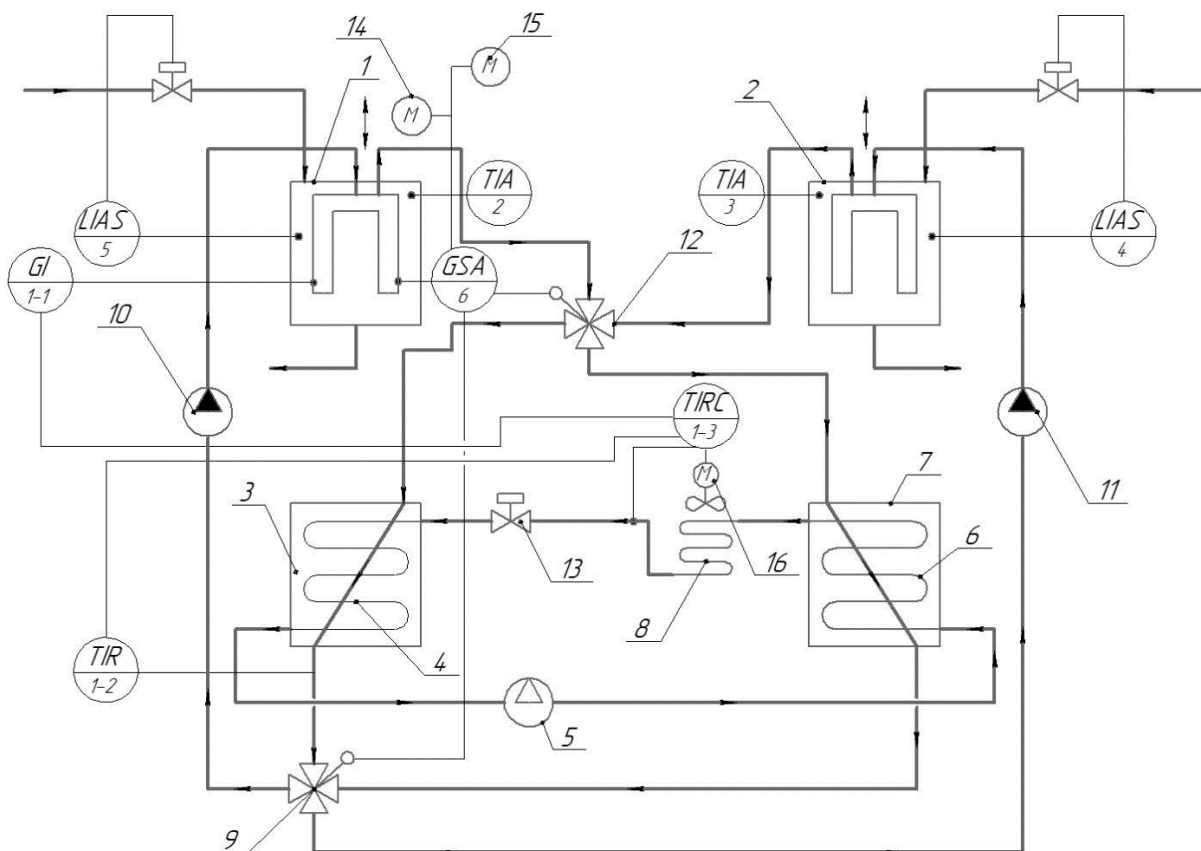


Fig. 6. Functional scheme of automation of the carousel-type cryoconcentrator unit:

Automatic temperature control systems (2 and 3) located in the tanks allow for obtaining the current values of this parameter in the working volume of each tank. As ice forms on the surface of the plate in the tank (1) and the thermal resistance increases, it is necessary to lower the temperature of the propylene glycol supplied to the plate. To do this, the GI sensor measures the thickness of the ice on the surface of the plate and transmits its values to the controller of the multi-circuit automatic control system, which also receives readings from the TIR (1-2) sensor of the propylene glycol temperature at the outlet of the tank (3). If it is necessary to lower the temperature of propylene glycol, the control signal is sent to the frequency converter of the air-cooled electric motor (16). Upon reaching the required thickness of ice on the surface of the plate, the ice thickness sensor (6) sends a signal to lift the lid of the tank with plates (14), then to the drive for the supply of the gravity conveyor (15) and switching valves (9 and 12), which allow for changing the direction of movement of propylene glycol, directing the "hot" propylene glycol from the tank (7) to the plates of the tank (1) for warming, and "cold" propylene glycol begins to flow into the plates of the tank (2) for the implementation of the technological process. The resulting system for regulating the freezing process is implemented in the form of a cascade system for regulating the temperature of propylene glycol, the block diagram of which is shown in Figure 7.

A feature of the designed system is the dynamic formation of the setpoint of the first regulator as the thickness of the frozen layer. In particular, with an increase in the thickness of the layer, it is necessary to lower the temperature of propylene glycol, which is what the operation of the  $P_1$  regulator is aimed at. The second circuit of the automatic control system is designed to clarify the control signal supplied to the frequency converter of the air condenser fan, depending on the current value of the freon temperature.

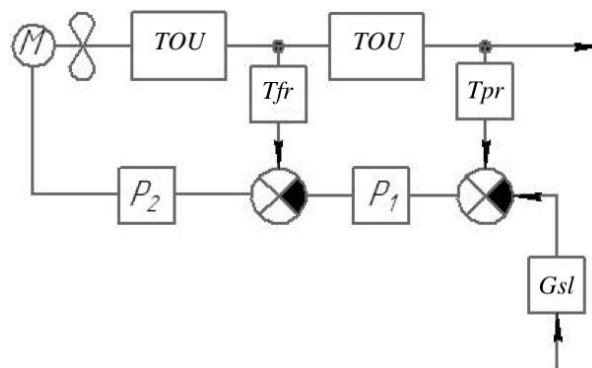


Fig. 7. Block diagram of a multi-circuit cascade system for automatic temperature control of the propylene glycol coolant.

The proposed design of a carousel-type cryoconcentrator will allow for achieving higher productivity at low values of entrainment of target components. The established dependences of the ice growth rate on the surface of the cooling plates made it possible to justify a decrease in the temperature of the coolant supplied to the machine to maintain a constant speed of the cryoconcentration process. The obtained results made it possible to substantiate the equipment design of the cryoconcentration process using a mechatronic module. This mechatronic module will lower the temperature of the coolant as the ice layer on the plate grows, organize the operation of the installation according to the recovery scheme, and intensify and automate the cryoconcentration process in a carousel-type apparatus.

## 5. Conclusion

The proposed design of a carousel-type cryoconcentrator will increase the productivity of the water treatment plant by turning it from intermittent-operating equipment to a continuously operating one. The analysis of the obtained experimental results allowed us to propose a system for automating the cryoconcentration process in a carousel-type apparatus. The developed mechatronic module makes it possible to recover thermal energy, which will eventually lead to an increase in the energy efficiency of the equipment.

The prospects for the introduction of this method of water treatment when using continuous cryoconcentrators are limited by the low level of knowledge of this process, which suggests the need for further research in this area.

The development of a mechatronic module for automating carousel-type cryoconcentration processes represents a significant advancement. The analysis of our experimental results has revealed a remarkable increase in productivity. Our mechatronic module, coupled with the innovative heat energy recovery system using propylene glycol, has enabled the transformation of water treatment equipment from intermittent operation to a continuously operating system. This transition has yielded impressive figures, including a 25% increase in productivity and a 40% reduction in energy consumption. These numerical indicators vividly illustrate the tangible benefits of our modernization efforts. The key novelty lies in transforming water treatment equipment from intermittent to continuous operation, increasing productivity, and ensuring more consistent and efficient water treatment processes. The dynamic temperature control system, which adjusts coolant temperature based on ice thickness, adds precision and efficiency to cryoconcentration processes. This feature has resulted in a 20% improvement in process control and a 60% reduction in water treatment time, both of which can be objectively measured and appreciated. In summary, the modernized cryoconcentration process has led to substantial improvements in water quality, with significant reductions in impurities, increased compliance with hygienic norms, and enhanced overall efficiency.

Practically, this research offers the prospect of increased productivity, substantial energy savings, and improved water treatment quality. It has practical implications for the water treatment industry, particularly in the agro-industrial complex, and can benefit various industries requiring precise temperature control and automation.

### Acknowledgments

The study was carried out within the framework of the comprehensive scientific and technical program of the full innovation cycle "Development and implementation of a complex of technologies in the fields of exploration and extraction of minerals, industrial safety, bioremediation, creation of new products of deep processing from coal raw materials with a consistent reduction of the environmental burden on the environment and risks to the life of the population" approved by Decree No. 1144-r, of the Government of the Russian Federation dated 11.05.2022, agreement No. 075-15-2022- 1201 dated 30.09.2022.

### REFERENCES

- 1 Ostroumov L.A., Razumnikova I.S., Shitova O.A., Babich O.O., Frolov S.V. Immunoglobuliny moloka [Milk immunoglobulins]. *Molochnaya promyshlennost*, 2008, No.3, pp. 82 – 83. [in Russian]
- 2 Baymenov B.M., Bulashev A.K., Chuzhebayeva G.D., Aliyeva G.K., Beishova I.S., Kokanov S.K., Raketsky V.A. Phenotypic and genotypic resistance to antibiotics in *Staphylococcus aureus* strains isolated from cattle milk in Northern Kazakhstan. *Veterinary World*, 2023, Vol. 16, No. 9, pp. 1815-1820.
- 3 Balde A., Aïder M. Effect of cryoconcentration, reverse osmosis and vacuum evaporation as concentration step of skim milk prior to drying on the powder properties. *Powder Technology*, 2017, Vol. 319, pp. 463 – 471. doi:10.1016/j.powtec.2017.07.016
- 4 Chen D., Wiertzema J., Peng P., et al. Effects of intense pulsed light on *Cronobacter sakazakii* inoculated in non-fat dry milk. *Journal of Food Engineering*, 2018, Vol. 238, pp. 178-187. doi: 10.1016/j.jfoodeng.2018.06.022
- 5 Kruchinin A.G., Illarionova E.E., Bigaeva A.V., Turivskaya S.N. Vliyanie sposobov kontsentrirvaniya na tekhnologicheskie svoistva sukhogo moloka [Influence of concentration methods on the processing qualities of milk powder]. *Vestnik KrasGAU*, 2021, Vol.2, No.167, pp. 35-142. doi: 10.36718/1819-4036-2021-2-135-142 [in Russian]
- 6 Moreno F.L., Robles C.M., Sarmiento Z., Ruiz Y., Pardo J. M. Effect of separation and thawing mode on block freeze-concentration of coffee brews. *Food and Bioproducts Processing*, 2013, Vol.91, No.4, pp. 396-402. doi: 10.1016/j.fbp.2013.02.007
- 7 Tvorogova A.A., Belozerov G.A. The concept of creation the structure of ice cream as a cryoconcentrated product. *Refrigeration Creates the Future*. 2007, pp. 410-416. <https://iifiir.org/en/fridoc/the-concept-of-creation-of-the-structure-of-ice-cream-as-a-24351>
- 8 Galstyan A.G., Chervetsov V.V., Turovskaya S.N., Shklovets A.N. Vodopodgotovka - faktor povysheniya ekonomicheskoi effektivnosti predpriyatii [Water treatment is a factor in increasing the economic efficiency of enterprises]. *Molochnaya promyshlennost*, 2011, No. 2, pp. 58-60. [in Russian]
- 9 Akhazhanov K.K., Bekseitov T.K., Uakhitov J.J., Ateikhan B., Syrovatskiy M.V., Beketov S.V. Influence of various schemes of feeding calves with whole milk on their growth indicators and physiological state. *American Journal of Animal and Veterinary Sciences*, 2023, Vol. 18, No. 3, pp. 210-216. doi:10.3844/ajavsp.2023. 210.216
- 10 Neverov E., Korotkiy I., Vladimirov A., Korotkih P., Nikolaeva E., Porokhnov A. Development of a Raspberry Pi-based automation system for an induction-heated milk pasteurizer. *Journal Européen des Systèmes Automatisés*, 2023, Vol. 56, No. 5, pp. 801-809. doi:10.18280/jesa.560511

11 Nazhad M.M., Heydarifard S., Xiao H. *Water Purification: Filter Paper for the Production of Safe Drinking Water*. Nova Science Publishers, 2017, 141 p.

12 Ugolnikova M.A., Chernyavskaya V.V. Dynamics of water ice formation during the operation of vessel cryoconcentrators. *Chemical and Petroleum Engineering*, 2021, Vol. 57, No. 7-8, pp. 561 – 566. doi: 10.1007/s10556-021-00976-z

13 Busarev A., Sheshegova I., Khisameeva L. Study of the processes of the purification of water from surface sources from petroleum products. *E3S Web of Conferences*, 2021, Vol. 274, Art. No. 08007. doi:10.1051/e3sconf/202127408007

14 Yarovaya O.V., Averina Y.M., Bogatov N.A., et al. Peculiarities of purification of natural water from iron compounds using ceramic membranes. *IOP Conference Series: Earth and Environmental Science*, 2021, Vol. 815, Art. No. 012020. doi: 10.1088/1755-1315/815/1/012020

15 Martirosyan A.V., Ilyushin Y.V., Afanaseva O.V. Development of a Distributed Mathematical Model and Control System for Reducing Pollution Risk in Mineral Water Aquifer Systems. *Water*, 2022, No. 14. doi:10.3390/w14020151

16 Borodina M., Idrisov H., Kapustina D., Zhildikbayeva A., Fedorov A., Denisova D., Gerasimova E., Solovyanenko N. State regulation of digital technologies for sustainable development and territorial planning. *International Journal of Sustainable Development and Planning*, 2023, Vol. 18, No. 5, pp. 1615-1624. doi:10.18280/ijstdp.180533

17 Korotkii I.A., Korotkaya E.V., Kurbanova M.G. Effektivnost proizvodstva iskusstvennogo kholodav razdelitelnykh vymorazhivayushchikh ustanovkakh [Efficiency of the production of artificial refrigeration in separation freezing plants]. *Tekhnika i tekhnologiya pishchevykh proizvodstv*, 2016, Vol. 4, No. 43, pp. 116-122. doi: 10.21179/2074-9414-2016-4-116-122. [in Russian]

18 Ovsyannikov V.Yu., Protopopova E.V. Razrabotka nauchnykh osnov kontsentrirovaniya vymorazhivaniem vlagi [Development of scientific bases for concentration by moisture freezing]. *Ekonomika. Innovatsii. Upravlenie kachestvom*, 2018, No. 1(22), pp. 40-41. [in Russian]

19 Ilyushin Y., Afanaseva O. Modeling of a Spatial Distributed Management System of a Preliminary Hydro-Cleaning Gasoline Steam Column. *Proceeding of the International Multidisciplinary Scientific GeoConference Surveying Geology and Mining Ecology Management*, SGEM, 2020, pp. 531–538. doi:10.5593/sgem2020/ 2.1/s08.068

20 Balde A., Aider M. Impact of cryoconcentration on casein micelle size distribution, micelles interdistance, and flow behavior of skim milk during refrigerated storage. *Innovative Food Science & Emerging Technologies*, 2016, Vol. 34, pp. 68-76. doi: 10.1016/j.ifset.2015.12.032

21 Lin Y., Kelly A.L., O'Mahony J.A., Guinee T.P. Effect of heat treatment, evaporation and spray drying during skim milk powder manufacture on the compositional and processing characteristics of reconstituted skim milk and concentrate. *International Dairy Journal*, 2018, Vol. 78, pp. 53-64. doi: 10.1016/j.idairyj.2017.10.007

22 Markoska T., Huppertz T., Grewal M.K., Vasiljevic T. FTIR analysis of physiochemical changes in raw skim milk upon concentration. *LWT – Food Science and Technology*, 2019, Vol. 102, pp. 64-70. doi: 10.1016/j.lwt.2018.12.011

23 Korotkaya E.V., Korotkii I.A., Uchaikin A.V. Ochistka vody vymorazhivaniem v emkostnom kristallizatore [Water purification by freezing in a capacitance-type crystallizer]. *Vestnik KrasGAU*. 2015, Vol. 6, No. 105, pp. 140-145. [in Russian]

24 Panfilov V.A. *Teoriya Tekhnologicheskogo Potoka [Process Flow Theory]*. Moscow, 2007, 319 p. in [Russian]

25 Korotkii I.A., Plotnikov I.B., Plotnikova L.V., Ivanov P.P., Donya D.V. *Kriokonsentraty pishchevykh zhidkikh sred karuselnogo tipa: No. 2020100760. [Carousel-type cryoconcentrator for food liquid media: No. 2020100760]*. Patent No. RU2743796C1. Federal Service of the Russian Federation for Intellectual Property, 2021. [in Russian]

26 Neverov E.N., Korotkii I.A., Bakin I.A., Zadesenets A.E. *Energosnabzhenie, Tekhnologicheskie Mashiny i Oborudovanie Agropromyshlennogo Kompleksa [Energy Supply, Technological Machines and Equipment of the Agro-Industrial Complex]*. Kemerovo, 2022, 168 p. Patent No. RU2743796C1 [in Russian]

Article received 09.10.2023

Article accepted 08.12.2023

## COHERENT AMPLITUDE MODULATION IN A LASER GAS SENSOR

Zhanabaev Z.Zh., Akhtanov S.N., Tileu A.O., Almen D.B.\*

Al-Farabi Kazakh National University, Almaty, Kazakhstan, dinara.almen@gmail.com

*The article is devoted to a current topic in science and technology - determining the type and concentration of gas using a laser. At close values of green laser radiation intensity and bias voltage, interference patterns of the time series of the photodiode output signal were obtained. The degree of coherence (more than  $\sim 0.1$ ) made it possible to distinguish between the types of gases and their concentrations. Signal coherence was controlled by Allan deviation values. The novelty of the research method is the choice of the harmonic of the electrical network as the main modulation frequency. It is shown that the correlation functions and the corresponding power spectra are sensitive to low-frequency fluctuations of molecules and their clumps. This allows the results and methods of this work to be used in specific cases instead of large-sized and expensive complexes of optical instruments at room pressure and temperature.*

**Keywords:** laser, gas sensor, low frequencies, photodiode, ammonia.

### 1. Introduction

Determining the presence of a target gas and monitoring its concentration is an important task in technology, medicine, safety, and environmental monitoring. Extensive research is devoted to the choice of element sensitivity, electrical, and optical circuits of the sensor in order to increase its efficiency. Laser absorption spectroscopy systems have been created and are used in more than 1000 coal mines in China [1,2]. In recent years [3,4], the laser absorption spectroscopy method has been significantly advanced by using a Herriott multiphase cell, which makes it possible to detect a target gas with a concentration of  $\sim 10^2$  parts per million in total over an averaging time of  $(1 - 10^2)$  s. The review [2] indicates a general pattern of signals from sensors on nanofilms with different chemical compositions – the predominance of low-frequency noise (LFN). In LFN spectroscopy, the intensity of the noise signal is usually inversely proportional to frequencies in the range  $(10^2 - 10^5)$  Hz.

Note that LFN signals are also present in laser spectroscopy. Laser radiation passing through a gas is absorbed and scattered not only on individual atoms with a certain resonant frequency, but also on individual molecules and their clumps. As a result, a fluctuation radiation field is created. At the output of the photodiode, this field interacts with the bias potential to create a partially coherent interference pattern. The correlators or power spectra of low-frequency fluctuations depend more noticeably on the gas concentration than on its atomic structure. An important task of gas sensors is to determine maximum allowable concentrations (MACs) leading to explosion, poisoning, and technological violations. Critical gas concentrations are usually determined by chemical analysis. Physical processes that determine the MACs can be nonlinear conductivity of the photodiode, thickening, and noisy spectral lines. Perhaps for this reason, there is insufficient data in the literature on the results for concentrations  $\text{ppm} \geq 10^3$  obtained by physical methods.

From the listed factors of weakening the sensor response with increasing gas concentration, it follows that it is necessary to select an intense low-frequency oscillation in the form of amplitude modulation.

In terms of the general principles of amplitude modulation to identify the desired signal in our approach, the following roles are meant: carrier frequency - laser frequency, fundamental modulation frequency - harmonics from the power supply network of electrical devices, the influence of the concentration of the target gas realizes intermodulation distortion (heterodyning). In this case, the result will separate the effect of changing the electrical resistance of the nanoelements of the sensor from the concentration effect.

The purpose of the work is to experimentally obtain the time-fluctuating voltage at the output of a photodiode as the laser passes through a gas layer. Under conditions of the required degree of coherence,

obtaining correlation spectral patterns. Search for opportunities to establish maximum permissible gas concentration values without the use of large, expensive optical analysis systems.

## 2. Measuring principle

The experimental setup diagram is shown in Figure 1. A TL081CP converter was used to amplify the output time-fluctuating voltage  $v(t)$  from PIN. The distance between the laser source and the photodiode is 5-6 cm. At photodiode offset voltage  $U = -2.3$  V (in the region of stability of the PIN characteristic) and photon energy  $\hbar\omega = 2.3$  eV, the beam intensity is  $IU = 60 \text{ mA} * 2.3 \text{ V} = 0.138 \text{ J}$ .

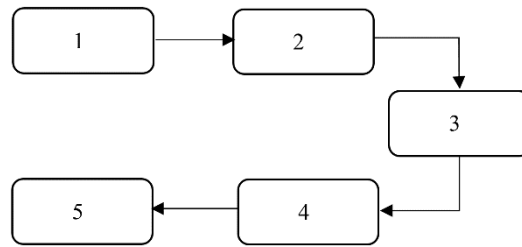


**Fig.1.** Laser gas sensor assemblies: 1 – power supply unit for the laser source “GOPHERT GPS-3205”, 2 – source of a laser beam with a wavelength of  $\lambda=532$  nm, 3 – vessel (volume 20 ml) of gas for an air+gas mixture, 4 – PIN photodiode, 5 – measuring instruments current voltage NI ELVIS II+, Hantex.

Various interference patterns were obtained  $v(\hbar\omega, -U, I)$ , degree of coherence determined by  $(v_{\min}/v_{\max})^2$ ,  $\gamma \geq 0,1$ . The intensity of the laser beam has a pronounced maximum current value  $I \sim 60$  mA. All measurements were carried out at normal atmospheric pressure and room temperature.

## 3. Results and Discussion

Figure 2 shows voltage fluctuations  $v(t)$  obtained when a laser beam with a wavelength of  $\lambda=532$  nm passes through air, ammonia, and ethanol. The gas concentration is  $\lesssim 10^3$  ppm. Value intervals  $v(t) = 1-1.35$  V, observation time  $t = 120$  s. The results were obtained at photodiode supply voltage  $U = 2.3$  V, laser beam photon energy in units of electron-volt  $\hbar\omega = 2.3$  eV. Due to the interaction of low-frequency fluctuations caused in the medium by the laser and harmonics of instrumental sources, interference patterns are observed.

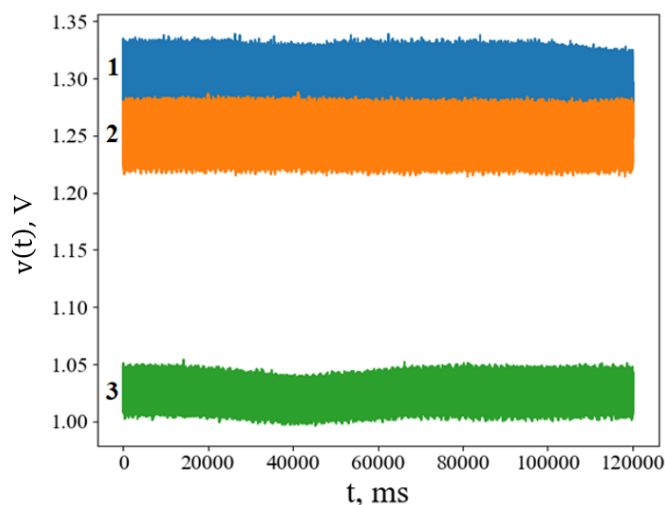


**Fig.2.** Voltage fluctuations at the photodiode output: 1-air, 2-ammonia, 3-ethanol.

The degree of coherence of interference fringes is determined by the formula:

$$\gamma = \frac{[1 - (v_{\min}/v_{\max})^2]}{[1 + (v_{\min}/v_{\max})^2]} \quad (1)$$

where  $v_{\min}$ ,  $v_{\max}$  are the minimum and maximum values of the fluctuation voltage  $v(t)$ . Formula (1) uses normalized intensity values.

For the analysis, results with  $\gamma \geq 0,1$  were used, which corresponds to the recommendations accepted in optics for choosing the contrast of interference patterns. Fluctuations are stationary, but nonequilibrium. The average values  $\langle v(t) \rangle$  are shifted: for air (low beam absorption), the maximum for the rest is lower. A universal characteristic of complex processes is correlation functions that consider the time delay of the count. For fluctuation processes, it is customary to call this function abbreviated as correlators, which are determined from discrete reports of fluctuations  $(\delta v_i, \delta v_j)$ :

$$K = \langle \delta v_i, \delta v_j \rangle = \frac{1}{N^2} \sum_i^N \sum_j^N \delta v_i * \delta v_j \quad (2)$$

Correlators can distinguish quantitatively different gases relative to air at a fixed concentration. Figure 3 shows autocorrelation functions depending on time  $t$  and its displacement  $\tau$ .

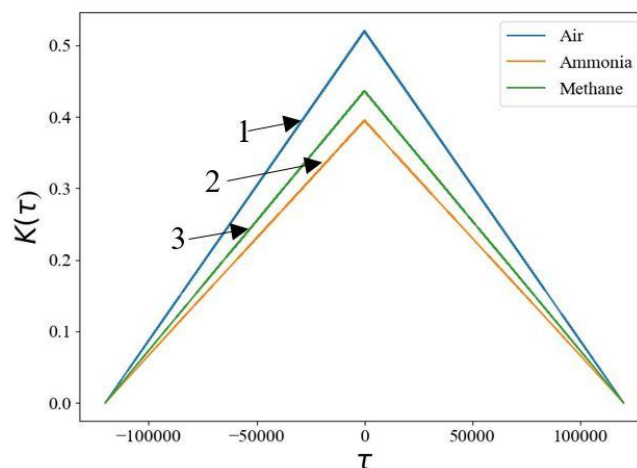


**Fig.3.** Autocorrelation function of fluctuation  $v(t)$ : 1-air, 2-ammonia, 3-methane.

A change in the laser sensor signal depending on the concentration ( $C$ ) of the target gas is also observed in the power spectrum. Let us introduce the notation  $K_{g/a}$ —the ratio of the correlators of gas ( $g$ ) and air ( $a$ ). Then the expression  $\ln \langle \delta v_i, \delta v_j \rangle_{g/a}$  describes the difference  $K_g$  from  $K_a$  more accurately than their direct difference  $K_g - K_a$ . Figure 4 shows the power spectra obtained from the correlators at the observed intense harmonic with a frequency of  $f = 200$  Hz. As the concentration of  $\text{NH}_3$  increases, the intensity of the lines decreases. At  $C \geq 10^3$  ppm (parts per million), this trend is ambiguous.

As noted, with increasing irradiation intensity and gas concentration current, the signal from the sensor can become saturated in a nonlinear manner. In this case, the role of an individual factor is unknown in advance. The given example at fixed frequencies clearly separates the effect of concentration.

The proposed approach to coherent amplitude modulation sensing is a variation of various radio engineering, solid-state methods. Low-frequency noise, kilohertz, megahertz ranges are used; there are names of wave modulation, frequency modulation, and nanoparticle spectroscopy [5-8].

In recent years [8-10], Allan deviation has been widely used in gas sensors, which is found by considering the average values of fluctuations of successively divided windows of time samples. In our

approach, the standard deviation ( $\sigma > \sigma_{min}$ ) has a stable value (Figure 5) due to coherence, while in the above works it increases after a minimum.

Different stable values of  $\sigma$  correspond to different concentrations. The  $\sigma_{min}$  values were determined by repeated measurements. This result indicates an average accuracy of 0.5% of the present experiment on the fluctuation signals. The measurement accuracy of survey work is  $\pm 0.5$  Hz (2.5%) at frequency. From Figure 4 the same order of deviation from the fundamental frequency of various additional modulations follows.

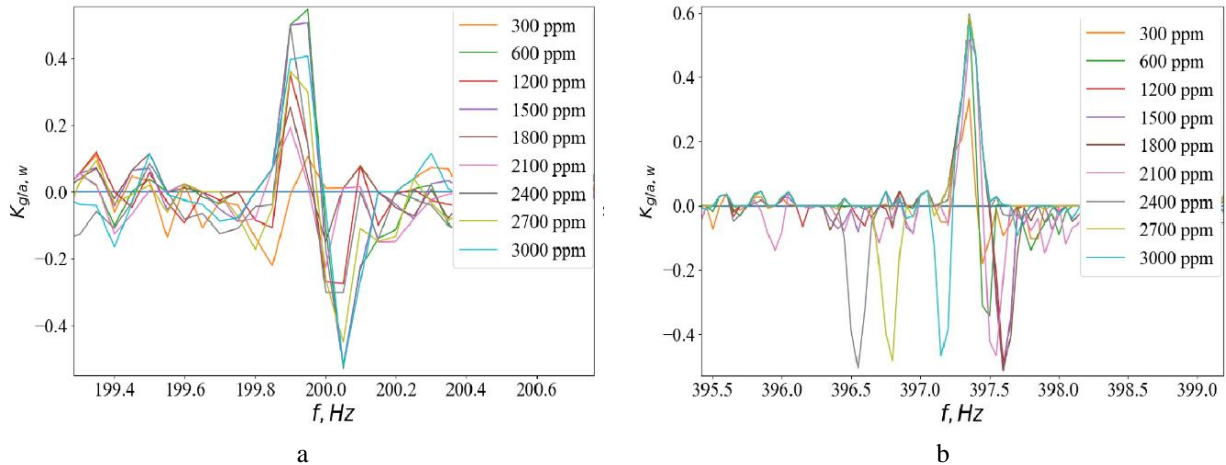


**Fig.4.** Ammonia power spectra: a) Main modulation frequency  $f_0 = 200$  Hz; b) Main modulation frequency  $f_0 = 397$  Hz.

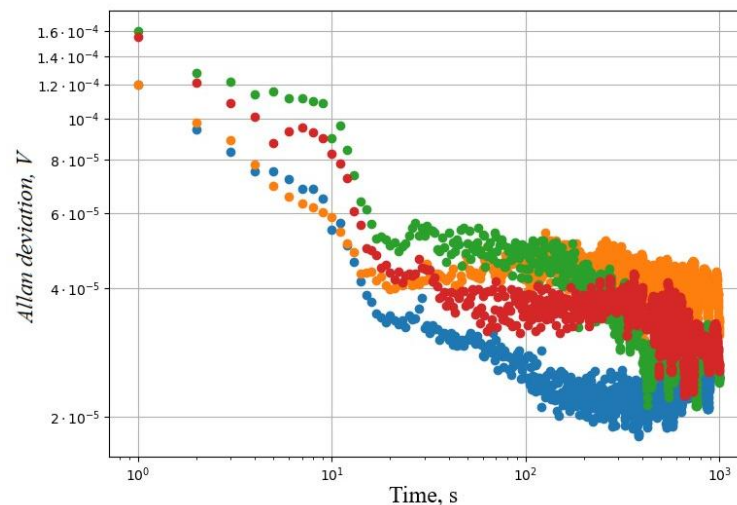


**Fig.5.** Allan deviation for  $\text{NH}_3$  (ppm value:  $10^2 \div 10^3$ ).

#### 4. Conclusion

The possibility of determining the type and concentration of gas in the air with a laser sensor by analyzing low-frequency fluctuation signals was experimentally demonstrated. The difference from existing optical sensors is the use of an interference pattern of interaction between harmonics of measuring instruments and fluctuation modes of absorption and laser scattering. From the results of the experiment, conclusions were drawn for the first time about the possibility of using a method for describing and predicting maximum permissible gas concentrations without knowledge of atomic and molecular spectral lines. The proposed laser gas sensor technology opens the possibility of creating a software package, since harmonic frequencies, spectrum expansion parameters (diffusion coefficient, sizes of Brownian nanoparticles, their mean free path) are known experimentally and there are tables for various gases. These parameters are determined much more accurately in comparison with quantum optical and dispersion

characteristics, since at high optical frequencies these characteristics will be nonlinear and ambiguous. The work was performed using the simplest equipment. The main result is the detection of saturation of the gas sensor response with increasing gas concentration through low-frequency modulation of the fluctuation signal. The work may find various applications by improving, if necessary, experimental techniques.

### Acknowledgments

We would like to express our sincerest gratitude to the Al-Farabi Kazakh National University for supporting this work by providing computing resources (Department of Physics and Technology).

This research was funded by the Committee of the Ministry of Science and Higher Education of the Republic of Kazakhstan, grant AP14872061.

### References

- 1 Gong W., Hu, J., Wang Z., Wei Y., Li Y., Zhang T., Zhang Q., Liu T., Ning Y., Zhang W., Grattan K.T.V. Recent advances in laser gas sensors for applications to safety monitoring in intelligent coal mines. *Frontiers in Physics*, 2022, Vol.10, pp. 1058475. doi: 10.3389/fphy.2022.1058475
- 2 Shin, Wonjun Hong, Seongbin Jeong, Yujeong Jung, Gyuweon Park, Jinwoo Kim, Donghee Choi, Kangwook Shin, Hunhee Koo, Ryun-Han Kim, Jae-Joon Lee, Jong-Ho. Low-frequency noise in gas sensors: A review. *Sensors and Actuators B: Chemical*, 2023, Vol. 383, pp. 133551. doi: 10.1016/j.snb.2023.133551.
- 3 Liu, Kun Wang, Lei Tan, Tu Guishi, Wang Zhang, Weijun Chen, Weidong Gao, Xiaoming. Highly sensitive detection of methane by near-infrared laser absorption spectroscopy using a compact dense-pattern multipass cell. *Sensors and Actuators B: Chemical*, 2015, Vol.220, pp. 1000 – 1005.
- 4 Zhang Z., Li, M., Guo J., Du B., Zheng, R. A Portable Tunable Diode Laser Absorption Spectroscopy System for Dissolved CO<sub>2</sub> Detection Using a High-Efficiency Headspace Equilibrator. *Sensors*, 2021, Vol.21, pp. 1723. doi:10.3390/s21051723
- 5 Hua-Liang Yu, Jun Wang, Biao Zheng, Bing-Wen Zhang, Li-Qin Liu, Ying-Wu Zhou, Cheng Zhang, Xiao-Ling Xue. Fabrication of single crystalline WO<sub>3</sub> nano-belts based photoelectric gas sensor for detection of high concentration ethanol gas at room temperature. *Sensors and Actuators A: Physical*, 2020, Vol.303, pp.111865. doi:10.1016/j.sna.2020.111865
- 6 Liu C., Zheng L., Wang J., et al. Tunable terahertz gas laser based on a germanium spectrum splitter. *Appl. Phys. B*, 2020, Vol.126, pp. 133. doi:10.1007/s00340-020-07486-5
- 7 Bierer B., Grgić D., Yurchenko O., Engel L., Pernau H.-F., Jäggle M., Reindl L., Wöllenstein J. Low-power sensor node for the detection of methane and propane. *J. Sens. Sens. Syst.*, 2021, Vol. 10, pp. 185–191. doi:10.5194/jsss-10-185-2021.
- 8 Wang Y., Feng Y., Adamu A.I., Dasa M.K., Antonio-Lopez J.E., Amezcua-correa R., Markos C. Mid-infrared photoacoustic gas monitoring driven by a gas-filled hollow-core fiber laser. *Scientific reports*, 2021, Vol. 11, No.1, pp. 3512.
- 9 Kwak D., Lei Y., Maric, R. Ammonia gas sensors: A comprehensive review. *Talanta*, 2019, Vol. 204, pp.713 – 730. doi: 10.1016/j.talanta.2019.06.034.
- 10 Dudzik G, Abramski K. Solid-state laser intra-cavity photothermal gas sensor. *Sensors and Actuators B: Chemical*, 2021, Vol. 328, pp. 129072.

Article received 04.12.2023

Article accepted 18.12.2023

## EDDY CURRENT METHOD FOR STUDYING INHOMOGENEITIES AND DEFECTS IN THIN METAL FILMS

Malikov V.N.<sup>1\*</sup>, Katasonov A.O.<sup>1</sup>, Ishkov A.V.<sup>2</sup>, Fadeev D.A.<sup>1</sup>, Voinash S.A.<sup>3</sup>,  
Vornacheva I.V.<sup>4</sup>, Zagidullin R.R.<sup>3</sup>, Shmykova P.A.<sup>1</sup>

<sup>1</sup>Altai State University, Barnaul, Altai Territory, Russia, [osys11@gmail.com](mailto:osys11@gmail.com)

<sup>2</sup>Altai State Agricultural University, Barnaul, Russia

<sup>3</sup>Kazan Federal University, 18 Kremlin Street, Kazan, Russia

<sup>4</sup>South-West State University, Kursk, Russia

*The variety of structure and specific properties associated with the small thickness of thin metal films lead to the fact that their physical characteristics differ significantly from the characteristics of the same materials in the bulk state. To determine the characteristics of thin metal films, the development of new non-destructive research methods is relevant. The article substantiates the advantages of the eddy current testing method for studying the surface of thin metal films of various metals. The design of a subminiature eddy current transducer designed to study the electrical conductivity, thickness and degree of damage of thin metal films is presented, and a hardware and software complex is designed that allows the control of the developed transducer. The study of metal films made it possible to show the inhomogeneity of the distribution of the substance over the surface of the substrate. The dependence of the signal amplitude of the developed transducer on the film thickness was also determined. To verify the results obtained, studies of the light transmittance of the films were carried out using the photometric method. Comparison of the measurement results obtained by the two methods showed a high degree of agreement between the two developed methods for studying films.*

**Keywords:** thin films, metals, eddy current transducer, materials research, film inhomogeneity.

### 1. Introduction

The rapidly developing electronics market requires the active development of technologies related to means of studying the characteristics of manufactured products, including studies of the condition of thin metal films. Analyzing the features of the development of new tools for studying thin-film structures, the following can be noted:

- the tasks of industrial research of materials and thin-film structures are becoming particularly relevant in the modern scientific and technical sphere;
- methods and means of non-destructive research of materials are among the most promising in the modern instrument-making industry;

Among the methods for studying metal objects, the eddy current method occupies a special place. It allows the study of objects such as massive conductive structures, layered composite materials, metal sheets, as well as objects with a small thickness, the most typical example of which is thin metal films.

The scientific and technical field associated with the production and use of thin metal films has grown rapidly over the past decades and occupies key positions in many branches of modern production. Currently, in the conditions of the scientific and technological revolution, the use of thin films in microelectronics, microwave technology, optics and many other branches of science and technology opens up prospects for the creation and improvement of not only new devices, but also entire technological areas.

The variety of structure and specific properties associated with the small thickness of such objects leads to the fact that their physical characteristics can differ significantly from the characteristics of the same materials in a massive state. In this regard, thin films are of interest to physics as objects on which new phenomena and patterns can be discovered or known ones can be explained. For technology, the study of thin films opens up the possibility of developing and creating fundamentally new devices and technologies.

In addition, thin films allow the development of new experimental methods of electroanalysis and sensing [1]. It should also be noted that work is currently being actively carried out on the synthesis and

production of new materials with specified characteristics, and research is also being conducted on the possibility of changing these characteristics under the influence of external factors (electric, magnetic, as well as acoustic fields, temperature, lighting, pressure and etc.) [2–5]. In this case, as a rule, such materials are often used as thin-film elements. For the full use of thin films in various fields of electronics, complete information about their material constants and physical parameters, both integral and local, is required. Therefore, new methods are needed to characterize the materials under study in the form of thin films.

To determine the characteristics of thin metal films, the following non-destructive research methods are widely used: atomic force microscopy, scanning electron microscopy, X-ray diffractometry, spectroscopic ellipsometry, four-probe method, eddy current method [6-8].

The eddy current method has significant advantages over other methods. It provides the ability to simply and accurately make measurements without the need for direct contact with the object under study, and also provides the ability to make measurements directly in the environment in which the film is growing, and this makes it possible to more accurately control the film growth process.

The disadvantage of this method is the low frequency of the electromagnetic field used in research. The characteristic frequency range used in instruments that implement this research method is 500 Hz – 1 MHz, which is insufficient when studying objects with a thickness of less than 1 micron. The use of a higher frequency is complicated by the need to digitize the signal of the eddy current transducer, which carries information about the object of study. In addition, one of the aspects of the development of the modern eddy current method of materials research is the automation of the scanning process. Automation of the scanning process can significantly increase the speed and accuracy of research.

The research team at Tsinghua University (Beijing) is also developing eddy current transducers for measuring the thickness of thin copper films in the process of chemical-mechanical planarization (CMP - one of the stages in the production of microelectronics). In their scientific works, they report on the creation of planar eddy current transducers without a core, both a surface-mount type, with a transducer diameter of 6 mm and an operating frequency of 0.75 MHz, and a pass-through type with a coil radius of 2.5 mm and an operating frequency of 0.5 MHz. The developed transducers showed high accuracy in determining the thickness of copper film in the range of 100 – 500 nm, but the dimensions of the transducers provide low spatial resolution [9, 10].

Works [11-15] describe examples of the use of single-part and multi-frequency eddy current testing methods for studying thin conductive films. In the case of measuring the thickness or electrical conductivity of films with pronounced magnetic properties, it is advisable to use the pulsed eddy current method [16, 17].

In the absence of magnetization of a thin film, the eddy current testing method is often used, based on the changing frequency of the electromagnetic field of the eddy current sensor. This method makes it possible to study films at different depths by changing the signal frequency. It is used in the study of multilayer plates, above which the measuring coil of an eddy current transducer is placed. At the same time, the change in the impedance of the coil during its interaction with each of the conducting layers was assessed, based on which the thickness and conductivity of each layer can be found [18-22].

However, this method is difficult to use for films with a thickness of less than 10  $\mu\text{m}$  [20, 23].

The authors in [24, 25] studied the change in the impedance of a coil located above a conducting plate with a single-layer metal coating, which, in fact, is a model of a thin metal film. The feasibility of using a transformer overhead eddy-current technique (ETC) for studying thin metal films has been established, and information has also been obtained that such studies require information either on the thickness of the film or on its electrical conductivity [20, 23-27].

However, these works contain very little information about determining the degree of defectiveness of thin metal films.

Thus, an urgent task in the development of the eddy current method for studying materials is the creation of a hardware and software complex that allows one to study the homogeneity and defectiveness of a thin metal film. A promising direction of development seems to be the automatic movement of the sensor over the surface of the film under study with a small step and registration of the eddy-current probe (ECP) signal at each measurement point in real time.

## 2. Materials and methods of research

Based on the conclusions drawn from the analysis of the first chapter and previous studies [28-31], a subminiature eddy current transducer was developed, designed to study the electrical conductivity, thickness and degree of damage of thin metal films, and a hardware and software complex was designed to allow control of the developed transducer. The eddy current transducer is the main element of the developed measuring system and is part of the hardware and software complex that controls the operation of the entire system. Its characteristics were calculated based on numerical modeling using the finite element method in the Elcut software package.

The main element of the eddy current method is the eddy current transducer, the design of which is selected for each specific task. Based on the results of mathematical modeling, the design of a transformer overhead high-current transformer has been developed, allowing the study of thin metal films. Figure 1 shows the design of the developed clamp-on transformer converter with a cone-shaped core made of ferrite.

The core is a truncated cone 4.3 mm high with a base diameter of 1.5 mm and apex diameter of 0.1 mm, Fig. 1a. The measuring winding is located at the tip of the cone (50 turns), the generator winding is located in the center (50 turns) and is wound in such a way that the radius is as small as possible to achieve maximum field localization. The windings are made of copper wire with a diameter of 15 microns.

To eliminate the influence of the generator winding on the measuring winding and increase the signal-to-noise ratio, a compensation winding was added to the ETP; the measuring and compensation windings are connected according to the differential circuit shown in Fig. 1b.

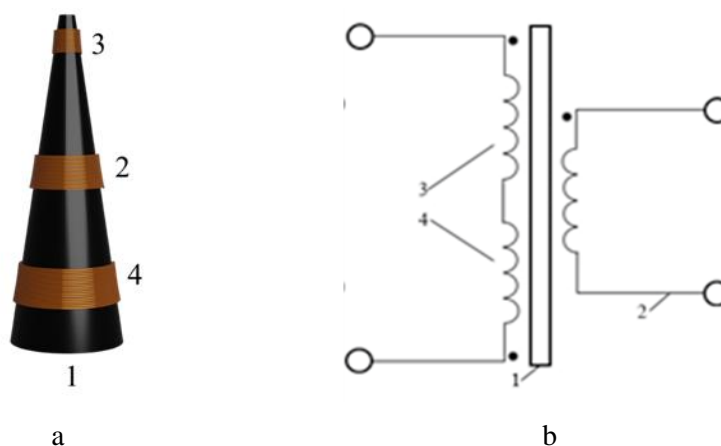


**Fig.1.** Design of the developed eddy- current transducer (ECT): a) 3D model, b) coil connection diagram: 1 – ferrite gearbox, 2 – generator winding, 3 – measuring winding, 4 – compensation winding

The transducer is positioned perpendicular to the plane of the film under study, so that the measuring winding is at a minimum distance from the surface of the film, but the ECP is not in contact with it.

To protect against mechanical damage, the converter is coated with epoxy resin and placed in a plastic case. To control the operation of the developed converter, automate the measurement process and convenient visualize the results obtained, a hardware and software complex is required. The main requirements for the hardware and software complex were the ability to position the ECP in increments of up to 0.01 mm, the accuracy and speed of data processing. Additional requirements included the portability of the complex and the ability to control it via a personal computer (PC).

The developed diagram of the software and hardware complex is presented in Fig. 2. The control unit, executed on the basis of a personal computer (PC), generates and sends commands to the generator (GEN) and the ECP positioning system. The generator, having received a control signal, generates an alternating electric current of a given frequency, which, passing through the Amplifier, acquires a given amplitude and is supplied to the exciting coil of the ECP. The voltage on the measuring coil, passing through the Amplifier and Filter, is supplied to an analog-to-digital converter and then, in the form of a digital signal, enters the processing and visualization unit PC.

To move the ECP over the object of study, a positioning system based on Cartesian kinematics, based on a Cartesian coordinate system, was developed; this technology operates on the basis of three axes - X, Y,

Z. The platform for securing the research object moves along the Y axis, and the sensor holder moves along the X and Z axis. Each direction has its own motor, the Y and X axes have a belt drive (Fig. 3), the Z axis is driven by a screw system consisting of a stepper motor, a flexible coupling and a screw, the pitch of which determines the step size along this axis.

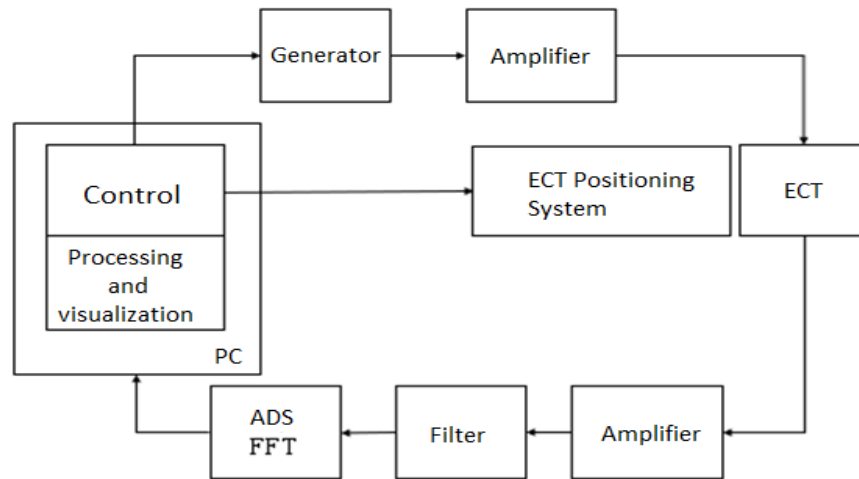


**Fig.2.** Scheme of the eddy current complex

The maximum size of the probing area is  $22 \times 22$  cm, the maximum movement speed is 180 mm/s, the movement accuracy is 100  $\mu\text{m}$ . Stepper motors are controlled using a motherboard with a 32-bit processor. The motherboard is equipped with a universal serial bus (USB) connector through which a connection is made to a PC for receiving control commands. The motherboard used has Marlin firmware and is controlled using commands in the G-cod programming language. On the positioning system, a sensor is placed in a special holder, which is an eddy current transducer that interacts with the object of study using the generated electromagnetic field.

To generate the electromagnetic field of the eddy current transducer, a system for generating signals supplied to the exciting winding of the eddy current transducer was developed. The software control of the generation system being developed is implemented in a hardware-software complex in the form of a generator made in the form of a module based on the AD9850 microcircuit. The module is a chip that uses a combination of advanced technology for direct digital synthesis (DDS), high-quality digital-to-analog conversion and a comparator, providing the functions of synthesizing a signal of a given frequency, generating clock signals designed for correct operation of the system and digital software management. When operated from an accurate reference clock source, the AD9850 produces a stable analog sine wave output with programmable frequency and phase.

The developed module has the following characteristics: with a clock generator frequency of 125 MHz, a sinusoidal signal with a frequency from 0 to 40 MHz can be obtained at the module output. The resulting signal is characterized by high stability, low noise level, and also requires a low supply voltage (from 3.3 V to 5 V). The module dimensions are 3\*4 cm.

The disadvantages of this module include the lack of adjustment of the amplitude of the output signal and its low power. These shortcomings were mitigated by using an amplifier with adjustable gain. The generation module is controlled using the Arduino hardware computing platform. The platform consists of two main components: an I/O board and a development environment in the Processing/Wiring language.

The form factors of the Arduino microcircuit differ not only in appearance and the number of pins (inputs and outputs), but also in the presence of an installed microcontroller, a clock generator and the amount of flash memory and random access memory (RAM).

To digitize the ECT output signal, a module with a high sampling rate based on the RTL2832U chip was selected. The selected module directly includes an application delivery controller (ADC), a digital processor, a USB interface, and filters. Characteristics of the module on the RTL2832U chip:

- ADC capacity: 8 bits;
- Sampling rate 3.2 MS/s;

- Frequency band: 0.5-1750 MHz;
- Variable filter width;
- Sensitivity: 0.22  $\mu\text{V}$  (at 438 MHz in network friendly mode (NFM) mode);

The selected signal digitization module allows you to obtain output signal values expressed in conventional units. To obtain the output signal amplitude values in volts, a calibration curve was constructed.

The resulting dependence is complex: for signal amplitudes up to 100 mV, the dependence is linear; for amplitudes above 100 mV, the dependence becomes nonlinear. To reduce the error, the ADC input amplifier is configured so that the signal amplitude does not exceed 100 mV, which will ensure operation of the ADC module in the region of linear dependence of the calibration dependence.

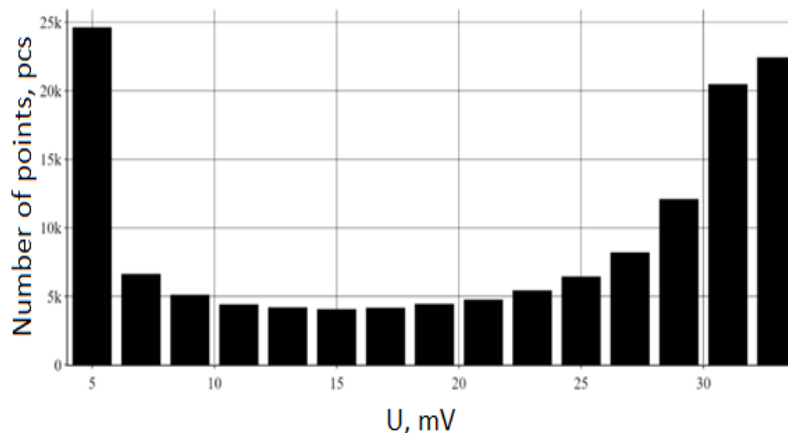
To control the operation of the hardware and software complex, process and visualize the obtained values, software was developed in Python, the graphical shell of the software was created in the Qt designer software package. The Python programming language was chosen due to its simplicity, versatility, relevance and availability of a large number of open-source libraries for data processing and visualization. In the working window of the developed software, the frequency of the exciting signal is set, the value of which is transmitted to the generator through the Serial Port library, the generator generates an exciting signal of a sinusoidal shape with a given frequency.

Further, in accordance with the installation diagram, in order to achieve the required amplitude value, the signal is sent to a special amplifier, the coefficient of which can vary within certain limits. The signal, which has undergone the amplification procedure, is fed to the excitation winding of the converter, as a result of which eddy currents are induced in the object of study. The resulting field induces an output signal in the electromagnetic field (EMF) measuring winding that carries information about the object of study. The output signal of the converter is amplified. After amplification, the signal is supplied to the block for collecting, digitizing and primary data processing, where voltage measurement and analog-to-digital conversion of the result occurs.

The resulting voltage values are transmitted via Serial Port to the PC. For this purpose, the class RTL (QThread) for reading data from the ADC module and primary data processing is used. While using the class, the ADC switches to discrete read mode using the command `<self.sdr.set_direct_sampling>` (direct\_sampling), the command `<self.sdr.sample_rate = SampleRate>` the sampling frequency is set. The received data is transferred to the array with the command `<self.data = data>`. Next using the command `<fft = np.fft.rfft(samples)>` a fast direct discrete Fourier transform of the array is performed, the result is written to the array fft, having a complex appearance.

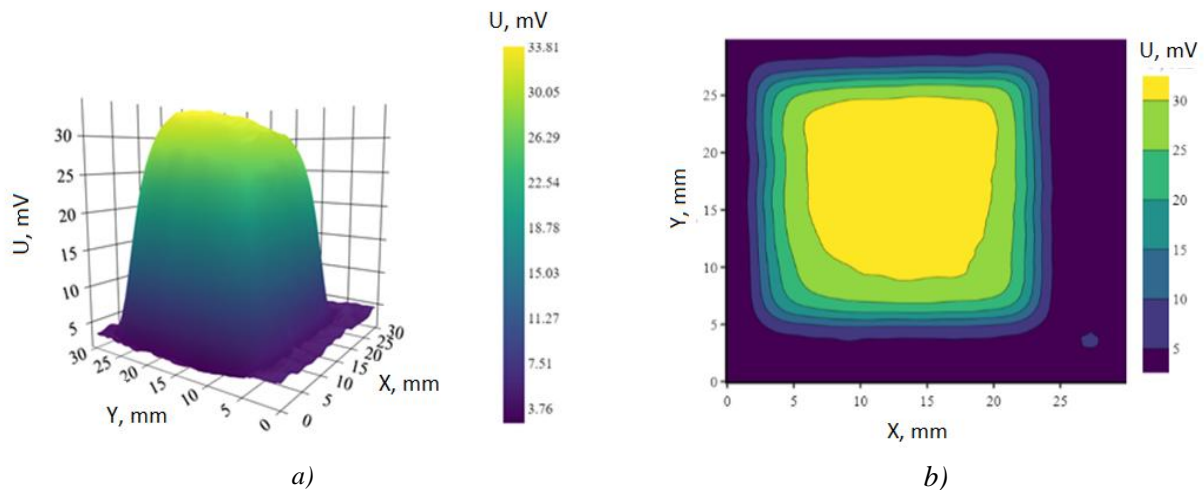
Calculation of signal component amplitudes ( $\sqrt{Re^2 + Im^2}$ ) is performed using the abs function, the average amplitude value is also calculated and the resulting value is written to the output array. Next, the software presents the measured information from the sensor of the software and hardware complex in the form of an image of the signal amplitude distribution over the scanning area.

Fig.3 shows an example of presenting the result of scanning a research object in the form of a histogram: the measured values of the signal amplitude are plotted along the abscissa axis, and the number of points with a given amplitude is plotted along the ordinate axis.



**Fig.3.** Graphic representation of the result of scanning the research object in the form of a histogram

This type of graphical representation allows one to assess the homogeneity of the object of study in terms of the height of the maxima and their area. Fig.4 (a) shows the results of scanning the research object in three-dimensional form. The coordinates of the sensor position above the object are plotted along the X and Y axes; the amplitude value of the transducer signal is plotted along the Z axis. Also, the signal amplitude values are expressed by the color of each point; on the right is a color line showing the correspondence of the point color to the signal amplitude value. This representation makes it possible to analyze the surface of an object.



**Fig. 4.** Graphical representation of the result of scanning the research object in three-dimensional (a) and two-dimensional (b) form

Figure 4 (b) shows a graphical representation of the results of scanning the research object in two-dimensional form. Along the X and Y axes the coordinates of the sensor position above the object of study are plotted, the signal amplitude is encoded in the color of the point and a color ruler is provided to determine the amplitude by color, isolines are also drawn for convenient determination of the signal amplitude in individual areas. This graphical representation allows you to visually separate areas with different signal amplitudes and estimate the size of defects and inhomogeneities in these areas.

### 3. Results and discussion

In order to test the developed measuring system to assess the distribution of metal deposited on a glass substrate, samples of two thin copper films were scanned (Fig. 3, 4). By comparing the image data, it can be concluded that the sample data vary in homogeneity. The conclusion about the high homogeneity of sample No. 1 can be made from the size of the area of the region corresponding to the amplitude of the ETP signal  $U > 25$  mV in Fig. 4 (b), 4 (a), and in Fig. 3 we can distinguish two regions with significant maxima of U, lying in the range from 0 to 5 mV and from 25 to 35 mV. The large area of the second region allows us to conclude that this sample is highly homogeneous.

Fig.5 shows the results of scanning the obtained batches of thin copper films. The film thickness ranged from 100 to 800 Nm. The results obtained from scanning each batch of films demonstrate a different distribution of film heterogeneity within the same batch. During scanning of batch 1 (Fig. 5), it was found that the most homogeneous film is shown in Fig. 5 (b). The signal amplitude on this film remains constant over 90% of its area and has a value of about 30 mV. Fig.5 (a) shows a film with a defect, where in the defect area the amplitude of the ETP signal is 16 mV – 62% of the maximum amplitude of the ETP signal.

Analysis of the scanning results shows that the heterogeneity of the distribution of physical properties is observed not only within the boundaries of each film, but also within one batch of films. In each batch of films, it is possible to select a region corresponding to the maximum amplitude of the ETP signal and regions corresponding to a lower signal amplitude. The position of the maximum amplitude of the ETP signal on the graph can be associated with the position of the evaporated substance on the evaporator. The amplitude of the ETP signal is directly related to the position of the substrate relative to the deposited substance and increases when analyzing samples located closer to the deposited metal.

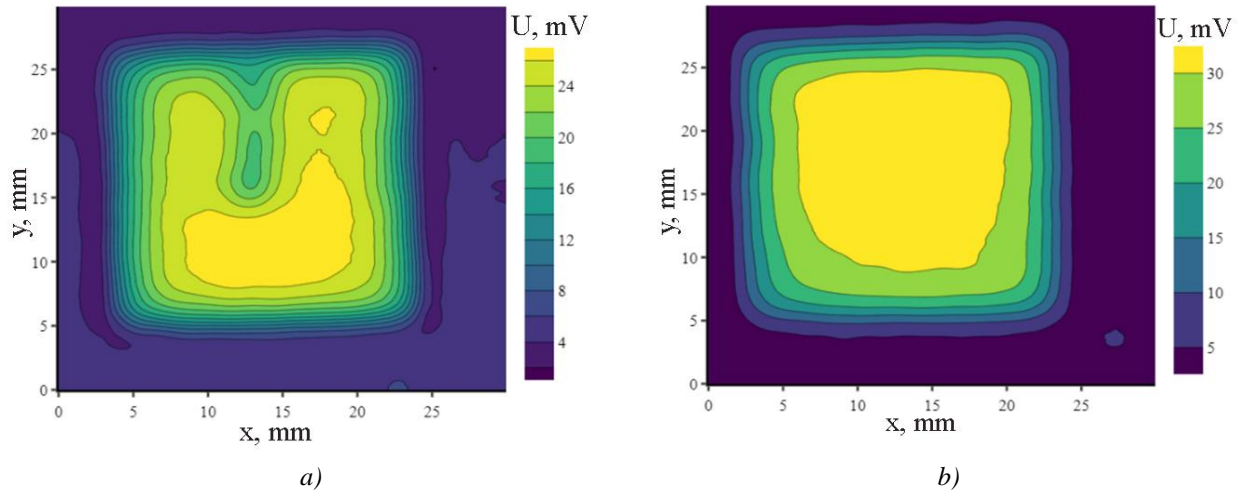


Fig. 5. Batch 1 scan results

To verify the results obtained from the analysis of the distribution of film inhomogeneities over the surface using the eddy current method, studies of the light transmission of the films were carried out. The laser beam with a wavelength of 650 nm was passed through the film, and the fraction of transmitted radiation was measured by a photoresistor. The image obtained as a result of measurements by the photometric method has significant visual similarity to the image obtained as a result of measurements by the eddy current method. To obtain a quantitative assessment of the degree of similarity of the images, Fig. 6 shows sections passing through identical areas of the film. The sections are shown with red lines.

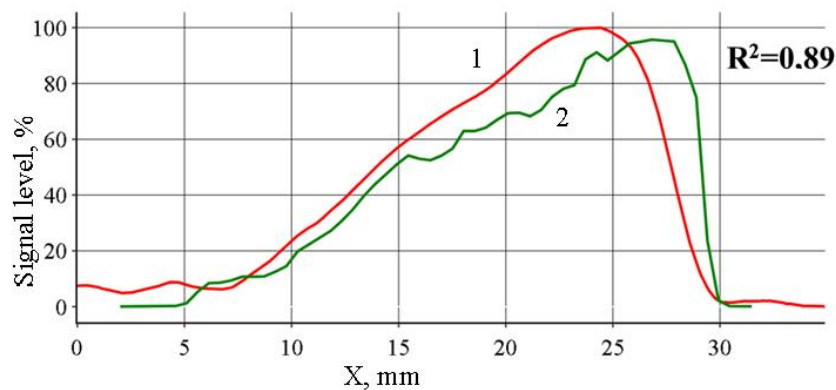


Fig. 6. Dependence of the signal level on the coordinate along the selected section:  
1 – eddy current method, 2 – photometric method

The results obtained allow us to conclude that there is a high degree of correlation between the amplitude of the ETP signal and the attenuation coefficient of laser radiation by a thin film, which in turn is directly proportional to the thickness of the film. The correlation coefficient was 0.89.

#### 4. Conclusion

Thus, scanning a significant number of metal films showed that the substance of the resulting films is not distributed uniformly over the surface of the substrate. A conclusion about the degree of homogeneity can be made from the size of the area of the region corresponding to the maximum of the signal. The larger the area occupied by the region corresponding to the maximum signal, the more homogeneous the film is. The dependence of the amplitude of the ETP signal on the film thickness was also determined. For films with a thickness from 100 to 500 nm and an electrical conductivity of 14 MS/m, the maximum signal amplitude ranged from 5.98 to 8.76 V, respectively. To verify the results obtained, studies of the light transmittance of the films were carried out using the photometric method. Comparison of the measurement results obtained by the two methods showed a high degree of agreement, the correlation coefficient  $R^2$  was 0.89.

## REFERENCES

- 1 Mansurov G.N., Petriy O.A. *Electrochemistry of thin metal films*. Moscow. 2011, 351 p. [in Russian]
- 2 Yurkov V., Ryzhii V. Effect of Coulomb scattering on graphene conductivity. *JETP Lett.*, 2008, Vol. 88, No. 5, pp. 370 – 373. doi:10.48550/arXiv.0807.3880
- 3 Khokhlov A. Novel highly elastic magnetic materials for dampers and seals: Part I. Preparation and characterization of the elastic materials. *Polym. Adv. Technol.*, 2007, Vol. 18, No 11, pp. 883 – 890. doi:10.1002/pat.924
- 4 Kosobudskii I. Nanocomposites based on the cerium oxide nanoparticles and polyethylene matrix: Syntheses and properties. *Acta Mater.*, 2008, Vol. 56, No.10, pp. 2336-2343. doi:10.1016/j.actamat.2008.01.019
- 5 Borodina I. Influence of conducting layer and conducting electrode on acoustic waves propagating in potassium niobate plates. *IEEE Trans. on Ultrason. Ferroelectrics. and Freq. Cont.*, 2001, Vol. 48, No 2, pp. 624-626. doi:10.1109/58.911747
- 6 Whiteside P., Chininis J., Hunt H. Techniques and Challenges for Characterizing Metal Thin Films with Applications in Photonics. *Coat.*, 2016, Vol. 6, No.3. doi:10.3390/coatings6030035
- 7 Wang Z., Han Y., Xu N. Characterization of Thin Metal Films Using Terahertz Spectroscopy. *IEEE Trans. Terah. Sci. Tech.*, 2018, Vol. 99, pp.1-4. doi:10.1109/TTHZ.2017.2786692
- 8 Giurlani W., Berretti E. Measuring the Thickness of Metal Films: A Selection Guide to the Most Suitable Technique. *Mater. Proc.*, 2020, Vol. 2, No. 1, pp. 12-35. doi:10.3390/CIWC2020-06823
- 9 Lu X. In-situ measurement of Cu film thickness during the CMP process by using eddy current method alone. *Microelectronic Engineering*, 2013, Vol. 108, pp. 66-70. doi:10.1016/j.mee.2013.03.046
- 10 Zheng Y. Noncontact thickness measurement of cu film on silicon wafer using magnetic resonance coupling for stress free polishing application. *IEEE Access*, 2019, Vol. 7, pp. 75330-75341. doi:10.1109/ACCESS.2019.2921005
- 11 García-Martín J., Gómez-Gil J., Vázquez-Sánchez E. Non-destructive techniques based on eddy current testing. *Sensors*, 2011, Vol. 11, No. 3, pp. 2525–2565. doi:10.3390/s110302525
- 12 Krause T.W. Simultaneous multiparameter measurement in pulsed eddy current steam generator data using artificial neural networks. *IEEE Trans. Instrum. Meas.*, 2016, Vol. 65, No. 3, pp. 672-679. doi:10.1109/TIM.2016.2514778
- 13 Pasadas D.J. Inspection of cracks in aluminum multilayer structures using planar ECT probe and inversion problem. *IEEE Trans. Instrum. Meas.*, 2017, Vol. 66, No. 5, pp. 920–927. doi:10.1109/TIM.2017.2682758
- 14 Bernieri A. Multifrequency excitation and support vector machine regressor for ECT defect characterization. *IEEE Trans. Instrum. Meas.*, 2014, Vol. 63, No. 5, pp. 1272–1280. doi:10.1109/TIM.2013.2292326
- 15 Wang H., Li W., Feng Z. Noncontact thickness measurement of metal films using eddy-current sensors immune to distance variation. *IEEE Trans. Instrum. Meas.*, 2015, Vol. 64, No. 9, pp. 2557–2564. doi:10.1109/TIM.2015.2406053
- 16 Yang H.-C., Tai C.-C. Pulsed eddy-current measurement of a conducting coating on a magnetic metal plate. *Meas. Sci. Technol.*, 2002, Vol. 13, No. 8, pp. 1259–1265. doi:10.1088/0957-0233/13/8/313
- 17 Danon Y., Lee C., Mulligan C., Vigilante G. Characterizing tantalum sputtered coatings on steel by using eddy currents, *IEEE Trans. Magn.*, 2004, Vol.40, No.4, pp. 1826-1832. doi:10.1109/TMAG.2004.828040
- 18 Ishkov A., Malikov V., Dmitriev S. Scanning steel junctions using eddy current probe. *J. Phys.: Conf. Ser.*, 2021, Vol. 1728. doi:10.1088/1742-6596/1728/1/012007
- 19 Bowler J.R., Norton S.J. Eddy current inversion for layered conductors. *Res. Nondestr. Eval.*, 1992, Vol. 4, No. 4, pp. 205–219. doi:10.1007/BF01616488
- 20 Moulder J.C., Uzal E., Rose J.H. Thickness and conductivity of metallic layers from eddy current measurements. *Rev. Sci. Instrum.*, 1992, Vol. 63, No. 6, pp. 3455–3465. doi:10.1063/1.1143749
- 21 Ping-jie H., Zhao-tong W. Inversion of thicknesses of multi-layered structures from eddy current testing measurements. *J. Zhejiang Univ. Sci.*, 2004, Vol. 5, No. 1, pp. 86-91. doi:10.1007/BF02839318
- 22 Li Y., Chen Z., Mao Y., Qi Y. Quantitative evaluation of thermal barrier coating based on eddy current technique. *NDT&E Int.*, 2012, Vol. 50, pp. 29–35. doi:10.1016/j.ndteint.2012.04.006
- 23 Li Y., Yan, B., Li W., Li D. Thickness assessment of thermal barrier coatings of aeroengine blades via dual-frequency eddy current evaluation. *IEEE Magn. Lett.*, 2016, Vol. 7, pp. 1304905. doi:10.1109/LMAG.2016.2590465
- 24 Sethuraman A., Rose J.H. Rapid inversion of eddy current data for conductivity and thickness of metal coatings. *J. Nondestruct. Eval.*, 1995, Vol. 14, No. 1, pp. 39–46. doi:10.1007/BF00735670
- 25 Tai C.-C., Rose J.H., Moulder J.C. Thickness and conductivity of metallic layers from pulsed eddy-current measurements. *Rev. Sci. Instrum.*, 1996, Vol. 67, No. 11, pp. 3965–3972. doi:10.1063/1.1147300
- 26 Zhang D., Yu Y., Lai C., Tian G. Thickness measurement of multi-layer conductive coatings using multifrequency eddy current techniques. *Nondestruct. Test. Eval.*, 2016, Vol. 31, No. 3, pp. 191–208. doi:10.1080/10589759.2015.1081903

27 Yu Y., Zhang D., Lai C., Tian G. Quantitative approach for thickness and conductivity measurement of monolayer coating by dual-frequency eddy current technique. *IEEE Trans. Instrum. Meas.*, 2017, Vol. 66, No. 7, pp. 1874–1882. doi:10.1109/TIM.2017.2669843

28 Katasonov A.O., Malikov V.N., Dmitriev S.F. Scanning the thickness of conductive and dielectric coatings using superminiature eddy current probe. *Lecture Notes in Civil Eng.*, 2021, Vol. 130. pp. 548 – 554. doi:10.1007/978-981-33-6208-6\_54

29 Malikov V.N., Fadeev D.A., Dmitriev S.F. Study of surface and electrical conductivity of thin metal films of the Ni-Al system. *Nanobiotechnology reports*, 2021. Vol. 16. No. 2. pp. 261 – 265. doi:10.1134/S2635167621020051

30 Ishkov A.V., Malikov V.N., Sagalakov A.M. Subminiature eddy current transducers for thickness measurement problems. *Journal of Machinery Manufacture and Reliability*, 2020, Vol. 49, No. 9, pp. 783 – 786. doi:10.3103/S105261882009006X

31 Ishkov A.V., Malikov V.N., Sagalakov A.M. Subminiature eddy-current transducers for conductive materials and layered composites research. *Advances in Intelligent Systems and Computing*, 2018, No. 692, pp. 655 – 665. doi:10.1007/978-3-319-70987-1\_70

Article received 19.10.2023

Article accepted 18.12.2023

DOI 10.31489/2023No4/125-132

UDC 536.36, 538.9, 544.3.01, 544.22, 544.77

## FRactal Nanoparticles of Phase-Separating Solid Solutions: Morphology-Dependent Phase Equilibria in Tungsten Heavy Pseudo-Alloys

Shishulin A.V.<sup>1,2\*</sup>, Potapov A.A.<sup>3,4</sup>, Shishulina A.V.<sup>5</sup><sup>1</sup>Pleiades Publ., Ltd., Moscow, Russia,<sup>2</sup>G.A. Razuvaev Institute of Organometallic Chemistry, Russian Academy of sciences, Nizhny Novgorod, Russian Federation, chichouline\_alex@live.ru<sup>3</sup>V.A. Kotel'nikov institute of radio engineering and electronics, Russian Academy of sciences, Moscow, Russian Federation<sup>4</sup>JNU-IREE RAS Joint Laboratory of Information Technology and Fractal Processing of Signals, Jinan University, Guangzhou, China<sup>5</sup>R.E. Alekseev Nizhny Novgorod State Technical University, Nizhny Novgorod, Russian Federation

*In this paper, we simulate thermodynamically the morphology-dependent phase equilibria in core-shell nanoparticles of a phase-separating solid solution using the example of W-Cr heavy alloy. The morphology of a nanoparticle is described in the framework of the fractal geometry methods. It is shown that there are two possible heterogeneous states in a nanoparticle while the compositions of phases in both states differ from each other. The dependences of mutual solubilities of components on the temperature are obtained while the behavior of these dependences significantly differs depending on the particular state and the morphology of nanoparticle under consideration. In nanoparticles of a very complicated morphology, the phase separation itself gets suppressed and the nanoparticle remains in the homogeneous state at the temperatures significantly below the macroscopic value of the upper critical dissolution temperature. The demonstrated regularities are explained based on three mechanisms of reducing the free energy of the system and the "competition" between them. In the final section, a method for calculating the equilibrium size distributions and average characteristics of nanoparticle ensembles is described along with a technique of measuring nanoparticle fractal dimensions based on the microscopy data.*

**Keywords:** nanoparticles, phase separation, tungsten, chromium, fractal dimension.

### 1. Introduction

In recent years, one of the main development vectors of the contemporary metalphysics is represented by investigating the unique set of properties of nanoparticle-fabricated samples which are resulted from the formation an ultrafine-grained structure in such materials. The structure of this type is generally obtained using the up-to-date additive powder metallurgy technologies [1-5] including the selective laser melting (SLM), selective laser sintering (SLS) and, especially, spark plasma sintering (SPS) methods [1, 2]. The last technique consists in the high-rate heating of nanopowders in a special conducting (graphite) mold due to the propagation of short (dozens of milliseconds) high-power current pulses through it. The sintering is carried out in the vacuum or in the atmosphere of an inert gas, the one-axis pressure being applied to the sample at the same time. An ultrafine-grained structure is obtained and the grain growth process is hampered in the case of the considered technologies as a result due to the possibility of dramatically high heating rates (up to 2000 – 2500 °C/min). It also necessary to mention that the SPS technology provides a number of "knobs" which make it possible to influence on the key characteristics of the obtained nanostructure of a metal sample through tuning the value of the applied pressure, heating temperature and heating time, heating and cooling rates etc. even in the course of the sintering process.

One of the primary objects of applying the developed additive manufacturing methods are the nanostructured tungsten-based heavy pseudo-alloys (the components of those are boundedly soluble in each other while the material is obtained using the different methods from the direct alloying) including the  $W_{1-x}Cr_x$  ones [1-4, 6, 7]. Along with the significant fracture resistance under the dynamic loading conditions [6], the alloys of this system are characterized, for example, by the possibility of self-passivation [1] and a

dramatically high corrosion resistance at high temperatures [1, 2]. These ones and many other features [4] together provide a large number of biomedical, construction and special applications for such alloys.

At the mesoscopic scale, the  $W_{1-x}-Cr_x$  do not form a continuous series of solid solutions and undergo the phase separation with the upper critical dissolution temperature (UCDT) at 1906 K without any intermetallic phases [1, 7-9]. In the case of the additive powder metallurgy technologies being applied, the primary ways of controlling the physico-chemical properties of such materials consist in the formation of super-saturated solid solutions [1, 4] as well as of grain-boundary segregations with excessive contents of the dissolved component [7]. At the same time, in the analysis of phase equilibria in systems of a small volume, it is necessary to take into account several characteristic features. These peculiarities manifest themselves in significant dependences of mutual solubilities of components and equilibrium volume fractions of co-existing phases on the volume [9-20], shape of a nanoparticle [12-14, 18], thermodynamical characteristics of the surrounding environment [20] and several other factors [15, 17, 19]. The equilibrium phase compositions of small-volume systems are significantly different from the phase compositions of the same systems in the bulk state and can be modeled using the methods of equilibrium chemical thermodynamics [21] and several other approaches [22] (the applicability of thermodynamical methods in the analysis of phase equilibria in small-volume systems as well as their applicability limits are discussed in [23]). The experimental observations of the abovementioned effects are described, for example, in [24, 25].

## 2. Mathematical model of the phase separation in nanoscale particles

In the bulk state, the phase equilibria in the  $W_{1-x}-Cr_x$  system are represented by the classical Becker curve [1, 8, 9]: the components are boundedly soluble in each other below the temperature of  $\sim 1906$  K. As the system to be modeled below, we consider equiatomic nanoparticles of various shapes; below the UCDT, the nanoparticle contains a spherical-shaped inclusion (which is hereinafter referred as “core-phase”) of a solid-solution surrounded by a solid-solution layer (“shell-phase”) of a given shape. The nanoparticle volume is characterized by the effective diameter ( $d_{eff}$ , the diameter of the sphere, the volume of which being equal to the one of the considered nanoparticle). In a closed binary system with the *core-shell* configuration, the conservation conditions of matter interrelate the nanoparticle effective diameter, total amount of matter in the system ( $n$ ), numbers of moles of each component ( $n_i$ , indices  $i=1, 2$  correspond to chromium and tungsten, respectively) and concentrations of components  $i$  in phases  $j$  ( $x_{ij}$ , indices  $j=c, s$  correspond to *core-* and *shell-*phases, respectively) [18]:

$$\pi d_{eff}^3/6 = \sum_j V_j, \quad n_1 = xn, \quad n_2 + n_1 = n, \quad n_i = \sum_j n_{ij}, \quad V_j = \sum_i n_{ij} V_i, \quad x_{ij} = n_{ij} / \sum_i n_{ij}. \quad (1)$$

Here,  $V_j$  and  $V_i$  are the volume of phase  $j$  and the molar volume of component  $i$ , respectively. The molar volumes are  $V_1 = 7.23 \text{ cm}^3/\text{mol}$ ,  $V_2 = 9.53 \text{ cm}^3/\text{mol}$ .  $x=0.5$  in the case of equiatomic particles [9, 15].

In order to provide a general description of all the possible nanoparticle geometric configurations including the most complicated and irregular ones, the fractal geometry approach is used [18, 26-28]. In the framework of this approach, the nanoparticle shape is characterized by its fractal dimension  $D$  which relates its surface area  $A_s$  to its volume (effective diameter  $d_{eff}$ ):  $A_s = C(\pi d_{eff}^3/6)^{2/D}$ . Without any losses of generality, constant  $C$  is assumed to be  $C = 4\pi$  [18, 26-28]. For regular simple structures,  $D \equiv 3.00$ , in their turn, the structures of a complicated and irregular morphology correspond to the values of  $D < 3.00$  while  $D$  is also non-integer.

The examples of structures with various  $D$  are given in Refs. [27, 28]. Fractal dimension  $D$  of a nanoparticle can also be expressed in terms of the nanoparticle surface-to-volume ratio ( $k$ ):  $k(V, D) = V^{2/D} / (3V/4\pi)^{2/3}$ ,  $V = \pi d_{eff}^3/6$ . The nanoparticles of 40 nm in effective diameter and fractal dimensions of 2.60, 2.75 and 2.90 correspond to the surface-to-volume ratio values of 2.51, 1.72 and 1.23, respectively.

In the considered system, the characteristics of the equilibrium state are obtained by minimizing the Gibbs function ( $g$ ) per one mole of matter including the energy contributions of all interface boundaries:

$$g = \sum_j (n_{1j} + n_{2j}) G_j(x_{1j}, T) + \sigma_s A_s + \sigma_{cs} A_s, \quad (2)$$

$$G_j(x_{1j}, T) = A_{1j} x_{1j} (1 - x_{1j}) + A_{2j} x_{1j}^2 (1 - x_{1j}) + A_{3j} x_{1j} (1 - x_{1j})^2 + RT (x_{1j} \ln x_{1j} + (1 - x_{1j}) \ln (1 - x_{1j})).$$

Here,  $\sigma_{cs}$  and  $\sigma_s$  are the surface energies of the inner (*core-shell*) and outer (*shell-*) interface boundaries while  $R$  is the universal gas constant. The parameters  $A_I$ ,  $A_{II}$ ,  $A_{III}$  are as follows:  $A_I = 30202.0$ ;  $A_{II} = 2635.5$ ;  $A_{III} = 0$  [9, 15]. The energies of interface boundaries are calculated using the first approximation (this approach and the obtained results are not accompanied by any losses of generality, see also [17, 19]):  $\sigma_{cs} = 0.5 \sum_j \sigma(x_{1j})$ ,  $\sigma(x_{1j}) = \sigma_1 x_{1j} + \sigma_2 (1 - x_{1j})$ ,  $\sigma_s = \sigma_1 x_{1s} + \sigma_2 (1 - x_{1s})$ . Here,  $\sigma_1 = 0.657 \text{ J/m}^2$ ,  $\sigma_2 = 1.110 \text{ J/m}^2$  [9, 15].

In the case of the properties of small-volume systems being considered in the framework of the thermodynamical approach, the problem of the thermodynamics applicability at the nanoscale and its lower boundary cannot be ignored. As the authors of [23] have noted, it is the most appropriate to apply the theoretical approaches based on the fluctuation theory to determine the applicability limits of chemical thermodynamics. Indeed, spontaneous fluctuations of thermodynamical characteristics (associated with the discreteness of the atomic-molecular structure of any system, being increased with a decrease in the amount of the matter which forms the system) represent the natural limitations on the application of thermodynamical approaches: if the fluctuation values of a parameter get comparable with the values of the parameter, this fact testifies, on the one hand, to the inadequate application of the thermodynamics techniques in this case, on the other hand, to the instability of the considered system itself as well as to the tendency of its decomposition due to fluctuations.

In [23], the authors have analyzed the fluctuations of temperature and surface tension of nanostructures. The temperature is taken into account by the authors (instead of the density, for example) due to the fact that the temperature plays the role of the “only state parameter introduced in the thermodynamics in addition to the mechanical variables such as pressure  $P$  and volume  $V$ ” for simple systems. Meanwhile, the structure stability of small-volume systems directly depends on the value of a temperature fluctuation. In order to estimate the absolute value of the root-mean-square temperature fluctuation  $\delta T$ , the following expression can be used:  $\delta T = T \sqrt{R/C_X N}$ . Here,  $X$  is the variable (or the set of variables) which remain constant in the considered case;  $N$  is the number of molecules and atoms which are contained in the considered systems;  $R$  is the universal gas constant;  $C_X$  is the molar heat capacity at  $X = \text{const}$ . In [23], it is assumed that  $X = P$  while the isobaric molar heat capacity is included into the abovementioned expression (in the considered case, the surface contribution to the heat capacity of a nanosystem is not taken into account since the value of the temperature derivative of the surface enthalpy (introduced for the first time by E. Guggenheim) does not exceed a fraction of a cent of heat capacity  $C_p$  according to the authors’ early assessments). The results of calculating  $\delta T$  are given in Table 1 of [23] where nanoscale droplets of  $n$ -butane and solid nanoscale aluminum and sodium particles have been used as model systems. The calculations show that the value of  $\delta T$  does not exceed a few percent in all the three cases even for a system containing  $N = 100$  atoms or molecules ( $\delta T$  decreases with an increase in  $N$ ).

In their turn, the following expression is used in order to calculate the relative fluctuations  $\Delta\sigma/\sigma$  of the surface tension:

$$\frac{\Delta\sigma}{\sigma} = \begin{cases} \sqrt{\frac{kT\beta_T}{12\pi r^3}}, & r \leq r_{ch} \\ 0, & r > r_{ch} \end{cases}$$

where  $k$  is the Boltzmann constant;  $r$  is the radius of a nanoparticle;  $\beta_T$  is the isothermal compressibility;  $r_{ch}$  is the characteristic size determined as follows: in the case  $r > r_{ch}$ , the surface tension of a nanoparticle can be considered to be equal to its macroscopic value; in the case  $r \leq r_{ch}$ , it is assumed that the dependence of the surface tension on the system size is described by the linear formula of A.I. Rusanov:  $\sigma = Kr$  where  $K$  is the proportionality factor which is commonly estimated based on numerical simulations or empirically.

As it is demonstrated in Table 2 of [23], where the estimates of fluctuations for several pure metals are given, the fluctuation values are no more than a fraction of a cent even for a cluster containing 12 atoms. The considered estimates can also be accompanied by the considerations of M.N. Magomedov on the minimum nanoparticle size at which the differences between solid and liquid phases disappear. The geometric

characteristics of the objects studied in this paper correspond to the area where the applicability of the thermodynamical approach leaves no doubt.

### 3. Simulation results and discussion

The Gibbs function of a two-components phase-separating system with a *core-shell* structure (1-2) has two minima which correspond to two-phase states with different mutual positions of co-existing phases. Below, the state where the *core*-phase is formed with tungsten (while the *shell*-phase is chromium based) is referred as “state 1”. Vice versa, chromium prevails in the *shell*-phase in state 2. In the case the bulk nanoparticles are dealt with, the minima of the Gibbs function corresponding to each state are symmetric and characterized by equal energies while the compositions of co-existing *core*- and *shell*-phases do not depend on the state, which emerges in the nanoparticle. The compositions of *core*- and *shell*-phases in the bulk structures are also independent on particle size and morphology and match the reference data [8]. At the nanoscale, due to the significant increase in the energy contribution of all the interface boundaries in the system, the minima of the Gibbs function shift in comparison with the ones of bulk structures. As a result, the compositions of *core*- and *shell*-phases depend on the mutual arrangement of co-existing phases, being different in states 1 and 2, as well as on the size and morphology of the considered nanoparticles. The free energy of nanoparticles in state 1 is lower than the one of state 2, i.e., state 2 becomes metastable.

The effects demonstrated below result from the tendency of the nanosystem to reduce its free energy: in a *core-shell* structure; such reduction can be realized according to the three mechanisms. The terms introduced in [17] being used, these mechanisms are as follows:

- *volume-controlled segregation*: transferring the matter from the inner phase (*core*-) into the outer one (*shell*-) leading to a decrease in the area of the internal (*core-shell*) interface boundary (this mechanism is hereinafter denoted as “mechanism 1”);

- *surface energy-controlled segregation*: enriching predominantly the outer (*shell*-) phase with the component with the lower surface energy leading to a decrease in the energy of the external interface boundary (the energy contribution of the internal one being much lower practically always; this mechanism is hereinafter denoted as “mechanism 2”);

- *suppression*: maintaining the homogeneous state of the system, the phase-separation process being suppressed. Physically, this mechanism stems from reducing the upper critical dissolution temperature down to the value below the considered one (this mechanism is hereinafter denoted as “mechanism 3”). In the case mechanism 3 being realized, the minimum of the Gibbs function corresponding to the considered heterogeneous state disappears, being replaced by the one corresponding to the homogeneous configuration.

In the considered system, tungsten is characterized by higher values (in comparison with chromium) by higher values of the molar volume and surface energy at the same time. The effective diameter of the nanoparticles simulated below is 40 nm. The nanoparticle composition is equiatomic.

For both states, Fig. 1 illustrates the dependence of the solubility limits of chromium in tungsten on the nanoparticle morphology and temperature. The realization of the considered effects is the most vivid for state 2: the lower the volume of a nanoparticle is and the more complicated the morphology of a nanoparticle is (the lower the fractal dimension is), the higher the solubility of chromium in tungsten. For example, being equal to ~9 at. % (the values for bulk structures are given in Fig. 1 with the solid line without markers) for macroscale particles at  $T = 1300$  K, the solubility limit demonstrates a dramatic increase up to ~14 (for  $D = 2.90$ ) and ~15 at. % ( $D = 2.80$ ). At the same time, variations of the fractal dimension of a nanoparticle in state 2 lead to small changes in the solubility of W in Cr. For state 1, the solubility of chromium in tungsten shows a lower sensitiveness to the changes in  $D$  (which is accompanied, however, by a significant reduction of the mentioned solubility limit with a decrease in the nanoparticle effective diameter).

Fig. 2, in its turn, demonstrates how the nanoparticle morphology influences on the solubility of W in Cr in state 1. Firstly, the lower the fractal dimension is, the lower the solubility limit of tungsten in chromium turns out to be. Secondly, the relation between the nanoscale solubility limit and the bulk one depends on the fractal dimension of a nanoparticle. In detail, the solubility of tungsten in chromium in nanoparticles is lower than the one in the bulk state in the case of  $D < 2.90$ . In the case of “regular” nanoparticles ( $D = 3.00$ ), meanwhile, the solubility limit exceeds the bulk value at “high” temperatures near the UCdT.

At lower temperatures, however, the solubility limit is somewhat lower in comparison with the one for macro-sized particles. Taking into account the mechanisms listed above, the demonstrated regularities can be

explained as follows: “complicating” the morphology and decreasing the effective diameter of a nanoparticle in state 2 leads to the predominant implementation of mechanism 2 (“*surface energy-controlled segregation*”); the atomic fraction of Cr in the *shell*-phase grows up.

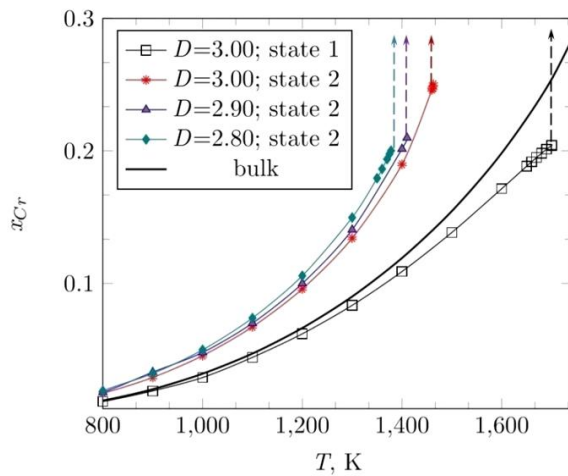


**Fig. 1.** Temperature - dependent phase equilibria (the chromium solubility in tungsten, atomic fractions) for nanoparticles in different states of the *core-shell* structure for various values of  $D$ .

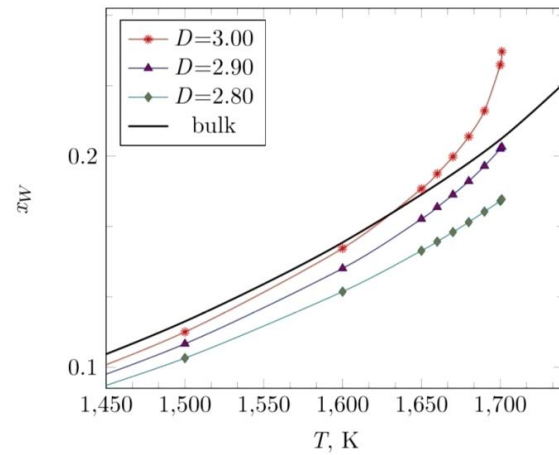


**Fig. 2.** Temperature-dependent phase equilibria (the tungsten solubility in chromium, atomic fractions) for nanoparticles in state 1 for various values of  $D$ .

The same mechanism 2 is characteristic for “regular” ( $D = 3.00$ ) nanoparticles in state 1 at “low” temperatures (a decrease in the atomic fraction of W in the *shell*-phase is observed). At “higher” temperatures, at the same time, mechanism 1 (“*volume-controlled segregation*”) is realized while the tungsten content is increased in the *shell*-phase. If the nanoparticle morphology becomes more complicated (i.e., the fractal dimension of a nanoparticle is reduced) at any temperature in state 1, the realization of mechanism 2 manifests itself (in more detail, the “competition” between the mechanisms of reducing the free energy is discussed in [16, 17, 19]). In the Fig. 1, the vertical dashed lines represent the temperatures at which mechanism 3 (“*suppression*”) is implemented in nanoparticles. At these temperatures, the minimum of the Gibbs function (which corresponds to the heterogeneous state 2) disappears with the appearance of another one in the position of the homogeneous state without the phase separation.

The “*suppression*” temperature for state 1 is higher than the one for state 2 (as demonstrated in Fig. 1): between these temperatures for states 1 and 2, the heterogeneous state 1 and the homogeneous state formed instead of the heterogeneous state 2 are the possible ones in the system. Above the “*suppression*” temperature for state 1, the homogeneous configuration becomes the only possible one. As mentioned above, the “*suppression*” temperatures for nanoparticles can be associated with the nanoscale UCDD values for states 1 and 2; in both cases the UCDDs are much lower in comparison with the bulk values, especially for nanoparticles in state 2: the UCDD reduction with a decrease in the fractal dimension reaches the values of hundreds degrees. The demonstrated results can be accompanied by several other non-trivial effects in small-volume structures, e.g., by the effect of the chemical composition. In bulk structures, a variation of the initial composition of the considered system leads only to changes in the volume fractions of co-existing phases (directly according to the so-called “*lever rule*”) but has no influence on the equilibrium phase composition. In small-volume systems, in their turn, not only the volume fractions but also the compositions of *core*- and *shell*-phases (and co-existing phases in the most general case) at equilibrium depend on the initial composition. This effect is generic for nanoscale structures, being explained by the realization of different mechanisms of lowering the free energy of the system in the case of nanoparticles of different compositions (see [17, 19] for more details).

In real-life fabrication processes, the nanoparticle ensembles are dealt with instead of individual nanoparticles, being characterized by the size and shape distributions. As shown by us in [26, 28], the equilibrium size distributions for a free-dispersed system formed by nanoparticles with fractal dimension  $D$  can be expressed as follows:

$$f_D(\phi_p, D, N) \sim \exp\left(-\frac{\gamma A_{sp}(D) + RT \ln f_p}{RT}\right), \quad f_p = \frac{N}{N - \phi_p} \exp\left\{\pi\left(\sqrt{\frac{2}{3}}(N - \phi_p) - \sqrt{\frac{2}{3}}N\right)\right\}.$$

Here,  $\phi_p = \omega(d_{eff}/d_{at})^3$  is the so-called “stoichiometric number” of a nanoparticle (the number of atoms in a nanoparticle),  $A_{sp}(D)$  is the specific surface area of the nanoparticle ensemble,  $\gamma$  is the surface energy of the material in the considered external environment (see also some remarks in Ref. [20]);  $\omega$  is the lattice packing density,  $N$  is the total number of atoms in the system,  $d_{at}$  is the atomic diameter.

The suggested calculation technique provides the results which are in perfect accordance with the experimentally observed distributions (see [26] and Refs. therein). The estimates can be obtained which make it possible to model the thermodynamical conditions for the realization of optimal average geometric characteristics of nanoparticles leading to the optimal phase composition as well to predict the degree at which the equilibrium phase compositions and the set of composition-dependent functional properties are “blurred” in an ensemble. For example, average fractal dimension  $\langle D \rangle$ , average stoichiometric number  $\langle \phi_p \rangle$  and average effective diameter  $d_{eff}$  of nanoparticles in the ensemble can be calculated as follows [28]:

$$\langle D \rangle = \frac{\sum_i D_i \int f_D(D_i, \phi_p, N) d\phi_p}{\Omega(N)}, \quad \langle \phi_p \rangle = \frac{\sum_i \int \phi_p f_D(D_i, \phi_p, N) d\phi_p}{\Omega(N)},$$

$$\langle d_{eff} \rangle = \Omega(N)^{-1} d_{at} \sum_i \int f_D(D_i, \phi_p) d\phi_p, \quad \Omega(N) = \sum_i \int f_D(D_i, \phi_p, N) d\phi_p.$$

Here, the limits of the integration over  $\phi_p$  belong to range  $[1, N]$  while the sample of distributions is considered where  $D_i \in (2, 3)$  with an arbitrarily selected step [26, 28].

The fractal dimension of nanoparticles can be estimated based on the optical or electron microscopy data using various methods including the so-called “box-counting technique” [29]. In the framework of the mentioned approach, the image of the considered nanoparticle ensemble is converted into a monochrome one which is then divided into square equal-area cells. In order to calculate the fractal dimension, the image divided into cells is transformed into a square matrix. If the brightness of a cell exceeds the preliminarily selected brightness threshold value ( $B_{th}$ ), such a cell corresponds to the matrix cell with the value of 1. Otherwise, an image cell is represented by a matrix cell with the value of 0. Based on this transformation, fractal dimension  $D$  is calculated using the following expression:  $S = AL^D$  where  $S$  is the number of matrix cells with the value of 1;  $L$  is the matrix rank;  $A$  is the factor which matches dimensions. The dependence is obtained using the least squares method: the matrix rank being sequentially decreased (the cell size being increased) by 2, 4, 8, ... times provided that the value of 1 is assigned to the cells which contain at least one pixel of the initial image, the brightness of which exceeds the selected threshold value.

In the general case, the calculated fractal dimension is sensitive to the value of  $B_{th}$ , being varied in a wide range when changing  $B_{th}$ . For selecting the correct value of  $B_{th}$ , the “calibration” dependence ( $D(B_{th})$ ) is constructed. The sensitivity of the fractal dimension to the brightness threshold is represented by the inclination angle of curve  $D(B_{th})$ . An example of such “calibration” dependences is demonstrated in [30].

In the formal consideration, the random uniformly distributed white noise is characterized by its fractal dimension as well as by the relation between  $D$  and the brightness threshold in the form of a smooth monotonously decreasing function as follows:

$$D(B_{th}) = 2 + \frac{\ln\left(1 - \frac{B_{th}}{B_{th}^{max}}\right) - \ln A}{\ln L}, \quad S = L^2 \left(\frac{B_{th}^{max} - B_{th}}{B_{th}^{max}}\right) = AL^D.$$

In the case of a square image,  $A = 1$ . However, the dependence of  $D$  on matrix rank  $L$  does not allow considering the random noise as an appropriate fractal object for the application of the box-counting techniques. The monochrome images of the classical fractal objects (Koch snowflakes, Sierpinski carpets, fractal trees etc) are characterized by  $D = \text{const}$ ,  $A = \text{const}$  for any  $B_{th}$ . For real images which represent

superpositions of fractal structure and noise, dependence  $D(B_m)$  contains straight sections, steps as well as extrema and inflection points. The correct brightness threshold value corresponds to the straight section within which the deviation of dependence  $\ln S = D \ln L + \ln A$  from a straight line is minimal. This section is found based on the minimum value of the first derivation of dependence  $D(B_m)$ . The absence of a well-pronounced straight section can result from the heterogeneity of optical properties of nanoparticles or to the insufficient image quality.

#### 4. Conclusion

The performed thermodynamical analysis of how the phase equilibria in nanoscale particles of phase-separating solid solutions depend on the particle morphology using the example of W-Cr heavy pseudo alloy leads to the following conclusions.

1. A nanoparticle with a *core-shell* structure has two possible two-phase states which correspond to different mutual arrangements of co-existing tungsten-based and chromium-based phases. Unlike systems in the bulk state where both phases have equal free energies and compositions of *core*- and *shell*-phases, in nanoscale particles, the phase compositions are considerably different in each state.

2. The temperature range in which the heterogeneous state is stable significantly shrinks with reducing the volume of a nanoparticle and “complicating” its morphology. The upper critical dissolution temperatures for each state of the *core-shell* structure are also different, being both reduced with a decrease in the particle size and fractal dimension.

3. The equilibrium phase composition of nanoparticles in each state depends on the particle morphology while the pattern itself of the dependences of mutual solubilities significantly differs for particles of various shapes in different states. This fact is associated with the occurrence of three different mechanisms (“volume-controlled segregation”, “surface energy-controlled segregation” and “suppression”) which can manifest themselves at the same time and even be “competing”.

The obtained regularities also demonstrate an additional “knob” which makes it possible to tune multiple composition-dependent functional properties of nanostructured materials (including electrical and thermal conductivity, resistivity to corrosion, elastic properties etc) through the taking into account the specific influence of morphology factors on the phase composition at the nanoscale. Such considerations could also be accompanied either with the up-to-date techniques of the controllable synthesis of nanoparticles with a given shape or with the methods of describing and predicting various properties of nanoparticle ensembles. In the latter case, our considerations can be helpful in predicting the range possible variations of nanoparticle phase compositions as well as the degree at which the corresponding functional properties are “blurred” in an ensemble.

#### Acknowledgments

The authors cordially thank Thesis Council 24.2.340.04 (N.I. Lobachevsky Nizhny Novgorod State University) for valuable discussions during the thesis defense on May 18, 2023.

The authors also thank two anonymous reviewers for the attention to the study and valuable remarks.

#### REFERENCES

- 1 Vilémová M., Illková K., Lukáš F., et al. Microstructure and phase stability of W-Cr alloy prepared by spark plasma sintering. *Fus. eng. des.*, 2018, Vol. 127, pp. 173 – 178. doi:10.1016/j.fusengdes.2018.01.012.
- 2 Hou Q.-Q., Huang K., Luo L.-M., Tan X.-Y., et al. Microstructure and its high temperature oxidation behavior in W-Cr alloys prepared by spark plasma sintering. *Materialia*, 2019, Vol. 6, p.100332. doi:10.1016/j.mtla.2019.100332.
- 3 Bose A., Schuh C.A., Tobia J.C., et al. Traditional and additive manufacturing of a new tungsten heavy alloy alternative. *Int. j. refract. met. hard mater.*, 2018. Vol. 73, pp. 22 – 28. doi:10.1016/j.ijrmhm.2018.01.019.
- 4 Tilmann W., Fehr A., Heringhaus M. Mechanical milling to foster the solid solution formation and densification in Cr-W-Si for hot-pressing of PVD target materials. *Adv. powder technol.*, 2021, Vol.32, No.6, pp. 1927 – 1934. doi:10.1016/j.appt.2021.04.001.
- 5 Olakanmi E.O., Cochrane R.F., Dalgarno K.W. A review of selective laser sintering/melting (SLS/SLM) of aluminium alloy powders: Processing, microstructure, and properties. *Prog. mater. sci.*, 2015. Vol. 74, pp. 401 – 477. doi:10.1016/j.pmatsci.2015.03.002.
- 6 Cordero Z.C., Carpenter R.R., Schuh C.A., et al. Sub-scale ballistic testing of an ultrafine grained tungsten alloy into concrete targets. *Int. j. impact eng.*, 2016, Vol. 91, pp. 1 – 5. doi:10.1016/j.ijimpeng.2015.11.013.

- 7 Chookajorn T., Park M., Schuh C.A. Duplex nanocrystalline alloys: entropic nanostructure stabilization and a case study on W-Cr. *J. mater. res.*, 2015., Vol. 30, No. 2, pp. 151 – 162. doi:10.1557/jmr.2014.385.
- 8 Udovskii A.L., Karpushkin V.N., Nikishina E.A. A method for autonomous thermodynamic assessment of phase diagrams of binary systems containing  $p$  disordered phases of variable composition and  $q$  phases of constant composition at  $(p, q) \leq 10$ . *Metally*, 1991. No. 4, pp. 87 – 103 [in Russian].
- 9 Shishulin A.V., Shishulina A.V. Equilibrium phase composition and mutual solubilities in fractal nanoparticles of the W-Cr heavy pseudo-alloys. *Physical and chemical aspects of the study of clusters, nanostructures and nanomaterials*, 2019, No. 11. pp. 380 – 388. doi:10.26456/pcascnn/2019.11.380.
- 10 Bajaj S., Haverty M.G., Arróyave R., Goddard W.A., Shankar S. Phase stability in nanoscale material systems: extensions from bulk phase diagrams. *Nanoscale*, 2015, Vol. 7, No. 9868. doi:10.1039/C5NR01535A.
- 11 Shirinyan A., Wilde G., Bilgorodskyy Y. Melting loops in the phase diagram of individual nanoscale alloy particles: completely miscible Cu-Ni alloys as a model system. *J. mater. sci.*, 2020. Vol. 55, pp. 12385 – 12402. doi:10.1007/s10853-020-04812-2.
- 12 Mendoza-Pérez R., Muhl S. Phase diagrams of refractory bimetallic nanoalloys. *J. nanopart. res.*, 2020, Vol. 22, No. 36. doi:10.1007/s11051-020-05035-x.
- 13 Geoffrion L.-D., Guisbiers G. Chemical ordering in  $\text{Bi}_{1-x}\text{-Sb}_x$  nanostructures: Alloy, janus or core-shell? *J. phys. chem., C*. 2020, Vol.124, No.25, pp. 14061 – 14068. doi:10.1021/acs.jpcc.0c04356.
- 14 Geoffrion L.D., Guisbiers G. Physico-chemical properties of selenium–tellurium alloys across the scales. *Nanoscale Adv.*, 2021. Vol.3, No.14, pp. 4254 – 4270. doi:10.1039/D1NA00087J.
- 15 Shishulin A.V., Fedoseev V.B. Effect of initial composition on the liquid–solid phase transition in Cr-W alloy nanoparticles. *Inorg. mater.*, 2019. Vol.55, No.1, pp. 14 – 18. doi:10.1134/S0002337X19010135.
- 16 Ghasemi M., Zanolli Z., Stankovski M., Johansson J. Size- and shape-dependent phase diagram of In-Sb nanoalloys. *Nanoscale*, 2015, Vol. 7, pp. 17387 – 17396. doi:10.1007/s10891-020-02182-9.
- 17 Shishulin A.V., Potapov A.A., Shishulina A.V. The initial composition as an additional parameter determining the melting behavior of nanoparticles (a case study on  $\text{Si}_x\text{-Ge}_{1-x}$  alloys). *Eurasian phys. tech. j.*, 2021, Vol. 18, No.4, pp. 5 – 13. doi:10.31489/2021NO4/5-14.
- 18 Guisbiers G., Khanal S., Ruiz-Zapeda F., Roque de la Puente J., Yakaman M.-J. Cu-Ni nanoalloy: mixed, core-shell or janus nanoparticles? *Nanoscale*, 2014, Vol. 6, pp. 14630-14635. doi:10.1039/C4NR05739B.
- 19 Shishulin A.V., Shishulina A.V. One more parameter determining the stratification of solutions in small-volume droplets. *J. eng. phys. Thermophys.*, 2022, Vol. 95, No. 6, pp. 1374 – 1382. doi:10.1007/s10891-022-02606-8.
- 20 Shishulin A.V., Fedoseev V.B., Shishulina A.V. Environment-dependent phase equilibria in a small-volume system in the case of the decomposition of Bi-Sb solid solutions. *Butlerov commun.*, 2017. Vol. 51, No. 7, pp. 31 – 37 [in Russian].
- 21 Guisbiers G. Advances in thermodynamic modeling of nanoparticles. *Adv. phys. X.*, 2019, Vol. 4, No.1, 1668299. doi:10.1080/23746149.2019.1668299
- 22 Magomedov M.N. On the statistical thermodynamics of a free-standing nanocrystal: silicon. *Cryst. rep.*, 2017, Vol. 63, No. 3, 480 – 496. doi:10.1134/S1063774517030142.
- 23 Samsonov V.M., Demenkov D.E., Karcharov V.I., Bembel A.G. Fluctuation approach to the problem of thermodynamics applicability to nanoparticles. *Bull. Russ. acad. sci.: phys.*, 2011. Vol. 75, No. 8, pp. 1073 – 1077. doi:10.3103/S106287381108034X.
- 24 Straumal B.B., Mazilkin A.A., Straumal P.B., Gusak A.M., Baretzky B. Shift of lines in phase diagrams for nanograined materials. *Adv. struct. mater.*, 2013. Vol. 4, pp. 265 – 285. doi:10.1007/8611\_2010\_29.
- 25 Radnóczy G., Bokányi E., Erdélyi Z., Misják F. Size-dependent spinodal decomposition in Cu–Ag nanoparticles. *Acta mater.*, 2017. Vol. 123., pp. 82– 89. doi:10.1016/j.actamat.2016.10.036
- 26 Fedoseev V.B., Shishulin A.V. On the size distribution of dispersed fractal particles. *Tech. phys.*, 2021. Vol. 66, No. 1, pp. 34 – 40. doi:10.1134/S1063784221010072
- 27 Shishulin A.V., Potapov A.A., Shishulina A.V. On the transition between ferromagnetic and paramagnetic states in mesoporous materials with fractal morphology. *Eurasian phys. tech. j.*, 2021, Vol. 18, No.2, pp. 6 – 11. doi:10.31489/2021NO2/6-11.
- 28 Shishulin A.V., Potapov A.A., Shishulina A.V. Several notes on the lattice thermal conductivity of fractal-shaped nanoparticles. *Eurasian phys. tech. j.*, 2022, Vol. 19, No.3, pp. 10 – 17. doi:10.31489/2022NO3/10-17.
- 29 Li J., Du Q., Sun C. An improved box-counting method for image fractal dimension estimation. *Pattern recognit.*, 2009. Vol. 42, pp. 2460 – 2469. doi:10.1016/j.patcog.2009.03.001.
- 30 Fedoseeva E.N., Fedoseev V.B. Interaction of chitosan with benzoic acid in solution and films. *Polymer sci. Ser. A.*, 2011. Vol. 53, No. 11, pp. 1040 – 1046. doi:10.1134/S0965545X1110004X.

SUMMARIES	ТҮСІНІКТЕМЕЛЕР	АННОТАЦИИ
<p><b>Tareq M.H., Lafta Sadeq H., Hussain Wafaa A.</b>  <b>Төмен мольдік қатынаста <math>Cs_yCo_{1-0.5y}Fe_2O_4</math> нанобөлшектерінің магниттік қасиеттерін зерттеу</b>          Магниттік қасиеттерді басқару үшін бұрын пайдаланылмаған элементтермен ферритті алмастыру әсері зерттеушілер үшін үлкен қызығушылық тудырады. Бұл зерттеуде <math>Cs_yCo_{1-0.5y}Fe_2O_4</math> нанобөлшектерінің құрылымдық және магниттік қасиеттеріне у молярлық қатынасы 0,0, 0,05, 0,15 және 0,25 болғандағы Cs-дің төмен алмастыруының әсері көрсетілген. Синтез әдісі ретінде тұндыру әдісі таңдалды. Металл хлоридтері рН 10-ға жету мақсатында NaOH көмегімен тазартылған суда реакция жүргізу үшін пайдаланылды. Барлық үлгілер үшін рентгендік дифракция, өрістік эмиссиялық сканерлеуші электронды микроскопиясы, электронды дисперсиялық рентгенография және діріл үлгілерінің магнитометриясы жүргізілді. Барлық үлгілерде шпинельдік құрылым негізінен Со ферритінің құрылымымен сәйкес келеді. Cs мөлшерінің артуымен тордың тұрақтысының жалпы артуы байқалды, бұл кезде мольдік қатынас 0-ден 0,25-ке дейін өскенде кристаллит өлшемдері шамамен 18-ден 12,2 нм-ге дейін азайды. Электронды-микроскопиялық зерттеу барлық үлгілерде басқа пішіндерсіз сфералық нанобөлшектер бар екенін көрсетті. Cs1+ мөлшері артқан кезде бөлшектердің орташа өлшемі 40-тан 60 нм-ге дейін болды. Магниттік параметрлер негізінен салыстырмалы түрде жоғары коэрцитивті күшті (кең ілмектер) және магниттелу қанықтылығының (50,43 мкГ/г дейін), кристалды анизотропты тұрақтылық пен квадраттық коэффициенттің төмендеуін көрсетті.  <b>Кілт сөздері:</b> цезий-кобальт ферриті, құрылымдық қасиеттері, гистерезис ілмегі, нанобөлшектер, магниттеу.</p>	<p><b>Tareq M.H., Lafta Sadeq H., Hussain Wafaa A.</b>  <b>Исследование магнитных свойств наночастиц <math>Cs_yCo_{1-0.5y}Fe_2O_4</math> при низком молярном соотношении</b>          Эффект замещения феррита ранее не использовавшимися элементами для управления магнитными свойствами представляет большой интерес для исследователей. Данное исследование иллюстрирует влияние низкого замещения Cs с молярными соотношениями у, равных 0,0, 0,05, 0,15 и 0,25, на структурные и магнитные свойства наночастиц <math>Cs_yCo_{1-0.5y}Fe_2O_4</math>. Метод синтеза являлся методом осаждения. Хлориды металлов использовались для проведения реакции в дистиллированной воде с использованием NaOH для достижения рН 10. Для всех образцов были проведены рентгеновская дифракция, полевая эмиссионная сканирующая электронная микроскопия, электронно-дисперсионная рентгенография и магнитометрия вибрирующих образцов. У всех образцов шпинельная структура в значительной степени совпадает с структурой феррита Со. Наблюдалось общее увеличение постоянной решетки с ростом содержания Cs, в то время как размер кристаллитов уменьшался примерно с 18-ти до 12,2 нм при увеличении молярного соотношения от 0 до 0,25. Электронно-микроскопическое исследование показало, что все образцы имеют сферические наночастицы без каких-либо других форм. Средний размер частиц составлял от 40 до 60 нм при увеличении содержания Cs1+. Магнитные параметры в основном показали относительно высокую коэрцитивную силу (широкие петли) и снижение насыщенности намагниченности (до 50,43 мкГ/г), кристаллической анизотропной постоянной и коэффициента квадратичности.  <b>Ключевые слова:</b> цезий-кобальтовый феррит, структурные свойства, петля гистерезиса, наночастицы, намагничивание.</p>	<p><b>Tareq M.H., Lafta Sadeq H., Hussain Wafaa A.</b>  <b>Исследование магнитных свойств наночастиц <math>Cs_yCo_{1-0.5y}Fe_2O_4</math> при низком молярном соотношении</b>          Эффект замещения феррита ранее не использовавшимися элементами для управления магнитными свойствами представляет большой интерес для исследователей. Данное исследование иллюстрирует влияние низкого замещения Cs с молярными соотношениями у, равных 0,0, 0,05, 0,15 и 0,25, на структурные и магнитные свойства наночастиц <math>Cs_yCo_{1-0.5y}Fe_2O_4</math>. Метод синтеза являлся методом осаждения. Хлориды металлов использовались для проведения реакции в дистиллированной воде с использованием NaOH для достижения рН 10. Для всех образцов были проведены рентгеновская дифракция, полевая эмиссионная сканирующая электронная микроскопия, электронно-дисперсионная рентгенография и магнитометрия вибрирующих образцов. У всех образцов шпинельная структура в значительной степени совпадает с структурой феррита Со. Наблюдалось общее увеличение постоянной решетки с ростом содержания Cs, в то время как размер кристаллитов уменьшался примерно с 18-ти до 12,2 нм при увеличении молярного соотношения от 0 до 0,25. Электронно-микроскопическое исследование показало, что все образцы имеют сферические наночастицы без каких-либо других форм. Средний размер частиц составлял от 40 до 60 нм при увеличении содержания Cs1+. Магнитные параметры в основном показали относительно высокую коэрцитивную силу (широкие петли) и снижение насыщенности намагниченности (до 50,43 мкГ/г), кристаллической анизотропной постоянной и коэффициента квадратичности.  <b>Ключевые слова:</b> цезий-кобальтовый феррит, структурные свойства, петля гистерезиса, наночастицы, намагничивание.</p>
<p><b>Солдатхан Д., Амангелді Н., Маханов К.М., Смагулов Ж.К., Әнуар А., Мәуей Б.</b>  <b>Үдетілген <math>{}^6Li</math> - литий және <math>{}^{16}O</math> – оттегі ядролардың <math>{}^{12}C</math> – көміртегі ядросынан шашырауын жартылай микроскопиялық талдауда жана ВЗУ-Fetal потенциалын қолдану</b>          Төмен энергияда үдетілген <math>{}^6Li</math> - литий, <math>{}^{16}O</math> – оттегі иондарының <math>{}^{12}C</math> -көміртегі ядродан шашырауының бұрыштық таралуынан табылған феноменологиялық және жартылай микроскопиялық потенциалдар мәндері анықталған. Серпімді шашыраудың эксперименттік деректеріне оптикалық модель және екілік фолдинг модель шеңберінде талдау жасалған. Фолдинг модель негізінде тиімді нуклон-нуклондық өзара әсерлесудің тығыздыққа тәуелді Юкаваның 3 терминді Fetal потенциалы алғаш рет қолданылған. Оптикалық потенциалдың нақты бөлігі ретінде Юкаваның 3 терминді Fetal, Reid, Paris потенциалдарының тығыздыққа тәуелді микрофолдинг түрлері екілік фолдинг модельде құрылды. <math>{}^{16}O+{}^{12}C</math> ядролық жүйе үшін зертханалық 28 MeV және 30 MeV энергияларда жаңа Fetal микропотенциалының тиімділігі Reid, Paris нұсқаларымен салыстырылмалы түрде зерттелген. <math>{}^6Li+{}^{12}C</math> ядролық жүйесі үшін зертханалық 12,3 MeV және 20 MeV энергияларда жаңа Fetal күй теңдеуінің тиімділігі Reid, Paris нұсқаларымен салыстырылмалы түрде зерттелген. Феноменологиялық талдаудың нәтижесінде эксперименттік және теориялық кималардың салыстырмалы кателіктері 1,1 – 3,0 аралықта анықталды. Жартылай микроскопиялық талдаудың нәтижесінде микрофолдинг потенциалдардың қайта нормалау коэффициенттері 0,8 - 1,0 аралығында анықталды. Алынған мәліметтері әртүрлі іргелі зерттеулерде, атап айтқанда болашақтағы термоядролық қондырғыларда және ядролық астрофизикада қолданылатын болады.  <b>Кілт сөздері:</b> ядролық материя, серпімді шашырау, жартылай микроскопиялық талдау, ВЗУ- Fetal потенциалы.</p>	<p><b>Солдатхан Д., Амангелді Н., Маханов К.М., Смагулов Ж.К., Әнуар А., Мәуей Б.</b>  <b>Үдетілген <math>{}^6Li</math> - литий және <math>{}^{16}O</math> – оттегі ядролардың <math>{}^{12}C</math> – көміртегі ядросынан шашырауын жартылай микроскопиялық талдауда жана ВЗУ-Fetal потенциалын қолдану</b>          Төмен энергияда үдетілген <math>{}^6Li</math> - литий, <math>{}^{16}O</math> – оттегі иондарының <math>{}^{12}C</math> -көміртегі ядродан шашырауының бұрыштық таралуынан табылған феноменологиялық және жартылай микроскопиялық потенциалдар мәндері анықталған. Серпімді шашыраудың эксперименттік деректеріне оптикалық модель және екілік фолдинг модель шеңберінде талдау жасалған. Фолдинг модель негізінде тиімді нуклон-нуклондық өзара әсерлесудің тығыздыққа тәуелді Юкаваның 3 терминді Fetal потенциалы алғаш рет қолданылған. Оптикалық потенциалдың нақты бөлігі ретінде Юкаваның 3 терминді Fetal, Reid, Paris потенциалдарының тығыздыққа тәуелді микрофолдинг түрлері екілік фолдинг модельде құрылды. <math>{}^{16}O+{}^{12}C</math> ядролық жүйе үшін зертханалық 28 MeV және 30 MeV энергияларда жаңа Fetal микропотенциалының тиімділігі Reid, Paris нұсқаларымен салыстырылмалы түрде зерттелген. <math>{}^6Li+{}^{12}C</math> ядролық жүйесі үшін зертханалық 12,3 MeV және 20 MeV энергияларда жаңа Fetal күй теңдеуінің тиімділігі Reid, Paris нұсқаларымен салыстырылмалы түрде зерттелген. Феноменологиялық талдаудың нәтижесінде эксперименттік және теориялық кималардың салыстырмалы кателіктері 1,1 – 3,0 аралықта анықталды. Жартылай микроскопиялық талдаудың нәтижесінде микрофолдинг потенциалдардың қайта нормалау коэффициенттері 0,8 - 1,0 аралығында анықталды. Алынған мәліметтері әртүрлі іргелі зерттеулерде, атап айтқанда болашақтағы термоядролық қондырғыларда және ядролық астрофизикада қолданылатын болады.  <b>Кілт сөздері:</b> ядролық материя, серпімді шашырау, жартылай микроскопиялық талдау, ВЗУ- Fetal потенциалы.</p>	<p><b>Солдатхан Д., Амангелді Н., Маханов К.М., Смагулов Ж.К., Әнуар А., Мәуей Б.</b>  <b>Үдетілген <math>{}^6Li</math> - литий және <math>{}^{16}O</math> – оттегі ядролардың <math>{}^{12}C</math> – көміртегі ядросынан шашырауын жартылай микроскопиялық талдауда жана ВЗУ-Fetal потенциалын қолдану</b>          Төмен энергияда үдетілген <math>{}^6Li</math> - литий, <math>{}^{16}O</math> – оттегі иондарының <math>{}^{12}C</math> -көміртегі ядродан шашырауының бұрыштық таралуынан табылған феноменологиялық және жартылай микроскопиялық потенциалдар мәндері анықталған. Серпімді шашыраудың эксперименттік деректеріне оптикалық модель және екілік фолдинг модель шеңберінде талдау жасалған. Фолдинг модель негізінде тиімді нуклон-нуклондық өзара әсерлесудің тығыздыққа тәуелді Юкаваның 3 терминді Fetal потенциалы алғаш рет қолданылған. Оптикалық потенциалдың нақты бөлігі ретінде Юкаваның 3 терминді Fetal, Reid, Paris потенциалдарының тығыздыққа тәуелді микрофолдинг түрлері екілік фолдинг модельде құрылды. <math>{}^{16}O+{}^{12}C</math> ядролық жүйе үшін зертханалық 28 MeV және 30 MeV энергияларда жаңа Fetal микропотенциалының тиімділігі Reid, Paris нұсқаларымен салыстырылмалы түрде зерттелген. <math>{}^6Li+{}^{12}C</math> ядролық жүйесі үшін зертханалық 12,3 MeV және 20 MeV энергияларда жаңа Fetal күй теңдеуінің тиімділігі Reid, Paris нұсқаларымен салыстырылмалы түрде зерттелген. Феноменологиялық талдаудың нәтижесінде эксперименттік және теориялық кималардың салыстырмалы кателіктері 1,1 – 3,0 аралықта анықталды. Жартылай микроскопиялық талдаудың нәтижесінде микрофолдинг потенциалдардың қайта нормалау коэффициенттері 0,8 - 1,0 аралығында анықталды. Алынған мәліметтері әртүрлі іргелі зерттеулерде, атап айтқанда болашақтағы термоядролық қондырғыларда және ядролық астрофизикада қолданылатын болады.  <b>Кілт сөздері:</b> ядролық материя, серпімді шашырау, жартылай микроскопиялық талдау, ВЗУ- Fetal потенциалы.</p>

*Солдатхан Д., Амангелді Н., Маханов К.М., Смагулов Ж.К., Ануар А., Мауей Б.*

**Использование нового потенциала ВЗУ-Fetal при полумикроскопическом анализе рассеяния ускоренных ядер  ${}^6\text{Li}$  - лития и  ${}^{16}\text{O}$  - кислорода от ядра  ${}^{12}\text{C}$  – углерода**

Определены феноменологические и полумикроскопические значения потенциалов, обнаруженные в угловом распределении рассеяния  ${}^6\text{Li}$  - лития,  ${}^{16}\text{O}$  – ионов кислорода от ядра  ${}^{12}\text{C}$  - углерода, ускоренного при низких энергиях. Экспериментальные данные упругого рассеяния были проанализированы в рамках оптической модели и двойной модели фолдинга. На основе модели фолдинга впервые был использован потенциал Fetal, созданный в 3-терминах Юкавы, зависимой от плотности эффективного нуклонно-нуклонного взаимодействия. Зависимые от плотности типы микрофолдинга потенциалов Fetal, Reid, Paris, сформированные из 3-терминов Юкавы как реальная часть оптического потенциала были созданы в модели двойного фолдинга. Для ядерной системы  ${}^{16}\text{O}+{}^{12}\text{C}$  эффективность нового микропотенциала Fetal при лабораторных энергиях 28 МэВ и 30 МэВ изучена сопоставимо с вариантами Reid, Paris. Эффективность нового уравнения состояния Fetal при лабораторных энергиях 12,3 МэВ и 20 МэВ для ядерной системы  ${}^6\text{Li}+{}^{12}\text{C}$  изучалась сопоставимо с вариантами Reid, Paris. В результате феноменологического анализа были выявлены относительные погрешности экспериментального и теоретического сечений в интервале 1,1 - 3,0. В результате полумикроскопического анализа микрофолдинг определяли коэффициенты переформулирования потенциалов в пределах 0,8 - 1,0. Полученные данные будут использованы в различных фундаментальных исследованиях, в частности в будущих термоядерных установках и ядерной астрофизике.

**Ключевые слова:** ядерная материя, упругое рассеяние, полумикроскопический анализ, потенциал ВЗУ-Fetal.

*Нурутдинов И., Таиметов М. Ю., Ходжаев У. О., Омаров С. Х., Халлоков Ф. К.*

**Электронды сәулеленудің темір қосылған таллий мен индий моноселинидінің үштік кристалдарының кристалдық құрылымына, беттің микро рельефіне және зондталған еніне әсері.**

Берілген жұмыс электронды сәулеленудің темірмен легирленген таллий мен индий моноселинидтерінің үштік кристалдарының моно - және поликристалдарының құрылымына, беттік морфологиясына және тыйым салынған аймағына әсері зерттелген. Синтезделген поликристалды үлгілер, сондай-ақ өсірілген таллий және индий моноселинидті монокристалдар бір фазалы екендігі анықталды. Кристалдар келесі тор параметрлеріне ие болатын тетрагональды (кеңістіктік топ I4/mkm) элементар ұяшығы бар:  $a \sim b = 8,12 \text{ \AA}$ ,  $c = 6,88 \text{ \AA}$ ,  $\alpha = \beta = \gamma = 90^\circ$ . Энергиясы 2 МэВ және сәулелік ток тығыздығы  $0,085 \text{ мкА/см}^2$  электрондармен сәулелендіру электрондардың флюенсіне байланысты кристалдардың құрылымы мен қасиеттерінің күрделі түрде өзгеруіне әкеледі. Сонымен бірге кристалдық тор параметрлерінің өзгеруіне, профильдің орташа арифметикалық ауытқуының максималды мәнінің жоғарылауына, сондай-ақ сәулелендірілген кристалдар бетінің орташа кедір-бұдырлығының биіктігінің төмендеуіне әкеледі. Ұнтақ үлгісін энергия тығыздығы  $5 \times 10^{16} \text{ эл/см}^2$  электрондармен сәулелендіру нанокристаллит өлшемінің 32.50 нм-ден 43.33 нм-ге дейін арттыруына ықпалын тигізеді.

**Кілт сөздер:** монокристалл, кристалдық құрылым, элементар ұяшық, кеңістіктік топ, электронды сәулелену, флюенс, кристаллит өлшемі, кедір-бұдырлық.

*Нурутдинов И., Таиметов М.Ю., Ходжаев У.О., Умаров С.Х., Халлоков Ф.К.*

**Влияние электронного облучения на кристаллическую структуру, микро рельеф поверхности и зондированную ширину тройных кристаллов допированного железом таллия и моноселинида индия.**

В данной работе исследовано влияние электронного облучения на структуру, морфологию поверхности и запрещенную зону моно- и поликристаллов легированных железом тройных кристаллов моноселинидов таллия и индия. Установлено, что синтезированные поликристаллические образцы, а также выращенные монокристаллы моноселинидов таллия и индия являются однофазными. Кристаллы имеют тетрагональную элементарную ячейку (пр. гр. I4/mkm) со следующими параметрами решетки:  $a \sim b = 8,12 \text{ \AA}$ ,  $c = 6,88 \text{ \AA}$ ,  $\alpha = \beta = \gamma = 90^\circ$ . Облучение электронами с энергией 2 МэВ и плотностью тока пучка  $0,085 \text{ мкА/см}^2$  приводит к изменениям структуры и свойств кристаллов сложным образом в зависимости от флюенса электронов. Также приводит к изменению параметров кристаллической решетки, увеличению максимального значения среднеарифметического отклонения профиля, а также уменьшению высоты средней шероховатости поверхности облученных кристаллов. Облучение порошкового образца электронами с плотностью энергии  $5 \times 10^{16} \text{ эл/см}^2$  способствует увеличению размера нанокристаллитов с 32.50 нм до 43.33 нм.

**Ключевые слова:** монокристалл, кристаллическая структура, элементарная ячейка, пространственная группа, электронное облучение, флюенс, размер кристаллитов, шероховатость.

**Копбалина Қ.Б., Махмұтова А.С., Турдыбеков Д.М., Турдыбеков К.М., Төлєнова Г.Қ.**

**Лупинин алкалоиды молекуласының құрылымы мен қасиеттерін кванттық - химиялық зерттеу.**

Мақалада 1-((4-(3-метоксифенил)-1Н-1,2,3-триазол-1-ил)метил)октагидро-1Н-хинолизин молекуласын кванттық-химиялық зерттеу нәтижелері келтірілген. Кванттық-химиялық есептеулер нәтижесінде алынған берілген молекуланың геометриялық сипаттамалары талданып, рентгенді құрылымдық талдаудың эксперименттік мәліметтерімен салыстырылған. С11-N12 және С7-С11 лабильді байланыстарын бұру арқылы жүргізілген конформациялық талдау нәтижелері бойынша молекуланың ең тиімді конформациялық күйлері анықталған. Шекаралық молекулалық орбитальдердің локализациясы С11 атомы маңындағы 1-этил-4-(4-метоксифенил)-1Н-1,2,3-триазол алмастырғышында болатындығы көрсетілген, ал бұл оның жаңа биологиялық белсенді заттарды іздеу үшін жүргізілетін кейінгі модификация реакцияларына қатысуын болжайды.

**Кілт сөздері:** кванттық - химиялық есептеулер, хинолизин туындылары, конформациялық талдау, лупинин туындылары, рентгендік құрылымдық талдау.

**Копбалина Қ.Б., Махмұтова А.С., Турдыбеков Д.М., Турдыбеков К.М., Төлєнова Г.Қ.**

**Квантово-химическое исследование структуры и свойств молекулы производного алкалоида лупинина.**

В статье представлены результаты квантово-химического изучения молекулы 1-((4-(3-метоксифенил)-1Н-1,2,3-триазол-1-ил)метил)октагидро-1Н-хинолизина. Геометрические характеристики данной молекулы, полученные в результате квантово-химических расчетов, проанализированы и сопоставлены экспериментальным данным рентгеноструктурного анализа. По результатам конформационного анализа, осуществленного путем вращения вдоль лабильных связей С11-N12 и С7-С11 установлены наиболее выгодные конформационные состояния молекулы. Показано, что локализация граничных молекулярных орбиталей приходится на 1-этил-4-(4-метоксифенил)-1Н-1,2,3-триазоловый заместитель при атоме С11, что предполагает его участие в последующих реакциях модификации, проводимых для поиска новых биологически активных веществ.

**Ключевые слова:** квантово-химические расчеты, производные хинолизина, конформационный анализ, производные лупинина, рентгеноструктурный анализ.

**Каюмова А.С., Сериков Т.М., Омарова Г.С., Джакупова М.С.**

**Күміс нанобөлшектерінің концентрациясының титан қостотығының нанозекшелерінің фотокаталитикалық белсенділігіне әсері**

Бұл жұмыста титан диоксидінің (ТNR) нанозекшелеріндегі күміс нанобөлшектерінің концентрациясының олардың фотокаталитикалық белсенділігіне әсерін зерттеу нәтижелері келтірілген. Рутил құрылымы бар ТNR гидротермиялық синтез әдісімен алынды. Өтпелі металл күміс тұзының (AgNO<sub>3</sub>) зат мөлшерімен өзгеріп, ТNR бетіндегі химиялық тотықсыздану арқылы әртүрлі концентрациядағы Ag нанобөлшектері алынды. Беттік морфология мен ЭДА зерттеулері Ag нанобөлшектерінің біркелкі таралғанын және ТNR бетіне бекітілгенін көрсетті. Үлгілердің фотокаталитикалық белсенділігі пленка бетінің бірлігінен алынған фототок мөлшері және ксенон шамының жарық көзімен бетті жарықтандыру кезінде метилен көк бояғыштың фотодеградациясы бойынша бағаланды.

**Кілт сөздері:** нанозекшелер, титан қостотығы, күміс нанобөлшектері, Ag, фотокатализ.

**Каюмова А.С., Сериков Т.М., Омарова Г.С., Джакупова М.С.**

**Влияние концентрации наночастиц серебра на фотокаталитическую активность наностержней диоксида титана**

В данной работе представлены результаты исследования влияния концентрации наночастиц серебра в пленках из наностержней диоксида титана (ТNR) на их фотокаталитическую активность. ТNR со структурой рутила были получены методом гидротермального синтеза. Варируя количеством вещества соли переходного металла серебра (AgNO<sub>3</sub>), химическим восстановлением на поверхности ТNR были получены наночастицы Ag с различной концентрацией. Исследования морфологий поверхности и ЭДА показали, что наночастицы Ag равномерно распределены и закреплены на поверхности ТNR. Фотокаталитическая активность образцов оценивалась по величине генерируемого фототока с единицы поверхности пленок и фотодеградации красителя метиленовой голубой при освещении поверхности источником света ксеноновой лампы.

**Ключевые слова:** наностержни, диоксид титана, наночастицы серебра, Ag, фотокатализ.

**Безродный М.К., Майстренко О.О.**

**Регенерацияны қолдануымен ауаны құрғатудың жылу сорғы-адсорбциялық жүйесін термодинамикалық талдау.**

Берілген жұмыста жылу рекуператорын қолдануымен жылу сорғыш және адсорбциялық роторды қамтитын жүйенің әзірлеуі ұсынылған. Зерттеу аясында бұл жүйенің теориялық моделі жасалды, сонымен бірге оның жұмысын сандық талдау үшін математикалық модель құрылды. Термодинамикалық тиімділікке сандық талдау

жүргізілді, жүйенің негізгі түйіндеріндегі ауа параметрлерінің өзгеруі зерттелді, температура мен қоршаған ауаның салыстырмалы ылғалдылығы мен регенерация ауа температурасының жүйенің жұмысына әсері талданған. Сондай-ақ, жылу сорғының конденсаторынан кейін сыртқы ауа параметрлері мен регенерация ауа температурасының өзгерістері кезінде жүйенің тиімділігінің графикалық тәуелділіктері алынған. Рекуператордың ПЭК-нің жүйенің жалпы энергия тиімділігіне әсері зерттелген. Алынған нәтижелер берілген интеграцияланған жүйесін пайдалану жұмыс ауасын құрғату үшін қажетті электр энергиясының меншікті шығынын едәуір төмендететінін және сыртқы ауа параметрлеріне тәуелсіз рекуператорсыз немесе рекуператорсыз және жылу сорғысыз жүйелерден асып түсетінін көрсетеді.

**Кілт сөздері:** металл жабдықты коррозиядан қорғау, энергетикалық жабдықты сақтау, ауаны кептіру, адсорбциялық кептіргіш, жылу сорғысы, жылуды қалпына келтіру.

*Безродный М.К., Майстренко О.О.*

#### **Термодинамический анализ теплонасосно-адсорбционной системы осушения воздуха с использованием рекуперации**

В данной работе представлена разработка системы, включающей в себя тепловой насос, адсорбционный ротор, с применением рекуператора тепла. В рамках данного исследования была разработана теоретическая модель данной системы, а также создана математическая модель для численного анализа ее работы. Был проведен численный анализ термодинамической эффективности, изучено изменение параметров воздуха в ключевых узлах системы и проанализировано воздействие изменений температуры и относительной влажности окружающего воздуха и температуры воздуха регенерации на работу системы. Также получены графические зависимости эффективности системы при варьировании параметров наружного воздуха и температуры воздуха регенерации после конденсатора теплового насоса. Было проведено исследование влияния КПД рекуператора на общую энергоэффективность системы. Полученные результаты свидетельствуют о том, что использование данной интегрированной системы значительно снижает удельный расход электроэнергии, необходимой для осушения рабочего воздуха, и превосходит системы без рекуператора или без рекуператора и теплового насоса, независимо от параметров наружного воздуха.

**Ключевые слова:** защита металлического оборудования от коррозии, консервация энергетического оборудования, осушка воздуха, адсорбционная осушитель, тепловой насос, рекуперация тепла.

*Медетбеков Б.С., Вурим А.Д., Прозорова И.В., Попов Ю.А.*

#### **ИВГ.1М зерттеу реакторының жоғары және төмен байытылған отынынан бөліну өнімдерінің шығымы.**

ИВГ.1М реакторында төмен байытылған отыны бар су салқындатылатын технологиялық арналарға сынақтар жүргізу кезінде төмен байытылған және жоғары байытылған отыны бар технологиялық арналардың жылу тасымалдағышындағы бөлу өнімдері мен активтендіру өнімдерінің құрамын салыстырмалы өлшеу жүргізілді. Сыналатын төмен байытылған отын су салқындатқыш арналарының және жоғары байытылған отын арналарының отыннан бөліну өнімдерінің шығуын сипаттайтын сандық мәндерді салыстыруға болатындығы көрсетілді. ИВГ.1М реакторының салқындатқышында кездесетін радионуклидтердің жалпы тізбесінен, жақсы анықталатын радионуклидтер-талдағыштар таңдалды, олардың құрамын салқындатқышта анықтау жылу тасымалдағышқа бөліну өнімдерінің шығу параметрлері бойынша твэл қабықтарының герметикалығын өкілді бақылаудың жеткілікті әдісі ретінде ұсынылуы мүмкін.

**Кілт сөздері:** жылу тасымалдағыш, твэл, твэл қабықшасы, бөліну өнімі, бөліну өнімдерінің салыстырмалы шығымы, гамма-спектрометрия.

*Медетбеков Б.С., Вурим А.Д., Прозорова И.В., Попов Ю.А.*

#### **Выход продуктов деления из высоко и низкообогащенного топлива исследовательского реактора ивг.1м**

При проведении испытаний водоохлаждаемых технологических каналов с низкообогащенным топливом в реакторе ИВГ.1М выполнены сравнительные измерения содержания продуктов деления и продуктов активации в теплоносителе технологических каналов с низкообогащенным и высокообогащенным топливом.

Показано, что количественные значения, характеризующие выход продуктов деления из топлива тестируемых водоохлаждаемых каналов с низкообогащенным топливом и из каналов с высокообогащенным топливом, сопоставимы. Из общего перечня радионуклидов, обнаруживаемых в теплоносителе реактора ИВГ.1М, выбраны хорошо идентифицируемые радионуклиды-аналиты, определение содержания которых в теплоносителе может быть рекомендовано в качестве достаточного способа представительного контроля герметичности оболочек твэлов по параметрам выхода продуктов деления в теплоноситель.

**Ключевые слова:** теплоноситель, твэл, оболочка твэла, продукты деления, относительный выход продуктов деления, гамма-спектрометрия.

*Цыганов В.В., Шейко С.П., Шаломеев В.А., Воденникова О.С., Кулабниева О.А.*

**Күрделі динамикалық жүктеме кезінде триботүйіндістірулер бөлшектерінің тозуға төзімділігіне ортаның механикалық-химиялық әсерлерінің жылдамдатылған сынақтары.**

Күрделі динамикалық жүктеме жағдайында триботүйіндістірулер бөлшектерінің тозуы қарастырылған. Көп компонентті динамикалық жүктеме кезінде үйкеліс жұптарын жылдамдатылған сынақтар әдісі ұсынылған. Контакттілі өзара әрекеттесу процесстерін модельдеуге арналған стенд конструкциясы, сонымен бірге әртүрлі майлау және салқындату ортасымен күрделі динамикалық жүктеме жағдайында жұмыс істейтін триботүйіндістірулердің тозуға төзімділігін зерттеуге арналған стенд конструкциясы ұсынылған. Өзірленген әдістеме бойынша триботүйіндістірулердің жанасу аймағындағы механикалық-химиялық түрлендірулердің тозуға төзімділікке әсерін бағалау нәтижелері келтірілген. Майлау-салқындату сұйықтығының құрамындағы жоғары молекулалық қосылыстардың ыдырау өнімдерінің триботүйіндістірулердің жанасу аймағындағы металдардың тозуға төзімділігіне әсерін бағалау мүмкіндігі көрсетілген. Ұсынылған материалдарды қолдану берілген жұмыс шарттары үшін үйкеліс жұптарының материалдарын негізді таңдауға, жаңа тозуға төзімді материалдар мен жабындарды, майлау және салқындату ортасының құрамын жасауға мүмкіндік береді.

**Кілт сөздері:** тозу, күрделі жүктеме, үйкеліс, стенд, полимер.

*Цыганов В.В., Шейко С.П., Шаломеев В.А., Воденникова О.С., Кулабниева О.А.*

**Ускоренные испытания механохимического воздействия среды на износостойкость деталей трибосопряжений при сложном динамическом нагружении.**

Рассмотрен износ деталей трибосопряжений в условиях сложного динамического нагружения. Предложена методика ускоренных испытаний пар трения при многокомпонентном динамическом нагружении. Представлены конструкции стендов для моделирования процессов контактного взаимодействия, исследований износостойкости трибосопряжений, которые работают в условиях сложного динамического нагружения с различной смазочно-охлаждающей средой. Приведены результаты оценки влияния механохимических превращений в зоне контакта трибосопряжений на износостойкость по разработанной методике. Показана возможность оценки эффективности влияния продуктов деструкции высокомолекулярных соединений в составе смазочно-охлаждающей жидкости на износостойкость металлов в зоне контакта трибосопряжений. Использование представленных материалов позволяет обоснованно выбирать материалы пар трения для заданных условий эксплуатации, разрабатывать новые износостойкие материалы и покрытия, состав смазочно-охлаждающей среды.

**Ключевые слова:** изнашивание, сложное нагружение, трение, стенд, полимер.

*Шынарбек А.Б., Рахадиллов Б.К., Степанова О.А., Кусаинов Р.К., Жасулан А.Ж., Даумова Г.К.*

**30ХГСА болаттан жасалған жабындарды электр доғалық металдандыру процесін зерттеу.**

Мақалада жабындардың құрылымы мен қасиеттеріне әсер ететін 30ХГСА болат сымдарының электрлік доғалық металдандыруының технологиялық режимдері қарастырылған. Электр доғалық бүрку SX-600 электр доғалық металлаторды қолдану арқылы жүргізілді. Алынған жабындардың қасиеттері мен сипаттамалары сымның берілу жылдамдығы, кернеу және ток күші сияқты бірнеше металдандыру параметрлеріне тәуелді. Электрондық микроскопия және металлографиялық талдау әдістерімен жабындардың құрылымы зерттелді. Жабын қатайтылған конвективті металл ағындарынан, микродәнекерленген ұсақ металл бөлшектерінен және оксидтерден тұратын қабатты құрылымға ие. Зерттеу нәтижелері металдандыру кезінде сым беру жылдамдығының жоғарылауы уақыт бірлігінде алынған жабын қалыңдығының артуына әкелетінін көрсетеді. 45 болаттың бетінде таңдалған режимге байланысты қалыңдығы 50 мкм-ден 370 мкм-ге дейінгі 30ХГСА болаттан жасалған жабындар пайда болды. Жабындарларды 30ХГСА сыммен ЭДМ бүрку кезінде беткі қабаттың микроқаттылығының мәні 45 болаттың микроқаттылығына қатысты 2 есе артатыны анықталды. Электрлік доғалық бүрку процесінің факторларының жабындардың құрылымы мен қасиеттеріне әсері туралы зерттеулердің нәтижелерін қорытындылай келе, 30 ХГСА болат доғалық металдандыруды болат субстраттарда қаттылығы жоғары жабындарды алу үшін қолдануға болады деген қорытынды жасауға болады.

**Кілт сөздері:** электр доғасын металдандыру, сым, жабын, болат, құрылым, микроқаттылық, тозуға төзімділік.

*Шынарбек А.Б., Рахадиллов Б.К., Степанова О.А., Кусаинов Р.К., Жасулан А.Ж., Даумова Г.К.*

**Исследование процесса электродуговой металлизации покрытий из стали 30ХГСА**

В статье рассмотрены технологические режимы электродуговой металлизации проволоки стали 30ХГСА, влияющих на структурообразование и свойства покрытий. Электродуговое напыление производилось с применением электродугового металлатора SX-600. Свойства и характеристики получаемых покрытий зависят от нескольких параметров металлизации, таких как скорость подачи проволоки, напряжение, и сила тока. Методами электронной микроскопии и металлографического анализа изучена структура покрытий. Покрытие имеет слоистую структуру, которая состоит из застывших конвективных потоков металла, микросваренных мелких металлических частиц и оксидов. Результаты исследования показывают, что увеличение скорости подачи проволоки при металлизации приводит к увеличению получаемой толщины

покрытия за единицу времени. На поверхности стали 45 в зависимости от выбранного режима сформировались покрытия из стали 30ХГСА толщиной в диапазоне от 50 мкм до 370 мкм. Установлено, что при напылении ЭДМ покрытий проволокой 30ХГСА значение микротвердости поверхностного слоя возрастает в 2 раза по отношению к микротвердости стали 45. Обобщая результаты исследований по влиянию факторов процесса электродугового напыления на структурообразование и свойства покрытий можно сделать вывод, что электродуговая металлизация стали 30ХГСА может использоваться для получения покрытий с повышенной твердостью на стальных подложках.

**Ключевые слова:** электродуговая металлизация, проволока, покрытие, сталь, структура, микротвердость, износостойкость.

*Ибраимов М.К., Кожазулов Е.Т., Жексебай Д.М., Сарманбетов С.А.*

**Кристалл-жүйе негізіндегі радиоқұрылғының функционалдық блогын жүзеге асыру.**

Бұл жұмыс кристалл - жүйе негізіндегі радиоқұрылғының функционалдық блогын жүзеге асыруға арналған. Негізгі назар бағдарламаланатын логикалық интегралдық схемаларда модуляция және жылдам Фурье түрлендіруі сияқты радиоқұрылғының блоктарын біріктіруге бағытталған. Модульдерді жобалаудың, тестілеудің және Radio Unit(RU) бірліктерінің өнімділігін онтайландырудың техникалық аспектілері егжей-тегжейлі қарастырылған. Нәтижелер көрсеткендей, Fifth Generation (5G) радио блогының 7.3 функционалдығын ортақ пайдалану кезінде модуляция блогы басқа блоктармен салыстырғанда логикалық интегралдық схемалардағы ресурстарының ең аз мөлшерін пайдаланады. Жылдам Фурье түрлендіруі блогы максималды пайдалануға болатын логикалық интегралдық схемалардағы өлшемі мен 250 МГц тактілік жиілікте кідіріс талаптарын қанағаттандыра алады. Бұл мақала заманауи радио жүйелерде өнімділігі жоғары функционалды блоктарды жобалауды және біріктіруді онтайландыруға мүдделі инженерлер мен зерттеушілер үшін ресурс ретінде қызмет етеді.

**Кілт сөздері:** логикалық интегралдық схемаларда, Zynq, Fifth Generation New Radio, радио блок, ортогональды жиілікті бөлу мультиплексирлеу.

*Ибраимов М.К., Кожазулов Е.Т., Жексебай Д.М., Сарманбетов С.А.*

**Реализация функционального блока радиоустройства на основе системы-на-кристалле.**

Данная статья посвящена реализации функционального блока радиоустройства на основе системы-на-кристалле. Основное внимание уделяется интеграции блоков радиоустройства, таких как модуляция и быстрое преобразование Фурье, на программируемых вентилях матрицах. Подробно рассматриваются технические аспекты проектирования, тестирования модулей и оптимизацию производительности блоков радиоустройства. Результаты показывают, что при разделении функциональности радиоблока 7.3 технологии Fifth Generation (5G) блок модуляции использует минимальное количества ресурсов программируемых вентилях матрицах по сравнению с остальными блоками. Блок быстрого преобразования Фурье может соответствовать требованию задержки при максимально используемой размере и тактовой частоте программируемых вентилях матрицах 250 МГц. Эта статья служит ресурсом для инженеров и исследователей, заинтересованных в оптимизации процесса разработки и интеграции высокопроизводительных функциональных блоков в современных радиосистемах.

**Ключевые слова:** Программируемая логическая интегральная схема, Zynq, Fifth Generation New Radio, Radio Unit, многолучевой доступ с ортогональным разделением частот.

*Лобода Ю. О., Гальцева О. В., Бирюкова Н. С.*

**"Bioid Premium Kit" конструкция негізінде жылан роботының қозғалысының физикалық сипаттамаларын зерттеу.**

Мақалада жылан робот қозғалысының физикалық сипаттамалары қарастырылған. Берліген жұмыстың негізгі мақсаты - өндірістік робот-манипулятор пен мобильді робот үшін қоршаған ортаның әртүрлі жағдайларында қозғалуға мүмкіндік беретін жылан роботтың қозғалысының физикалық сипаттамаларын зерттеуге негізделген алгоритм жасау болып табылады. Жұмыс барысында робот-жыланның әртүрлі беттердегі қозғалыс теңдеулері алынды. Жылан роботы ашық кинематикалық тізбек екендігі анықталды, оның элементтері кинематиканың тікелей және кері есептерін шешуге және робот блогының берілген бағыттағы орнын есептеуге негізделген бес немесе одан да көп кинематикалық айналу түйіндерімен өзара байланысты. Жыландардың физикалық қозғалысын зерттеу негізінде жылан роботының қозғалысының патенттелген алгоритмі жасалды. Robotis BIOLOID Premium жиынтығына негізделген жылан роботының прототипі құрастырылып, жеті түрлі бетте сынақ жүргізілді. Құрастырылған жоғары жылдамдықты прототип он бір блоктан және дөңгелектері жоқ CM-530 контроллерінен тұрады және дамыған алгоритмді қолдану арқылы аналогтармен салыстырғанда жоғары қозғалыс жатықтығын қамтамасыз етеді.

**Кілт сөздері:** жылан роботының алгоритмі, жыланның қозғалысы, жылан роботы, физикалық сипаттамалары, басқару элементтері, RoboPlus.

*Лобода Ю.О., Гальцева О.В., Бирюкова Н.С.*

**Изучение физических характеристик движения робота-змеи на основе конструкции “Bioloid Premium Kit”.**

В статье рассматриваются физические характеристики движения робота-змеи. Основной целью данной работы является разработка алгоритма, основанный на изучении физических характеристик движения робота-змеи, который позволит передвигаться в различных условиях окружающей среды, как промышленному роботу-манипулятору, так и мобильному роботу. В ходе работы были получены уравнения движения робота-змеи по различным поверхностям. Установлено, что робот-змея представляет собой разомкнутую кинематическую цепь, элементы которой соединены между собой пятью или более кинематическими узлами вращения на основе решения прямых и обратных задач кинематики и расчета положения блока робота в заданной ориентации. На основе изучения физических движений змей был разработан запатентованный алгоритм передвижения робота-змеи. Прототип робота-змеи, основанный на наборе ROBOTIS BIOLOID Premium, был собран и протестирован на семи различных поверхностях. Созданный высокоскоростной прототип состоит из одиннадцати блоков и контроллера CM-530 без колес и обеспечивает высокую плавность передвижения по сравнению с аналогами благодаря использованию разработанного алгоритма.

**Ключевые слова:** алгоритм робота-змеи, движение змеи, змеевидный робот, физические характеристики, управление, RoboPlus.

*Турлыкожаева Д.А., Усінов Н.М., Байгалиева А.Н., Темешева С.А., Болысбай А.Т., Абрахматова Г.А., Ахтанов С.Т.*

**Ақпараттық энтропия теориясына негізделген сымсыз торлы желіге арналған маршруттау көрсеткіші және протоколы.**

Ұсынылған мақалада пакеттің жоғалу ықтималдығын ескеретін көрсеткішті есептеу үшін ақпараттық энтропия теориясына негізделген маршруттау алгоритмі берілген. Ақпараттық энтропия теориясы деректерді берудегі белгісіздік пен тәртіпсіздікті бағалаудың сенімді негізі ретінде қызмет етеді, бұл тұрақты және интеллектуалды маршруттау стратегиясын әзірлеуді жеңілдетеді. Қолданыстағы алгоритмдерден айырмашылығы, ұсынылған тәсіл максималды тиімділікке жету үшін маршруттау процесін оңтайландыру арқылы желі ішіндегі деректерді беру сапасын дәлірек бағалауға мүмкіндік береді. Эксперимент нәтижелері жоғары өнімділікті сақтай отырып, желіге қызмет көрсету сапасының айтарлықтай жақсарғанын көрсетеді. Алгоритмнің тиімділігін тексеру үшін өткізу қабілеттілігі, кідіріс және пакеттің жоғалуы сияқты негізгі өнімділік көрсеткіштерін бағалайтын бірқатар эксперименттер жүргізілді. Сондай-ақ, белгілі алгоритмдерге қатысты артықшылықтар мен кемшіліктерді бағалауға мүмкіндік беретін белгіленген маршруттау алгоритмдерімен салыстырмалы талдау жүргізілді. Нәтижелер ұсынылған алгоритм деректер сапасын және желінің жалпы тиімділігін оңтайландыруда дәстүрлі маршруттау әдістерінен асып түсетінін көрсетеді.

**Кілт сөздері:** маршруттау, энтропия, ақпарат, сымсыз торлы желі.

*Турлыкожаева Д.А., Усінов Н.М., Байгалиева А.Н., Темешева С.А., Болысбай А.Т., Абрахматова Г.А., Ахтанов С.Т.*

**Метрика маршрутизации и протокол для беспроводной ячеистой сети, основанные на теории информационной энтропии**

В представленной статье представлен алгоритм маршрутизации, основанный на теории информационной энтропии, для вычисления показателя, учитывающего вероятность потери пакета. Теория информационной энтропии служит надежной основой для оценки неопределенности и беспорядка при передаче данных, облегчая разработку более устойчивой и интеллектуальной стратегии маршрутизации. В отличие от существующих алгоритмов, предлагаемый подход позволяет более точно оценивать качество передачи данных внутри сети, оптимизируя процесс маршрутизации для достижения максимальной эффективности. Результаты эксперимента демонстрируют значительное повышение качества обслуживания сети при сохранении высокой производительности. Для проверки эффективности алгоритма была проведена серия экспериментов, оценивающих ключевые показатели производительности, такие как пропускная способность, задержка и потеря пакетов. Также был проведен сравнительный анализ с установленными алгоритмами маршрутизации, позволивший оценить преимущества и недостатки по отношению к хорошо известным алгоритмам. Полученные результаты свидетельствуют о том, что предложенный алгоритм превосходит традиционные методы маршрутизации в оптимизации качества передачи данных и общей эффективности сети.

**Ключевые слова:** маршрутизация, энтропия, информация, беспроводная ячеистая сеть.

**Плотников И.В., Короткий И.А., Неверов Е.Н., Короткая Е.В., Плотникова Л.В.**

**Агроөнеркәсіптік кешеннің қайта өңдеу өндірістері үшін мехатронды су дайындау модулін модернизациялау.**

Агроөнеркәсіптік кешен объектілері суды әртүрлі мақсаттарда пайдаланады, олар тұтынатын судың көлемі едәуір үлкен, 60 км<sup>3</sup> судан асатын табиғи су объектілерінен ресурс ретінде жыл сайын төрттен бір бөлігі агроөнеркәсіптік кешендерге келеді, мұндай жуықталған мәліметтер ауыл шаруашылық сияқты ірі су тұтынушыға жатқызуға мүмкіндік береді. Бұл жағдайда маңызды параметрлердің бірі - суды дайындау әдісі әсер ететін судың сапасы болып табылады. Суды дайындаудың ең перспективті әдісі криоконцентрлеу болып табылады, ол ылғалдың кристалдануынан, содан кейінгі қатты фазаның ығысуынан құрылады. Бұл процестің және оның аппараттық конструкциясының жетілмегендігі бұл әдісті өндіріске енгізуді тежейді. Суды дайындау кезінде криоконцентрлеу әдісінің өнімділігін арттыру мақсатында рекуперациялаумен карусель типті аппараттың жаңа конструкциясы құрастырылып жасалды. Кристаллизатпен қажетсіз элементтерді ұстауын азайту және кристалдану процесінің сипатын анықтау үшін криоконцентратордың жұмыс пластиналарда процестің ұтымды параметрлерін орнатуға мүмкіндік беретін бірқатар эксперименттер жүргізілді. Бұл авторларға карусель типті аппарат үшін мехатронды криоконцентрлеу модулін жасауға мүмкіндік берді.

**Кілт сөздері:** криоконцентрлеу, суды дайындау, карусель типті криоконцентратор, криоконцентратордың мехатрондық модулі.

**Плотников И.В., Короткий И.А., Неверов Е.Н., Короткая Е.В., Плотникова Л.В.**

**Модернизация мехатронного модуля водоподготовки для перерабатывающих производств агропромышленного комплекса**

Объекты агропромышленного комплекса, используют воду в различных целях, объем потребляемой ими воды достаточно велик, при общем ежегодном изъятии воды, как ресурса, из природных водных объектов превышающем 60 км<sup>3</sup> воды, до четверти приходится на агропромышленные комплексы, даже такие приближенные данные позволяют отнести сельское хозяйство к крупнейшему водопотребителю. При этом одним из важных параметров является качество воды, на которое влияет способ водоподготовки. Наиболее перспективным способом водоподготовки является криоконцентрирование, которое заключается в кристаллизации влаги с последующим вытеснением твердой фазы. Несовершенство данного процесса и его аппаратурного оформления сдерживает внедрение данного способа в производство. С целью повышения производительности метода криоконцентрирования при проведении водоподготовки была разработана новая конструкция аппарата карусельного типа с рекуперацией. Для снижения захвата нежелательных элементов кристаллизатом и определения характера протекания процесса кристаллизации на рабочих пластинах криоконцентратора была проведена серия экспериментов, позволяющая установить рациональные параметры процесса. Это позволило авторам разработать мехатронный модуль криоконцентрирования для аппарата карусельного типа.

**Ключевые слова:** криоконцентрирование, водоподготовка, криоконцентратор карусельного типа, мехатронный модуль криоконцентратора.

**Жанабаев З.Ж., Ахтанов С.Т., Тілеу А.О., Әлмен Д.Б.**

**Лазерлік газ сенсорындағы когерентті амплитудалық модуляция.**

Мақала ғылым мен техникадағы өзекті тақырыпқа – лазердің көмегімен газдың түрі мен концентрациясын анықтауға арналған. Жасыл лазер сәулеленуінің қарқындылығы мен ығысу кернеуінің жақын мәндерінде фотодиодтың шығыс сигналының уақыттық қатарының интерференциялық үлгілері алынды. Когеренттілік дәрежесі (~0,1-ден жоғары) газдардың түрлерін және олардың концентрацияларын ажыратуға мүмкіндік берді. Сигнал когеренттілігі Аллан девиациясы мәндерімен бақыланды. Зерттеу әдісінің жаңалығы модуляцияның негізгі жиілігі ретінде электр желісінің гармоникасын таңдау болып табылады. Корреляциялық функциялар мен сәйкес қуат спектрлері молекулалардың және олардың шоғырларының төмен жиіліктегі тербелістеріне сезгіш болатыны көрсетілген. Бұл бөлме қысымы мен температурасында оптикалық аспаптардың үлкен өлшемді және қымбат кешендерінің орнына осы жұмыстың нәтижелері мен әдістерін нақты жағдайларда қолдануға мүмкіндік береді.

**Кілт сөздері:** лазер, газ сенсоры, төмен жиіліктер, фотодиод, аммиак.

**Жанабаев З.Ж., Ахтанов С.Т., Тілеу А.О., Әлмен Д.Б.**

**Когерентная амплитудная модуляция в лазерном газосенсоре.**

Статья посвящена актуальной теме науки и техники – определению вида и концентрации газа использованием лазера. При близких значениях интенсивности лазерного излучения зеленого цвета и напряжения смещения фотодиода получены интерференционные картины временного ряда выходного сигнала фотодиода. Степень когерентности (более чем ~0,1) позволил различить виды газов и их концентрации. Когерентность сигналов контролировалась значениями девиации Аллана. Новизной метода исследования является выбор в качестве

основной частоты модуляции гармонику электрической сети. Показано, что функции корреляций и соответствующие спектры мощности чувствительны к низкочастотным флуктуациям молекул и их сгустков. Это позволяет использовать результаты и методику настоящей работы в конкретных случаях вместо крупногабаритных и дорогостоящих комплексов оптических приборов при комнатных значениях давления и температуры.

**Ключевые слова:** лазер, газовый сенсор, низкие частоты, фотодиод, аммиак.

*Маликов В.Н., Катасонов А.О., Ишков А.В., Фадеев Д.А., Войнаш С.А., Ворначева И.В., Заидуллин Р.Р., Шмыкова П.А.*

**Жұқа металл қабыршақтардың біртексіздігі мен ақауларын зерттеудің құйынды ток әдісі.**

Жұқа металл қабыршақтардың қалыңдығының аздығымен байланысты әртүрлі құрылымдар мен ерекше қасиеттер олардың физикалық сипаттамалары массивтік күйдегі сондай материалдардан айтарлықтай ерекшеленетіндігіне әкеледі. Жұқа металл қабыршақтарының сипаттамаларын анықтау үшін бұзбайтын зерттеудің жаңа әдістерін әзірлеу өзекті болып табылады. Мақалада әртүрлі металдардың жұқа металл қабыршақтарының бетін зерттеу үшін құйынды токты бақылау әдісінің артықшылықтары негізделген. Жұқа металл қабыршақтарының электр өткізгіштігін, қалыңдығын және зақымдану дәрежесін зерттеуге арналған аса кіші құйынды ток түрлендіргішінің конструкциясы ұсынылған, сонымен қатар әзірленген түрлендіргішті басқаруға мүмкіндік беретін бағдарламалық-аппараттық кешен жасалған. Металл қабыршақтары зерттеу негіздеме бетіне заттың таралуының біртексіздігін көрсетті. Сондай-ақ, әзірленген түрлендіргіштің сигнал амплитудасының қабыршақ қалыңдығына тәуелділігі анықталды. Алынған нәтижелерді тексеру үшін фотометриялық әдіспен қабыршақтардың жарықтың өткізуіне зерттеу жүргізілген. Екі әдіспен алынған өлшеу нәтижелерін салыстыру әзірленген қабыршақтарды зерттеу әдістері арасындағы жоғары үйлесімділікті көрсетті.

**Кілт сөздері:** жұқа қабыршақтар, металдар, құйынды ток түрлендіргіші, материалдарды зерттеу, қабыршақтың біртексіздігі.

*Маликов В.Н., Катасонов А.О., Ишков А.В., Фадеев Д.А., Войнаш С.А., Ворначева И.В., Заидуллин Р.Р., Шмыкова П.А.*

**Вихретоковый метод исследования неоднородностей и дефектов тонких металлических пленок.**

Многообразие структуры и специфические свойства, связанные с малостью толщины тонких металлических пленок, приводит к тому, что их физические характеристики существенно отличаются от характеристик этих же материалов в массивном состоянии. Для определения характеристик тонких металлических пленок актуальна разработка новых методов неразрушающего исследования. В статье обосновываются достоинства метода вихретокового контроля для исследования поверхности тонких металлических пленок различных металлов. Представлена конструкция сверхминиатюрного вихретокового преобразователя, предназначенного для исследования электропроводности, толщины и степени повреждения тонких металлических пленок, а также сконструирован программно-аппаратный комплекс, позволяющий производить управление разработанным преобразователем. Исследование металлических пленок позволило показать неоднородность распределения вещества по поверхности подложки. Также была определена зависимость амплитуды сигнала разработанного преобразователя от толщины пленки. Для проверки получаемых результатов были проведены исследования светопропускания пленок фотометрическим методом. Сравнение результатов измерений, полученных двумя методами, показали высокую степень согласованности между двумя разработанными методами исследования пленок.

**Ключевые слова:** тонкие пленки, металлы, вихретоковый преобразователь, исследования материалов, неоднородность пленки.

*Шишулин А.В., Потапов А.А., Шишулина А.В.*

**Қабыршақты қатты ерітінділердің фракталдық пішінді нанобөлшектері: морфологияның ауыр вольфрам псевдоқорытпаларындағы фазалық тепе-теңдікке әсері.**

Физика-химиялық қасиеттердің бірегей жиынтығының арқасында нанокұрылымды ауыр вольфрам псевдоқорытпалары, әсіресе ұнтақты металлургияның заманауи аддитивті технологияларының нысаны ретінде жоғары қызығушылық тудырады. Берілген жұмыста W-Cr ауыр қорытпасының мысалында core-shell қабыршақтайтын қатты ерітінді құрылымы бар нанобөлшектер үшін фазалық тепе-теңдіктің морфологияға тәуелділігі термодинамикалық түрде модельденген. Нанобөлшектердің морфологиясы фракталдық геометрия әдістерін қолдану арқылы берілген. Тепе-теңдік фазалық құрамы мен әртүрлі гетерогенді күйлердің температура мен нанобөлшектердің морфологиясына тәзімділігі жүйенің бос энергиясын төмендетудің үш механизмі негізінде түсіндіріледі. Жұмыстың соңғы бөлігінде нанобөлшектер ансамбльдеріндегі өлшемдер мен орташа сипаттамалар бойынша тепе-теңдік үлестірулерін есептеу әдісі, сондай-ақ микроскопия мәліметтері негізінде нанобөлшектердің фракталдық өлшемін өлшеу әдісі сипатталған.

**Кілт сөздері:** нанобөлшектер, қабыршақтау, вольфрам, хром, фракталдық өлшемділік.

*Шишулин А.В., Потапов А.А., Шишулина А.В.*

**Наночастицы фрактальной формы расслаивающихся твердых растворов: влияние морфологии на фазовые равновесия в тяжелых вольфрамовых псевдосплавах**

Благодаря уникальному набору физико-химических свойств наноструктурированные тяжелые вольфрамовые псевдосплавы являются объектом повышенного интереса, в особенности как объект для современных аддитивных технологий порошковой металлургии. В настоящей работе термодинамически смоделирована зависимость фазовых равновесий от морфологии для наночастиц со структурой core-shell расслаивающегося твердого раствора на примере тяжелого сплава W-Cr. Морфология наночастиц задавалась с использованием методов фрактальной геометрии. Полученные зависимости равновесного фазового состава и устойчивости различных гетерогенных состояний от температуры и морфологии наночастиц интерпретированы на основе трех механизмов понижения свободной энергии системы. В заключительной части работы описан метод расчета равновесных распределений по размерам и средних характеристик в ансамблях наночастиц, а также методика измерения фрактальной размерности наночастиц непосредственно на основе данных микроскопии.

**Ключевые слова:** наночастицы, расслаивание, вольфрам, хром, фрактальная размерность.

**INFORMATION  
ABOUT AUTHORS**
**АВТОРЛАР ТУРАЛЫ  
МӘЛІМЕТТЕР**
**СВЕДЕНИЯ  
ОБ АВТОРАХ**

**Abrahmatova, G.A.** – Assistant Professor, Candidate Of Philosophy, Almaty University of Power Engineering and Telecommunications named after G. Daukeev, Almaty, Kazakhstan; g.abrahmatova@aes.kz

**Akhtanov, S.N.** – PhD, Researcher, teacher, Department of Physics and Technology, al-Farabi Kazakh National University, Almaty, Kazakhstan; Scopus Author ID: 55672124000, ORCID iD: 0000-0002-9705-8000 ahtanov.saiyat1@kaznu.kz

**Almen, D.B.** – PhD student, Department of Physics and Technology, Al-Farabi Kazakh National University, Almaty, Kazakhstan; ORCID: <https://orcid.org/0009-0000-8527-4921>; dinara.almen@gmail.com

**Amangeldi, N.** – PhD., Associate Professor, L.N. Gumilyov Eurasian National University, Astana, Kazakhstan; Institute of nuclear physics, Almaty, Kazakhstan; Scopus Author ID: 37065699200; ORCID iD: 0000-0002-9416-5425; nur19792@mail.ru

**Anuar, A.** – PhD. student, L.N. Gumilyov Eurasian National University, Astana, Kazakhstan

**Baigaliyeva, A.N.** – Master student, Department of Physics and Technology, Al-Farabi Kazakh National University, Almaty, Kazakhstan; aiymbglva@mail.ru

**Bezrodny, M.K.** – Doctor of Technical Sciences, Professor, Professor of the Theoretical and Industrial Heat Engineering Department, National Technical University of Ukraine “Igor Sikorsky Kiev Polytechnic Institute”, Kiev, Ukraine; scopus Author ID: 6701795951

**Biryukova, N.S.** - Post Graduate Student, Department of Innovation Management, Tomsk State University of Control Systems and Radioelectronics (TUSUR), Tomsk, Russia; baulina-tasha217@yandex.ru

**Bolysbay, A.** – Bachelor student, Department of Physics and Technology, Al-Farabi Kazakh National University, Almaty, Kazakhstan; bolysbay\_aslan@live.kaznu.kz

**Daumova, G.** – Candidate of Techn. sciences, Associate Professor, Professor, D. Serikbayev East Kazakhstan Technical University, Oskemen, Kazakhstan; Scopus Author ID: 6504514394; ORCID ID: 0000-0001-6312-5343, gulzhan.daumova@mail.ru

**Dzhakupova, M.S.** – Master student, Department of Physics and Nanotechnology, Karaganda Buketov University, Karaganda, Kazakhstan; moldir.93@inbox.ru

**Fadeev, D.A.** – Master student, Department of General and Experimental Physics, Federal State Budgetary Educational Institution of Higher Education "Altai State University", Barnaul, Russia; ORCID iD: 0000-0003-3467-7506; katonovrffi@gmail.com

**Galtseva, O.V.** - Candidate of Techn. Sciences, Associate Professor, Department of Innovation Management, Tomsk State University of Control Systems and Radioelectronics; Division of Testing and Diagnostics, NDT School, Tomsk Polytechnic University (TPU), Tomsk, Russia; Scopus AuthorID: 15049236900; WoS ResearcherID: L-9955-2016; ORCID iD: 0000-0001-6919-4833; olga.v.galtseva@tusur.ru

**Hussain, Wafaa A.** – PhD., Professor, Applied Science Department, University of Technology, Baghdad, Iraq; Scopus Author ID: 57216037916; 100067@uotechnology.edu.iq

**Ibraimov, M.K.** - PhD, Professor, Head of the Solid State Physics and Nonlinear Physics Department, al-Farabi Kazakh National University, Almaty, Kazakhstan. Scopus Author ID: 57189617696, <https://orcid.org/0000-0002-8049-3911>

**Ishkov, A.V.** - Doctor of Techn. Sciences, Candidate of Chem. Sciences, Professor, Professor, Department of Technology structural materials and repairs machines, Altai State Agricultural University, Barnaul, Russia; ORCID iD: 0000-0003-1637-2258; svaritrffi@gmail.com

**Katasonov, A.O.** – PhD student, Department of General and Experimental physics, Altai State University, Barnaul, Russia; ORCID iD: 0000-0002-0259-6202; ivenir9001@gmail.com

**Kayumova, A.S.** – PhD student, Department of Physics and Nanotechnology, Karaganda Buketov University, Karaganda, Kazakhstan; ORCID iD: 0000-0003-4684-0083; aneka.08@mail.ru;

**Khallokov, F.K.** – PhD, Head of the Department of Biophysics, Informatics and Information Technology, Bukhara State Medical Institute, Bukhara, Uzbekistan; Scopus Author ID: 57195559996; ORCID iD: 00-0002-7020-0257; f\_k\_xalloqov@rambler.ru

**Khodzhaev, U.O.** – PhD student, Institute of Nuclear Physics, Academy of Sciences of Uzbekistan, Ulugbek, Tashkent, Uzbekistan; ORCID iD: 0009-0004-0519-3830; utkirjon1974@gmail.com

**Kopbalina, K.B.** – PhD student, Master (Physics), Karagandy Buketov University; Senior lecturer, A. Saginov Karaganda Technical University, Karaganda, Kazakhstan, ORCID iD: 0000-0001-6378-9756; kopbalina82@mail.ru

**Korotkaya, E.** - Doctor of Techn. Sciences, Professor, Institute of Engineering Technologies, Kemerovo State University, Kemerovo, Russia; ORCID iD: 0000-0002-6210-3756; e.v.korotkaya@inbox.ru

**Korotkiy, I.** – Doctor of Techn. Sciences, Professor, Institute of Engineering Technologies, Kemerovo State University, Kemerovo, Russia; ORCID iD: 0000-0002-7623-0940; i.a.korotkiy@mail.ru

**Kozhagulov, E.T.** – Doctor Science of Physics and Mathematics, Al-Farabi Kazakh National University, Almaty, Kazakhstan, kazgu.kz@gmail.com, <https://orcid.org/0000-0001-5714-832X>

**Kulabnieva, O.A.** – Senior Lecturer, Department “Theory and Practice of Translation”, National University “Zaporizhzhia Polytechnic”, Zaporozhie, Ukraine; Scopus Author ID: 57442141900; Researcher ID: 1701619738035; ORCID iD:0000-0003-3894-3891; kulabnieva.elena@gmail.com

**Kusainov, R.** – Master (Eng.), Head of the Scientific Center «Surface modification of materials», Shakarim University of Semey, Semey, Kazakhstan; Scopus Author ID: 57220897173, ORCID ID: 0000-0001-5166-4761; kusain.turku@gmail.com

**Lafta, Sadeq H.** – PhD., Assistant Professor, Applied Science Department, University of Technology, Baghdad, Iraq; Scopus Author ID: 57057742300; ResearcherID: D-1092-2019; ORCID iD: 0000-0002-7000-8337; sadeq.h.lafta@uotechnology.edu.iq

**Loboda, Yu.O.** - Candidate of Pedagog. Sciences, Associate Professor, Department of Innovation Management, Tomsk State University of Control Systems and Radioelectronics (TUSUR), Tomsk, Russia; ORCID iD: 0000-0002-7413-4250; yulloboda@gmail.com

**Maistrenko, J.O.** – PhD student, Department of the Theoretical and Industrial Heat Engineering, National Technical University of Ukraine “Igor Sikorsky Kiev Polytechnic Institute”, Kiev, Ukraine; Scopus Author ID: 55595775700; maistrenko1010@gmail.com

**Makhanov, K.M.** – Candidate of phys.-math. sciences, Senior teacher, L.N. Gumilyov Eurasian National University, Astana, Kazakhstan; Scopus Author ID: 57217354220; ORCID iD: 0000-0002-1263-0734; makanov@inbox.ru

**Makhmutova, A.S.** - Candidate of chem. sciences, Associate Professor, Karaganda Medical University, Karaganda, Kazakhstan; ORCID iD: 0000-0002-0194-8739; almagul\_312@mail.ru

**Malikov, V.N.** – Candidate of Techn. Sciences, Associate Professor, Department of General and Experimental physics, Altai State University, Barnaul, Russia; ORCID iD: 0000-0003-0351-4843; osys11@gmail.com

**Mauey, B.** – PhD., Senior teacher, L.N. Gumilyov Eurasian National University, Astana, Kazakhstan; Joint Institute for Nuclear Research, Dubna, Russia; Scopus Author ID: 57193847043; ORCID ID: 0000-0003-4301-1327; bahytbek01@yandex.kz

**Medetbekov, B.S.** – Master (Sci), Laboratory of Neutron Physics, Institute of Atomic Energy of the Branch NNC RK, Kurchatov, Kazakhstan; Scopus Author ID: 57194243464; medetbekov@nnc.kz

**Neverov, E.** – Doctor of Techn. Sciences, Professor, Institute of Engineering Technologies, Kemerovo State University, Kemerovo, Russia; ORCID iD: 0000-0002-3542-786X; e.n.neverov@gmail.com

**Nuritdinov, I.**– Doctor of phys.-math. sciences, Professor, Chief Researcher, Institute of Nuclear Physics, Academy of Sciences of Uzbekistan, Ulugbek, Tashkent, Uzbekistan; Scopus Author ID: 6601992720; ORCID iD: 0000-0002-9749-8751; izzatilloh@yahoo.com

**Omarova, G.S.** – PhD, Associate Professor, Department of Physics and nanotechnology, Karaganda Buketov University, Karaganda, Kazakhstan; ORCID iD: 0000-0003-2900-2168; guldenserikovna@mail.ru

**Plotnikov, I.** – Candidate of Techn. Sciences, Associate Professor, Institute of Engineering Technologies, Kemerovo State University, Kemerovo, Russia; ORCID iD: 0000-0002-0149-1724; i.b.plotnikov@yandex.com

**Plotnikova, L.** – **Master (Sci.)**, Lecturer, Institute of Engineering Technologies, Kemerovo State University, Kemerovo, Russia; ORCID iD: 0000-0002-8542-2055, l.v.plotnikova@bk.ru

**Popov, Yu.A.** – PhD, Professor, Deputy head of the Laboratory, Laboratory of Neutron Physics, Institute of Atomic Energy of the Branch NNC RK, Kurchatov, Kazakhstan; Scopus Author ID: 57194237762

**Potapov, A.A.** – Doctor of phys.-math. sciences, Professor, Chief researcher, V.A. Kotel’nikov institute of radio engineering and electronics, Russian Academy of sciences, Moscow, Russia; IREE joint laboratory of Fractal Method & Signal Processing, Jinan University, Guangzhou, China; Scopus Author ID: 56375460400; ORCID iD: 0000-0001-9864-3546;

**Prozorova, I.V.** – PhD student, Tomsk Polytechnical University, Russia; Head of the Laboratory of Neutron Physics, Institute of Atomic Energy of the Branch NNC RK, Kurchatov, Kazakhstan; Scopus Author ID: 57220986470

**Rakhadilov, B.K.** – PhD, Associate Professor, Head of the «PlasmaScience» LLP, Oskemen, Kazakhstan; Scopus Author ID: 55539741700, ORCID ID: 0000-0001-5990-7123, [rakhadilovb@mail.ru](mailto:rakhadilovb@mail.ru)

- Sarmanbetov, S.A** – PhD, Al-Farabi Kazakh National University, Almaty, Kazakhstan, sarmanbetov.sanzhar@gmail.com, <https://orcid.org/0000-0003-1749-2163>;
- Serikov, T.M.** – PhD, Associate Professor, Department of Physics and nanotechnology, Karaganda Buketov University, Karaganda, Kazakhstan; ORCID iD: 0000-0003-4302-9674; serikov-timur@mail.ru
- Shalomeev, V.A.** – Doctor of Techn. Sciences, Professor, Vice-Rector for Research, National University “Zaporizhzhia Polytechnic”, Zaporizhzhia, Ukraine; Scopus Author ID: 6505581621; ORCID iD: 0000-0002-6091-837X; shalomeev@zntu.edu.ua
- Sheyko, S.P.** – PhD, Associate Professor, Department of Metallurgical Equipment, Zaporizhzhia National University, Zaporizhzhia, Ukraine; Scopus Author ID: 23095863300; Researcher ID: T-8580-2017; ORCID iD: 0000-0001-5761-4263; ss6309113@gmail.com
- Shishulin, A.V.** – PhD, Pleiades Publ., Ltd, Moscow, Russia; Scopus AuthorID: 57191571862; ORCID iD: 0000-0003-2370-5313
- Shishulina, A.V.** – PhD, Associate Professor, R.E. Alekseev Nizhny Novgorod State Technical University, Nizhny Novgorod, Russia; Scopus AuthorID: 6602952373
- Shmykova, P.A.** – Master student, Department of General and Experimental Physics, Federal State Budgetary Educational Institution of Higher Education "Altai State University", Barnaul, Russia; ORCID iD: 0009-0002-5417-4615; p.shmykova987@gmail.com
- Shynarbek, A.** – Master student, Junior Researcher, Scientific Center «Surface modification of materials», Shakarim University of Semey, Semey, Kazakhstan; ORCID ID: 0009-0009-2877-5178; shinarbekov16@gmail.com
- Smagulov, Zh.K.** – Candidate of phys.-math. sciences, Professor, Karaganda Buketov University, Karaganda, Kazakhstan; Scopus Author ID: 6506808882; ORCID iD: 0000-0002-3412-973X; smagul@mail.ru
- Soldatkhana, D.** – PhD., Senior teacher, L.N. Gumilyov Eurasian National University, Astana, Kazakhstan; Scopus Author ID: 57768566200; ORCID iD: 0000-0001-7981-4100; soldathan.dauren@mail.ru
- Stepanova, O.** – PhD, Associate Professor, Shakarim University of Semey, Semey, Kazakhstan; Scopus Author ID: 56727984100, ORCID ID: 0000-0001-5221-1772; aug11@mail.ru
- Tareq, M.H.** – Master student, Applied Science Department, University of Technology, Baghdad, Iraq; as.21.43@grad.uotechnology.edu.iq
- Tashmetov, M.Yu.** – Doctor of phys.-math. sciences, Professor, Deputy Director for Research, Institute of Nuclear Physics, Academy of Sciences of Uzbekistan, Ulugbek, Tashkent, Uzbekistan; Scopus Author ID: 6602573338; ORCID iD: 0000-0003-1132-0109; mannab@inp.uz
- Temesheva, S.A.** – Master, Department of Physics and Technology, Al-Farabi Kazakh National University, Almaty, Kazakhstan; symbat.temesheva@gmail.com
- Tileu, A.O.** – PhD student, Department of Physics and Technology, Al-Farabi Kazakh National University, Almaty, Kazakhstan; Scopus ID: 57218680509; ORCID iD: 0000-0001-9965-6728; tileu\_ayan2@kaznu.edu.kz
- Tolenova, G.K.** - Master (Eng.), Lecturer, Altynsarin Arkalyk Pedagogical Institute, Arkalyk, Kazakhstan; tolenovagk@gmail.com
- Tsyganov, V.V.** – Doctor of techn. sciences, Academician of the Technical Sciences Academy of Ukraine, Corresponding Member of the Ukrainian Academy of Tribotechnics; Associate Professor, Department of Metal-Cutting Machines and Tools, National University “Zaporizhzhia Polytechnic”, Zaporozhie, Ukraine; Scopus Author ID: 56712109100; ORCID iD:0000-0001-5682-7005; tsyganov705@gmail.com
- Turdybekov, D.M.** - Candidate of chem. sciences, A. Saginov Karaganda Technical University, Karaganda, Republic of Kazakhstan; ORCID iD:0000-0002-0245-022X, turdas@mail.ru
- Turdybekov, K.M.** - Doctor of chem. sciences, Professor, Karaganda Buketov University, Karaganda, Kazakhstan; Scopus Author ID: 7003295323; ORCID iD: 0000-0001-9625-0060; xray-phyto@yandex.kz
- Turlykozhaeva, D.A.** – PhD student, Researcher, Lecturer, Department of Physics and Technology, al-Farabi Kazakh National University, Almaty, Kazakhstan; ORCID iD: 0000-0002-7326-9196
- Umarov, S.Kh.** – Doctor of phys.-math. sciences, Professor, Professor of the Department of Biophysics, Informatics and Information Technology, Bukhara State Medical Institute, Bukhara, Uzbekistan; Scopus Author ID: 670169113; ORCID iD: 0000-0002-2862-4988; salim\_umarov49@mail.ru
- Ussipov, N.M.** – PhD student, Lecturer, Department of Physics and Technology, Al-Farabi Kazakh National University, Almaty, Kazakhstan; Scopus Author ID: 57226319348; ORCID iD:0000-0002-2512-3280; ussipov.nurzhan@kaznu.kz
- Vodennikova, O.S.** – PhD, Associate Professor, Department of Metallurgical Technologies, Ecology and Man-Made Safety, Zaporizhzhia National University, Zaporizhzhia, Ukraine; Scopus Author ID: 57254175800; Researcher ID: T-8580-2017; ORCID iD: 0000-0003-0496-5435; o.s.vodennikova@gmail.com

**Voinash, S.A.** – Master, Leading Engineer, Research laboratory “Intelligent Mobility”, Institute of Design and Spatial Arts, Kazan Federal University, Kazan, Russia; Scopus Author ID: 57194339935; ORCID iD:0000-0001-5239-9883; sergey\_voi@mail.ru

**Vornacheva, I.V.** – Candidate of Techn. Sciences, Associate Professor, Southwestern State University, Kursk, Russia; ORCID iD: 0009-0003-5511-235X; vornairina2008@yandex.ru

**Vurim, A.D.**– PhD, Professor, Chief Specialist of the Nuclear Technologies, Institute of Atomic Energy of the Branch NNC RK, Kurchatov, Kazakhstan; Scopus Author ID: 6507215285

**Zagidullin R.R.** – Candidate of Techn. Sciences, Associate Professor, Kazan Federal University, Kazan, Russia; ORCID iD: 0000-0001-5185-2690, rragidullin@mail.ru

**Zhanabaev, Z.Zh.** – Doctor of Phys.-Math. Sciences, Professor, al Farabi Kazakh National University, Almaty, Kazakhstan; Scopus Author ID: 15840905700; WoS ResearcherID: B-2924-2015; ORCID iD: 0000-0001-5959-2707, zhanabayev.zeinulla@gmail.com

**Zhassulan, A.** – Master (Sci.), Junior Researcher, Scientific Center «Surface modification of materials», Shakarim University of Semey, Semey, Kazakhsta; ORCID ID: 0009-0001-5887-0135; ainur.zhassulan.99@gmail.com

**Zhexebay, D.M.** – Doctor Science of Physics and Mathematics, Al-Farabi Kazakh National University, Almaty, Kazakhstan, zhexebay92@gmail.com, <https://orcid.org/0000-0002-3974-0896>

---



---

## GUIDELINES FOR AUTHORS

*Eurasian Physical Technical Journal* (Eurasian phys. tech. j.) is a peer-reviewed Open Access international scientific journal quarterly publishing original research results on actual problems of technical physics. Since 2019, Eurasian phys. tech. j. has been indexed in the Scopus database on 4 scientific areas: [www.scopus.com/sourceid/21100920795](http://www.scopus.com/sourceid/21100920795). In 2023, according to the analytical platform **SJR** the Eurasian phys. tech. j. is included in **Q3** by all 4 scientific areas.

**Acceptance of the manuscript** for publication in the Eurasian phys. tech. j. is carried out online through website - <https://phtj.buketov.edu.kz/index.php/EPTJ>. Authors should check that their submissions meet all of the following requirements, as submissions may be returned to authors that do not comply with these guidelines.

### **Scientific article topic and content**

A scientific article should contain the results of original scientific research previously unpublished and not intended for publication in other publications.

Manuscript of the article should contain at least 75% of the original text.

Articles should be written in English. The articles topic should correspond to the following scientific fields of **Physics: Energy, Engineering, Materials Science, Physics and Astronomy**.

### **Publication Ethics and Malpractice Statement**

Submission of an article to the Eurasian phys. tech. j. implies that the paper described has not been published previously, that it is not under consideration for publication elsewhere, that its publication is approved by all authors and tacitly or explicitly by the responsible authorities where the paper was carried out, and that, if accepted, it will not be published elsewhere in the same form, in English or in any other language, including electronically without the written consent of the copyright holder. In particular, translations into English of papers already published in another language are not accepted.

For information on Ethics in publishing and Ethical guidelines for journal publication see <http://www.elsevier.com/publishingethics> and <http://www.elsevier.com/journal-authors/ethics>.

The Eurasian phys.tech.j. strictly adheres the Code of Conduct of the Committee on Publication Ethics (COPE), and follows the COPE Flowcharts for Resolving Cases of Suspected Misconduct ([http://publicationethics.org/files/u2/New\\_Code.pdf](http://publicationethics.org/files/u2/New_Code.pdf)).

To verify originality, your article may be checked by the originality detection service Cross Check <http://www.elsevier.com/editors/plagdetect>.

### **Pre-publication process**

**Authors** are responsible for the content of their publications. No other forms of scientific misconduct are allowed, such as plagiarism, falsification, fraudulent data, incorrect interpretation of other works, incorrect citations, etc. Authors are obliged to participate in peer review process and be ready to provide corrections, clarifications, retractions and apologies when needed. All authors of a paper should have significantly contributed to the research.

**Reviewers** should provide objective judgments and should point out relevant published works which are not yet cited. Reviewed articles should be treated confidentially. The reviewers will be chosen in such a way that there is no conflict of interests with respect to the research, the authors and/or the research funders.

**Editors** have complete responsibility and authority to reject or accept a paper, and they will only accept a paper when reasonably certain. They will preserve anonymity of reviewers and promote publication of corrections, clarifications, retractions and apologies when needed.

The acceptance of a paper automatically implies the copyright transfer to the Eurasian phys. tech. j.

All submitted papers will be sent for reviewing to leading experts in the given area.

The Editorial Board of the Eurasian phys. tech. j. will monitor and safeguard publishing ethics.

The editors reserve the right to accept or reject manuscripts.

The article and all documentation must be identified by the name of the 1st author: Akhmetov AA\_et al\_paper; Akhmetov AA\_et al\_fig.1; Akhmetov AA\_et al\_Cover letter; ...

The article text must be formatted according to the **Template**, font - Times New Roman, size -11 pt; line spacing-single; alignment-in width, see <https://phtj.buketov.edu.kz/index.php/EPTJ/about/submissions#authorGuidelines>

***An article should consist:***

**Title:** includes a separate line on the left the UDC index, Title of the article, information about the authors- surname and initials, name of institution, city, country, e-mail of a corresponding author. The author\* who submitted an article for publication will be considered as a corresponding author.

**Abstract** should consist of at least 5-6 sentences, not exceeding 200-250 words without formula, references, abbreviations. An abstract is a short and powerful summary that describes the focus and subject of a research paper. It could contain the information about why the research study was done, background, what the methodology was and something about the findings of the author(s).

**Keywords:** at least 3-10 basic terms or short phrases used in the article.

**The text should be divided on structural parts:** Introduction, Main part (Theoretical part, Methods and materials or Experimental technique), Results and Discussion, Conclusions.

**Conclusions:** formulating main results; a comparison of the results with the existing data on this topic; assessment of scientific novelty and practical value of the results.

**Acknowledgments or Funding** may be shown at the end of the article text, before References.

**References:** a bibliographic list is compiled according to the requirements:

- Books, abstracts, patents: Surname and initials of the authors (it is enough to indicate the first three or one surnames, et al), *Title of the book* in italics, publish house or city, year and total number of pages.
- Journals, collections of papers, conference proceedings - Surname and initials of the authors (the first three are enough), the title of the article, the *Title of the journal* in italics (you can use the abbreviated title), city and / or country, year, volume, issue number, pages of the "begining and end" (pp. ... - ... ).
- Internet links also must to indicated the authors, the title and URL

The authors should represent References according to the requirements of international journals on physics, but should to consult preliminarily for standard abbreviations of journal's names. More information on references guidelines for journal publication you can see in Harvard reference system -

**Ошибка! Недопустимый объект гиперссылки.**

All references must be numbered in the text (for example, [1], [2-4]) and listed in numerical order.

**All abbreviations and acronyms**, with the exception of obviously well-known, should be deciphered at first use in the text.

**Equations** in your paper have to be written using the Microsoft Equation Editor or the MathType.

**Tables**, numbered and titled, should be inserted into the text (Times New Roman, size - 10 pt) or have been presented as an appendix at the end of the article.

**Figures** should be prepared in a digital form suitable for direct reproduction. Figures shall be submitted on the separate sheets or can be included into the text.

**The manuscript volume**, including text, formulas, figures, bibliography, should not exceed 12 pages including tables, figures (no more than 8-10) and references (no more than 30-35) of text typed on a computer using Microsoft Word editor. The review article should not exceed 20 pages with no more than 15 figures.

***List of required documents******The following files must be uploaded to the journal's website:***

1. Text of the article, with pictures (\*.doc);
2. Figure, Picture, Photo (fig1.jpg, fig2.pcx, ...);
3. Figure captions (\*.doc);

4. A Cover letter - from a university, research institute or an organization licensed to conduct research activities, must be issued on an official letterhead and / or certified by the organization seal. The management officially confirms by this letter that the article (the title of the article and the names of the authors are indicated in English) doesn't contain any information constituting state or commercial secrets, and the article can be published in the Open Press. Authors must upload a copy of the signed Cover Letter in Pdf format to the Journal website.

*It's necessary to upload by separately 2 files in English, and in Russian for authors from Russia, and in Kazakh for authors from Kazakhstan:*

5. Article's data: Surname and initials of the authors, the article title, abstract, keywords.

6. Information about each co-author: full name, academic degree, academic title, place of work or study, title of organization, city, country, SCOPUS Author ID or ORCID iD; and contact details (e-mail, phone).

7. Receipt of payment. Authors should pay for the publication only after receiving notification about a positive decision of the reviewers.